Elastic Modulus Prediction of Polymer Nanocomposites: Production and Characterization of Cellulose Nanocrystal Reinforced Polyamide Nanocomposites

by

Eyup Can Demir

A thesis submitted in partial fulfillment of the requirements for the degree of

Doctor of Philosophy

Department of Mechanical Engineering
University of Alberta

Abstract

Polymer nanocomposites can fulfill their potential use in engineering applications as researchers and engineers gain a better understanding of nanocomposites' modelling, production, and characterization methods. Recent polymer nanocomposite studies point out that existing modelling tools either require a significant amount of computational power or cannot capture experimental outcomes due to oversimplifications. This research mainly focuses on the development of a model for polymer nanocomposites to predict their elastic properties efficiently and accurately and to understand the parameters that have direct effects on the properties of the nanocomposites. The thesis also presents experimental work that involves development of an innovative additive manufacturing method and the detailed characterization of polymer nanocomposites.

A novel model that consists of a three-phase Mori-Tanaka model coupled with the Monte-Carlo approach is developed to predict the elastic modulus of nanocomposites. As opposed to existing models, this model defines agglomerates and utilizes a machine learning tool to identify three phases of the proposed composite system from simulated dispersion or micrograph images. Three phases of the proposed composite system are defined as agglomerates, free particles (non-agglomerated particles), and matrix. The parameters that define these three phases and other parameters such as particle loading, orientation, aspect ratio, agglomerate property are systematically investigated to perform a sensitivity study on parameters of the developed model. This sensitivity study reveals that agglomeration tendency is highly dependent on particle dispersion and critical distance defined in the model. The sensitivity study also prove that the

model is sufficiently general that it can be applied to various types of polymer nanocomposites to predict their properties. The model is verified with polyamide 6 (PA6) cellulose nanocrystals (CNC) nanocomposites that are produced using spin coating method. The proposed novel model and existing conventional model predictions are compared, and it is shown that the proposed model can follow the trend of experimental results much better than the conventional ones.

Further, an innovative direct extrusion-based additive manufacturing technique is used for nanocomposite production and the experimental findings are again compared to that of model's predictions to see the applicability of the model in 3D printed nanocomposites. This production technique can be used for nanocomposite production in prototyping or customized engineering parts at a laboratory scale. It eliminates the filament production and use in extrusion-base additive manufacturing. CNC and PA12 are used to study the proposed direct additive manufacturing technique. CNC is dispersed and PA12 is dissolved in a common solvent and then cast on the silicone baking mate for drying. The cast mixture is turned into powder and then extruded using a small pellet extruder that is designed as 3D printing head to obtain nanocomposite extrudates. The extrudates are uniaxially tested and demonstrated great enhancement in their mechanical properties. Due to promising results, a commercial 3D printer is equipped with this extruder head and dog-bone PA12 nanocomposites prepared and uniaxially tested. While elastic modulus substantially increases, yield strength shows a slight improvement. A detailed TEM analysis is performed at various CNC loadings and the retrieved TEM images are analyzed to predict the elastic modulus of PA12 nanocomposites using the proposed model. A good agreement is observed between model predictions and experimental results. The result of this work shows, for the first time that, PA12 can be 3D printed with CNC, and our direct extrusion technique can be utilized for small batch productions in research laboratories.

Preface

Certain sections of this thesis have been published or will be submitted to be published in peer-reviewed journals. These sections were conducted in collaboration with others.

Chapter 1 provides an introduction and background of the thesis.

Chapter 2 has been published in the Journal of Composite Materials as *E. C. Demir, A. Benkaddour, D. R. Aldrich, M. T. McDermott, C. I. Kim, and C. Ayranci," A predictive model towards understanding the effect of reinforcement agglomeration on the stiffness of nanocomposites," Vol. 56, Issue 10, 2022.* The author contributed to modelling conceptualization and development, code writing in Python, code optimization in MATLAB, specimen production and testing, data analysis, and manuscript preparation. Dr. A. Benkaddour contributed to specimen production and editing. D. R. Aldrich contributed code transfer from Python to MATLAB and code optimization in MATLAB. Dr. M. T. McDermott, Dr. C. I. Kim and. Dr. C. Ayranci contributed to modelling conceptualization and editing.

Chapter 3 has been submitted to the Journal of Composite Materials and is currently under review as *E. C. Demir, M. T. McDermott, C. I. Kim, and C. Ayranci," Towards better understanding the stiffness of nanocomposites via modelling parameters and experiments,"* The author contributed a manuscript conceptualization and development, code writing in

Python, code optimization in MATLAB, specimen production and testing, data analysis, manuscript preparation. Dr. M. T. McDermott, Dr. C. I. Kim and. Dr. C. Ayranci contributed to modelling conceptualization and editing.

Chapter 4 will be submitted to a peer-reviewed journal for publication. The author contributed to the experimental design, production, and characterization. Testing of specimens, data analysis, image analysis, code development, and model implication based on image analysis. Dr. Irina Garces contributed to the experimental setup. Dr. M. T. McDermott, Dr. C. I. Kim and Dr. C. Ayranci supervised the production and modelling steps and contributed to editing.

Chapter 5 will be submitted to a peer-reviewed journal for publication. The author conducted the experimental work, production, testing and data analysis, and digital image correlation. Dr. M. T. McDermott, Dr. C. I. Kim, and Dr. C. Ayranci's supervised the work and contributed to manuscript editing.

Chapter 6 concludes the thesis with future recommendations.

Dedicated

To my love Yagmur and my baby Defne

To my parents Nazli and Zeki

To my siblings Dilara and Deniz

To my hero, grandmother Gullu Yurdakul

Acknowledgment

First and foremost, I would like to thank my supervisor Cagri Ayranci who has always been more than a supervisor. I always felt his support, sometimes as a professor, sometimes as a friend, and sometimes as someone from my family. I was always comfortable while consulting him on any topic related to research, career, life in Edmonton, camping, food, business, and almost everything in this journey. Cagri hocam thank you for every minute that you spent with me! I learned a lot from you as a research and teaching assistant. They are all invaluable to me. I am aware this journey comes to an end; however, I know we will be in touch and probably work together in the coming years.

I would like to extend my thanks to Dr. Chun Il Kim who was always ready to help me with the mathematical and modelling perspective of the research. Dr. Kim kept me motivated to learn and think about mathematical problems. Dr. Kim, I appreciate your guidance on this journey. I would like to thank Dr. Mark McDermott who always asked great questions in our meetings. He always brought fun to the science and meetings along with Cagri. Dr. McDermott, I appreciate your guidance, discussions, and support in this work!

Now, it is time to thank my lab mates. A very special thanks go to my colleague, friend, and co-founder Irina Garces. Irina has been always there not just for me but for everyone that I know from Mechanical Engineering Department. I always saw her working on various things and motivating someone including me! I will miss our chat during the research in the lab. I know we will work together in the future. Thanks for everything! Abdelhaq Benkaddour, you are a great person, friend, and researcher. I always consulted you whenever I have questions related to chemistry or life. I know you were always there no matter what the topic was. I appreciate your friendship and guidance. I want to thank Yu Chen and Laura Chen for their support in managing the labs. I knew I could trust you anytime related to teaching assistantship or laboratory management. I want to thank Nicole Jankovic as she was always helpful on experiments and chemistry discussions. Kacie Norton, thank you so much on your help with my difficult TEM sample preparation. Lastly, I

would like to thank my remaining lab mates for creating a friendly environment in and out of the lab Samir, Daniel, Abiy, Allan, Bora, Beste, Alyaan, and Panxi.

I want to thank special people who made this research possible with their friendship in Edmonton. David Sulz and Tanya Berry, you are my great friends that made me feel Edmonton and Canada are also a home for me. I cannot list the memories that we had, thank you so much. I also would like to thank my ECC friends; Rick, Gavin, Nicola, Milad, Mory, and Shiva. Wednesdays were always fun with you. I want to extend my deepest thanks to Sinem Senol for making me feel I have a big sister in Edmonton. Thank you so much all.

I would like to thank my mother-in-law, Aynur Sarioglu, for coming here as soon as I broke my ankle in this spring. She came right away from Turkey to help us out. She was endless support for Yagmur, Defne and me. Kenan abi, thanks a lot for being with us in one of our most stressful times. You always brought fun to the table in these difficult times.

I want to thank my parents Nazli and Zeki, my siblings, Dilara, Deniz, and Yusuf and my grandmother Gullu. I feel lucky to be a member of this great, open-minded, and curious family. I would not be here at all without your encouragement, support, and love. I love you all.

My love Yagmur, we got into Ph.D./Canada journey together and today I am completing the Ph.D. work. I and everyone know that I would not come here and complete this work without your support and encouragement. You always directed me in the right direction when I was in difficult situations. I love your solid view on how to solve a problem. When I was tired, you always said it is okay! Thank you so much!

Defne, you are my last but biggest motivation for completing this Ph.D. While I am writing this, I am smiling because I am thinking about your 2-month-old eyes, nose, lips, ears and of course cheeks. You are so cute! Thanks for coming into our life!

Table of Contents

List of Tables

List of Figures

Chapter 1

Introduction

Polymer nanocomposites can be favourable over their traditional counterparts as a low amount of nanofillers can provide cost-effective, light weight, and easy processability solutions for various applications including textile [1], transportation [2], construction [3], sports equipment [4], electronics [5][6], and the biomedical [7] industries. One of the earliest applications of polymer nanocomposites is in the automotive industry. Toyota's patent on the nanoclay-polyamide system in 1988 is considered a turning point for the commercial capabilities of nanocomposites [8]. Toyota launched the first automotive application of polymer nanoclay composites with Nylon-6 in timing belt covers in 1993. Then, they continued to produce body panels, and bumpers using nanoclay [5]. Toyota's adoption of nanocomposites demonstrated the commercial value of nanocomposites, which resulted in increased interest in discovering the advantages of nano-size fillers over macro-scale fillers in composite applications. For example, Wilson Sporting Goods offers a double core tennis ball where the core of the ball is coated with a nanoclay-filled butyl-based rubber [5]. The coating greatly restricts airflow from the core of the ball thanks to the great barrier properties of nanoclay-filled rubber. Ube Industries is another company that uses nanocomposites as a

commercial product [5]. They commercialized nylon-clay nanocomposite films that provide two times higher permeability than nylon and are used in food packaging [5]. These are only a few commercialization examples of nanocomposites. This commercialization potential and promising properties of polymer nanocomposites motivate the researchers to work on this research area. The increase in the number of publications on polymer nanocomposite over the years, shown in Figure 1.1, clearly exhibits the popularity of polymer nanocomposites in academia.

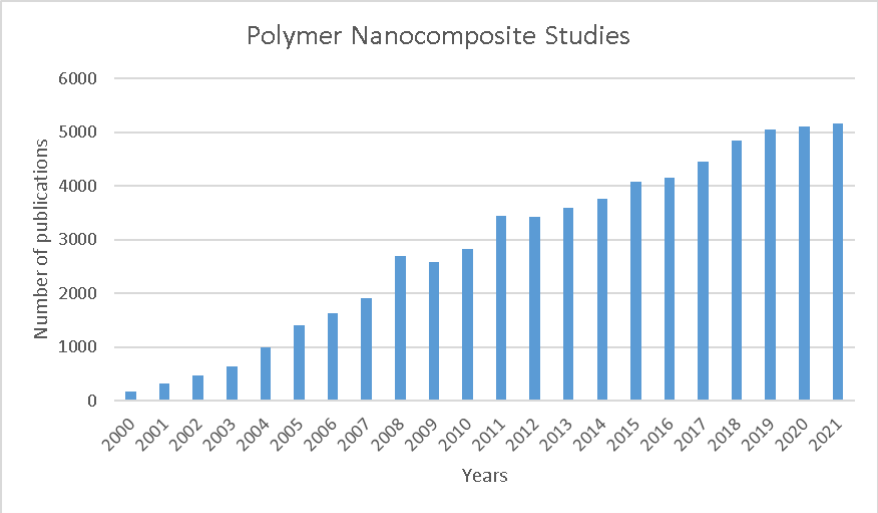

Figure 1.1. The number of publications on polymer nanocomposite studies. The graph is generated using “polymer” and “nanocomposite” keywords in the Scopus database.

Advancements in polymer nanocomposites are only possible with a comprehensive understanding of effect of the constituents on the overall material. Although experimental research uncovers the relationship between the material structure, process, and properties and theoretical research guides scientific reasoning and future work, nanocomposites' sophisticated characterization and manufacturing methods bring enormous cost to establishing structure, process, and property relationships. Thus, understanding the property changes of nanocomposites using predicting models is necessary to design and produce nanocomposite materials efficiently. While it can be

theorized that low concentrations of nanoparticles could remarkably improve polymers' properties due to nanoparticles' large surface-to-volume ratio and exceptional properties, studies show that this is challenging in practice. The main reasons for not obtaining theoretical values include incompatibility between filler and matrix, filler agglomeration, poor interface, and processing difficulties.

Reinforcement of polymers with nanofillers is a growing area of research [9,10]. Some common nanofillers to reinforce polymers are carbon nanotubes [11–13], nanoclay [14–16] and cellulose nanocrystals [17–19]. Various polymers are reinforced with these nanofillers; however, engineering thermoplastics have an important place as they are already used in numerous critical places and applications including automobile [20] and aerospace [21] parts, housing [22], sports equipment [4],load-bearing units [23], sensors [24], and mechanic energy storage [25]. Each application could require different properties and design criteria such as transparency, conductivity, chemical resistivity, or high-temperature durability. Stiffness is one of many design criteria that carries significant importance for mechanical engineering applications.

This study proposes a model to predict the elastic moduli of nanocomposites at various nanoparticle concentrations and proposes an innovative 3D production method to expand nanocomposite applications, particularly for low-volume and laboratory-scale nanocomposite production. The proposed model is based on the Mori-Tanaka model that is coupled with the Monte-Carlo approach. The model is validated with cellulose nanocrystals (CNC) reinforced polyamide composites that are prepared using solvent and melt-based processes. The melt-based process is adapted to an innovative 3D printing method to obtain CNC reinforced polyamide composites. The outcomes of this thesis could be beneficial for engineers to form design curves

for nanocomposites and broaden the use of 3D printing in nanocomposite productions, particularly with cellulose nanocrystals in polyamides.

1.1 Background

Optimal nanoparticle loading in a polymeric material can be achieved with accurate material property predictions. Over the last five decades, researchers have developed various numerical and analytical tools to predict materials' property changes [26]. Figure 1.2 shows a general material modelling approach as a diagram.

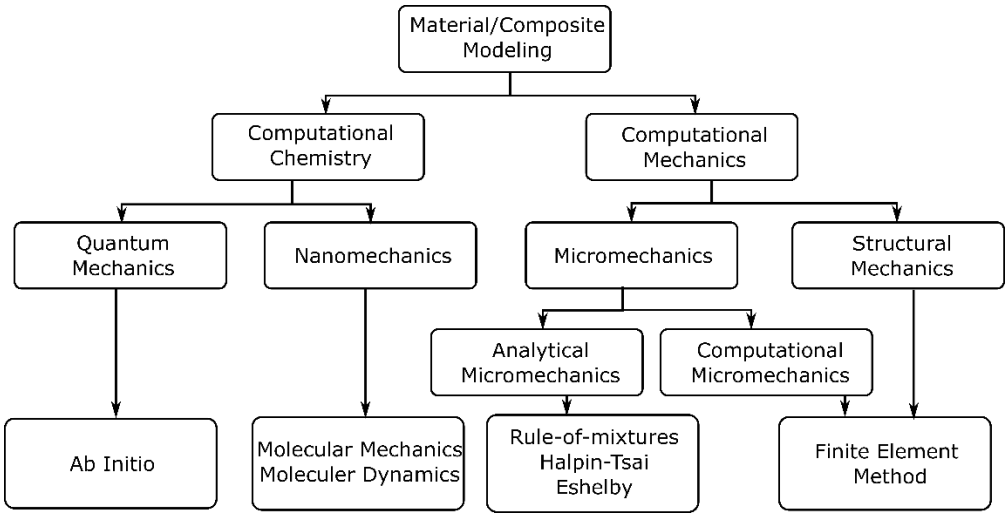

Figure 1.2. Material modelling diagram adapted from [26].

Analytical micromechanics that is developed for traditional macro sized fillers is a topic of debate whether analytical micromechanics and continuum mechanics can be applied to nanocomposites; however, many studies show strong predictions [27,28]. Sandler et. al, [13] highlighted that the stiffness of electrospun nanocomposites' can be assessed using Voigt and Reuss modes as long as nanoparticle concentration is known. They used carbon nanotubes and carbon fiber as a reinforcing agent in the polyamide 12 matrix and observed a discrepancy between the model predictions and

the experimental results [13] . They noted that heterogeneous matrix crystallization due to the different reinforcing agents created this discrepancy. In another study, Goinj et. al, [29] modified Halpin-Tsai with experimental factors and suggested that there is a well-agreement between experimental results and model predictions. While these studies tell that micromechanics can be applied to nanocomposite materials, the counter argument is that they oversimply the nanocomposite systems with their assumptions such as perfect bonding between nanoparticles and matrix and uniform nanoparticle dispersion.

Molecular dynamics is another effective tool that is employed to predict the stiffness of nanocomposites. Lin et. al., [30] simulated graphene-reinforced Poly(methyl methacrylate) and predicted their stiffness using molecular dynamics. They suggested that there is a large discrepancy between molecular dynamics results and the Voigt and Reuss model predictions. It was noted that the latter could not be appropriate to predict nanocomposites' stiffness due to invalid assumptions [30]. Arash et. al., [31] suggested that the scattered experimental data in carbon nanotube reinforced nanocomposites can be captured by molecular dynamics simulations as molecular dynamics can provide detailed information on interfacial interactions. Molecular dynamics has capabilities to simulate detailed interactions at the molecular level; however, it requires high computational power as it covers systems to the level of millions of atoms in 1x1x1 μ^3 [32]. On the other hand, nanocomposite material expands to macro-size engineering applications which require other modelling approaches. Further, the possibility of inaccurate force fields could limit molecular dynamics applications [32].

Lastly, the finite element method (FEM) is a commonly used method to predict the mechanical behaviour of polymer nanocomposites. It is a numerical method that is used to solve mathematical equations. Liu et al., [33] calculated the effective material properties of CNT reinforced polymer

nanocomposites using nanoscale representative volume element and FEM. They used 3-dimensional elasticity theory and extended the rule of mixtures to estimate the elastic modulus of representative volume elements. The method was applied for only one CNT in a matrix and may not converge to a valid solution for complex structures. Wang et. al., [34] used a 3-dimensional micromechanical finite element method to predict the effect of the nano-reinforcement. They proposed an interfacial region and calculated the properties based on averaging the elastic properties of the nanoparticles and the matrix. Although the FEM method can be useful for predicting the mechanical response of parts, the computation is costly in FEM, and inappropriately established problem and solution settings can result in diverse outcomes.

The literature is currently missing a model that can accurately predict the stiffness of nanocomposites at different nanoparticle concentrations. Agglomeration of nanoparticles, the interface between nanoparticles and matrix and/or the nanoscale effect on matrix make the composite system difficult to model. Although small-length scale models and simulations can be accurate, they require high computational power and take a long time to execute. On the other hand, conventional models may fail to predict the elastic modulus of nanocomposites due to their aforementioned idealized assumptions. A model that can accurately predict the elastic modulus of nanocomposites without involving high computational resource is needed for stiffness-critical engineering applications. While some conventional models predict linear or exponential elastics modulus values with respect to nanoparticle loadings, empirical findings show that the elastic modulus of nanocomposites increases until an optimal point and then reaches a plateau value or decreases with the increasing nanoparticle loading. Differences in the trend of conventional model predictions and experimental outcomes lead to discrepancies. In this work, a novel model that

couples a continuum-based model with the Monte-Carlo method to lower these discrepancies by accurately predicting the elastic modulus of nanocomposites.

The proposed model has various parameters. A systematic parametric study is required for a model to understand the importance and effect of model parameters on the elastic modulus of nanocomposites. Thus, a sensitivity analysis of model parameters is conducted, and the capabilities of the model are studied. The proposed model is verified with various cellulose nanocrystal reinforced polyamides where the used production methods promote innovative nanocomposite manufacturing.

The promising properties of polymer nanocomposites [31,35–37], the demand for multifunctional materials [38] and advancement in 3D printing motivated researchers and start-ups to use extrusion-based additive manufacturing (EBAM) in 3D nanocomposite production [11,39–41]. A common EBAM uses a filament as the building material for 3D printing [42]. Many researchers melt blend nanoparticles and polymers during filament production [43–45]. Although EBAM with filament use is a scalable production method, the melt blending during filament production leads to agglomeration of nanoparticles [46,47] and requires a high amount of materials. These two issues limit the efficiency of nanocomposite research where only a small amount of material is available.

Various mixing methods such as twin-screw extruders [48] or internal batch mixers [49] have been used for better nanoparticle dispersion at commercial [48] or newly developed small lab-scale extruders [50]. Although some promising results were obtained [50,51]; the agglomeration, right amount of material and obtaining consistent diameter in filament production, and double heating cycle, are still ongoing issues with filament used in 3D nanocomposite printing. The thesis promotes an innovative 3D printing method that eliminates the production and use of filaments

and provides a good dispersion of nanoparticles. A direct extrusion-base additive manufacturing method with solvent mixing is explored for nanocomposite production. The feasibility of the method is studied with a natural fiber reinforced engineering polymer, more precisely with cellulose nanocrystals reinforced polyamide 12 nanocomposites.

Natural fibers have been utilized as green reinforcing agents to reinforce polymers due to their natural abundance and high stiffness. Woods and plants are natural composites made up of approximately 40-50 w% cellulose microfibrils of reinforcing agent and a matrix containing lignin, waxes, hemicellulose and trace elements [52]. Thus, it can be claimed that cellulose is the most abundant organic polymer on the earth. Cellulose $(C_6H_{10}O_5)_5$ is renewable and biodegradable material that can be found in various crystalline (I, II, III, and IV) and amorphous forms.

The high-strength nano-size crystalline part of the cellulose is called cellulose nanocrystals (CNC). Owing to cellulose's hierarchical structure, shown in Figure 1.3, CNC can be extracted via mechanical or chemical treatments. Among the many methods used for CNC extraction [53], chemical treatment is the most commonly used method to extract CNC from wood plump [53]. In this chemical process, cellulose is first hydrolyzed by a strong acid such as hydrochloric or sulfuric acid. Then, sonication is used to dissolve amorphous cellulose and to release nanosize crystalline cellulose. This method results in rod-like CNC with a high aspect ratio (length to diameter ratio). The morphology and surface chemistry of CNC depends on the source and extraction strategy. For example, cotton provides an aspect ratio of 27 [54] and tunicin provides an aspect ratio of 67 [55]. Similarly, the extraction strategy changes the surface chemistry. The use of sulfuric acid as a hydrolyzing agent forms anionic sulphate ester groups on the CNC surface [53]. The surface of CNC can be physically coated or chemically grafted to adjust surface polarity. The modified or non-modified CNC is blended into a polymeric matrix to obtain outstanding mechanical

properties; however, mechanical properties could be different than predicted mechanical properties.

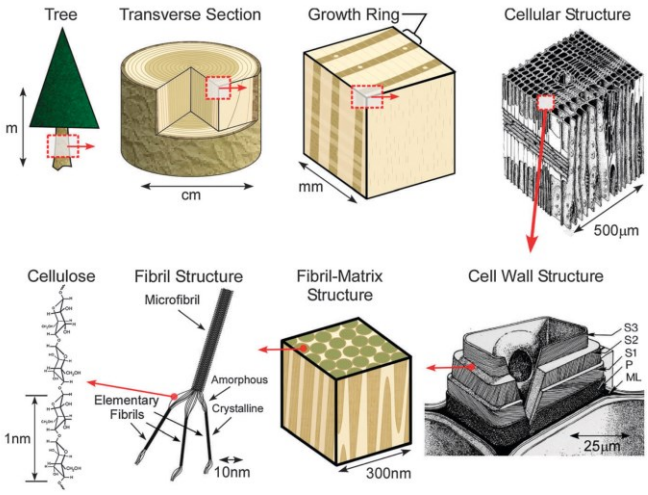

Figure 1.3. Schematics of the hierarchical structure of tree and cellulose, copy right is obtained from [56] IOP Publishing Ltd.

Polyamides (PA), commonly known as nylons, are one of the first engineering plastics. They are semicrystalline structure polymers with high service temperatures and have a high degree of chemical resistance, stiffness, and toughness [57]. Varieties of polyamides (PA6, PA6,6, PA11 PA12 etc.) are manufactured and named according to their monomer type. Figure 1.4 shows the monomer structure of the Polyamide 6 (PA6) and Polyamide 12 (PA12). The number of carbon between amide groups (RC(=O)NR′R″) is represented in the name of the polyamides. For example, while PA6 has 6 carbons between amide groups, PA12 has 12 carbons. Amide groups in monomers make the polyamides polar [58]. The polarity of polyamides depends on the amide group density in the monomer. Higher polarity results in more hydrogen bonding. Higher hydrogen [59] bonding brings them superior mechanical properties compared to other polymers [60].

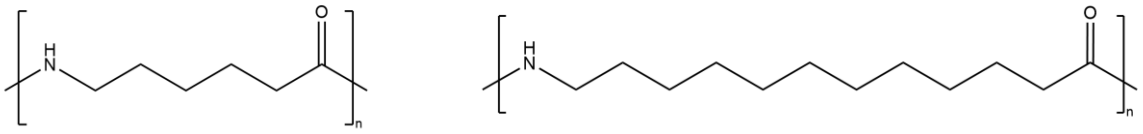

(a) (b)

Figure 1.4. Schematic illustration of the repeating unit of (a) PA6 and (b) PA12 adopted from [61].

Polyamide 6 and 12 are great candidates to explore CNC's reinforcing potential on their mechanical properties as they have different hydrophilicity and melting points. Polyamide 6 is extensively used for load-bearing applications, particularly in the automobile industry; however, the high processing temperature of PA6 could limit the use of cellulose nanocrystals. Polyamide 12 can also be an excellent matrix material for cellulose nanocrystal as it has a lower process temperature. Their distinct properties and interactions with CNC can lead to innovative manufacturing technologies for natural fiber-reinforced composites.

In this study, CNC is used to reinforce PA6 and PA12 with various production methods at different CNC concentrations. The produced nanocomposite samples are used to verify the developed model. The findings of this study could be used as a significant step for nanocomposite modelling, 3D nanocomposite production for lab-scale prototyping and CNC use in engineering polymers.

1.2 Research Motivation and Thesis Objectives

Various models predict the elastic modulus of nanocomposites; however, most of them fail to predict elastic modulus at high concentrations of nanoparticles accurately, or they require massive computational power with complex model preparation steps. A model that is easily applied to predict the elastic modulus of nanocomposite would help engineers advance manufacturing

technologies and optimize the use of nanoparticles. This study is aimed toward addressing this gap by contributing to the modeling, production and characterization of polymer nanocomposites.

To this end, there are 4 objectives to this thesis:

1- To develop an analytical model that is simple to apply and yet accurate enough to predict the elastic modulus of nanocomposites with respect to nanoparticle concentrations
2- To verify the model and define key parameters in the model to understand and capture the effect of agglomeration on the stiffness of nanocomposites
3- To explore an innovative method that offers nanocomposite production with good nanoparticle dispersion
4- To develop a novel production method for extrusion-based additive manufacturing of polymer nanocomposites: CNC reinforced polyamide 12

1.3 Content Overview

The thesis consists of 6 chapters. Some work in the thesis is published in peer-reviewed journals, and some are or will be submitted to peer-review journals.

Chapter 2 describes the development of a model and the experimental work required to verify the model. The Mori-Tanaka model and the Monte-Carlo approach for predicting agglomeration behaviour and nanocomposites' elastic modulus are presented. The developed model captures the experimental results of the CNC reinforced spin-coated PA6 films. This is the first study that shows CNC in PA6 matrix under a transmission electron microscope in the literature. This chapter is published in the Journal of Composite Materials [62].

Chapter 3 presents a sensitivity study of the developed model to better understand key parameters in the model. The effects of agglomeration, particle shape, aspect ratio, critical distance, and

particle dispersion on the elastic modulus are investigated. A version of this chapter is submitted for publication in a peer-reviewed journal and is currently under review.

Chapter 4 presents an innovative production method for extrusion-based additive manufacturing of polymer nanocomposites. The method investigates 3D printing for low-volume materials and promotes the elimination of the filament from extrusion-based additive manufacturing. The effect of CNC concentration on the crystallographic and mechanical properties of PA12 is shown. Detailed visual analysis and polymer characterization are conducted. Transmission electron microscopy images are used in the developed model to predict the elastic modulus of CNC reinforced PA12. A good agreement is observed between experimental results and predictions. A version of this chapter is being prepared to be submitted to a peer-reviewed journal.

Chapter 5 focuses on the application of the method Chapter 5 focuses. PA12 specimens are 3D printed with the addition of CNC for the first time. The effects of CNC on the mechanical behaviour of the specimens are investigated. A version of this chapter is being prepared to be submitted to a peer-reviewed journal.

Chapter 6 concludes the entire thesis with some future recommendations.

REFERENCES

[1] M. Ouederni, Polymers in textiles, INC, 2020. https://doi.org/10.1016/b978-0-12-816808-0.00010-x.

[2] A. Patil, A. Patel, R. Purohit, An overview of Polymeric Materials for Automotive Applications, Mater. Today Proc. 4 (2017) 3807–3815. https://doi.org/10.1016/j.matpr.2017.02.278.

[3] A.M. Hameed, M.T. Hamza, Characteristics of polymer concrete produced from wasted construction materials, Energy Procedia. 157 (2019) 43–50. https://doi.org/10.1016/j.egypro.2018.11.162.

[4] M.S. Laad, Polymers in sports, INC, 2020. https://doi.org/10.1016/b978-0-12-816808-0.00015-9.

[5] A. Dasari, Y. Zhong-Zhen, Y.-W. Mai, Polymer Nanocomposites: Towards Multi-Functionality, 2016. http://dx.doi.org/10.1021/bk-2002-0804.ch011.

[6] Y. Wang, K.S. Chen, J. Mishler, S.C. Cho, X.C. Adroher, A review of polymer electrolyte membrane fuel cells: Technology, applications, and needs on fundamental research, Appl. Energy. 88 (2011) 981–1007. https://doi.org/10.1016/j.apenergy.2010.09.030.

[7] J.W. Leenslag, A.J. Pennings, R.R.M. Bos, F.R. Rozema, G. Boering, Resorbable materials of poly(l-lactide). VII. In vivo and in vitro degradation, Biomaterials. 8 (1987) 311–314. https://doi.org/10.1016/0142-9612(87)90121-9.

[8] A. Okada, Y. Fukushima, M. Kawasumi, S. Inagaki, A. Usuki, S. Sugiyama, J. Wiley, C. Chemical, T. Dictionary, U.S. 4,739,007, (1988).

[9] H. Kargarzadeh, M. Mariano, J. Huang, N. Lin, I. Ahmad, A. Dufresne, S. Thomas, Recent developments on nanocellulose reinforced polymer nanocomposites: A review, Polymer (Guildf). 132 (2017) 368–393. https://doi.org/https://doi.org/10.1016/j.polymer.2017.09.043.

[10] S. Fu, Z. Sun, P. Huang, Y. Li, N. Hu, Some basic aspects of polymer nanocomposites: A critical review, Nano Mater. Sci. 1 (2019) 2–30. https://doi.org/10.1016/j.nanoms.2019.02.006.

[11] A. Mora, P. Verma, S. Kumar, Electrical conductivity of CNT/polymer composites: 3D printing, measurements and modeling, Compos. Part B Eng. 183 (2020) 107600. https://doi.org/10.1016/j.compositesb.2019.107600.

[12] M. Rouway, M. Nachtane, M. Tarfaoui, N. Chakhchaoui, L.E. Omari, F. Fraija, O. Cherkaoui, Mechanical Properties of a Biocomposite Based on Carbon Nanotube and Graphene Nanoplatelet Reinforced Polymers: Analytical and Numerical Study, J. Compos. Sci. . 5 (2021). https://doi.org/10.3390/jcs5090234.

[13] J.K.W. Sandler, S. Pegel, M. Cadek, F. Gojny, M. Van Es, J. Lohmar, W.J. Blau, K. Schulte, A.H. Windle, M.S.P. Shaffer, A comparative study of melt spun polyamide-12 fibres reinforced with carbon nanotubes and nanofibres, Polymer (Guildf). 45 (2004) 2001–2015. https://doi.org/10.1016/j.polymer.2004.01.023.

[14] Y. Xia, M. Rubino, R. Auras, Interaction of nanoclay-reinforced packaging nanocomposites with food simulants and compost environments, 1st ed., Elsevier Inc., 2019. https://doi.org/10.1016/bs.afnr.2019.02.001.

[15] K. Hbaieb, Q.X. Wang, Y.H.J. Chia, B. Cotterell, Modelling stiffness of polymer/clay

nanocomposites, Polymer (Guildf). 48 (2007) 901–909. https://doi.org/10.1016/j.polymer.2006.11.062.

[16] N. Sheng, M.C. Boyce, D.M. Parks, G.C. Rutledge, J.I. Abes, R.E. Cohen, Multiscale micromechanical modeling of polymer/clay nanocomposites and the effective clay particle, Polymer (Guildf). 45 (2004) 487–506. https://doi.org/10.1016/j.polymer.2003.10.100.

[17] P.M. Visakh, S. Thomas, K. Oksman, A.P. Mathew, Cellulose nanofibres and cellulose nanowhiskers based natural rubber composites: Diffusion, sorption, and permeation of aromatic organic solvents, J. Appl. Polym. Sci. 124 (2012) 1614–1623. https://doi.org/10.1002/app.35176.

[18] K.N.M. Amin, N. Amiralian, P.K. Annamalai, G. Edwards, C. Chaleat, D.J. Martin, Scalable processing of thermoplastic polyurethane nanocomposites toughened with nanocellulose, Chem. Eng. J. 302 (2016) 406–416. https://doi.org/10.1016/j.cej.2016.05.067.

[19] K. Oksman, Y. Aitomäki, A.P. Mathew, G. Siqueira, Q. Zhou, S. Butylina, S. Tanpichai, X. Zhou, S. Hooshmand, Review of the recent developments in cellulose nanocomposite processing, Compos. Part A Appl. Sci. Manuf. 83 (2016) 2–18. https://doi.org/10.1016/j.compositesa.2015.10.041.

[20] S.A. Begum, A.V. Rane, K. Kanny, Applications of compatibilized polymer blends in automobile industry, Elsevier Inc., 2019. https://doi.org/10.1016/B978-0-12-816006-0.00020-7.

[21] S.W. Ghori, R. Siakeng, M. Rasheed, N. Saba, M. Jawaid, The role of advanced polymer materials in aerospace, Elsevier Ltd, 2018. https://doi.org/10.1016/B978-0-08-102131-

6.00002-5.

[22] M. Moradibistouni, B. Vale, N. Isaacs, Evaluating the use of polymers in residential buildings: Case study of a single storey detached house in New Zealand, J. Build. Eng. 32 (2020) 101517. https://doi.org/10.1016/j.jobe.2020.101517.

[23] A. Nouri, A. Rohani Shirvan, Y. Li, C. Wen, Additive manufacturing of metallic and polymeric load-bearing biomaterials using laser powder bed fusion: A review, J. Mater. Sci. Technol. 94 (2021) 196–215. https://doi.org/10.1016/j.jmst.2021.03.058.

[24] B. Adhikari, S. Majumdar, Polymers in sensor applications, Prog. Polym. Sci. 29 (2004) 699–766. https://doi.org/10.1016/j.progpolymsci.2004.03.002.

[25] J.H.D. Foard, D. Rollason, A.N. Thite, C. Bell, Polymer composite Belleville springs for an automotive application, Compos. Struct. 221 (2019) 110891. https://doi.org/10.1016/j.compstruct.2019.04.063.

[26] P.K. Valavala, G.M. Odegard, Modeling techniques for determination of mechanical properties of polymer nanocomposites, Rev. Adv. Mater. Sci. 9 (2005) 34–44, https: doi=10.1.1.543.5381.

[27] G.M. Odegard, T.C. Clancy, T.S. Gates, Modeling of the mechanical properties of nanoparticle/polymer composites, Polymer (Guildf). 46 (2005) 553–562. https://doi.org/10.1016/j.polymer.2004.11.022.

[28] M. Arroyo, T. Belytschko, Continuum mechanics modeling and simulation of carbon nanotubes, Meccanica. 40 (2005) 455–469. https://doi.org/10.1007/s11012-005-2133-y.

[29] F.H. Gojny, M.H.G. Wichmann, U. Köpke, B. Fiedler, K. Schulte, Carbon nanotube-reinforced epoxy-composites: Enhanced stiffness and fracture toughness at low nanotube

content, Compos. Sci. Technol. 64 (2004) 2363–2371. https://doi.org/10.1016/j.compscitech.2004.04.002.

[30] F. Lin, Y. Xiang, H.S. Shen, Temperature dependent mechanical properties of graphene reinforced polymer nanocomposites – A molecular dynamics simulation, Compos. Part B Eng. 111 (2017) 261–269. https://doi.org/10.1016/j.compositesb.2016.12.004.

[31] B. Arash, Q. Wang, V.K. Varadan, Mechanical properties of carbon nanotube/polymer composites, Sci. Rep. 4 (2014) 1–8. https://doi.org/10.1038/srep06479.

[32] R.C. Bernardi, M.C.R. Melo, K. Schulten, Enhanced sampling techniques in molecular dynamics simulations of biological systems, Biochim. Biophys. Acta - Gen. Subj. 1850 (2015) 872–877. https://doi.org/10.1016/j.bbagen.2014.10.019.

[33] Y.J. Liu, X.L. Chen, Evaluations of the effective material properties of carbon nanotube-based composites using a nanoscale representative volume element, Mech. Mater. 35 (2003) 69–81. https://doi.org/https://doi.org/10.1016/S0167-6636(02)00200-4.

[34] H.W. Wang, H.W. Zhou, R.D. Peng, L. Mishnaevsky, Nanoreinforced polymer composites: 3D FEM modeling with effective interface concept, Compos. Sci. Technol. 71 (2011) 980–988. https://doi.org/10.1016/j.compscitech.2011.03.003.

[35] J.R. Potts, D.R. Dreyer, C.W. Bielawski, R.S. Ruoff, Graphene-based polymer nanocomposites, Polymer (Guildf). 52 (2011) 5–25. https://doi.org/10.1016/j.polymer.2010.11.042.

[36] N. Lin, A. Dufresne, Physical and/or chemical compatibilization of extruded cellulose nanocrystal reinforced polystyrene nanocomposites, Macromolecules. 46 (2013) 5570–5583. https://doi.org/10.1021/ma4010154.

[37] C.L. Morelli, M.N. Belgacem, M.C. Branciforti, M. C. B. Salon, J. Bras, R.E.S. Bretas, Nanocomposites of PBAT and cellulose nanocrystals modified by in situ polymerization and melt extrusion, Polym. Eng. Sci. 56 (2016) 1339–1348. https://doi.org/10.1002/pen.24367.

[38] G. Postiglione, G. Natale, G. Griffini, M. Levi, S. Turri, Conductive 3D microstructures by direct 3D printing of polymer/carbon nanotube nanocomposites via liquid deposition modeling, Compos. Part A Appl. Sci. Manuf. 76 (2015) 110–114. https://doi.org/10.1016/j.compositesa.2015.05.014.

[39] Z.X. Khoo, J.E.M. Teoh, Y. Liu, C.K. Chua, S. Yang, J. An, K.F. Leong, W.Y. Yeong, 3D printing of smart materials: A review on recent progresses in 4D printing, Virtual Phys. Prototyp. 10 (2015) 103–122. https://doi.org/10.1080/17452759.2015.1097054.

[40] W. Xu, X. Wang, N. Sandler, S. Willför, C. Xu, Three-Dimensional Printing of Wood-Derived Biopolymers: A Review Focused on Biomedical Applications, ACS Sustain. Chem. Eng. 6 (2018) 5663–5680. https://doi.org/10.1021/acssuschemeng.7b03924.

[41] Z. Ouyang, H.-Y. Yu, M. Song, J. Zhu, D. Wang, Ultrasensitive and robust self-healing composite films with reinforcement of multi-branched cellulose nanocrystals, Compos. Sci. Technol. 198 (2020) 108300. https://doi.org/10.1016/j.compscitech.2020.108300.

[42] T.D. Ngo, A. Kashani, G. Imbalzano, K.T.Q. Nguyen, D. Hui, Additive manufacturing (3D printing): A review of materials, methods, applications and challenges, Compos. Part B Eng. 143 (2018) 172–196. https://doi.org/10.1016/j.compositesb.2018.02.012.

[43] N. Mohan, P. Senthil, S. Vinodh, N. Jayanth, A review on composite materials and process parameters optimisation for the fused deposition modelling process, Virtual Phys. Prototyp.

12 (2017) 47–59. https://doi.org/10.1080/17452759.2016.1274490.

[44] A. Giubilini, G. Siqueira, F.J. Clemens, C. Sciancalepore, M. Messori, G. Nyström, F. Bondioli, 3D-Printing Nanocellulose-Poly(3-hydroxybutyrate- co-3-hydroxyhexanoate) Biodegradable Composites by Fused Deposition Modeling, ACS Sustain. Chem. Eng. 8 (2020) 10292–10302. https://doi.org/10.1021/acssuschemeng.0c03385.

[45] S. Dinesh Kumar, K. Venkadeshwaran, M.K. Aravindan, Fused deposition modelling of PLA reinforced with cellulose nanocrystals, Mater. Today Proc. 33 (2020) 868–875. https://doi.org/10.1016/j.matpr.2020.06.404.

[46] D. Zhu, Y. Ren, G. Liao, S. Jiang, F. Liu, J. Guo, G. Xu, Thermal and mechanical properties of polyamide 12/graphene nanoplatelets nanocomposites and parts fabricated by fused deposition modeling, J. Appl. Polym. Sci. 134 (2017) 1–13. https://doi.org/10.1002/app.45332.

[47] H. Kim, T. Fernando, M. Li, Y. Lin, T.L.B. Tseng, Fabrication and characterization of 3D printed BaTiO3/PVDF nanocomposites, J. Compos. Mater. 52 (2018) 197–206. https://doi.org/10.1177/0021998317704709.

[48] R. Hashemi Sanatgar, C. Campagne, V. Nierstrasz, Investigation of the adhesion properties of direct 3D printing of polymers and nanocomposites on textiles: Effect of FDM printing process parameters, Appl. Surf. Sci. 403 (2017) 551–563. https://doi.org/10.1016/j.apsusc.2017.01.112.

[49] V. Francis, P.K. Jain, Experimental investigations on fused deposition modelling of polymer-layered silicate nanocomposite, Virtual Phys. Prototyp. 11 (2016) 109–121. https://doi.org/10.1080/17452759.2016.1172431.

[50] Y. Chen, I.T. Garces, T. Tang, C. Ayranci, Cellulose nanocrystals reinforced shape memory polymer cardiovascular stent, Rapid Prototyp. J. 27 (2021) 37–44. https://doi.org/10.1108/RPJ-01-2020-0019.

[51] K. Kim, J. Park, J. hoon Suh, M. Kim, Y. Jeong, I. Park, 3D printing of multiaxial force sensors using carbon nanotube (CNT)/thermoplastic polyurethane (TPU) filaments, Sensors Actuators, A Phys. 263 (2017) 493–500. https://doi.org/10.1016/j.sna.2017.07.020.

[52] D. Fengel, G. Wegener, Wood: chemistry, ultrastructure, reactions, Walter de Gruyter, 2011 https://doi.org/10.1002/pol.1985.130231112,

[53] A. Dufresne, Nanocellulose: a new ageless bionanomaterial, Mater. Today. 16 (2013) 220–227. https://doi.org/https://doi.org/10.1016/j.mattod.2013.06.004.

[54] T. Ebeling, M. Paillet, R. Borsali, O. Diat, A. Dufresne, J.-Y. Cavaillé, H. Chanzy, Shear-induced orientation phenomena in suspensions of cellulose microcrystals, revealed by small angle X-ray scattering, Langmuir. 15 (1999) 6123–6126. https://doi.org/10.1021/la990046+.

[55] M.N. Anglès, A. Dufresne, Plasticized starch/tunicin whiskers nanocomposites, Struct Anal Macromol. 33 (2000) 8344–8353, https://doi.org/10.1021/ma0008701..

[56] M.T. Postek, A. Vladár, J. Dagata, N. Farkas, B. Ming, R. Wagner, A. Raman, R.J. Moon, R. Sabo, T.H. Wegner, J. Beecher, Development of the metrology and imaging of cellulose nanocrystals, Meas. Sci. Technol. 22 (2011). https://doi.org/10.1088/0957-0233/22/2/024005.

[57] K.M. Cantor, P. Watts, Part I : Plastics , Elastomeric and Nanocomposite Materials, Appl. Plast. Eng. Handb. (2011).

[58] B.K. Kandola, 6 - Nanocomposites, in: A.R. Horrocks, D.B.T.-F.R.M. Price (Eds.), Woodhead Publishing, 2001: pp. 204–219. https://doi.org/https://doi.org/10.1533/9781855737464.204.

[59] G. Wypych, PA-12 polyamide-12, Handb. Polym. 171 (2016) 246–250. https://doi.org/10.1016/b978-1-895198-92-8.50077-x.

[60] C.A. Harper, Handbook of Plastics, Elastomers, and Composites, Fourth Edition, 4th ed., McGraw-Hill Education, New York, 2002. https://www.accessengineeringlibrary.com/content/book/9780071384766.

[61] G. Wypych, PA-6 polyamide-6, Handb. Polym. (2016) 215–220. https://doi.org/10.1016/b978-1-895198-92-8.50070-7.

[62] E.C. Demir, A. Benkaddour, D. Aldrich, M.T. Mcdermott, C. Il Kim, C. Ayranci, A predictive model towards understanding the effect of reinforcement agglomeration on the stiffness of nanocomposites, J. Compos. Mater. (2022). https://doi.org/10.1177/00219983221076639.

Chapter 2

A Predictive Model Towards Understanding the Effect of Reinforcement Agglomeration on the Stiffness of Nanocomposites

2.1 Introduction

Nanocomposites have been extensively investigated for use in various applications, such as wearable sensors, flexible electronics, soft robotics, blood vessel prosthesis, and bone tissue scaffolds [1–6]. The high surface-to volume ratio of nanofillers enables significant enhancement of mechanical properties even at low loading which opens pathways to high-performance, lightweight materials. The addition of nanofillers can alter the polymer crystallinity, crystalline morphology, or chain conformation and thus, influence the mechanical response [7]. While understanding a number of variables is of critical importance, conventional composite theories assume that each phase maintains its initial properties, and the addition of nanofillers does not change the properties of the matrix. Researchers have modified conventional theories by introducing dominant parameters (*i.e.,* interface, agglomeration, shape of nanofillers) to predict mechanical response [8–12]. However, the cohesive forces between nanoparticles become dominant and lead to non-uniform filler dispersion, *i.e*., particle agglomerations, especially at higher concentrations of nanofillers. Agglomerates result in inefficient load transfers and localized stress concentration sites that dramatically reduce the mechanical properties of nanocomposites.

As a result, agglomeration of the nanofiller inhibits the expected promise of nanocomposites. [13–17].

It is important to explore and model the effects of agglomerates on the mechanical response of nanocomposites to achieve the benefit of nanofillers' properties. Conventional continuum-based models (*e.g.*, Reuss, Voigt, and Halpin-Tsai Models) are often utilized and/or modified to predict the stiffness of short-fiber composites [7,13,14] via homogenization of two phases [15–18]. These models presume uniform distribution of fillers, uniform stress or strain throughout the composite, and perfect bonding [17,18]. However, these assumptions potentially oversimplify the state of composite systems and thus often fail to predict the general response of nanocomposites. For instance, the conventional models predict a linear or exponential increase in elastic modulus of composites with respect to the concentration of fillers; however, experimental observations indicate that the elastic modulus of nanocomposites reaches a plateau value or decreases with increasing loading [19–23]. It is often observed that conventional models predict the elastic modulus at very low concentrations and often diverge from experimental findings as nanofiller concentration increases [19,24–26]. Consideration of the individual state of agglomerates is necessary for accurate predictions at high concentrations, which can be achieved by combining the continuum-based models and statistical approaches.

In the present study, we address deficiencies in current models with a three-phase analytical Mori-Tanaka model that incorporates agglomerate, free filler, and matrix phases for the prediction of the elastic modulus of nanocomposites. In particular, a statistical approach, based on a Monte-Carlo approach is used to achieve natural distributions of fillers within the composite. A hierarchical clustering method based on machine learning is integrated into the model to automate the23etectionn of agglomerates and to decrease the execution time of the code. The model is

capable of investigating the effect of key variables such as aspect ratio, orientation and distribution of filler, the volume fraction of agglomerate, and material property of each constitute. The model is applied to cellulose nanocrystal (CNC) reinforced polyamide 6 (PA6) nanocomposites, and it can be used to understand and study the effect of agglomerates in nanocomposites and predict their mechanical properties.

2.2 Modeling

A polymer nanocomposite, consisting of two constituents (*i.e.,* a filler and matrix), can be described by multiple phases/regions including filler, interface, agglomerate, and matrix. The interface and agglomeration phases have been studied in literature [9,27,28]. We expand the previous studies on agglomeration by developing a model that considers three phases: matrix phase (matrix-only region), free/individual filler phase (filler-only region where no agglomerate exists), and agglomerate phase (more than one filler particle surrounded by matrix). Each phase is analyzed separately and then homogenized to calculate the stiffness of a nanocomposite. The matrix and free filler phases can be accommodated by using the Mori-Tanaka model (see [29] and derivation therein). Thus, two critical points remain to be investigated and developed: *distribution of fillers* and *definition of agglomerate*. We used the Monte-Carlo method and defined the parameter *"critical distance"* to cover the former and latter, respectively.

2.2.1 Filler Dispersion:

It is almost impossible to obtain a perfect dispersion of fillers; therefore, agglomerates are prevalent in many nanocomposites. This inhomogeneity is one of the main reasons why the aforementioned conventional models struggle to predict experimental results of many

nanocomposite systems. Commonly observed elastic modulus vs. % filler trends for nanocomposites are shown in Figure 2.1. [30–32]

Conventional models generally agree with experimental results at low loadings (~ 0.5 – 1 w%), however, as filler content increases, the model predictions often fail. The introduction of a simple methodology into the model to computationally account for randomly distributed reinforcements in a *defined space* will be a powerful tool.

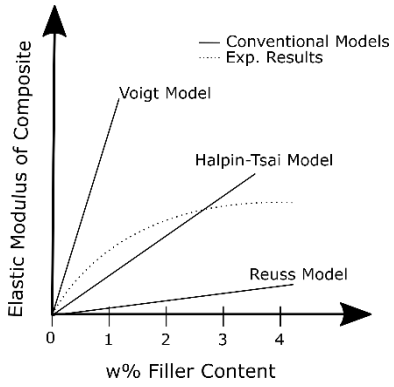

Figure 2.1. Schematic illustration of different conventional models and experimental results.

The dispersion of fillers is performed in a two-dimensional space because it is computationally efficient and can represent a slice of three-dimensional space. Numerous studies address dispersion and agglomeration based on two-dimensional scanning electron microscopy (SEM) and transmission electron microscopy (TEM) images [33–39]. The defined two-dimensional space can represent filler dispersion in the nanocomposite's repeating volume element (RVE). The number of fillers in the RVE is calculated based on their volume fraction, and then fillers are distributed in the defined space. The model presented here determines the fillers' locations using the Mersenne Twister algorithm, a pseudorandom number generator, in MATLAB code, and the center of fillers

represented by filled circles in the RVE. For the pseudorandom number generation, a uniform distribution was followed for the current study. Various distributions can be observed experimentally and may need to be adopted for different cases. The code is written to avoid overlapping circles. The schematics of an anticipated RVEs for randomly oriented and aligned fillers are given in Figure 2.2 (a) and (b), respectively. The effect of filler orientation is captured in the Mori-Tanaka model, and the center of fillers is used to define agglomeration in the simulation.

(a) (b)

Figure 2.2. Schematics of the defined space representing RVE for randomly oriented (a) and aligned fillers (b).

2.2.2 Definition of an Agglomerate

In literature, distances between fillers is measured and converted into a distribution map to quantify the state of agglomeration [33,38,39]. However, a clear definition of an agglomerate remains absent in the composite community. Schweizer et al. defined three states: contact aggregation, bridging, and steric stabilization [40]. Later, Liu *et al*. developed the three organization forms of fillers shown in Figure 2.3 to establish the dispersion state of fillers [37].

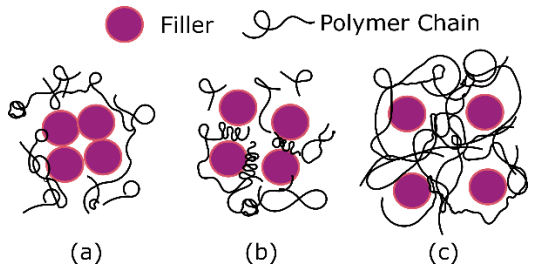

Figure 2.3. Three states of fillers: contact agglomerated fillers (a), bridge agglomerated fillers (b), and free/homogeneous distributed fillers (c), adopted from [37].

Recent developments in small-angle X-ray scattering technology make it possible to predict fillers' size, shape, and distribution in soft polymeric materials. Musino *et al.*, [41] correlate rheological measurements to SAXS analysis to determine at which concentration percolation threshold is achieved. Based on the calculated percolation threshold, they define *aggregates* in the system. These studies guided us in the current work to define the boundaries of agglomerates and establish how to identify agglomerated filler particles. For example, despite the difference in particle proximity between contacted agglomerates and bridge agglomerates shown in Figure 2.3, the latter should be considered as agglomerates because the strain fields of two closely spaced fillers can intersect. As a result of this intersection, load transfer from particle to matrix would be different from individual homogeneously distributed fillers. To our knowledge, from a mechanical point of view, there has not been a study to validate the distance between fillers in vicinity to define them as an agglomerate.

Clustering and classification problems have been addressed by data science and various clustering algorithms have been developed for classification. The agglomerative hierarchical clustering method, a machine learning method, can be adopted to determine agglomeration of nanofillers. In this method, each object represents a cluster and then clusters are merged until the desired cluster structure is obtained [42,43]. In this study, fillers are considered as objects and the distance

between them is a parameter to merge clusters. The *critical distance* parameter *γ[D]* is introduced to determine if two or more fillers are agglomerated and it is defined as multiplication of filler diameter. For example, the notation γ[D]=1.5 corresponds to 1.5 times the diameter of the filler (D). When the distance between the surfaces of two fillers is less than the *critical distance*, they are considered an agglomerate, given in Figure 2.4 (a). . Based on the location of the fillers, the proposed code categorizes the distributed fillers as agglomerated or free fillers. Each filler is labelled with numbers; however, agglomerated fillers were labelled with the same number so that the user can understand if agglomerates exist in the simulation. In doing so, we are able to analyze free fillers, agglomerates, the number of agglomerates, and the size of agglomerates.

(a) (b)

Figure 2.4. The closest distance between two fillers (a) and agglomerated fillers (b).

We use *"single linkage"* and *"cluster"* functions in MATLAB. The "*single linkage*" function calculates the "*Euclidean distance*" between fillers and uses it as an input for grouping purpose. The "*cut-off*" parameter, under the "*cluster*" function, was then used to label fillers as agglomerated if the closest distance between them is shorter than the *critical distance*. When agglomerates were detected, an imaginary circle was created as a boundary around agglomerated fillers to calculate the volume of each agglomerate. The number of filler particles within each agglomerate was counted and the volume fraction of fillers was determined. In summary, we are able to detect and record the locations and filler fractions of each agglomerate, the number of fillers within each agglomerate and the ratio of agglomerated filler to free filler.

The experimental observations and analysis in the literature [10,33,38,39,44–46] show that the properties of agglomeration are unknown, and many researchers correlate agglomerate presence with lower stiffness values in composites. The Reuss model, Eq. (1), was proposed as a reasonable model to calculate the lower range of stiffness of agglomerated regions.

$$\frac{\mathbf{1}}{\boldsymbol{E_a}} = \frac{\boldsymbol{v_m}}{\boldsymbol{E_m}} + \frac{\boldsymbol{v_f}}{\boldsymbol{E_f}} \qquad 1$$

where E_a is the elastic modulus of the agglomerate, E_m is the elastic modulus of the matrix, and E_f the elastic modulus of the filler, v_m the volume fraction of the matrix (for agglomerates, v_m is the matrix within the agglomerate), and v_f the volume fraction of the filler (for agglomerates, v_f is the filler within the agglomerate).

2.2.3 Three phase Mori-Tanaka Model

Eshelby's inclusion problem investigates stress, strain, and displacement fields both in the inclusion and the matrix [47]. Mori and Tanaka applied Eshelby's solution for an ellipsoidal inclusion problem in order to relate local average stress in the matrix to the transformation strain in the inclusions [29]. The established Mori-Tanaka model has been improved by many researchers. Tandon and Weng investigated the effect of the aspect ratio of the reinforcing inclusion with various geometry and established a closed form of the Mori-Tanaka model [48]. In this work, a three-phase Mori Tanaka model was used based on Benveniste's work [49]. The main equations to obtain Benveniste's closed form of the Mori-Tanaka model are given below. $\boldsymbol{T}$, $\bar{t}$, and t represents second-order tensor, vector, and scalar value, respectively. Subscript letters are the constitutes of the system. Strain in the inclusion is related to strain in the matrix with Eq. (2).

$$\overline{\boldsymbol{\varepsilon_f}} = \boldsymbol{A_f}\overline{\boldsymbol{\varepsilon_m}} \quad (2)$$

where $\overline{\varepsilon_f}$ and $\overline{\varepsilon_m}$ are the uniform strain vectors in the filler and matrix, respectively, and $\boldsymbol{A_f}$ is the strain concentration tensor given by Eq. (3)

$$\boldsymbol{A_f} = [\boldsymbol{I} + \boldsymbol{S_f}(\boldsymbol{C_m})^{-1}(\boldsymbol{C_f} - \boldsymbol{C_m})^{-1}] \quad (3)$$

where $\boldsymbol{I}$ is the identity tensor, $\boldsymbol{S_f}$ is the fourth order Eshelby tensor, which depends on geometry and poison's ratio, $\boldsymbol{C_m}$ is stiffness tensor of the matrix, and $\boldsymbol{C_f}$ is stiffness tensor of the filler. Stiffness tensor of the composite can be obtained by Eq. (4)

$$\boldsymbol{C} = (v_m\boldsymbol{C_m} + v_f\boldsymbol{C_f}\boldsymbol{A_f})(v_m\boldsymbol{I} + v_f\boldsymbol{A_f})^{-1} \quad (4)$$

The Mori-Tanaka model was developed for the unidirectional aligned composites; however, one can introduce orientation averaging tensor for randomly aligned fillers, described in [45], to calculate the stiffness of composites, which is given by Eq. (5)

$$\boldsymbol{C} = (\boldsymbol{v_m}\boldsymbol{C_m} + \boldsymbol{v_f}\{\boldsymbol{C_f}\boldsymbol{A_f}\})(\boldsymbol{v_m}\boldsymbol{I} + \boldsymbol{v_f}\boldsymbol{A_f})^{-1} \quad (5)$$

where the curly brackets {} stands for the indication of orientation averaging, given by Eq. (6). Subscript letters in Eq. (6) represent indices rather than the constitutes.

$$\{\boldsymbol{M_{ijkl}}\} = \frac{\boldsymbol{1}}{\boldsymbol{2\pi}}\int_{\boldsymbol{0}}^{\boldsymbol{2\pi}}\int_{\boldsymbol{0}}^{\boldsymbol{2\pi}}\boldsymbol{M_{ijkl}}(\boldsymbol{\theta},\boldsymbol{\varphi})\,\sin\boldsymbol{\varphi}\,\boldsymbol{d\varphi d\theta} \quad (6)$$

In a similar way, three phase Mori-Tanaka (free filler, agglomerate and matrix phases) can be established by Eq. (7)

$$\boldsymbol{C} = (\boldsymbol{v_m}\boldsymbol{C_m} + \boldsymbol{v_f}\{\boldsymbol{C_f}\boldsymbol{A_f}\} + \boldsymbol{v_a}\{\boldsymbol{C_a}\boldsymbol{A_a}\})(\boldsymbol{v_m}\boldsymbol{I} + \boldsymbol{v_f}\boldsymbol{A_f} + \boldsymbol{v_a}\boldsymbol{A_a})^{-1} \quad (7)$$

where $\boldsymbol{C_a}$ is stiffness tensor of the agglomerate, $\boldsymbol{A_a}$ is the strain concentration tensor for the agglomerate, and v_a is the volume fraction of the agglomerate. The strain concentration tensor for the $A_a$is calculated by Eq. (8)

$$\boldsymbol{A_a} = [\boldsymbol{I} + \boldsymbol{S_a}(\boldsymbol{C_m})^{-1}(\boldsymbol{C_a} - \boldsymbol{C_m})^{-1}] \quad 8$$

where $S_a$is the fourth order Eshelby tensor for an agglomerate. In this study, agglomeration formation is assumed to be spherical because of minimum surface energy configuration, mechanical stability and previous studies in the literature [46,50–52].

2.2.4 Monte-Carlo Method

The Monte-Carlo method is utilized to estimate the outcome of an uncertain event by generating a large number of likely outcomes. The method calculates possible results by leveraging a probability distribution and repeating the calculations/runs with various inputs. In our study, the uncertain event is the filler dispersion and the outcome is the composite modulus. For accurate composite modulus predictions, we expect to obtain statistically reliable outcomes where reliability measures the reproducibility results with repeated trials [53]. We set the number of trials in our study to one hundred considering the near infinite number of possible combinations and reasonable processing time.

As soon as the fillers were dispersed in the defined space, the MATLAB code saved the locations of fillers and the volume fraction of fillers for each agglomerate. The code extracted this information and averaged agglomerates based on their volume as if there was a single agglomerate in the composite. In the end, the nanocomposite contained three phases: the free fillers, the averaged agglomerate, and the matrix. The volume fractions and properties of constitutes obtained are utilized in the three-phase Mori-Tanaka model to calculate the stiffness of the nanocomposite.

Figure 2.5 (a) exhibits schematics of the workflow to calculate the stiffness of a nanocomposite for a certain number of fillers. Here, Ln represents the loading number (concentration of the filler), and R1 represents the first run of the simulation. After homogenization, box-plots were used to present the output of one hundred runs. Figure 2.5 (b) summarizes the steps/algorithm of the workflow for one run.

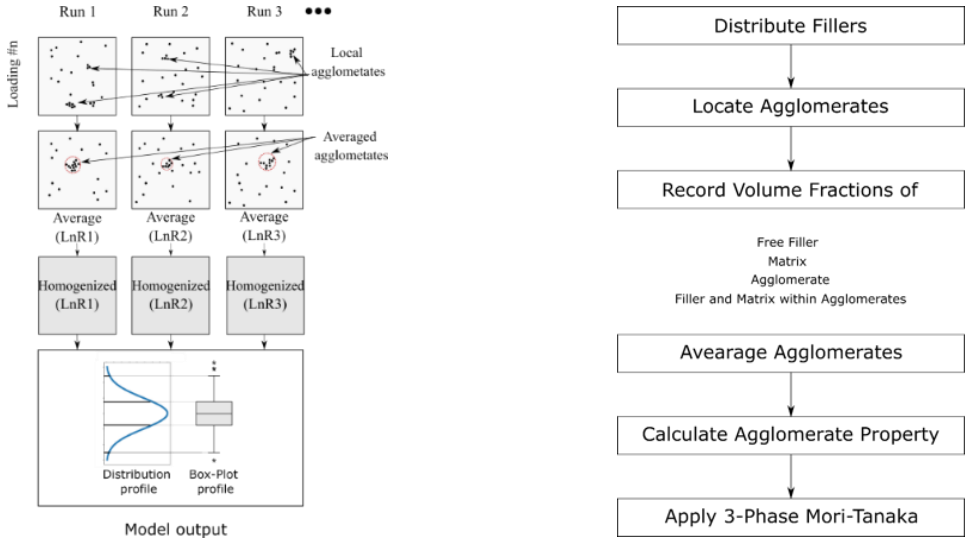

(a) (b)

Figure 2.5. Schematics (a) and steps (b) of the workflow.

2.3 Experimental Method

2.3.1 Materials & Manufacturing

Polymer nanocomposite samples were manufactured with a semicrystalline thermoplastic polyamide-6 (PA6, poly(hexano-6lactam)- $(C_6H_{11}NO)_n$) matrix, and cellulose nanocrystals (CNC, $(C_6H_{10}O_5)_n$) filler. PA6 pellets (Sigma Aldrich) had a density of 1.084 g/mL at 25 °C and transition temperature (T_g) of 62.5 °C. CNC was received in spray-dried powder form from CelluForce. The density of CNC is taken as 1.5 g/cm^3 [54]. Materials were used as received without any further

treatment. The samples were prepared on glass substrates via the spin coating method. First, CNC and PA6 were dried at 80 ºC for 24 hours before any suspension preparation. Then, the dried PA6 was dissolved in formic acid, 98% Sigma Aldrich, (the ratio of PA6/formic acid was 20 w/v%) by using a batch sonicator. After complete dissolution of PA6, CNC was added to the suspension based on the designed concentration, and the suspension was kept under agitation until the CNC was dispersed. The prepared suspensions were sonicated one more time before the spinning process for 45 minutes to disperse CNC within the matrix.

Two milliliters of the suspension were placed on a rectangular (75 mm x 25 mm) glass substrate. Then, it was accelerated to 2000 rpm in 15 seconds and spun at 3000 rpm for 30 seconds. After the spinning process, the film was left for around 5 minutes for any remaining solvent to evaporate. The manufacturing steps with a flowchart and photos are given in Figure 2.6. Samples contain different CNC concentrations in PA6 that vary from 0.0 to 15.0 w%.

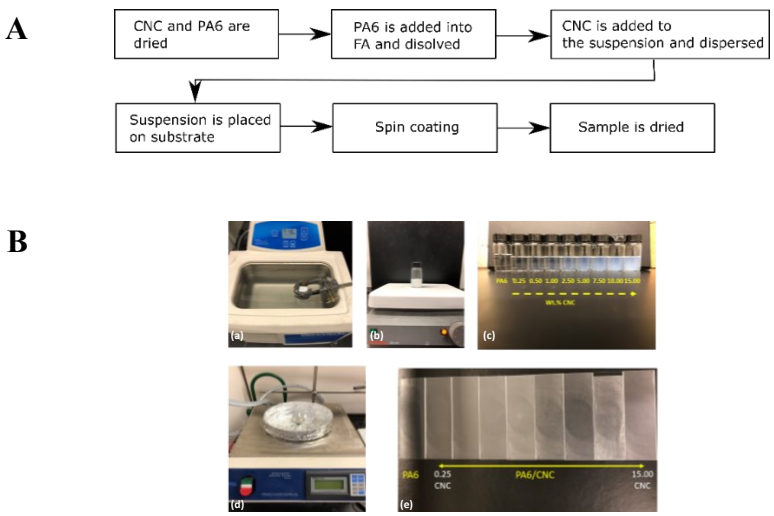

Figure 2.6. Flow chart (A) and photos (B) of PA6 dissolution in formic acid (a), dissolution of CNC in PA6/formic acid suspension (b), prepared suspensions before the second sonication of CNC/PA6/formic acid (c), spin coating (d) and obtained thin films on glass substrate I.

2.3.2 Characterization

2.1.1.1 Transmission electron microscopy (TEM)

Two TEMs (Philips 410 transmission electron microscope and JEOL JEM-ARM200CF S/TEM) were utilized at 100 kV accelerating voltage to understand the morphology, aspect ratio of the CNC, and agglomeration. Two different protocols were followed to prepare the samples of CNC and nanocomposites. In the first protocol, the CNC was dispersed in water (2.5 mg/100 ml), and 0.5 ml of solution was dropped on a TEM copper grip. The CNC was stained with phosphotungstic acid to increase the contrast. The stain solution was dropped on the grid, and excess of it was removed after 10 seconds. The second protocol involved embedding the nanocomposite sample into epoxy. A thin section (~120 nm) was microtomed along the longitudinal side of a piece of the sample, using a glass knife in a Reichert-Jung Ultracut E ultramicrotome. The microtomed samples were double-side stained with the extra-long protocol; uranyl acetate – 2.5 hours and lead citrate for 1 hour before the TEM analysis. All images were analyzed using the open source ImageJ software.

2.1.1.2 Tensile test

ASTM 882-12 standard was followed for testing the films and reporting mechanical properties. Produced films, ~5 μm thick, were cut into 10 mm x 75 mm rectangles by using a rotary cutter and a 3D printed custom cutting plate. The samples were stored overnight in a desiccator before testing. A C-shaped paper support was used to insert samples into the grips, prevent them from sliding from the grips, and reduce stress concentrations at the grips. TA Instrument ElectroForce 3200 with 10 N load cell was utilized. The distance between the grips was 50 mm. The grips were tightened to 4-in.lb torque. The paper support was cut from the middle before the test, and the

samples were tested with 0.083 mm/sec rate. A MATLAB code was developed to calculate the elastic modulus and measure the strength and strain-at-break of the composite. While non-uniform strain distribution is a concern due to the grip effect, using an extensometer is a challenging process for ~5 μm thick films. As allowed in the ASTM 882-12 standard, the aforementioned 50 mm grip distance was the gage length in this study [55].

2.4 Results and Discussion

2.4.1 TEM Analysis of CNC Particles and Nanocomposites

The filler used in this work are CNC. Figure 2.7 exhibits TEM image of fiber like CNC fillers. The aspect ratio (length/diameter) determined by analysis of the images was found to vary between 11 and 78. The average length of the particles was determined to be 152.0 ± 49.9 nm and average diameter is 6.0±3.4 nm. The average aspect ratio was calculated as 29.2 ± 12.6 for 100 particles from four different images. The filler and matrix were assumed to be isotropic, and their Poisson's ratio was set to 0.35 for the model.

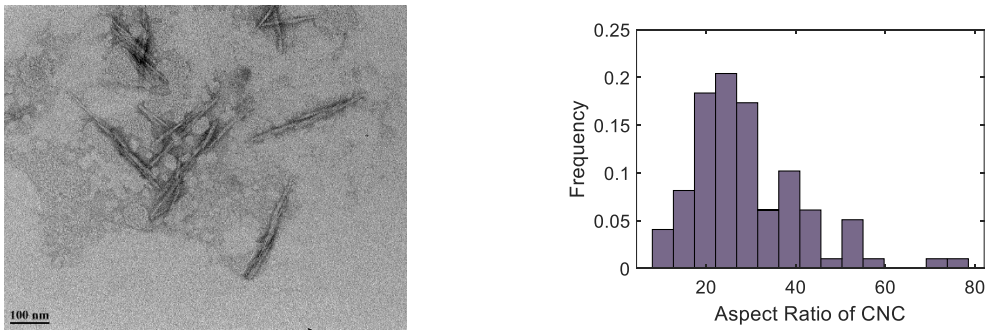

(a) (b)

Figure 2.7. TEM image of CNC (a) and measured aspect ratio (b).

TEM was also used to observe the CNC distribution and orientation in the composite. Figure 2.8 (a) and (b) show images of neat PA6 and PA6 containing 15.0 w% of CNC, respectively. We assign the darker fiber-like structures in Figure 2.8 (b) to the CNC due to their size, morphology, and aspect ratio. In addition, the darker structures are not observed in Figure 2.8 (a), supporting their assignment are the CNC particles. A closer inspection of Figure 2.8 (b) reveals a small number of agglomerates with a size generally under a micron. For example, fillers in the top left corner of Figure 2.8 (b) can be assumed to be agglomerated because they are already touching.

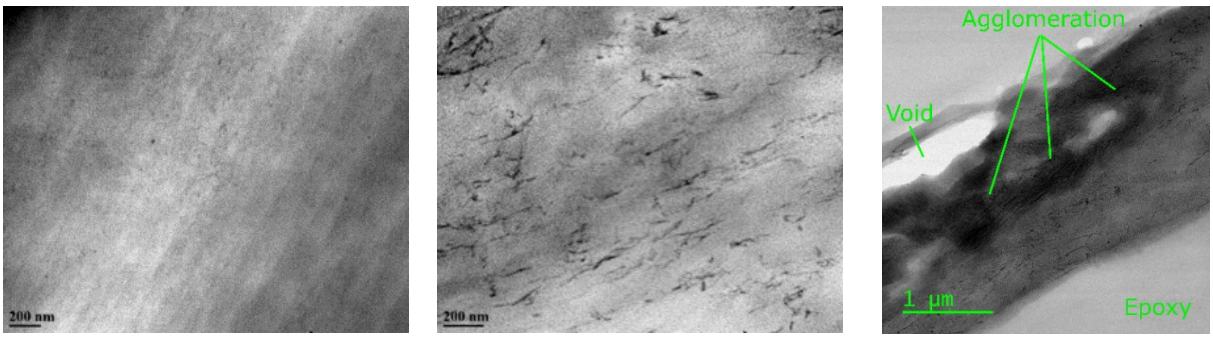

(a) (b) I

Figure 2.8. Side view TEM images of a neat PA6 film (a), 15.0 w% CNC reinforced PA6 (b), 15.0 w% CNC reinforced PA6 at lower magnification (c).

The lower magnification of the PA6-CNC composite in Figure 2.8 I reveals micron-size agglomerates. These large agglomerates result in a rougher surface and some voids at the interface of the epoxy and sample. Polymer matrix can be observed squeezed between the CNC fillers in the micron-size agglomerates in Figure 2.8 I. These matrix regions validate our approach that

agglomerates consist of matrix and filler. Further, from Figure 2.8I, we can conclude that agglomerates converge to a spherical shape compared to the rod-shaped free fillers.

The orientation of fillers is critical for the model and mechanical response of the sample. Our samples were prepared by spin-coating, which can influence the orientation if the CNC particles. Figure 2.9 (a) and (b) show low and high magnification TEM images that were analyzed to obtain an orientation distribution of the fillers. The angle of orientation of two hundred particles was measured with respect to the longitudinal direction of the specimen. Figure 2.9 (c) shows the distribution of the angle of deviation from the testing direction. Hence, we conclude that around 70% of the fillers deviate from the longitudinal direction by only up to 20°; therefore, the free fillers were assumed aligned for our modeling purposes.

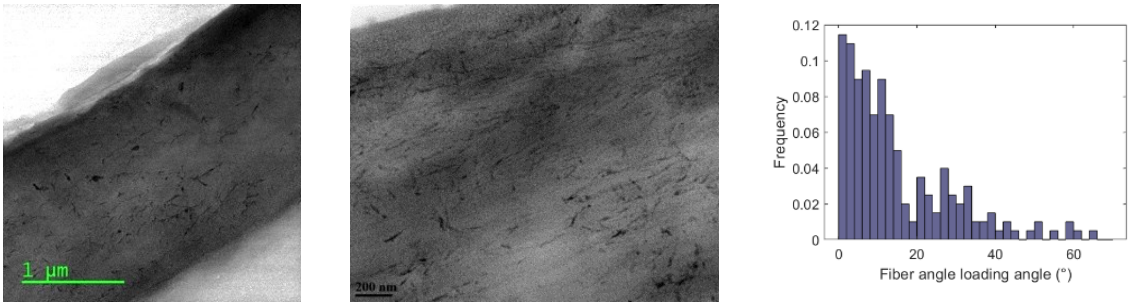

(a) (b) I

Figure 2.9. TEM images for filler orientation at low (a) and high (b) magnification. Distribution of the angle w.r.t the testing direction (c).

2.4.2 Uniaxial Tensile Tests

Nanocomposite samples of PA6 containing eight different CNC concentrations (0, 0.5, 1.0, 2.5, 5.0, 7.5, 10.0 and 15.0 w%) were prepared and at least five samples from each type were tested. Figure 2.10 (a) and (b) show a photo of a sample under the tensile test and a representative stress-

strain curves for each type of the samples. The white paper, seen in Figure 2.10 (a) was used to lower stress generated at the grips and prevent sliding of the films from the grips. In general, the addition of CNC less than 5 w% enhanced the stiffness, yield and ultimate strength, and lowered the strain-at-break compared to neat PA6.

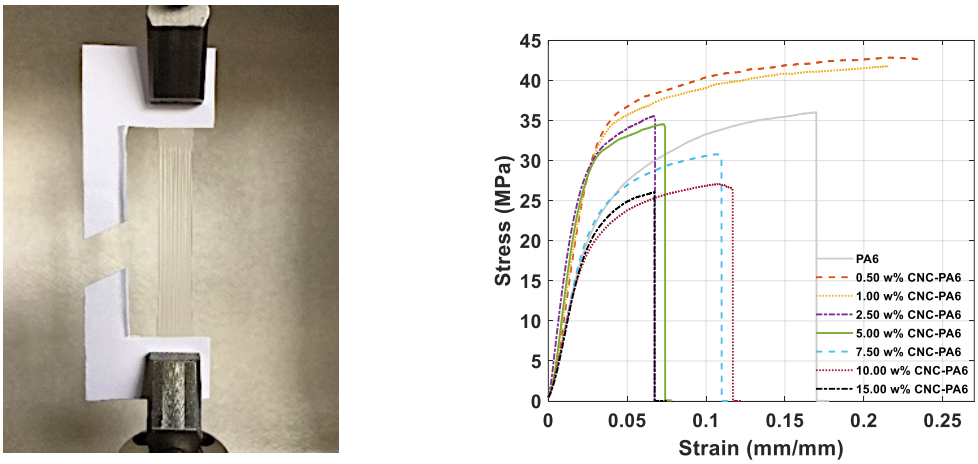

(a) (b)

Figure 2.10. Photo of a sample during a tensile test (a) and representative stress-strain curves for each sample type (b).

Table 2.1 lists the elastic modulus, tensile strength and strain-at-break values of the neat PA6 and PA6 nanocomposite samples. According to the one-way ANOVA test, there is a significant difference in the average elastic modulus, tensile strength and strain-at-break between the 8 groups (0-15 w% CNC PA6) ($F(7,35)=19.61$, $p<0.001$). Two-tail T-tests were performed to order the groups and to show a relative significant differences between groups.

Table 2.1. Mechanical properties of nanocomposites at different CNC w% in PA6.

CNC w% in PA6	0	0.5	1.0	2.5	5.0	7.5	10.0	15.0
Elastic Modulus (MPa)	911.0 ± 233.9^{c}	1366.0 ± 208.6^{ab}	1307.9 ± 257.5^{ab}	1627.9 ± 107.3^{a}	1556.3 ± 124.6^{ab}	913.3 ± 128.4^{c}	949.9 ± 140.1^{c}	821.0 ± 124.5^{c}

Tensile Strength (MPa)	38.8 ± 1.4[b]	44.9 ± 1.9[a]	43.6 ± 1.4[a]	38.7 ± 2.0[b]	38.2 ± 1.6[b]	32.4 ± 1.2[c]	28.2 ± 0.6[d]	25.9± 0.9[e]
Strain-at-break	0.207 ± 0.021[ab]	0.195 ± 0.043[b]	0.214 ± 0.010[a]	0.092 ± 0.036[c]	0.100 ± 0.018[cd]	0.139 ± 0.036[c]	0.123 ± 0.027[c]	0.081 ± 0.018[d]

The superscripts ([a],[b],[c],[d] and [e]) indicate the statistically important differences in the data sets in each rows ($p < 0.05$), as determined through one-way ANOVA analysis and T-test. The superscripts are ordered alphabetically, and the largest mean comes the earliest in the alphabet.

The average elastic modulus of neat PA6 was measured as 911.0 MPa (StDev = ± 233.9 MPa). The addition 0.5 w% CNC increased the elastic modulus of the composite to 1366.0 MPa (StDev = ± 208.6 MPa), which corresponds to approximately 50% increase. Although 1.0 w% CNC addition lowered the elastic modulus of the composite around 4% with respect to 0.5 w% CNC, maximum elastic modulus average, 1627.9 MPa (StDev = ± 107.3 MPa), was observed with the addition of 2.5 w% CNC, which is 79% increase with respect the neat PA6. The addition of 5.0 w% CNC and higher concentrations resulted in drop in the elastic modulus compared to 2.5 w% CNC composite. However, it is important to note that a sharp decrease (42%) in elastic modulus was observed in 7.5 w% CNC composite with respect to 5.0 w% CNC. It was observed that addition of 0.5 w% CNC (wrt. 0 w% CNC), 2.5 w% CNC (wrt. 1.0 w% CNC) and 7.5 w% CNC (wrt. 5.0 w% CNC) had resulted in statistically significant difference on the average elastic modulus as it can be seen from the data presented in Table 2.1. There is no significant difference between the neat PA6 and PA6 with concentrations higher than 7.5 w% CNC, thus it can be noted the addition of CNC higher than 5.0 w% does not increase the elastic modulus of neat PA6.

The average tensile strength of the neat PA6 was measured as 38.8 MPa (StDev = ± 1.4 MPa) and 0.5 w% CNC addition increased the tensile strength of the composite approximately 15%, which is the highest increase in tensile strength of the composite with respect to the neat PA6.

Statistically, 0.5 w% and 1.0 w% showed the highest average and there is no statistical difference between them. After this increase, the average tensile strength values of the composites started to drop; however, a sharp decrease in the tensile strength was observed in 7.5 w% CNC (15% wrt. 5.0 w% CNC and 17% wrt. neat PA6). It is important to note that the average tensile strength of 7.5, 10.0 and 15.0 w% CNC-PA6 was found to be lower than the neat PA6.

The average strain-at-break values of the composites at each concentration was measured lower than neat PA6 except for 1.0 w% CNC. The average strain-at-break of 1.0 w% CNC-PA6 was found to be 0.214 (StDev = ± 0.010), 3% higher than the average strain-at-break of neat PA6, which is not statistically different than the neat PA6. The lowest average strain-at-break was observed in 15 w% CNC.

Increase in the elastic modulus without loss in tensile strength at 0.5 w% and 2.5 w% shows effective strengthening impact of CNC on PA6 and suggest an efficient stress transfer between PA6 and CNC. However, decrease in the elastic modulus and tensile strength at 7.5 and higher w% of CNC loadings suggests that 7.5 w% CNC set the limit, and the agglomerates became detrimental to mechanical properties. Our findings in terms of the trend of elastic modulus and tensile strength are consistent with the results in Yousefian's and Peng studies [56][57]. It is important to note that, although the trends are similar, we observed 84% increase in elastics modulus (1629 MPa) with respect to the neat PA6 while Yousefian's observed the maximum increase as 24% (1312 MPa) and Peng observed 31% (1540 MPa) increase. The main difference between studies is the manufacturing methods which suggests that solvent mixing method can provide a better CNC dispersion and stress transfer than the melt mixing according to the mechanical test results.

Tensile strength and strain-at-break showed similar trends as expected because both properties heavily depend on the imperfections and stress concentration points. Further it can be argued that continues slight decrease in these properties with respect to CNC loading is also the result of the decrease in the polymer chain movement due to the increased particle content.

When the thickness of the samples is considered, any notch, agglomerate and void can decrease strength and strain-at-break suddenly. As the concentration of CNC becomes higher than 1.00 w%, strain-at-break, and tensile strength start dropping. This can be interpreted as a sign of agglomeration since agglomerates can form stress-concentration points. White regions in TEM image in Figure 2.8 I supports the idea of imperfections in the sample because voids are seen as a white colour under dark field TEM images. As noted in the literature [58], we can argue that the CNC particles were well-dispersed at low % CNC loadings; however, they tend to agglomerate at higher loading levels based on the mechanical properties and TEM images of the composites. According to the production method utilized in this study, the addition of CNC more than 5 w% is not recommended for the purpose of reinforcing.

2.4.3 Modeling

Figure 2.11 (a) exhibits locations of 4.5 v % dispersed fillers in the defined space ($1\mu m x 1\mu m$) as a result of the simulation. The distribution of fillers is based on the two main assumptions: locations of fillers are selected from the uniform distribution function, and fillers do not overlap. In the case of overlap, the code detects it and assigns a new location to the filler. In that way, the output is created without any overlapping fillers. The aim of dispersing fillers was to detect agglomerated fillers and establish the three phases to calculate the stiffness of the composites. In order to detect agglomerated fillers, the *critical distance* parameter $\gamma[D]$ was utilized. Figure 2.11 (b) shows a

zoomed-in view of an output. While black points represent the locations of the free fillers (non-agglomerated fillers), the same colored fillers represent agglomerated fillers. As we can see from Figure 2.11, the *critical distance* directly determines the number of agglomerates and the filler concentration within each agglomerate. If we were to choose *γ[D]=0* (surface contact), then all fillers would be free fillers (non-agglomerated), and the fillers cannot overlap in the program. In that case, the three-phase model would be converged to a two-phase model, and we would not be able to capture the mechanical response accurately. In that sense, choosing the right critical distance is crucial to predict the stiffness.

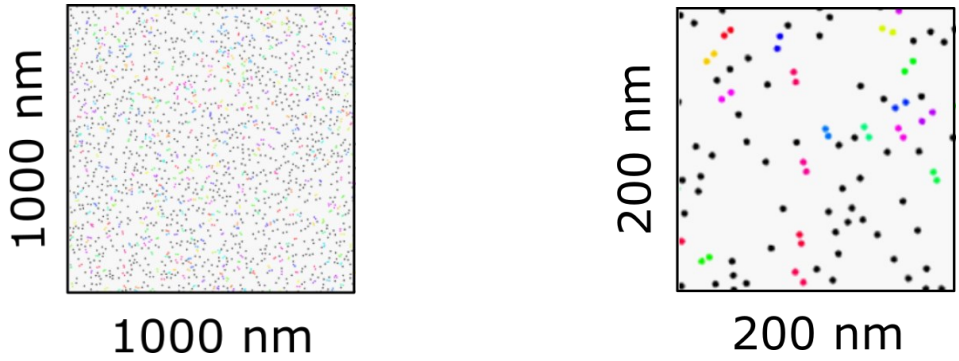

(a) (b)

Figure 2.11. Locations of the fillers: general view (a) and zoomed-in view (b).

The predictions of the elastic modulus of the nanocomposites with different *critical distances* and CNC concentrations are given in Figure 2.12. One-hundred outcomes for each concentration are shown by box-plots where box represents 25-75 % outcome and cross symbols represents outliers. For the Eshelby tensor calculations aspect ratio of fillers and agglomeration were As it can be seen in Figure 2.12, the modeling outputs can be as linear as the Mori-Tanaka prediction when we chose a *γ[D]* = 0, or they can evolve to the Reuss model around 10 v% loading when the *γ[D]* = 3. Two main factors play a key role here: *critical distance γ[D]* and the agglomeration property. The

impact of the *critical distance* and agglomerates can be seen in Figure 2.12 when predictions of the proposed model the conventional models are compared. Sheng *et al.,* studied FEA of polymer/clay composites and observed three states of the nanofillers as a result of their FEA stress analysis: “isolated”, “partly overlapped” and “completely overlapped” particles [59]. According to the scale of the FEA from their study, particles start to overlap between 10 and 20 nm, which corresponds $\gamma[D]$ = 1-3 in this study. Load transfer efficiency is the lowest in completely overlapped particles. This can guide us to determine the *critical distance*. Musino *et al.,* [41] investigated closest distance (range is from 0.4 to 2.0 radius of the fillers) between fillers to define as an aggregates. None of the studies discussed how *critical distance* depends on the material. More investigation on what kinds of material parameters govern the *critical distance* should be conducted theoretically and experimentally.

Experiments in the literature exemplified a drop in the elastic modulus after around 4 w% [60–63], which is similar to the modeling results when $\gamma[D]$ is approximately 2. In addition, the agglomeration property becomes dominant as its volume fraction increases. Since we used the Reuss model to calculate the stiffness of agglomerates, the results evolve to the Reuss model, and the trends show a drastic change as soon as it reaches around 5 w%, which actually represents the literature data [64–68]. In these studies, the elastic modulus of the composites experimentally converged to a stable value (a plateau region) as the filler concentration increases or drops after a certain point of filler concentration. The decrease in the mechanical properties was related to agglomerates based on the analysis of SEM or TEM images. Thus, the proposed model has the capability of capturing the effect of agglomerates.

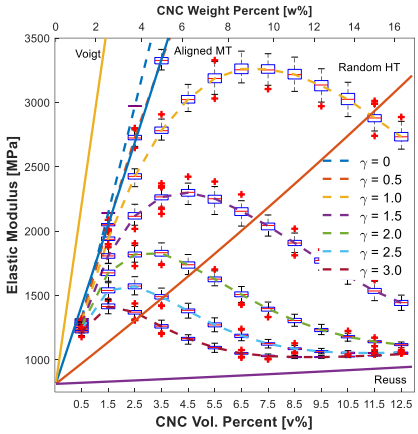

Figure 2.12. Elastic modulus versus CNC loading (v% and w% shown on the bottom and top x-axis, respectively) of the composite with different critical distances.

2.4.4 Comparison of Experimental Results and Model Predictions

The longitudinal elastic modulus (E_{11}) versus % CNC reinforced PA6 are shown in Figure 2.13. The figure includes proposed model predictions for *critical distance* $\gamma[D]$ = 2.5, experimental results, and the results of conventional models (Mori-Tanaka, Halpin-Tsai, Voigt, Reuss). The experimental results show a decrease in the elastic modulus of the samples after 5.00 w% CNC in PA6—the general trend is similar to studies in [59,67,68]. As discussed under the *Uniaxial Tensile Tests* section, some of the potential reasons for this drop can be due to agglomeration formation. The free filler may interact with the matrix more efficiently than agglomerates. The matrix may transfer the load non-uniformly to the agglomerates, the stress field of agglomerated fillers may overlap, and aspect ratio of the constitutes decreases. Each reason suggests the necessity of a model that contains agglomeration as a factor.

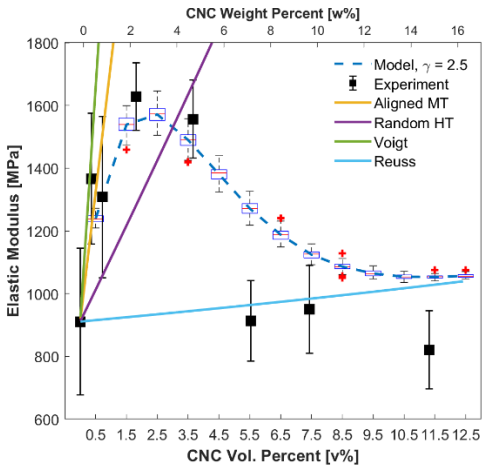

Figure 2.13. Elastic Modulus versus CNC loading (v% and w% shown on the bottom and top x-axis, respectively) of models' predictions and experimental results.

The trend of conventional models is unable to capture the experimental behaviour due to the lack of an agglomeration parameter in their model development. On the other hand, the proposed model reveals a relatively good agreement with experimental results compared to conventional models. The distribution of fillers and theoretical discussion on critical distance should be studied in deep for a better understanding of nanocomposites.

A sensitivity analysis of the proposed model would provide a better understanding of the nanocomposite system and exhibit the capabilities of the model. Work is in progress to conduct a sensitivity study as the second stage of the current study.

2.5 Conclusion

In this study, we evaluated the effect of nanofillers and agglomeration on the elastic modulus of a matrix by utilizing continuum-based analytical models. Nanocomposites were assumed to consist of three phases: the free filler, agglomeration, and matrix, which established the bases of the three-

phase Mori-Tanaka model developed in this study. Among these phases, the agglomeration phase has experimentally and computationally been difficult to deal with due to the complexity and randomness of manufacturing and the nature of nanofillers. We incorporated a Monte-Carlo method to disperse the fillers and detect the agglomerated fillers computationally to address previous modeling challenges. The *critical distance* was introduced as a parameter to identify and classify agglomerates and a hierarchical clustering method was employed. This provided a pathway to clearly define agglomerates and calculated volume fractions of the constitutes (matrix, free filler, agglomerated filler, and matrix). Based on the knowledge of agglomerated fillers and matrix and the necessary simplifications, the Reuss model was employed to calculate the stiffness of the agglomerates. The three-phase Mori-Tanaka model was then used to predict the elastic modulus of the nanocomposite. The prediction process was repeated one hundred times for each concentration to obtain reliable outcomes.

CNC reinforced PA6 samples were used as a model system and were manufactured with a spin-coating method. Detailed TEM characterization was performed in order to verify the proposed model. To our knowledge, this is the first TEM study that clearly displays CNC in a PA6 matrix. The predictions from the proposed model demonstrate a good agreement with the experimental results as opposed to the predictions from the conventional prediction models. As a summary, the current study contributes to the literature by: (a) defining agglomerates computationally and showing their impact on the stiffness theoretically, (b) utilizing a statistical approach and continuum-based analytical models to capture the agglomeration effect on stiffness, (c) verifying the proposed model and exploring the potentials of CNC as a reinforcement candidate. The proposed model can be implemented to various nanocomposites with necessary knowledge and/or assumptions for parameters such as orientation and distribution function of

fillers. TEM can be utilized to obtain these parameters or machine learning can be applied to predict them. In conclusion, the importance and drawbacks of agglomerates on the stiffness of nanocomposites were revealed by this study.

REFERENCES

[1] Y. Zhu, S. Murali, W. Cai, X. Li, J.W. Suk, J.R. Potts, R.S. Ruoff, Graphene and Graphene Oxide: Synthesis, Properties, and Applications, Adv. Mater. 22 (2010) 3906–3924. https://doi.org/https://doi.org/10.1002/adma.201001068.

[2] Z.-M. Huang, Y.-Z. Zhang, M. Kotaki, S. Ramakrishna, A review on polymer nanofibers by electrospinning and their applications in nanocomposites, Compos. Sci. Technol. 63 (2003) 2223–2253. https://doi.org/https://doi.org/10.1016/S0266-3538(03)00178-7.

[3] Z.X. Khoo, J.E.M. Teoh, Y. Liu, C.K. Chua, S. Yang, J. An, K.F. Leong, W.Y. Yeong, 3D printing of smart materials: A review on recent progresses in 4D printing, Virtual Phys. Prototyp. 10 (2015) 103–122. https://doi.org/10.1080/17452759.2015.1097054.

[4] Y. Lu, M.C. Biswas, Z. Guo, J.-W. Jeon, E.K. Wujcik, Recent developments in bio-monitoring via advanced polymer nanocomposite-based wearable strain sensors, Biosens. Bioelectron. 123 (2019) 167–177. https://doi.org/https://doi.org/10.1016/j.bios.2018.08.037.

[5] S.D. Purohit, R. Bhaskar, H. Singh, I. Yadav, M.K. Gupta, N.C. Mishra, Development of a nanocomposite scaffold of gelatin–alginate–graphene oxide for bone tissue engineering, Int. J. Biol. Macromol. 133 (2019) 592–602. https://doi.org/https://doi.org/10.1016/j.ijbiomac.2019.04.113.

[6] M. Amjadi, A. Pichitpajongkit, S. Lee, S. Ryu, I. Park, Highly Stretchable and Sensitive Strain Sensor Based on Silver Nanowire–Elastomer Nanocomposite, ACS Nano. 8 (2014) 5154–5163. https://doi.org/10.1021/nn501204t.

[7] T.D. Fornes, D.R. Paul, Modeling properties of nylon 6/clay nanocomposites using

composite theories, Polymer (Guildf). 44 (2003) 4993–5013. https://doi.org/10.1016/S0032-3861(03)00471-3.

[8] J.-J. Luo, I.M. Daniel, Characterization and modeling of mechanical behavior of polymer/clay nanocomposites, Compos. Sci. Technol. 63 (2003) 1607–1616. https://doi.org/https://doi.org/10.1016/S0266-3538(03)00060-5.

[9] Y. Li, A.M. Waas, E.M. Arruda, A closed-form, hierarchical, multi-interphase model for compositesDerivation, verification and application to nanocomposites, J. Mech. Phys. Solids. 59 (2011) 43–63. https://doi.org/10.1016/j.jmps.2010.09.015.

[10] K. Hbaieb, Q.X. Wang, Y.H.J. Chia, B. Cotterell, Modelling stiffness of polymer/clay nanocomposites, Polymer (Guildf). 48 (2007) 901–909. https://doi.org/10.1016/j.polymer.2006.11.062.

[11] E. Esmizadeh, G. Naderi, M.H.R. Ghoreishy, Modification of Theoretical models to predict mechanical behavior of PVC/NBR/organoclay nanocomposites, J. Appl. Polym. Sci. 130 (2013) 3229–3239. https://doi.org/10.1002/app.39556.

[12] J. Sapkota, A. Gooneie, A. Shirole, J.C. Martinez Garcia, A refined model for the mechanical properties of polymer composites with nanorods having different length distributions, J. Appl. Polym. Sci. 134 (2017). https://doi.org/10.1002/app.45279.

[13] P.K. Valavala, G.M. Odegard, Modeling techniques for determination of mechanical properties of polymer nanocomposites, Rev. Adv. Mater. Sci. 9 (2005) 34–44, https: doi=10.1.1.543.5381.

[14] C.C. Roach, Y.C. Lu, Analytical modeling of effect of interlayer on effective moduli of layered graphene-polymer nanocomposites, J. Mater. Sci. Technol. 33 (2017) 827–833.

https://doi.org/10.1016/j.jmst.2017.03.007.

[15] F.G. Ronald, Principles of Composite Material Mechanics, 2016, https://doi.org/10.1201/b19626.

[16] I. Taha, Y.F. Abdin, Modeling of strength and stiffness of short randomly oriented glass fiber—polypropylene composites, J. Compos. Mater. 45 (2011) 1805–1821. https://doi.org/10.1177/0021998310389089.

[17] R. Jones, Mechanics Of Composite Materials, in: 2nd ed., CRC Press, Boca Raton, 1999. https://doi.org/https://doi-org.login.ezproxy.library.ualberta.ca/10.1201/9781498711067.

[18] J.C.H. Affdl, J.L. Kardos, The Halpin-Tsai equations: A review, Polym. Eng. Sci. 16 (1976) 344–352. https://doi.org/10.1002/pen.760160512.

[19] L. Jiang, E. Morelius, J. Zhang, M. Wolcott, J. Holbery, Study of the Poly(3-hydroxybutyrate-co-3-hydroxyvalerate)/Cellulose Nanowhisker Composites Prepared by Solution Casting and Melt Processing, J. Compos. Mater. 42 (2008) 2629–2645. https://doi.org/10.1177/0021998308096327.

[20] D. Jun, Z. Guomin, P. Mingzhu, Z. Leilei, L. Dagang, Z. Rui, Crystallization and mechanical properties of reinforced PHBV composites using melt compounding: Effect of CNCs and CNFs, Carbohydr. Polym. 168 (2017) 255–262. https://doi.org/https://doi.org/10.1016/j.carbpol.2017.03.076.

[21] A.C. Corrêa, K.B.R. Teodoro, J.A. Simão, P.I.C. Claro, E. de Morais Teixeira, L.H.C. Mattoso, J.M. Marconcini, Cellulose nanocrystals from curaua fibers and poly[ethylene-co-(vinyl acetate)] nanocomposites: Effect of drying process of CNCs on thermal and mechanical properties, Polym. Compos. n/a (2020). https://doi.org/10.1002/pc.25493.

[22] H.-Y. Yu, Z.-Y. Qin, C.-F. Yan, J.-M. Yao, Green Nanocomposites Based on Functionalized Cellulose Nanocrystals: A Study on the Relationship between Interfacial Interaction and Property Enhancement, ACS Sustain. Chem. Eng. 2 (2014) 875–886. https://doi.org/10.1021/sc400499g.

[23] D.A. Osorio, E. Niinivaara, N.C. Jankovic, E.C. Demir, A. Benkaddour, V. Jarvis, C. Ayranci, M.T. McDermott, C.-F. De Lannoy, E.D. Cranston, Cellulose Nanocrystals Influence Polyamide 6 Crystal Structure, Spherulite Uniformity, and Mechanical Performance of Nanocomposite Films, ACS Appl. Polym. Mater. 3 (2021) 4673–4684. https://doi.org/10.1021/acsapm.1c00765.

[24] S.H. Sung, Y. Chang, J. Han, Development of polylactic acid nanocomposite films reinforced with cellulose nanocrystals derived from coffee silverskin, Carbohydr. Polym. 169 (2017) 495–503. https://doi.org/https://doi.org/10.1016/j.carbpol.2017.04.037.

[25] E.P. Giannelis, Polymer Layered Silicate Nanocomposites, Adv. Mater. 8 (1996) 29–35. https://doi.org/10.1002/adma.19960080104.

[26] Y. He, J. Zhu, W. Wang, H. Ni, Surface modification of cellulose nanocrystals with different acid anhydrides for improved dispersion in poly(butylene succinate), RSC Adv. 8 (2018) 38305–38314. https://doi.org/10.1039/c8ra07597b.

[27] S.-Y. Fu, X.-Q. Feng, B. Lauke, Y.-W. Mai, Effects of particle size, particle/matrix interface adhesion and particle loading on mechanical properties of particulate–polymer composites, Compos. Part B Eng. 39 (2008) 933–961. https://doi.org/https://doi.org/10.1016/j.compositesb.2008.01.002.

[28] J. Hwang, T. Yoon, S.H. Jin, J. Lee, T.-S. Kim, S.H. Hong, S. Jeon, Enhanced mechanical

properties of graphene/copper nanocomposites using a molecular-level mixing process, Adv. Mater. 25 (2013) 6724–6729. https://doi.org/10.1002/adma.201302495.

[29] T. Mori, K. Tanaka, Average stress in matrix and average elastic energy of materials with misfitting inclusions, Acta Metall. 21 (1973) 571–574. https://doi.org/https://doi.org/10.1016/0001-6160(73)90064-3.

[30] S. Geng, M.M.-U. Haque, K. Oksman, Crosslinked poly(vinyl acetate) (PVAc) reinforced with cellulose nanocrystals (CNC): Structure and mechanical properties, Compos. Sci. Technol. 126 (2016) 35–42. https://doi.org/https://doi.org/10.1016/j.compscitech.2016.02.013.

[31] M. Pereda, N.E. Kissi, A. Dufresne, Extrusion of polysaccharide nanocrystal reinforced polymer nanocomposites through compatibilization with poly(ethylene oxide), ACS Appl. Mater. Interfaces. 6 (2014) 9365–9375. https://doi.org/10.1021/am501755p.

[32] A. Junior de Menezes, G. Siqueira, A.A.S. Curvelo, A. Dufresne, Extrusion and characterization of functionalized cellulose whiskers reinforced polyethylene nanocomposites, Polymer (Guildf). 50 (2009) 4552–4563. https://doi.org/10.1016/j.polymer.2009.07.038.

[33] B.M. Tyson, R.K. Abu Al-Rub, A. Yazdanbakhsh, Z. Grasley, A quantitative method for analyzing the dispersion and agglomeration of nano-particles in composite materials, Compos. Part B Eng. 42 (2011) 1395–1403. https://doi.org/10.1016/j.compositesb.2011.05.020.

[34] L. Hui, R.C. Smith, X. Wang, J.K. Nelson, L.S. Schadler, Quantification of Particulate Mixing in Nanocomposites, in: 2008 Annu. Rep. Conf. Electr. Insul. Dielectr. Phenom.,

2008: pp. 317–320. https://doi.org/10.1109/CEIDP.2008.4772831.

[35] Z.P. Luo, J.H. Koo, Quantitative study of the dispersion degree in carbon nanofiber/polymer and carbon nanotube/polymer nanocomposites, Mater. Lett. 62 (2008) 3493–3496. https://doi.org/https://doi.org/10.1016/j.matlet.2008.03.010.

[36] H.S. Khare, D.L. Burris, A quantitative method for measuring nanocomposite dispersion, Polymer (Guildf). 51 (2010) 719–729. https://doi.org/https://doi.org/10.1016/j.polymer.2009.12.031.

[37] J. Liu, Y. Gao, D. Cao, L. Zhang, Z. Guo, Nanoparticle Dispersion and Aggregation in Polymer Nanocomposites: Insights from Molecular Dynamics Simulation, Langmuir. 27 (2011) 7926–7933. https://doi.org/10.1021/la201073m.

[38] S.R. Bakshi, R.G. Batista, A. Agarwal, Quantification of carbon nanotube distribution and property correlation in nanocomposites, Compos. Part A Appl. Sci. Manuf. 40 (2009) 1311–1318. https://doi.org/https://doi.org/10.1016/j.compositesa.2009.06.004.

[39] A. Golbang, M.H.N. Famili, M.M.M. Shirvan, A method for quantitative characterization of agglomeration degree in nanocomposites, Compos. Sci. Technol. 145 (2017) 181–186. https://doi.org/10.1016/j.compscitech.2017.04.013.

[40] J.B. Hooper, K.S. Schweizer, Contact Aggregation, Bridging, and Steric Stabilization in Dense Polymer−Particle Mixtures, Macromolecules. 38 (2005) 8858–8869. https://doi.org/10.1021/ma051318k.

[41] D. Musino, A.-C. Genix, E. Chauveau, T. Bizien, J. Oberdisse, Structural identification of percolation of nanoparticles, Nanoscale. 12 (2020) 3907–3915. https://doi.org/10.1039/c9nr09395h.

[42] L. Rokach, O. Maimon, Clustering Methods BT - Data Mining and Knowledge Discovery Handbook, in: O. Maimon, L. Rokach (Eds.), Springer US, Boston, MA, 2005: pp. 321–352. https://doi.org/10.1007/0-387-25465-X_15.

[43] F. Nielsen, Hierarchical Clustering BT - Introduction to HPC with MPI for Data Science, in: F. Nielsen (Ed.), Springer International Publishing, Cham, 2016: pp. 195–211. https://doi.org/10.1007/978-3-319-21903-5_8.

[44] Y. Zare, Study of nanoparticles aggregation/agglomeration in polymer particulate nanocomposites by mechanical properties, Compos. Part A Appl. Sci. Manuf. 84 (2016) 158–164. https://doi.org/10.1016/j.compositesa.2016.01.020.

[45] T. Thorvaldsen, Modelling the elastic stiffness of nanocomposites using the Mori-Tanaka method, 2015. https://doi.org/9788246425559.

[46] M.A. Ashraf, W. Peng, Y. Zare, K.Y. Rhee, Effects of Size and Aggregation/Agglomeration of Nanoparticles on the Interfacial/Interphase Properties and Tensile Strength of Polymer Nanocomposites, Nanoscale Res. Lett. 13 (2018) 214. https://doi.org/10.1186/s11671-018-2624-0.

[47] J.D. Eshelby, R.E. Peierls, The determination of the elastic field of an ellipsoidal inclusion, and related problems, Proc. R. Soc. London. Ser. A. Math. Phys. Sci. 241 (1957) 376–396. https://doi.org/10.1098/rspa.1957.0133.

[48] G.P. Tandon, G.J. Weng, The effect of aspect ratio of inclusions on the elastic properties of unidirectionally aligned composites, Polym. Compos. 5 (1984) 327–333. https://doi.org/10.1002/pc.750050413.

[49] Y. Benveniste, A new approach to the application of Mori-Tanaka's theory in composite

materials, Mech. Mater. 6 (1987) 147–157. https://doi.org/10.1016/0167-6636(87)90005-6.

[50] D.L. Shi, X.Q. Feng, Y.Y. Huang, K.C. Hwang, H. Gao, The effect of nanotube waviness and agglomeration on the elastic property of carbon nanotube-reinforced composites, J. Eng. Mater. Technol. Trans. ASME. 126 (2004) 250–257. https://doi.org/10.1115/1.1751182.

[51] J. Segurado, C. González, J. LLorca, A numerical investigation of the effect of particle clustering on the mechanical properties of composites, Acta Mater. 51 (2003) 2355–2369. https://doi.org/10.1016/S1359-6454(03)00043-0.

[52] M. Yourdkhani, P. Hubert, Quantitative Dispersion Analysis of Inclusions in Polymer Composites, ACS Appl. Mater. Interfaces. 5 (2013) 35–41. https://doi.org/10.1021/am301459q.

[53] D.J. Karras, Statistical methodology: II. Reliability and validity assessment in study design, part B, Acad. Emerg. Med. 4 (1997) 144–147. https://doi.org/10.1111/j.1553-2712.1997.tb03723.x.

[54] A. Dufresne, Nanocellulose: a new ageless bionanomaterial, Mater. Today. 16 (2013) 220–227. https://doi.org/https://doi.org/10.1016/j.mattod.2013.06.004.

[55] ASTM International, ASTM D882: Standard Test Method for Tensile Properties of Thin Plastic Sheeting, ASTM Stand. (2012) 12. https://doi.org/10.1520/D0882-12.2.

[56] H. Yousefian, D. Rodrigue, Effect of nanocrystalline cellulose on morphological, thermal, and mechanical properties of Nylon 6 composites, Polym. Compos. 37 (2016) 1473–1479. https://doi.org/10.1002/pc.23316.

[57] Y. Peng, D.J. Gardner, Y. Han, Characterization of mechanical and morphological

properties of cellulose reinforced polyamide 6 composites, Cellulose. 22 (2015) 3199–3215. https://doi.org/10.1007/s10570-015-0723-y.

[58] M.A. Bhuiyan, R. V Pucha, K. Kalaitzidou, 3D RVE Models Able to Capture and Quantify the Dispersion, Agglomeration, and Orientation State of CNT in CNT/PP Nanocomposites, Front. Mater. 3 (2016) 2. https://doi.org/10.3389/fmats.2016.00002.

[59] N. Sheng, M.C. Boyce, D.M. Parks, G.C. Rutledge, J.I. Abes, R.E. Cohen, Multiscale micromechanical modeling of polymer/clay nanocomposites and the effective clay particle, Polymer (Guildf). 45 (2004) 487–506. https://doi.org/https://doi.org/10.1016/j.polymer.2003.10.100.

[60] S. Azizi, R. Mohamad, Mechanical and barrier properties of kappa-carrageenan/cellulose nanocrystals bio-nanocomposite films, in: IOP Conf. Ser. Mater. Sci. Eng., Department of Bioprocess Technology, Bioprocessing and Biomanufacturing Research Centre, Faculty of Biotechnology and Biomolecular Sciences, Universiti Putra Malaysia, Selangor, 43400, Malaysia, 2018. https://doi.org/10.1088/1757-899X/368/1/012013.

[61] J. Shojaeiarani, D.S. Bajwa, N.M. Stark, Spin-coating: A new approach for improving dispersion of cellulose nanocrystals and mechanical properties of poly (lactic acid) composites, Carbohydr. Polym. 190 (2018) 139–147. https://doi.org/https://doi.org/10.1016/j.carbpol.2018.02.069.

[62] J.-G. Gwon, H.-J. Cho, S.-J. Chun, S. Lee, Q. Wu, S.-Y. Lee, Physiochemical, optical and mechanical properties of poly(lactic acid) nanocomposites filled with toluene diisocyanate grafted cellulose nanocrystals, RSC Adv. 6 (2016) 9438–9445. https://doi.org/10.1039/c5ra26337a.

[63] E. Fortunati, D. Puglia, F. Luzi, C. Santulli, J.M. Kenny, L. Torre, Binary PVA bio-nanocomposites containing cellulose nanocrystals extracted from different natural sources: Part I, Carbohydr. Polym. 97 (2013) 825–836. https://doi.org/https://doi.org/10.1016/j.carbpol.2013.03.075.

[64] H. Sojoudiasli, M.-C. Heuzey, P.J. Carreau, Mechanical and morphological properties of cellulose nanocrystal-polypropylene composites, Polym. Compos. 39 (2018) 3605–3617. https://doi.org/10.1002/pc.24383.

[65] N.H. Inai, A.E. Lewandowska, O.R. Ghita, S.J. Eichhorn, Interfaces in polyethylene oxide modified cellulose nanocrystal - polyethylene matrix composites, Compos. Sci. Technol. 154 (2018) 128–135. https://doi.org/https://doi.org/10.1016/j.compscitech.2017.11.009.

[66] J. Shojaeiarani, D.S. Bajwa, N.M. Stark, Green esterification: A new approach to improve thermal and mechanical properties of poly(lactic acid) composites reinforced by cellulose nanocrystals, J. Appl. Polym. Sci. 135 (2018). https://doi.org/10.1002/app.46468.

[67] J. Shojaeiarani, D.S. Bajwa, K. Hartman, Esterified cellulose nanocrystals as reinforcement in poly(lactic acid) nanocomposites, Cellulose. 26 (2019) 2349–2362. https://doi.org/10.1007/s10570-018-02237-4.

[68] L. Cao, C. Liu, D. Zou, S. Zhang, Y. Chen, Using cellulose nanocrystals as sustainable additive to enhance mechanical and shape memory properties of PLA/ENR thermoplastic vulcanizates, Carbohydr. Polym. 230 (2020) 115618. https://doi.org/https://doi.org/10.1016/j.carbpol.2019.115618.

Chapter 3

Towards Better Understanding the Stiffness of Nanocomposites via Modeling Parameters and Experiments

3.1 Introduction

Nanoparticles have great potential to enhance the mechanical properties of polymeric materials. Various nanoparticles are shown to improve the stiffness of polymers: nano clay [1][2], carbon nanotubes [3][4], cellulose nanocrystals (CNC) [5][6], layered aluminosilicates [7]. This improvement is mostly due to the nanoparticles' high surface-to-volume ratio [8][9], and extraordinary properties. It is also shown that the addition of nanoparticles can change the polymer crystallinity [1] and initiate specific interactions between polymer chains and nanoparticles [10], also known as polymer-particle interface.

The volume of polymer-particle interaction is maximized when nanoparticles are uniformly dispersed; however, nanoparticles tend to agglomerate due to their high surface area and energy. Particularly, high nanoparticle loadings could result in agglomeration [11] and cause overlaps of the polymer-particle interfaces. Beyond a certain particle concentration, agglomeration is shown to be a limiting or even detrimental factor to the targeted properties of polymers in many studies [12][13][14][15]. This adverse effect could cause mismatches between experimental findings and

model predictions. Therefore, producing polymer nanocomposites with accurately predicted properties is still a challenge [16] [17].

Predicting nanocomposites' elastic properties at various particle loading levels is an important aspect of nanocomposite studies. Accurate predictions increase the efficient use of nanoparticles and lower the cost and time spent on the experimental work. In recent years, many numerical and analytical models were developed to predict the elastic modulus of nanocomposites [18][19][20][21][22][23]. Numerical models, especially molecular-level simulations, such as molecular dynamics, may produce accurate predictions in small length scales; however, they require high computational power to achieve macro-scale responses due to complex interactions between simulated elements. On the other hand, analytical micromechanical models may serve as a viable alternative for predicting the elastic modulus of polymer nanocomposites. They are, in general, easy to use, low cost and reasonably accurate [6][24].

Short-fiber micromechanical models such as the Mori-Tanaka [25], have been used or modified to predict nanocomposites' behaviour. For example, Jinsu et al. used the Mori-Tanaka micromechanics to predict elastic moduli of the silane functionalized ceramic nanocomposite [26]. It was shown that the Mori-Tanaka model agrees well with the experimental data of 0.04 volume fraction of TiO_2 in acrylate matrix [26]. The Halpin-Tsai micromechanics is another short-fiber composite model that was modified and implemented to estimate material properties of nanocomposites. Zhang et al. [4] included carbon nanotube distribution, waviness, and networks for accurate predictions. Their model agrees well with two existing literature data; however, they suggested that a more compressive model capable of considering carbon nanotube agglomeration is needed. Researchers also introduced new variables to micromechanical models or used multiscale approach for more accurate predictions. Arash et al. [27] developed an effective

interface model that considers the interface between the reinforcing element and matrix to predict elastic modulus of carbon nanotube polymer composites. The properties of the interfacial region were obtained based on molecular simulations, and these properties were utilized in a modified Mori-Tanaka model. Kim et al. [28] investigated the mechanical properties of carbon nanotube modified carbon fiber reinforced epoxy composites by developing a multiscale composite model. The Halpin-Tsai model was applied to obtain carbon nanotube/Resin 2-phase system and then woven fiber micromechanics was used for integration of fibers into the model. The model overestimates the experimental results. Kim et al. [28] claimed that the assumption of perfect bonding increases the discrepancy between modeling and experimental results.

Many investigators included agglomeration as another variable into analytical micromechanical models for better predictions. Luo and Daniel [29] proposed a three-phase analytical model based on a hybrid use of the Mori-Tanaka model and rule of mixtures to predict the elastic modulus of polymer clay nanocomposites. The developed model incorporates random orientation of clay layers and various exfoliation levels to capture the mechanical responses. In their experimental work, only low concentration levels (up to 1 w%) of clays were utilized, and higher concentration levels were not explored. The predictions agree well with the experimental findings when empirical parameters are accurately implemented. Shi et al. [4] studied the CNC waviness and agglomeration and their effect on the mechanical responses of the composites. The authors employed Eshelby's inclusion model to predict the elastic modulus of the composite with a spherical inclusion/agglomeration assumption; however, they withheld the exact definition of agglomerates. Villoria and Miravete [30] focused on the effects of clusters on the stiffness of composites. They applied the Reuss model to predict the stiffness of clusters because it was assumed that fibers would stick side by side in agglomerated regions. Their study predicts

composite stiffness as a function of clustered fibers; however, agglomerated regions' definition needs further expansion.

Attempts to predict elastic properties of nanocomposites are invaluable; however, current studies in literature suggests that there is a gap of knowledge as the available analytical models are, in general, limited in their ability to capture experimental trends at high nanoparticle loadings. Intuition and existing analytical model predictions suggest that improvement in stiffness increases as the particle loading increases. On the other hand, the reinforcement is limited to an optimal particle loading. Additional particle loadings higher than the optimal particle loading become detrimental to the mechanical properties of nanocomposites [31] [32] [33] [34] [35]. It can be claimed that the existing analytical models do not account for the complex nature of nanocomposites and agglomeration, and thus they fail to predict elastic modulus of nanocomposites at high particle loadings.

Recently, we developed an analytical model that uses a three-phase Mori-Tanaka model and the Monte-Carlo method to predict the stiffness of nanocomposites [36]. The model predictions and experimental findings match well. A comprehensive study of the model's parameters can allow us to examine and understand the effect of agglomeration on nanocomposites to address the aforementioned gap in the literature.

Consequently, in this paper, we focus on and study the effect of the model's parameters to establish a sensitivity analysis for the model. We investigate the effect of critical design variables defined in the model, such as the critical distance, agglomerates' properties, aspect ratio, particle loading and various dispersion states of nanoparticles. The predictions of the proposed model are cross-examined with experimental results from the previous study [36] where polyamide 6 (PA6) is reinforced with cellulose nanocrystals (CNC).

3.2 Modelling

The current micromechanical models [37][38] assume uniformly dispersed particles; however, obtaining uniformly dispersed nanoparticles is unrealistic because of nanoparticles' high surface energy and area. This non-uniform dispersion state of nanoparticles could result in mismatches between model predictions and experimental results, particularly at high particle loadings. We aim to lower these mismatches by introducing agglomerate phase into the model. The model, in this study, combines the Monte-Carlo approach with analytical models to capture the effect of agglomeration on the elastic modulus of nanocomposites.

The previously developed model [36] aims to offer a simple yet accurate method to predict elastic properties of nanocomposites with respect to particle loading. Its mainframe is introduced here for ease of following; however, interested readers can see the details in the original publication [36] . The proposed model is developed based on six main steps: (1) particles are dispersed in a computational setting, (2) agglomerated particles are detected using a machine learning method, (3) agglomerates are averaged based on their volume fractions and particles concentrations, (4) the elastic modulus of the averaged agglomerate is calculated using analytical models, (5) a three phase Mori-Tanaka model is applied for homogenization, and (6) the Monte-Carlo method is utilized for obtaining statistical information about the elastic modulus of composites. Each step has various parameters, and these parameters are explained in the subsections of this section. For the visualization purpose, the schematics of the homogenization approach is given in Figure 3.1

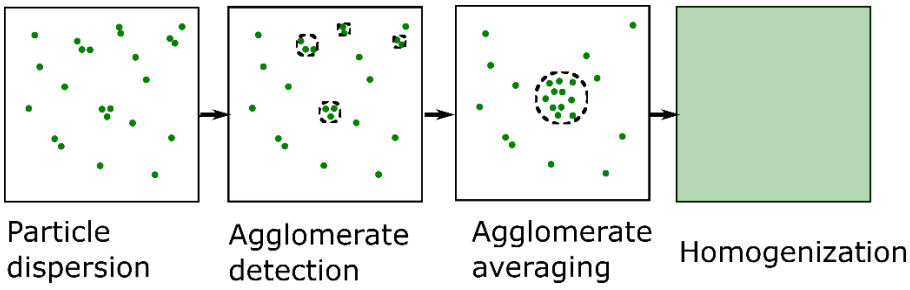

Figure 3.1. Schematics of the homogenization approach.

We assume that nanocomposites can be modelled using a three-phase Mori-Tanaka approach where the phases are the particle phase, the agglomerate phase, and the matrix phase. The application of this model requires the shape and aspect ratio of particles, as well as the elastic properties and volume fractions of the phases. The shape and aspect ratio of particles are assigned based on literature data; on the other hand, the elastic properties and volume fractions of the phases are determined using analytical and computational tools. The phases' volume fractions are calculated based on a computational approach that we developed. A two-dimensional space (1000x1000 nm) in a computational environment is set up for particle dispersion using MATLAB software. The number of particles is calculated based on a particle loading, and particles are dispersed in the two-dimensional space using the Mersenne Twister algorithm, a pseudorandom number generator. Various dispersion states are covered by changing value of dispersion parameter, $\mu[d]$ value (detailed in section 2.1).

The dispersed particles are classified either as agglomerated particles or free particles using the hierarchical clustering method, a machine learning method [39]. The implemented hierarchical clustering algorithm measures *Euclidian Distances* between particles to detect agglomerated particles. When the *Euclidian Distance* between two particles is shorter than the value of the critical distance parameter, $\gamma[d]$ (detailed in section 2.2), particles are considered to be agglomerated. In our approach, particles that are close enough (i.e. within the order of 10

nanometres) to each other are counted as agglomerated particles and matrix material can exist between them. These regions, i.e., agglomerated particles together with the matrix that is between agglomerated particles, are defined as agglomerated regions. A spherical border is drawn around agglomerated particles to define an agglomerate and to calculate particle concentration within each agglomerate. Once the particle concentrations and volume of each agglomerate is known, a volume-based averaging process is applied to obtain an averaged agglomerate. The final averaged agglomerate is taken as the agglomerate phase.

The volume fractions of the particle and matrix phases are calculated based on the detected agglomerated regions. The particle phase represents the free particles (non-agglomerated particles). Because the total number of agglomerated particles and initial particles are known, the number of free particles is easily calculated. The total volume of free particles is found by multiplying the volume of a particle by the number of free particles. In the end, the particle phase's volume fraction is obtained by dividing the volume of free particles by the composite volume. Lastly, the matrix phase's volume fraction is calculated by subtracting the volume fractions of the agglomerate and particle phases from one.

Once the volume fractions are calculated, the elastic properties of each phase are required to utilize the three-phase Mori-Tanaka method. The matrix material is tested for its properties whereas the particle phase's elastic properties are retrieved from the literature because testing the nanoparticle's properties is considerably challenging and requires another major study. For the agglomerate phase's properties, we used two micromechanical models: Halpin-Tsai and Reuss model (detailed in section 2.5).

The calculated volume fractions and elastic properties of the phases are inserted into the Mori-Tanaka model to homogenize the composite system and predict the elastic modulus of the

nanocomposite. Main modelling equations are presented here. Standard notation is used throughout the manuscript. The notations, *t, T* and $\boldsymbol{T}$ are vector, and scalar values, and second-order tensor, respectively. Subscript letters represent the phases of the system, such as $\boldsymbol{m}$ for matrix, $\boldsymbol{p}$ for particle and $\boldsymbol{a}$ for agglomerate phase. The closed-form of the three-phase Mori-Tanaka model is given by Eq. (9) [40]

$$\boldsymbol{C} = (v_m \boldsymbol{C_m} + v_f\{\boldsymbol{C_p A_p}\} + v_a\{\boldsymbol{C_a A_a}\})(v_m \boldsymbol{I} + v_p \boldsymbol{A_p} + v_a \boldsymbol{A_a})^{-1} \quad (9)$$

where $\boldsymbol{C}$ is the stiffness tensor of the composite, $\boldsymbol{C_m}$ is the stiffness tensor of the matrix, $\boldsymbol{C_p}$ is the stiffness tensor of the particle, $\boldsymbol{C_a}$ is the stiffness tensor of the agglomerate, $\boldsymbol{I}$ is the identity tensor, $\boldsymbol{A_p}$ is the strain concentration tensor of the particle, $\boldsymbol{A}_a$ is the strain concentration tensor of the agglomerate, v_m is the volume fraction of the matrix, v_p is the volume fraction of the particles and v_a is the volume fraction of the agglomerate, and the curly brackets "{}" stands for the indication of orientation averaging (detailed in section 4.3). The strain concentration tensor of $phase\ i$ is given by Eq. (10)

$$\boldsymbol{A_i} = [\boldsymbol{I} + \boldsymbol{S_i}(\boldsymbol{C_m})^{-1}(\boldsymbol{C_i} - \boldsymbol{C_m})^{-1}] \quad (10)$$

where $\boldsymbol{S}_i$ is the Eshelby tensor of $phase\ i$ and its closed form can be found in Mura's book [41].

In the last step of the model, the Monte-Carlo method is utilized to acquire comprehensive data about the elastic modulus of nanocomposites. The Monte-Carlo method uses repeated random sampling to predict an outcome range of an uncertain event or problem [42]. The uncertain problem, in this study, is the lack of knowledge about the exact dispersion state of particles. The dispersion state is the main foundation of stiffness prediction. In our model, random sampling corresponds to determining the particles' locations randomly in the defined space. As soon as particles are randomly dispersed, the aforementioned modelling steps are completed to calculate the volume fractions of the three phases. Based on the calculated volume fractions, the elastic

modulus of the composite is found using the three-phase Mori-Tanaka model. For accurate and reliable predictions, this process is repeated one hundred times for each particle loading. We kept the repetitions at one hundred to ensure the timely completion of Monte-Carlo and reach the near-infinite number of possible predictions. The results for each particle loading are illustrated in boxplots.

3.2.1 Particle Dispersion

In the developed model, we introduce a parameter $\mu[d]$ that controls the dispersion state of the particles in the computational setting. Experimentally, the dispersion state is usually quantified by measuring the distance between neighbouring particles that are observed on microscope images [43–45]. The investigators [43–45] measure and record neighbouring distances and present them as histogram diagrams. The obtained histograms are fitted into lognormal probability density functions to discuss the dispersion state of particles. Here, instead of evaluating microscope images to obtain lognormal distributions, we utilize lognormal probability density functions to generate synthetic dispersion states. A lognormal probability density function are formed based on two variables: the mean value (μ) and standard deviation (σ) of the variable's natural logarithm [44,46]. The dispersion parameter $\mu[d]$ is defined as the coefficient of particle diameter. The value of the dispersion parameter $\mu[d]$ is multiplied by the particle diameter to find the mean of logarithmic values (μ) that is used to establish lognormal probability density functions.

Particles' locations are determined based on random numbers that are generated from the established lognormal distribution. The location of the first particle is selected from the uniform distribution. For the second particle, a random angle and a random distance are chosen from the uniform probability distribution and lognormal probability distribution, respectively. The chosen

random values for the angle and distance are utilized to locate the second particle with respect to the location of the first particle. Each particle is located in the same manner – the angle and distance are selected to locate the new particle's location with respect to the previous particle's location. The dispersion of particles is continued until all particles are located. It is important to note that particles cannot occupy the same location in the model. Thus, in the case of particle intersection, a new location is assigned to the newest particle based on the random location selection from all possible locations.

In addition to the lognormal distribution, a uniform probability distribution is used to disperse particles. In the case of uniform distributions, the constant probability distribution function is used to assign the location of a particle. Once a particle is located, the next one is located using the uniform distribution. In the case of an overlap, a new location is assigned to the newest particle. Here, we aim to capture various dispersion states, from uniformly dispersed particles to agglomerated particles. Although different states of dispersion are established, agglomerates are needed to be defined and understood well to investigate their effects on the stiffness of nanocomposites.

3.2.2 Critical Distance

The critical distance parameter $\gamma[d]$ is introduced to differentiate agglomerated particles from non-agglomerated particles as the distinction between them has been vague in the composite literature. Existing agglomerate quantification studies analyze and compare different microscope images to show relative agglomeration states of nanoparticles instead of focusing on individual agglomerates [47]. The distinction between agglomerated and non-agglomerated particles can only be accommodated if individual agglomerates are defined and quantified. Here, the critical distance

parameter $\gamma[d]$ is proposed to detect agglomerated particles, define an agglomerate, and differentiate one agglomerate from another. The critical distance parameter is inspired by the "cut-off" argument defined in the "cluster" function that is used in the hierarchical clustering method in MATLAB.

The hierarchical clustering, a machine learning method, is used to group data sets into a cluster tree where the tree represents a hierarchy of clusters. Two hierarchical clustering methods exist: agglomerative (bottom-up approach) and divisive (top-down approach). In thus study, we utilize the agglomerative hierarchical clustering method because it is a built-in tool in MATLAB Statistics and Machine Learning Toolbox, and it is easier to comprehend intuitively. In the agglomerative hierarchical clustering method, particles start with their own cluster and then combine into bigger clusters based on the distance between them. This method can be described in three main steps: (1) the distance between particles is calculated using a "distance" metric, (2) particles are linked and grouped with a "linkage" method, and (3) the number of clusters (agglomerates) is determined using the value of "cutoff" argument.

In this study, the agglomerative hierarchical clustering method is adopted as a solution to detect agglomerates based on the location data set. Firstly, the distance between particles is calculated using the "Euclidean distance" metric. The "Euclidean distance" is the length of a line between two points that is calculated using the Pythagorean theorem. Secondly, the particles are linked together based on the "single" the linkage method. The "single" method takes the shortest distance between particles to link and group them. Herein, the "single" method is used because we assume that particles that are closest to each other should belong to the same agglomerate. Thirdly, each agglomerate is classified, and the number of agglomerates is found using the critical distance parameter. The critical distance parameter is used as the "Cut-off" argument that determines the

number of agglomerates in the system. If the critical distance is higher than the shortest distance between two particles or agglomerates, they are grouped together and become members of the same agglomerate. The critical distance parameter is defined as a function of the particle diameter and the value assigned to $\gamma[d]$ represents the coefficient of the particle diameter. For example, $\gamma[d] = 2$ means that the critical distance is 10 nm when the diameter of the particle is 5 nm. If the center-to-center distance of any particles is less than 10 nm, then they are counted as agglomerated particles, and particles belong to the same agglomerate. Thus, the value of $\gamma[d]$ is crucial for detecting agglomerated particles and differentiating one agglomerate from another.

The value of $\gamma[d]$ may depend on the constituents of the composite; however, data in the literature guides us to estimate a range. In a finite element analysis study, from Sheng et. al. study, strain fields intersect when the distance between fillers is less than 4 times the diameter of the fillers. In another study, Liu et al. studied nanoparticle dispersion with molecular dynamics and discuss the interaction between nanoparticles. Liu et. al. claimed that particles do not have to touch each other to be counted as agglomerates. A short separation of fillers by polymer chains is defined as the state of "local bridging of fillers". The short separation distance is in the range of 1 to 2 times the particle diameter. In this study, we follow a similar range (1-4 times particle diameter) to examine the effects of critical distance on the state of agglomerates.

The MATLAB code assigns a number to each agglomerate so that we can detect individual agglomerates and differentiate one from another. The number assigned to the agglomerate is also associated with particles within that agglomerate. For example, if we consider a case where there are two agglomerates, one with 3 particles and the other one with 5 particles. Here, the one with 3 particles are associated with number 1 and the one with 5 particles are associated with number 2. Hence, one can tell which particle belongs to which agglomerate. Once the agglomerates and the

particles within each agglomerate are numbered, we establish a spherical border around the agglomerated particles to define agglomerated regions. Figure 3.2 shows schematics of an agglomerate. The green filled circles represent the fillers, and the white region between them represents the matrix. Because agglomerated particles do not have to be in contact, an agglomerate can include particles and matrix within its border. The border is fit around the agglomerated particles such that the longest distance between two particles is assumed to be the diameter of the agglomerate. With the knowledge of the agglomerate boundary, the volume fraction of particles within the agglomerate can be calculated and monitored for various critical distance values.

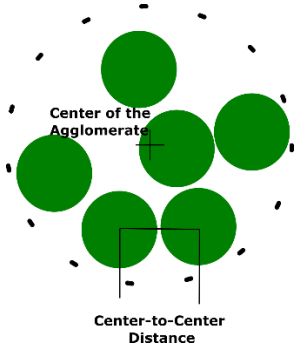

Figure 3.2. Schematics of an agglomerate for better understanding of a center-to-center distance.

3.2.3 Particle Orientation

Nanocomposites are stiffer in the direction of oriented fibers; however, representing and utilizing the orientation of fibers in modelling may vary and can be challenging. One possible representation of fibers' orientation is a probability distribution function. According to Advani and Tucker [48], this probability distribution function can be replaced by an orientation tensor for ease of calculation in continuum equations. The orientation of the fiber is required to establish the orientation tensor. Figure 3.3 describes the orientation of a fiber using spherical coordinate angles (θ, Φ) under three

main assumptions: fibers are rigid cylindrical, fibers' length and diameter are uniform, and the number of fibers per unit volume is uniform.

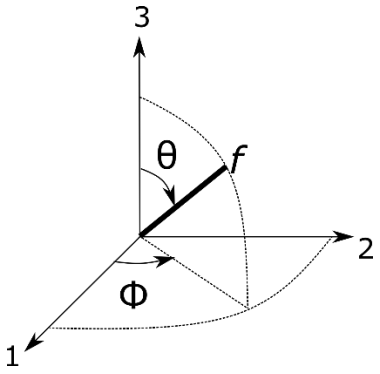

Figure 3.3. The definitions of $\boldsymbol{\theta}$, Φ, and $\boldsymbol{fiber\ f}$ in a cartesian coordinate system.

The probability of having a fiber between angles θ_1 and $\theta_1 + d\theta$ and Φ_1 and $\Phi_1 + d\Phi$ is given by the Eq. 11

$$P(\theta_1 \leq \theta \leq \theta_1 + d\theta, \Phi_1 \leq \Phi \leq \Phi_1 + d\Phi) = \varphi\,(\theta_1, \Phi_1)\, sin\,\theta_1\, d\theta d\Phi \qquad 11$$

where $\varphi\,(\theta_1, \Phi_1)$ is a probability distribution function. The orientation of a fiber can also be represented as a vector $\boldsymbol{f}$, and the components of the vector $\boldsymbol{f}$ in a cartesian coordinate system can be written by Eq. (12),(13), and (14)

$$f_1 = sin\,\theta \cos\Phi \qquad 12$$

$$f_2 = sin\,\theta\, sin\,\Phi \qquad 13$$

$$f_3 = \cos\theta \qquad 14$$

Because the orientation can be represented by $\boldsymbol{f}$, the distribution function can be written as $\varphi(\boldsymbol{f})$. If it is assumed that all possible directions of a fiber correspond to the unit sphere and a fiber is a unit vector, the surface integral of the unit sphere can be calculated by Eq. (15)

$$\int_{\theta=0}^{\pi}\int_{\Phi=0}^{2\pi}\varphi\,(\theta,\Phi)\,sin\,\theta\,d\theta d\Phi = \oint \varphi(\boldsymbol{f})d\boldsymbol{f} = 1 \qquad 15$$

Advani and Tucker [48] showed that the probability distribution function can be represented by tensors, and they provided a widely used orientation tensor that represents the orientation state of fibers. The fourth-order orientation tensor that is defined by dyadic products of the vector is given by Eq. (16)

$$T_{ijkl} = \oint f_i f_j f_k f_l \varphi(\boldsymbol{f})d\boldsymbol{f} \qquad 16$$

The integration of the product including all possible directions with φ as the weighting function can be used for the averaging process. The orientation averaging can be represented by $\{\,\}$ and expressed by Eq. (17)

$$\overline{\boldsymbol{T}_{ijkl}} = \{\boldsymbol{T}_{ijkl}\} = \int_0^{\pi}\int_0^{2\pi}\boldsymbol{T}_{ijkl}(\theta,\Phi)\sin\theta\,d\theta d\Phi \qquad 17$$

where $\boldsymbol{T}_{ijkl}(\theta,\Phi)$ is the orientation distribution in tensor format, $\overline{\boldsymbol{T}_{ijkl}}$ is the averaged orientation tensor and $\{\,\}$ represent averaging process [49].

3.2.4 Aspect Ratio of Particles

The aspect ratio, defined as the length to diameter ratio, is another key design parameter in composite modelling and manufacturing. Some micromechanical models, such as Shear-log, Halpin-Tsai, Mori-Tanaka take the aspect ratio as a variable. In this study, we investigate the effect of the aspect ratio using the Mori-Tanaka model.

In the three-phase Mori-Tanaka model, the aspect ratio of particle phase and agglomerate phase is required for the elastic modulus calculations. The aspect ratio of the agglomerate phase is taken as one because it is assumed that particles agglomerate in a spherical form due to the minimum surface energy requirement and mechanical stability [54][55]. On the other hand, we investigated the effect of the aspect ratio of the free particles on stiffness with three different values: 15, 30 and 60. We selected that range because the aspect ratio of reinforcement used in our experiments, CNC, changes from 10 to 70 depending on the source of CNC [50].

3.2.5 Material Properties

Material properties of the particle, agglomerate and matrix phases are needed for the model implementation. The matrix (PA6) is tested for its elastic modulus, and the particle's (CNC) elastic modulus is retrieved from the literature data [56] for calculations. The agglomerate phases' properties are more complicated than matrix and particle phase's properties, because of the lack of the agglomerate definition and studies in the literature. Although many studies examine the effect of agglomeration on the properties of composites [52], there is no consensus about the individual agglomerate's elastic modulus. Some studies [51] assume that agglomerates behave like a void, whereas others calculate their properties based on the Reuss model [28] or the Halpin-Tsai model [50]. In this study, either the Reuss model or Halpin-Tsai model are utilized to calculate the

elastic modulus of agglomerated regions. These models would provide a good range of possible outcomes, and the effects of stiffness of agglomerates on the stiffness of composite can be observed. The Reuss model is given by Eq. (18)

$$E_a{}^{-1} = v_{am}E_m{}^{-1} + v_{ap}E_p{}^{-1} \quad (18)$$

where E_a is the elastic modulus of the agglomerate, E_m is the elastic modulus of the matrix, and E_p is the elastic modulus of the particle; v_{am} is the volume fraction of the matrix within the agglomerate, and v_{ap} is the volume fraction of the particles within the agglomerate. Material properties of the particle and matrix for the agglomerate property calculation are kept the same as their individual properties.

The randomly orientated Halpin-Tsai model is calculated based on the particle volume fraction within agglomerated regions by Eq. (19)

$$E_a = {}^{5}/_{8}\,E_L + {}^{3}/_{8}\,E_T \quad (19)$$

where E_L is the longitudinal modulus and E_T is the transversal modulus. The longitudinal modulus E_L is calculated by Eq. (20) [51]

$$E_L = E_m \frac{1 + 2\beta v_{ap}\eta_l}{1 - \eta_l} \quad (20)$$

where β and η_l are geometrical parameters. β converges to 2 for transverse modulus and converges to $\boldsymbol{2\alpha}$ ($\boldsymbol{2\,{}^{l}/_{d}}$) for longitudinal modulus. The transversal modulus $\boldsymbol{E_T}$ is calculated by Eq. (21)

$$E_T = E_m \frac{1 + 2\beta v_{ap}\eta_t}{1 - \eta_t} \quad (21)$$

where η_t is a geometrical parameter for transversal modulus, and η_l and η_t are given by Eq. (22) and Eq. (23), respectively

$$\eta_l = \frac{\frac{E_P}{E_m} - 1}{\frac{E_p}{E_m} + \beta} \quad (22)$$

$$\eta_t = \frac{\frac{E_P}{E_m} - 1}{\frac{E_p}{E_m} + 2} \quad (23)$$

3.3 Experimental Methodology

The experimental work to validate the model was presented in a previous study [36]. Herein, we summarize the procedure, and readers are encouraged to see the previous study for detailed information.

PA6 was dissolved in formic acid, and then CNC was added to the suspension based on the target concentration. The prepared suspension was kept under agitation for approximately an hour. The prepared suspension was sonicated for 45 minutes before the spinning process. 2 mL of the suspension was cast on a rectangular glass substrate, and the glass substrate was spun at 2000 rpm for 15 seconds and at 3000 rpm for 30 seconds.

CNC-PA6 nanocomposite samples were tested using TA Instrument ElectroForce 3200 with 10 N load cells. The elastic modulus of samples was calculated from the linear region of the stress-strain curve and reported for comparison of the model predictions and experimental results.

3.4 Model Implications and Discussion

3.4.1 Effect of Critical Distance and Particle Orientation

The elastic modulus of randomly and aligned fiber composites are calculated with the critical distance parameter $\gamma[d]$ for the values of 1, 2, 3, and 4. The model outputs for the aligned and randomly oriented particles are given in Figure 3.4 (a) and (b), respectively. In the model predictions, the elastic modulus of agglomerates is calculated based on the Reuss model, the aspect ratio is taken as 30 and particles are dispersed uniformly.

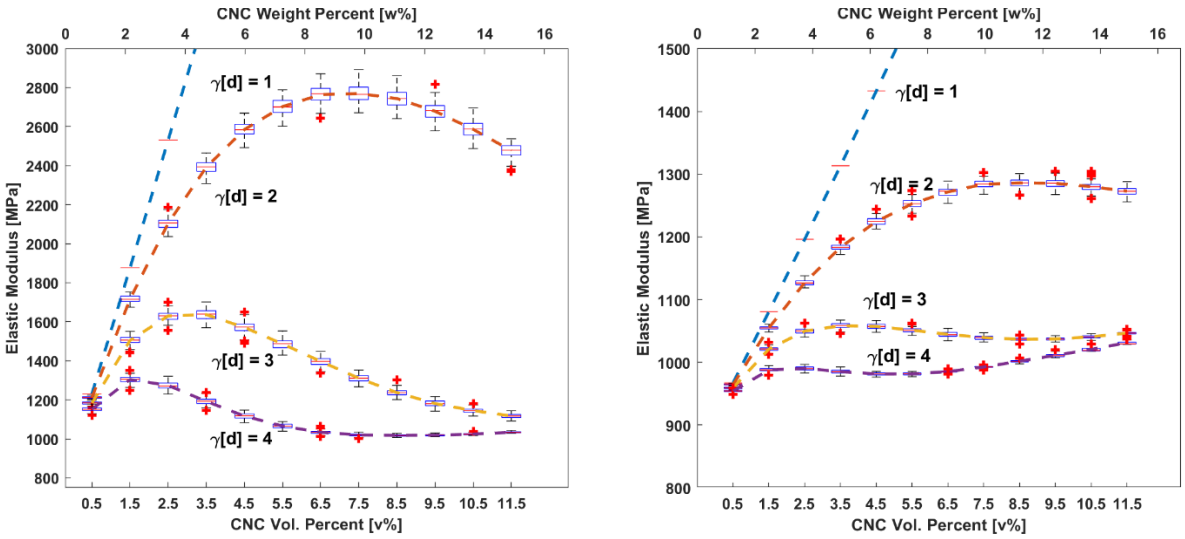

(a) (b)

Figure 3.4. Elastic modulus predictions of CNC-PA6 composite as a function of CNC loading for (a) aligned and (b) randomly oriented particles at various $\gamma[d]$ values.

The trends of predictions in Figure 3.4 (a) and (b) are similar at the same values of $\gamma[d]$; however, the trends vary among different $\gamma[d]$ values. The critical distance parameter $\gamma[d]$ is used to detect agglomerated and free particles. If the critical distance is higher than the shortest distance between two particles, those particles are counted as agglomerated particles. When $\gamma[d] = 1$, the model

predicts approximately a linear output with respect to particle loading because the three-phase Mori-Tanaka converges to the two-phase Mori-Tanaka: the particle and matrix phases without an agglomerate phase. Selection of $\gamma[d] = 1$ (critical distance of 5 nm) eliminates the chance of agglomerate formation because the closest distance between particles' centers cannot be lower than 5 nm. As a result, each particle behaves as a free particle, and an approximate linear trend is observed in the case of $\gamma[d] = 1$. On the other hand, the trend is highly different with the selection of $\gamma[d] = 2$ compared to the selection of $\gamma[d] = 1$. The predictions increase up to an optimal point of particle loading and then start to drop with particle over loadings. This prediction trend is also valid for $\gamma[d] = 3$ and $\gamma[d] = 4$, although the predicted values are different. There are three main reasons for this type of trend: (1) the high probability of agglomerate formation, (2) the low elastic modulus of agglomerates and (3) the low aspect ratio of agglomerates.

Particles are expected to agglomerate when $\gamma[d] > 1$ because the shortest distance between particles can only be lower than the critical distance at values of $\gamma[d] > 1$. The probability of agglomerate formation increases with increasing particle loadings and higher $\gamma[d]$ values. High particle loadings decrease the shortest distance between particles, and high $\gamma[d]$ values result in higher critical distances. Thus, increase in both parameters leads to the higher probability of agglomeration. The higher probability of agglomeration accelerates the agglomerate phase domination in overall model response, and the properties of agglomerates become major contributors to the model predictions. Because the Reuss model predicts lower than the two-phase Mori-Tanaka model and is used for predicting the elastic modus of agglomerates, the three-phase model predicts lower values after an optimal particle loading. The lowest elastic moduli are observed for $\gamma[d]$ value of 4 because the critical distance reaches its highest value among the four

values. This high value of critical distance yield easier particle agglomeration and low elastic modulus.

Another reason for lower model predictions after the optimal particle loadings at $\gamma[d] > 1$ is the low aspect ratio of agglomerates. We assume that the agglomerate phase is in spherical form and has an aspect ratio of one, which is much lower than the aspect ratio of CNC. This decrease in the aspect ratio, according to the Mori-Tanaka model calculations, also lowers the model predictions. The decrease in the aspect ratio of phases, the probability of agglomerate formation and the low elastic modulus of agglomerates result in differences between the prediction trends of various $\gamma[d]$ values.

The prediction values for the aligned particles are higher than randomly oriented ones, although the trends are similar at the same value of $\gamma[d]$. The dramatic influence of alignment on the elastic modulus can be seen when in Figure 3.4 (a) and (b) are compared at $\gamma[d] = 2$. According to the model predictions, the maximum elastic modulus for aligned particles is 2800 MPa, whereas it is approximately 1300 MPa for the randomly oriented particles. The particle alignment provides approximately 2.5 times stiffer nanocomposite than randomly oriented particles at 5.0 v% CNC loading. Stiffer nanocomposites in the longitudinal direction are obtained with aligned particle reinforced composite unless particle loadings are not higher than 7.5 v%. Although particle alignment provides stiffer nanocomposites in the longitudinal direction, obtaining aligned particles in nanocomposites could require a specialized manufacturing method such as electrospinning. The electric field can be used to align particles in electrospinning method; however, most of the engineering manufacturing methods such as injection molding could result in random orientation of particles. Manufacturing method should be taken into account while applying the model for the elastic model prediction of nanocomposites.

The impact of the particle concentration and $\gamma[d]$ value on agglomeration tendency is investigated by extracting the volume fractions of each constituent. Table 3.1 shows the volume fractions of each constituent at various particle loadings and $\gamma[d]$ levels. The initial volume fraction of particles (v_{ip}) is given in the first column of Table 3.1. Based on the initial volume fractions, the number of particles is calculated and reported in the third column. As expected, when the initial volume fraction of particles increases from 0.35 to 0.85, the number of particles increases from 1800 to 4372. Based on the selected $\gamma[d]$, the number of agglomerates and the volume fractions of each constitute are calculated. It can be seen that agglomerated particles, given in the fourth column, increase as v_{ip} and $\gamma[d]$ increase. However, the number of agglomerates (# Agg) does not increase in the same ratio, and it even decreases when $v_{ip} = 0.85$.

Table 3.1. Volume fractions and number of each constitute at various $\gamma[d]$ values and partcile v_p%

v_{ip}	$\gamma[d]$	# Particle	# Agg.	# Agg. Particles	v_p	Ave. v_a	Ave. v_{ap}	v_m
0.35	2	1800	367	980	0.016	0.084	0.226	0.9
0.35	3	1800	368	1463	0.007	0.21	0.135	0.783
0.85	2	4372	737	3803	0.011	0.392	0.188	0.597
0.85	3	4372	59	4318	0.001	0.579	0.145	0.42

The decrease in the number of agglomerates is related to the particle concentration and size of agglomerates. When $\gamma[d]$ is set to 2 for 0.85 v_{ip}, high number of small agglomerates are formed (737 agglomerates with 0.392 total average volume of fraction agglomerates). On the other hand,

when $\gamma[d]$ is set to 3 for 0.85 v_{ip}, low number of big agglomerates are formed (59 agglomerates with 0.579 total average volume of fraction agglomerates). Thus, it can be suggested that big agglomerates are formed with less concentrated particles. The volume fractions of particles within agglomerates (v_{ap}), in the eighth column, at 0.85 v_{ip} can be compared to observe the effect of $\gamma[d]$ at values of 2 and 3. Agglomerated particle fraction (v_{ap}) decreases from 0.188 to 0.145 when $\gamma[d]$ increases from 2 to 3 for the same initial particle fraction. It again suggests that big agglomerates are formed with less concentrated particles.

The volume fraction of free particles and matrix highly depend on $\gamma[d]$. It is clear that free particle fraction (v_p) drops with increasing $\gamma[d]$ for the same initial particle fractions. Similar trend is also observed for the matrix phase fractions. The matrix volume fraction (v_m), in the ninth column, decreases as (v_{ip}) and $\gamma[d]$ increases because of higher agglomerated matrix and particle fractions. Because the free particles are the main reinforcing elements, the model is expected to predict lower composite elastic modulus with increasing $\gamma[d]$.

3.4.2 Effect of Critical Distance and Agglomerate Property

The effect of $\gamma[d]$ and agglomerate's properties on the elastic modulus of randomly oriented particle nanocomposites is shown in Figure 3.5. The values of 2 and 4 for the $\gamma[d]$ are investigated along with two different models, which are applied to calculate agglomerates' properties: the Reuss and Halpin-Tsai models. While the $\gamma[d]$ values and properties of agglomerates are changed, the other parameters are fixed in the model calculations. Particles are assumed to be randomly oriented, and the aspect ratio (α) is taken as 30. Locations of particles are randomly selected from the uniform probability distribution function.

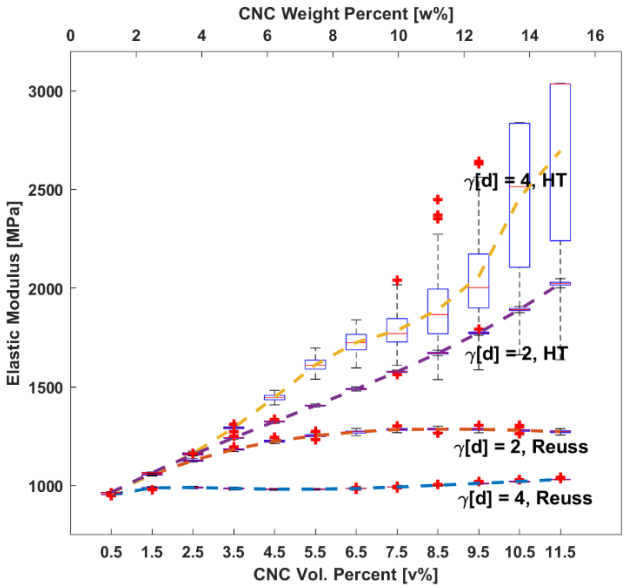

Figure 3.5. The effect of $\gamma[d]$ and agglomerate's property on the elastic modulus of randomly oriented particle nanocomposites based on the Reuss and Halpin-Tsai (HT) used for agglomeration.

In the case of the Halpin-Tsai model, the elastic modulus of nanocomposites increases with increasing particle loading regardless of the $\gamma[d]$ value. The average elastic modulus improves from 1890 MPa to 2700 MPa when the particle loading increases from 8.5v% to 11.5 v% with $\gamma[d] = 4$. The slope of this increase is 93.3 MPa/v%. In a similar manner, the average elastic modulus increases from 965 MPa to 1295 MPa when the particle loading increases from 0.5 v% to 3.5 v% when $\gamma[d] = 4$. The slope for the second case is 100.0 MPa/v%. It can be claimed that both slopes are very close to each other. A similar positive slope is also observed for the model predictions when $\gamma[d] = 2$. The slope of the predictions between 8.5-11.5 is 118 MPa/v%, and the slope between 0.5-3.5 is 91 MPa/v%. The increase in the slope shows that agglomeration results in more enhancement in the stiffness of the nanocomposite.

The prediction trends are quite different in the case of the Reuss model. We first observe an increase in the elastic modulus, and then a decrease regardless of the $\gamma[d]$ value. The increase is particularly observed at low particle loadings. For example, the average elastic modulus of the composite increases from 980 MPa to 1190 MPa when the particle loading is increased from 0.5 to 3.5 v% when $\gamma[d] = 2$. We see a similar improvement in the elastic modulus up to 1.5 v% particle loading, in the case of $\gamma[d] = 4$. The maximum average elastic modulus is obtained at 1.5 v% when $\gamma[d] = 4$ and 7.5 v% when $\gamma[d] = 2$. The higher than optimal particle loadings result in a decrease in the elastic modulus because of the agglomerates' properties. The agglomerates' properties start to dominate the overall response with high particle loadings and high $\gamma[d]$ values. Because the Reuss model predicts a lower value than the Halpin-Tsai and Mori-Tanaka models, the agglomerate domination lowers the elastic modulus of the composite. This decrease starts earlier with $\gamma[d] = 4$ due to the higher probability of agglomeration. Thus, it can be said that the impact of $\gamma[d]$ is apparent when the Reuss model is applied because of the low stiffness of agglomerates. As the agglomerate dominates in the composite material, overall response shifts to the Reuss model predictions at high particle loadings.

Predicting the mechanical behaviour of nanocomposites becomes difficult with increasing particle loadings because experimental findings vary substantially. For example, the elastic modulus values [57–60] reach a plateau value or decrease with particle over loading. Peng et al. [52] observed a plateau value at 3.5 w% of CNC in PA6 whereas Morelli et. al [53] observed that optimal particle loading is between 5-10 w% for unmodified CNC. These studies demonstrate that the optimal particle loading, and the amount of increase and decrease depend on experimental settings; however, the proposed model suggests that the combination of agglomerates' property and $\gamma[d]$ determines the overall composite reaction at high concentration levels. The trends in the elastic

modulus of composites in [57–60] validate that the Reuss model is more appropriate for the predictions of elastic modulus of agglomerates in the proposed model.

The critical distance parameter is the main parameter that controls the agglomerate formation, and higher $\gamma[d]$ values result in a higher agglomeration chance. In Figure 3.5, the values of 2 and 4 for $\gamma[d]$ are examined. The implementation of $\gamma[d] = 4$ in the model dramatically lowers the predictions in the case of the Reuss model due to agglomerate domination. Thus, the appropriate value of $\gamma[d]$ is crucial for accurate predictions. The exact value of the critical distance $\gamma[d]$ may depend on the material system or interface chemistry. Sheng et al. [2] modelled polymer/clay composite using finite element analysis. The particles are classified as "isolated", "partially overlapped" and "completely overlapped" according to the distance and load transfer efficiency. The load transfer efficiency starts to decrease as the distance between nanoparticles is approximately below 20 nm, and they define particles that are closer than these values as overlapping particles. The value of 20 nm corresponds to approximately 4 distance/diameter ratio of clay in their study. Therefore, it can be claimed that the value of $\gamma[d]$ between 1 and 4 is a reasonable range.

3.4.3 Effect of Orientation and Aspect Ratio of the Particles

The effect of orientation and aspect ratio of the particles is shown in Figure 3.6. Uniform probability distribution is utilized for the particle dispersion, and $\gamma[d]$ is kept at the value of 2. The Reuss model is applied to calculate the modulus of agglomerates in this case.

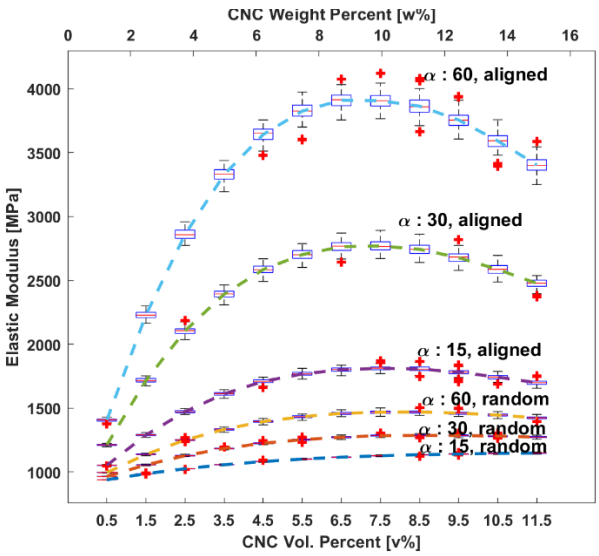

Figure 3.6. Predictions of elastic modulus of CNC-PA6 composites as a function of CNC concentrations for various orientation and aspect ratio ($\boldsymbol{\alpha}$) of the particles.

Figure 3.6 contains six predictions based on various aspect ratios and particle orientations. The highest three elastic modulus values are from the aligned composites. For a better understanding of the orientation effect, the aligned and randomly oriented CNC with the aspect ratio (α) value of 15 can be compared. The model predicts an average elastic modulus of 1750 MPa for aligned particles and 1225 MPa for randomly oriented particles at 7.5 v%, approximately 60 % difference. This difference is higher when the aspect ratio is set to a higher value. For example, the model predicts an average elastic modulus of 3800 MPa for aligned particles and 1460 MPa for randomly oriented particles at 7.5 v% with the aspect ratio of 60, approximately 170 % difference. This high difference suggests that particle orientation should be considered as a major contributor to the elastic modulus of nanocomposites. According to the six model predictions, it can be said that orientation carries more importance than the aspect ratio. The aligned particle composite with the aspect ratio of 15 provides approximately 50% higher elastic modulus than the randomly oriented particle composite with the aspect ratio of 60, which proves the importance of alignment.

The elastic modulus of nanocomposites is improved with an increasing aspect ratio according to the Mori-Tanaka model. This improvement is much higher when particles are aligned. For example, at 6.5 v% CNC, the increase in the elastic modulus is approximately 150 % (from 1600 MPa to 3600 MPa) for the aligned particles when the aspect ratio changes from 15 to 60; however, it is approximately 40 % (from 1125 MPa to 1460 MPa) for the randomly oriented particles at the same particle loading.

The maximum improvement with respect to neat PA6, ~330 % increase, is predicted to be at 7.5 v% with $\gamma[d]$ value of 2 and the aspect ratio of 60. However, the average CNC aspect ratio used in this study is approximately 30, and it is difficult to obtain fully aligned CNC reinforced composites. Thus, the maximum increase in elastic modulus would be expected to be lower than the 330% increase.

3.4.4 Effect of Dispersion and Critical Distance

The effect of dispersion is explored by selecting the location of particles from the lognormal probability distribution instead of using the uniform probability distribution. The main reason to choose lognormal distribution is that distances between neighbour particles obey lognormal distribution according to dispersion quantification studies [44] [47] [54].

The lognormal probability distribution is defined by μ (mean of logarithmic values) and σ (standard deviation of logarithmic values). It is challenging to know exact μ and σ values because they vary in the studies [44,47,55–59] depending on material system, production, and characterization methods. Instead of implementing an exact value, various μ values are used to study the dispersion effect on the composite's modulus. The parameter $\mu[d]$ is defined as the coefficient of the particle diameter in this section *i.e.,* $\mu[d] = 0.5$ means that the mean of

logarithmic values is 2.5. The more uniform particle dispersion is obtained with a higher $\mu[d]$ value.

The effects of the dispersion $\mu[d]$ and critical distance parameters $\gamma[d]$ on the elastic modulus of the composite at different particle loadings (1.0-15.0 w%) are presented with the surface plots in Figure 3.7. The surface plots are generated with 0.2 and 0.04 intervals of $\mu[d]$ and $\gamma[d]$, respectively. In these predictions, the agglomerate's property is calculated based on the Reuss model, the aspect ratio is taken as 30, and free particles are assumed to be aligned. The black spheres in the figures represent the average experimental results from the previous study [36]. The black spheres are located in the figures based on predictions' minimum mean squared error with respect to the obtained empirical data.

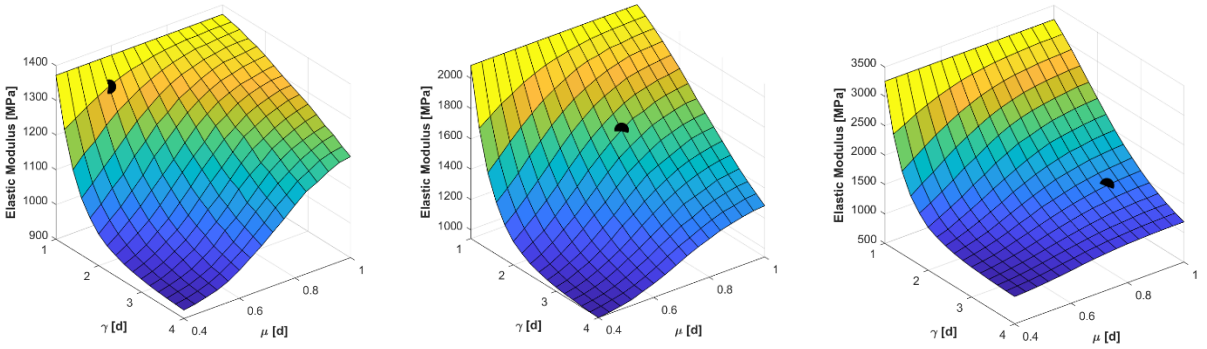

(a) (b) (c)

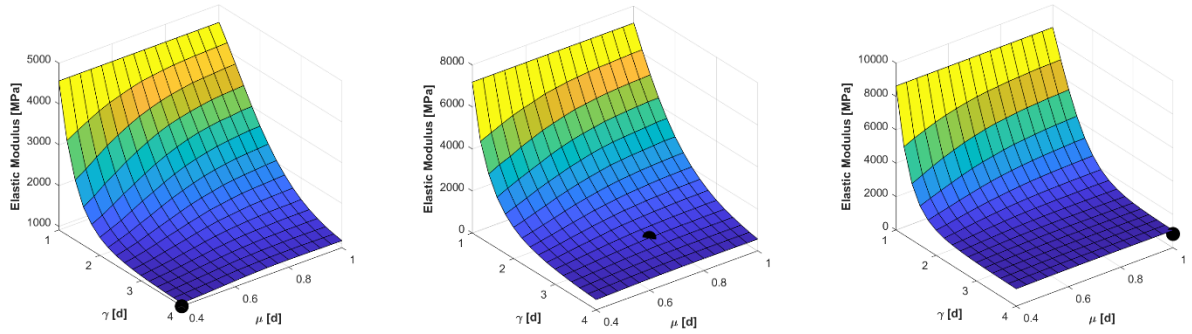

(d) (e) (f)

Figure 3.7. Predictions of elastic modulus of nanocomposites as functions of $\boldsymbol{\gamma[d]}$ and μ[$\boldsymbol{d}$] at 1.0 (a), 2.5 (b), 5.0 (c), 7.5 (d), 10.0 (e) and 15.0 (f) w% of CNC and corresponding empirical findings from [36] shown with black spheres.

The surface plots show that the model can predict empirical findings well for each CNC loading. The model calculates the highest outputs at $\gamma[d] = 1$ because the model assumes no agglomeration in the system, which results in a two-phase Mori-Tanaka model. On the contrary, the model predicts lower elastic modulus values at high $\gamma[d]$ values and high particle loadings because of agglomeration. The transition between high and low ends is well captured by setting various levels of $\gamma[d]$ and $\mu[d]$ at any particle loadings.

Experimental results are relatively high compared to neat PA6 (911 MPa) at 1.0, 2.5 and 5.0 w% CNC and they are captured with low $\gamma[d]$ and high $\mu[d]$. On the other hand, there is a dramatic drop in the elastic modulus values after 5.0 w% CNC loading. The drop and low elastic modulus values are captured with high $\gamma[d]$ and low $\mu[d]$ values. The high $\gamma[d]$ and low $\mu[d]$ values result in the domination of agglomerates in the model and since the Reuss model is used for agglomeration, the surface plots bend toward the lower end.

Higher values of $\mu[d]$ in the model generate a better dispersion and stiffer nanocomposites, and many experimental studies [68][69] suggested that well-dispersed particles provide stiffer nanocomposites. Azizi [68] et. al observed an improvement in the elastic modulus to a certain extent and then a decrease in the modulus after optimal particle loading. According to Azizi, poor dispersion of CNC result in the drop of the elastic modulus. Similar to the experimental work [68], the poor dispersion result in decrease in elastic modulus in the model. This drop after an optimal particle loadings, satisfactorily captured by the developed model. One can observe the effect of dispersion by examining Figure 3.7 (b) at various values of $\mu[d]$. The elastic modulus values increase with increasing $\mu[d]$ values (increasing dispersion) at a constant $\gamma[d]$ value. It is difficult to know exact value of $\mu[d]$ because the exact value may depend on the process, materials, and even on particle loading. A detailed study should be conducted to correlate the critical distance and the logarithmic mean of neighbour distance (μ) to the variables in the experiments. Each material system may require particular modeling inputs; however, it is shown here that the modeling outputs can capture a wide range of experimental results.

Another aim of this study is to cross-examine the model predictions with respect to particle loadings. Here, we fine-tune the values of the model parameters depending on the experimental setting. In the experimental study [36], the particles and the matrix were dissolved in a solvent before producing the samples. Various agitation methods were used to disperse particles uniformly in the suspension during the mixing process. Thus, it seems reasonable to use the uniform probability distribution to predict the locations of particles in the model. Based on TEM images of the previous study [36], free particles were mostly aligned, and the average aspect ratio was taken to 30. Here, we assume fully aligned particles with the aspect ratio of 30 for the calculations. Furthermore, based on the modeling predictions in this study and experimental results from the

literature, the Reuss model seems acceptable to calculate the agglomerates' elastic modulus. According to these assumptions, Figure 3.8 exhibits the predictions of elastic modulus of nanocomposites with respect to CNC particle loading along with some conventional analytical models. The proposed model agrees relatively well with the empirical findings compared to existing conventional models.

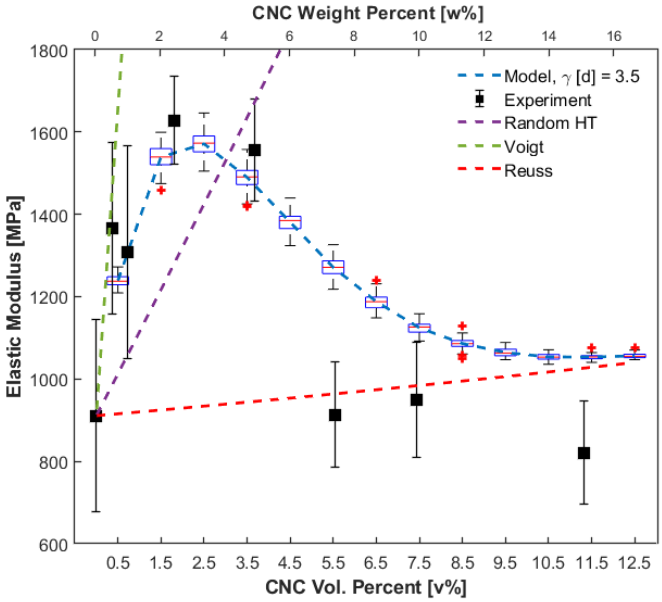

Figure 3.8. Predictions of elastic modulus of nanocomposites with respect to CNC concentration and empirical findings adapted from [36].

It is important to understand the deviations from empirical findings. In our predictions, we assumed aligned particles with a specific aspect ratio value. However, even if it is reasonable to assume particles are aligned, the complete particle alignment at the nanosize level is challenging to achieve. The alignment might also depend on the particle loading. In addition, particle size is likely to have distribution instead of a certain value; however, an average value is used in this study instead of distribution. These uncertainties are thought to be the main reasons for the difference between the model predictions and experimental results. In addition, the dispersion is

assumed to be uniform for all concentrations in these predictions, which may not be completely valid. The particle dispersion may change with increasing particle concentration due to increased viscosity or particle-particle interactions. Although variabilities exist in the model and the experimental setting, it can be said that the model satisfactorily captured the experimental results. The proposed model reflects the experimental trend well whereas common analytical models predict a linear relationship between the elastic modulus and particle loadings.

3.5 Conclusion

The proposed study focuses on a parametric study of our recently developed model that predicts the elastic modulus of nanocomposites based on the three-phase Mori-Tanaka model: free particles, agglomerated regions, and a matrix. The aim is to study the effect of agglomerations on nanocomposites at a broad range of reinforcement loadings. Since the agglomeration tendency of nanoparticles is a challenging problem to predict, the Monte-Carlo and hierarchical clustering method are proposed to capture the agglomerate formation. Along with agglomerate formation, a systematic study is performed to understand the effect of aspect ratio, critical distance, particle orientation, agglomerate property, and dispersion state of particles.

The critical distance parameter and elastic modulus of agglomerates are the key design parameters at high particle loadings. The critical distance parameter defines the agglomerated region that contains matrix and particles. Higher critical distance values result in easier agglomeration. As agglomerates are formed, the agglomerates' properties begin to dominate the general response of nanocomposites. In that sense, predicting agglomerates' properties become crucial for the model. Either the Halpin-Tsai or the Reuss models are assigned to predict agglomerates' properties and

examine agglomerates' effect on the elastic modulus of nanocomposites. While the Halpin-Tsai overestimates the elastic modulus, the Reuss model provides more reasonable results.

The aspect ratio, orientation and dispersion of particles are also investigated to understand the model's sensitivity. The drastic effect of aspect ratio and particle orientation on the elastic modulus of nanocomposites is observed at high particle loadings. At any aspect ratio, aligned fillers exhibits shows steeper slope than randomly oriented particles. It is concluded that alignment has more influence on the elastic modulus than the aspect ratio in the range of 15 to 60 for the case of uniform particle dispersion. Particle dispersion, another key parameter, is studied by locating the particles differently in the computational setting. The more uniform dispersion results in higher elastic modulus of nanocomposites regardless of other parameters. It is also observed that the agglomeration is inevitable at high particles even if particle locations are selected from uniform distribution function.

In this work, the capability of the previously developed model is analyzed with a systematic study. The proposed approach captures the experimental trend of elastic modulus of CNC reinforced PA6 samples relatively well compared to the conventional analytical models. As future of this work, the manufacturing methods and critical distance could be categorized based on the material system, and they could be correlated to the dispersion state of nanoparticles. With the existing data in the literature, we believe these correlations can be established via machine learning techniques.

REFERENCES

[1] T.D. Fornes, D.R. Paul, Modeling properties of nylon 6/clay nanocomposites using composite theories, Polymer (Guildf). 44 (2003) 4993–5013. https://doi.org/10.1016/S0032-3861(03)00471-3.

[2] N. Sheng, M.C. Boyce, D.M. Parks, G.C. Rutledge, J.I. Abes, R.E. Cohen, Multiscale micromechanical modeling of polymer/clay nanocomposites and the effective clay particle, Polymer (Guildf). 45 (2004) 487–506. https://doi.org/https://doi.org/10.1016/j.polymer.2003.10.100.

[3] J. Vera-Agullo, A. Glória-Pereira, H. Varela-Rizo, J.L. Gonzalez, I. Martin-Gullon, Comparative study of the dispersion and functional properties of multiwall carbon nanotubes and helical-ribbon carbon nanofibers in polyester nanocomposites, Compos. Sci. Technol. 69 (2009) 1521–1532. https://doi.org/https://doi.org/10.1016/j.compscitech.2008.11.032.

[4] D.-L. Shi, X.-Q. Feng, Y.Y. Huang, K.-C. Hwang, H. Gao, The effect of nanotube waviness and agglomeration on the elastic property of carbon nanotube-reinforced composites, J. Eng. Mater. Technol. Trans. ASME. 126 (2004) 250–257. https://doi.org/10.1115/1.1751182.

[5] A.C. Corrêa, K.B.R. Teodoro, J.A. Simão, P.I.C. Claro, E. de Morais Teixeira, L.H.C. Mattoso, J.M. Marconcini, Cellulose nanocrystals from curaua fibers and poly[ethylene-co-(vinyl acetate)] nanocomposites: Effect of drying process of CNCs on thermal and mechanical properties, Polym. Compos. n/a (2020). https://doi.org/10.1002/pc.25493.

[6] S.-Y. Fu, X.-Q. Feng, B. Lauke, Y.-W. Mai, Effects of particle size, particle/matrix interface

adhesion and particle loading on mechanical properties of particulate–polymer composites, Compos. Part B Eng. 39 (2008) 933–961. https://doi.org/https://doi.org/10.1016/j.compositesb.2008.01.002.

[7] B. Wetzel, F. Haupert, M. Qiu Zhang, Epoxy nanocomposites with high mechanical and tribological performance, Compos. Sci. Technol. 63 (2003) 2055–2067. https://doi.org/https://doi.org/10.1016/S0266-3538(03)00115-5.

[8] M.M.J. Treacy, T.W. Ebbesen, J.M. Gibson, Exceptionally high Young's modulus observed for individual carbon nanotubes, Nature. 381 (1996) 678. https://doi.org/http://dx.doi.org/10.1038/381678a0.

[9] F. Tanaka, T. Iwata, Estimation of the Elastic Modulus of Cellulose Crystal by Molecular Mechanics Simulation, Cellulose. 13 (2006) 509–517. https://doi.org/10.1007/s10570-006-9068-x.

[10] M. Pereda, N.E. Kissi, A. Dufresne, Extrusion of polysaccharide nanocrystal reinforced polymer nanocomposites through compatibilization with poly(ethylene oxide), ACS Appl. Mater. Interfaces. 6 (2014) 9365–9375. https://doi.org/10.1021/am501755p.

[11] C. Weiler, M. Egen, M. Trunk, P. Langguth, Force control and powder dispersibility of spray dried particles for inhalation, J. Pharm. Sci. 99 (2010) 303–316. https://doi.org/10.1002/jps.21849.

[12] M.Z. Rong, M.Q. Zhang, Y.X. Zheng, H.M. Zeng, R. Walter, K. Friedrich, Structure-property relationships of irradiation grafted nano-inorganic particle filled polypropylene composites, Polymer (Guildf). 42 (2001) 167–183. https://doi.org/10.1016/S0032-3861(00)00325-6.

[13] R.P. Singh, M. Zhang, D. Chan, Toughening of a brittle thermosetting polymer : Effects of reinforcement, J. Mater. Sci. 37 (2002) 781–788, https://doi.org/10.1023/A:1013844015493.

[14] S.P. Vinodhini, J.R. Xavier, Effect of graphene oxide wrapped functional silicon carbide on structural, surface protection, water repellent, and mechanical properties of epoxy matrix for automotive structural components, Colloids Surfaces A Physicochem. Eng. Asp. 639 (2022) 128300. https://doi.org/10.1016/j.colsurfa.2022.128300.

[15] X. Guan, B. Xu, J. Gong, Hierarchically architected polydopamine modified BaTiO3@P(VDF-TrFE) nanocomposite fiber mats for flexible piezoelectric nanogenerators and self-powered sensors, Nano Energy. 70 (2020) 104516. https://doi.org/10.1016/j.nanoen.2020.104516.

[16] H. Sojoudiasli, M.-C. Heuzey, P.J. Carreau, Mechanical and morphological properties of cellulose nanocrystal-polypropylene composites, Polym. Compos. 39 (2018) 3605–3617. https://doi.org/10.1002/pc.24383.

[17] A. Junior de Menezes, G. Siqueira, A.A.S. Curvelo, A. Dufresne, Extrusion and characterization of functionalized cellulose whiskers reinforced polyethylene nanocomposites, Polymer (Guildf). 50 (2009) 4552–4563. https://doi.org/10.1016/j.polymer.2009.07.038.

[18] V. Anumandla, R.F. Gibson, A comprehensive closed form micromechanics model for estimating the elastic modulus of nanotube-reinforced composites, Compos. Part A Appl. Sci. Manuf. 37 (2006) 2178–2185. https://doi.org/https://doi.org/10.1016/j.compositesa.2005.09.016.

[19] J. Sapkota, A. Gooneie, A. Shirole, J.C. Martinez Garcia, A refined model for the mechanical properties of polymer composites with nanorods having different length distributions, J. Appl. Polym. Sci. 134 (2017). https://doi.org/10.1002/app.45279.

[20] K. Baek, H. Shin, T. Yoo, M. Cho, Two-step multiscale homogenization for mechanical behaviour of polymeric nanocomposites with nanoparticulate agglomerations, Compos. Sci. Technol. 179 (2019) 97–105. https://doi.org/https://doi.org/10.1016/j.compscitech.2019.05.006.

[21] N. Hu, H. Fukunaga, C. Lu, M. Kameyama, B. Yan, Prediction of Elastic Properties of Carbon Nanotube Reinforced Composites, Proc. Math. Phys. Eng. Sci. 461 (2005) 1685–1710. https://doi.org/10.1098/rspa.2004.1422.

[22] K.-T. Lau, M. Chipara, H.-Y. Ling, D. Hui, On the effective elastic moduli of carbon nanotubes for nanocomposite structures, Compos. Part B Eng. 35 (2004) 95–101. https://doi.org/https://doi.org/10.1016/j.compositesb.2003.08.008.

[23] K. Hbaieb, Q.X. Wang, Y.H.J. Chia, B. Cotterell, Modelling stiffness of polymer/clay nanocomposites, Polymer (Guildf). 48 (2007) 901–909. https://doi.org/10.1016/j.polymer.2006.11.062.

[24] Y. Wang, Z.M. Huang, Analytical micromechanics models for elastoplastic behavior of long fibrous composites: A critical review and comparative study, Materials (Basel). 11 (2018). https://doi.org/10.3390/ma11101919.

[25] G.P. Carman, K.L. Reifsnider, Micromechanics of short-fiber composites, Compos. Sci. Technol. 43 (1992) 137–146. https://doi.org/10.1016/0266-3538(92)90004-M.

[26] J. Ha, Y. Song, N. Song, J.S. Yun, D. Lee, Designing an interpenetrating network of silane-

functionalized nanocomposites for enhanced particle dispersity and interfacial bonding strength, Ceram. Int. 48 (2022) 1827–1835. https://doi.org/10.1016/j.ceramint.2021.09.264.

[27] B. Arash, Q. Wang, V.K. Varadan, Mechanical properties of carbon nanotube/polymer composites, Sci. Rep. 4 (2014) 1–8. https://doi.org/10.1038/srep06479.

[28] C.E.E. Armbrister, O.I. Okoli, S. Shanbhag, Micromechanics predictions for two-phased nanocomposites and three-phased multiscale composites: A review, J. Reinf. Plast. Compos. 34 (2015) 605–613. https://doi.org/10.1177/0731684415574297.

[29] J.-J. Luo, I.M. Daniel, Characterization and modeling of mechanical behavior of polymer/clay nanocomposites, Compos. Sci. Technol. 63 (2003) 1607–1616. https://doi.org/https://doi.org/10.1016/S0266-3538(03)00060-5.

[30] R. Guzmán de Villoria, A. Miravete, Mechanical model to evaluate the effect of the dispersion in nanocomposites, Acta Mater. 55 (2007) 3025–3031. https://doi.org/https://doi.org/10.1016/j.actamat.2007.01.007.

[31] H.-Y. Yu, Z.-Y. Qin, C.-F. Yan, J.-M. Yao, Green Nanocomposites Based on Functionalized Cellulose Nanocrystals: A Study on the Relationship between Interfacial Interaction and Property Enhancement, ACS Sustain. Chem. Eng. 2 (2014) 875–886. https://doi.org/10.1021/sc400499g.

[32] L. Jiang, E. Morelius, J. Zhang, M. Wolcott, J. Holbery, Study of the Poly(3-hydroxybutyrate-co-3-hydroxyvalerate)/Cellulose Nanowhisker Composites Prepared by Solution Casting and Melt Processing, J. Compos. Mater. 42 (2008) 2629–2645. https://doi.org/10.1177/0021998308096327.

[33] S.H. Sung, Y. Chang, J. Han, Development of polylactic acid nanocomposite films

reinforced with cellulose nanocrystals derived from coffee silverskin, Carbohydr. Polym. 169 (2017) 495–503. https://doi.org/https://doi.org/10.1016/j.carbpol.2017.04.037.

[34] E.P. Giannelis, Polymer Layered Silicate Nanocomposites, Adv. Mater. 8 (1996) 29–35. https://doi.org/10.1002/adma.19960080104.

[35] Y. He, J. Zhu, W. Wang, H. Ni, Surface modification of cellulose nanocrystals with different acid anhydrides for improved dispersion in poly(butylene succinate), RSC Adv. 8 (2018) 38305–38314. https://doi.org/10.1039/c8ra07597b.

[36] E.C. Demir, A. Benkaddour, D. Aldrich, M.T. Mcdermott, C. Il Kim, C. Ayranci, A predictive model towards understanding the effect of reinforcement agglomeration on the stiffness of nanocomposites, J. Compos. Mater. (2022). https://doi.org/10.1177/00219983221076639.

[37] L.M. Hamming, R. Qiao, P.B. Messersmith, L. Catherine Brinson, Effects of dispersion and interfacial modification on the macroscale properties of TiO2 polymer-matrix nanocomposites, Compos. Sci. Technol. 69 (2009) 1880–1886. https://doi.org/10.1016/j.compscitech.2009.04.005.

[38] E.T. Thostenson, C. Li, T.W. Chou, Nanocomposites in context, Compos. Sci. Technol. 65 (2005) 491–516. https://doi.org/10.1016/j.compscitech.2004.11.003.

[39] F. Nielsen, Hierarchical Clustering BT - Introduction to HPC with MPI for Data Science, in: F. Nielsen (Ed.), Springer International Publishing, Cham, 2016: pp. 195–211. https://doi.org/10.1007/978-3-319-21903-5_8.

[40] Y. Benveniste, A new approach to the application of Mori-Tanaka's theory in composite materials, Mech. Mater. 6 (1987) 147–157. https://doi.org/10.1016/0167-6636(87)90005-6.

[41] T. Mura, Micromechanics of defects in solids, 2nd ed., Springer, Dordrecht, 1987. https://doi.org/https://doi.org/10.1007/978-94-009-3489-4.

[42] D.J. Karras, Statistical methodology: II. Reliability and validity assessment in study design, part B, Acad. Emerg. Med. 4 (1997) 144–147. https://doi.org/10.1111/j.1553-2712.1997.tb03723.x.

[43] V. Mirjalili, M. Yourdkhani, P. Hubert, Dispersion stability in carbon nanotube modified polymers and its effect on the fracture toughness, Nanotechnology. 23 (2012) 315701. https://doi.org/10.1088/0957-4484/23/31/315701.

[44] S.R. Bakshi, R.G. Batista, A. Agarwal, Quantification of carbon nanotube distribution and property correlation in nanocomposites, Compos. Part A Appl. Sci. Manuf. 40 (2009) 1311–1318. https://doi.org/https://doi.org/10.1016/j.compositesa.2009.06.004.

[45] M. Yourdkhani, P. Hubert, Quantitative dispersion analysis of inclusions in polymer composites, ACS Appl. Mater. Interfaces. 5 (2013) 35–41. https://doi.org/10.1021/am301459q.

[46] Z.P. Luo, J.H. Koo, Quantifying the dispersion of mixture microstructures, J. Microsc. 225 (2007) 118–125. https://doi.org/10.1111/j.1365-2818.2007.01722.x.

[47] B.M. Tyson, R.K. Abu Al-Rub, A. Yazdanbakhsh, Z. Grasley, A quantitative method for analyzing the dispersion and agglomeration of nano-particles in composite materials, Compos. Part B Eng. 42 (2011) 1395–1403. https://doi.org/10.1016/j.compositesb.2011.05.020.

[48] S.G. Advani, C.L. Tucker, The Use of Tensors to Describe and Predict Fiber Orientation in Short Fiber Composites, J. Rheol. (N. Y. N. Y). 31 (1987) 751–784.

https://doi.org/10.1122/1.549945.

[49] T. Thorvaldsen, Modelling the elastic stiffness of nanocomposites using the Mori-Tanaka method, 2015. https://doi.org/9788246425559.

[50] A. Dufresne, Nanocellulose: a new ageless bionanomaterial, Mater. Today. 16 (2013) 220–227. https://doi.org/https://doi.org/10.1016/j.mattod.2013.06.004.

[51] J.C.H. Affdl, J.L. Kardos, The Halpin-Tsai equations: A review, Polym. Eng. Sci. 16 (1976) 344–352. https://doi.org/10.1002/pen.760160512.

[52] Y. Peng, D.J. Gardner, Y. Han, Characterization of mechanical and morphological properties of cellulose reinforced polyamide 6 composites, Cellulose. 22 (2015) 3199–3215. https://doi.org/10.1007/s10570-015-0723-y.

[53] C.L. Morelli, N. Belgacem, R.E.S. Bretas, J. Bras, Melt extruded nanocomposites of polybutylene adipate-co-terephthalate (PBAT) with phenylbutyl isocyanate modified cellulose nanocrystals, J. Appl. Polym. Sci. 133 (2016). https://doi.org/10.1002/app.43678.

[54] T. Glaskova, M. Zarrelli, A. Borisova, K. Timchenko, A. Aniskevich, M. Giordano, Method of quantitative analysis of filler dispersion in composite systems with spherical inclusions, Compos. Sci. Technol. 71 (2011) 1543–1549. https://doi.org/https://doi.org/10.1016/j.compscitech.2011.06.009.

[55] H.S. Khare, D.L. Burris, A quantitative method for measuring nanocomposite dispersion, Polymer (Guildf). 51 (2010) 719–729. https://doi.org/https://doi.org/10.1016/j.polymer.2009.12.031.

[56] Z.P. Luo, J.H. Koo, Quantitative study of the dispersion degree in carbon nanofiber/polymer and carbon nanotube/polymer nanocomposites, Mater. Lett. 62 (2008) 3493–3496.

https://doi.org/https://doi.org/10.1016/j.matlet.2008.03.010.

[57] L. Hui, R.C. Smith, X. Wang, J.K. Nelson, L.S. Schadler, Quantification of Particulate Mixing in Nanocomposites, in: 2008 Annu. Rep. Conf. Electr. Insul. Dielectr. Phenom., 2008: pp. 317–320. https://doi.org/10.1109/CEIDP.2008.4772831.

[58] A. Golbang, M.H.N. Famili, M.M.M. Shirvan, A method for quantitative characterization of agglomeration degree in nanocomposites, Compos. Sci. Technol. 145 (2017) 181–186. https://doi.org/10.1016/j.compscitech.2017.04.013.

[59] J. Liu, Y. Gao, D. Cao, L. Zhang, Z. Guo, Nanoparticle Dispersion and Aggregation in Polymer Nanocomposites: Insights from Molecular Dynamics Simulation, Langmuir. 27 (2011) 7926–7933. https://doi.org/10.1021/la201073m.

Chapter 4

Towards Filamentless Extrusion-Based Additive Manufacturing of Nanocomposites: Cellulose Nanocrystals Reinforced Polyamide 12

4.1 Introduction

The enhancement of nanocomposites' mechanical properties is usually amplified with homogeneously dispersed nanoparticles [1–4]. Obtaining homogeneously dispersed nanoparticles is challenging due to nanoparticles' strong interactive forces and their incompatibility with matrix materials [5,6]. In addition to the chemical interaction, polymer viscosity limits the movements of particles and leads to agglomeration [7–9]. A chemical modification or a good degree of mixing is a crucial step to disperse particles homogeneously [10–12].

Researchers have modified nanoparticles chemically [13][14] or used various mixing systems [7,8] to obtain better nanoparticle dispersion. For example, Fortunati et. al.[14] used an acid phosphate ester of ethoxylated nonylphenol for cellulose nanocrystals (CNC) modification and showed that the modification improved the dispersion of CNC and the mechanical properties of poly(butylene/triethylene succinate). Boran et. al. [9] compared different mixing methods for melt blending of microcrystalline cellulose in a polyethylene matrix. They noted that single screw extruder and twin screw extrude have poor dispersive mixing capability unless they are equipped

with mixing elements such as include kneading disks. External flow mixer resulted in the best flexural properties [9]. Although the mixing methods have been improved with process optimization, surface modification and mixing elements, these traditional methods usually require high volume of material.

Small lab-scale devices have been developed for nanocomposite production where only small amounts of material are available at the research level. These lab-scale mixers usually operate with materials amount of fewer than 0.5 grams [15]. Some devices such as cup and rotor batch mixers only provide shear flow and even after long mixing times, their mixing efficiency is low [15]. Internal batch mixer and recirculating conical twin-screw extruders are introduced to offer better mixing technologies [15][7]; however, when the volume of the material is less than the required, well mixing is not obtained[15].

Solvent-based methods, such as casting, and spin coating are reported to provide better mechanical properties compared to extrusion and moulding techniques [16][17]. Low viscosity and slow evaporation of solvent allow nanoparticles to rearrange in polymer matrices which results in better mechanical properties [17]. Although solvent-based processes provide better mechanical properties, they are usually limited to two-dimensional shapes and a low number of applications. Further, some research-level nanocomposite applications such as patient-specific biomedical [18] or robotic load-bearing parts [19] require prototyping and 3-dimensional shapes. Thus, a new method is required for cutting-edge nanocomposite research where the amount of material is limited, and 3-dimensional customized parts are needed.

This study introduces an innovative nanocomposite preparation method that can be used in the direct 3D printing method without using a filament. This method involves solvent and melt mixing methods to obtain well-dispersed melt-formed nanocomposites. The method was validated with

cellulose nanocrystals (CNC) reinforced polyamide 12 (PA12). CNC is a promising biodegradable reinforcing agent [20,21] and PA12 is a robust engineer polymer that has a polar and apolar characteristics due to its amide group and long carbon chain [22,23]. These characteristics can lead to a well-dispersed CNC reinforced PA12 and various possible applications. Detailed material characterization was performed to show the feasibility of the method and the effect of CNC on crystal structure and mechanical properties of PA12. We also verify a previously developed model based on transmission electron microscopy (TEM) images and show its potential for other nanocomposite applications. The elastic modulus of nanocomposites is reported and compared with this previously developed 3-phase Mori-Tanaka model. Extensive image analysis is performed on TEM images to assess CNC orientation, agglomeration, and model application.

4.2 Experimental

4.1.1 Materials

Cellulose nanocrystals (CNC) was purchased as a spray-dried product from Celluforce and produced via traditional 64 w% sulfuric acid hydrolysis of wood pulp [24]. Extrusion grade polyamide 12 (PA12) pellets under the Rilsamid AESNO MED product name were obtained from Arkema Inc. The chemical name of the PA12 was provided in the technical data sheet as Azacyclotridenecan-2-one, and its melting point/range (T_m) was reported as 160 – 175 °C. Although the chemical formula of PA12 was not explicitly given in the technical data sheet, its IUPAC name Poly(dodecano-12-lactam) and chemical formula $(C_{12}H_{23}NO)_n$ are well-known as it is a member of the Nylon family. Liquid formic Acid, CH_2O_2, (98+% pure) was purchased from ACROS Organics through Fisher Scientific supplier. Black and Decker commercial coffee grander and silicone baking mat were used for powder preparation. Lastly, the V4 pellet extruder head

(direct-print head) was purchased from Mahor XYZ Industrial Additive Manufacturing and was adapted and modified for this study.

4.1.2 Preparation of CNC/PA12 Nanocomposites

Various CNC loadings of 0 –15.0 w% in PA12 were prepared using the solvent casting method. For each loading, 20 w/v solid to liquid ratio was followed *i.e.,* a total of 2 grams of solid was dissolved/dispersed in 10 ml of formic acid. Formic acid is one of the few solvents that can dissolve polyamides and disperse CNC due to its polar nature [25]. The appropriate mass of CNC (0 – 0.20 grams) was dispersed in formic acid using Crest ultrasonic bath sonicator for 30 minutes at room temperature. Then, PA12 pellets (1.80 – 2.00) were added into the vial accordingly. The vial was sealed with Parafilm M PM999 tape, heated to 68 °C and stirred at 150 rpm for 6 hours on Slicogex hotplates with aluminum quarter reaction blocks to dissolve PA12 in formic acid. The solution was vibrated 30 seconds for every hour using a vortex mixer from Fisher Scientific to ensure that PA12 did not solidify on the top of the solution. Six vials were prepared for each loading. Once pellets became invisible to the human eye, the solution was cast onto a silicone baking mat. The purpose was to obtain continuous polymer ribbons to produce the CNC/PA12 powder in the next step. The casted solution was left in the fume hood for 24 hours to make sure it was dried. Figure 4.1shows schematics and flow of composite preparation.

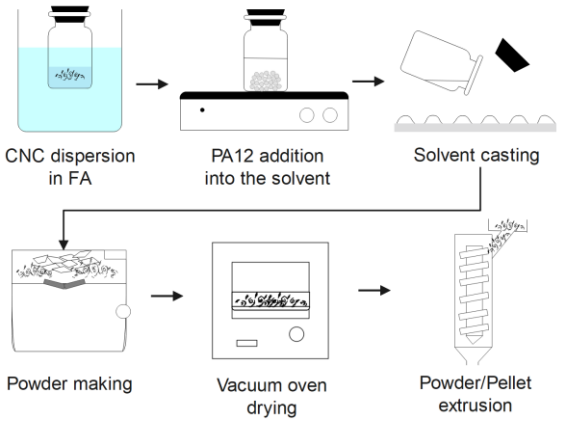

Figure 4.1. Schematics and flow of composite preparation.

The dried solid ribbons were easily removed from the mat and put into a grinder. The grinder was run at its standard power to obtain the powder. The produced powder was dried in a vacuum oven at 100 °C and at a pressure of 20 – 25 inHg for 24 hours to remove any remaining solvent and moisture. The dried powder was fed into the single screw V4 pellet extruder. The extruder head was set to the 260°. Filament samples were collected manually for every 100 mm of extruded material.

4.1.3 Fourier-Transform Infrared Spectroscopy

Fourier-transform infrared spectroscopy (FTIR) spectra was collected using Nicolet 8700 in absorption mode. Extruded samples were taken to the FTIR analysis to observe the effect of formic acid on the final product. The samples were cut into 0.5 mm pieces for the analysis. A total of 32 scans were obtained per sample with a resolution of 4 cm^{-1} (4000 – 650 cm^{-1}).

4.1.4 Differential Scanning Calorimetry

The thermal analysis of nanocomposites was conducted using the TA Q2000 DSC instrument with a temperature precision of 0.05 °C. Approximately 5 mg of samples were loaded into a hermetic

aluminum DSC pan. The temperature of the samples was equilibrated at 25 °C and then increased to 225 °C with a heating rate of 10 °C/min. The temperature was kept at 225 °C isothermally for 2 minutes and then lowered to 25 °C with a cooling rate of 10 °C/min. The heating and cooling cycles were performed under 20 mL/in nitrogen flow to prevent oxidation. The data received from the differential scanning calorimetry (DSC) instrument was used to calculate the crystallinity of nanocomposites. The degree of crystallinity of the polymer was calculated based on the equation (24).

$$\chi_p = \frac{\Delta H_f}{(1-\varphi) \times \Delta H_f^{100}} \times 100 \quad (24)$$

where χ_p is the degree of crystallinity of the PA12, ΔH_f is the heat of fusion for various nanocomposites, ΔH_f^{100} the heat of fusion for 100% crystalline PA12, and φ is the weight fraction of CNC in nanocomposites. ΔH_f^{100} for fully crystalline PA12 was taken as 209.3 J/g [26][27].

4.1.5 X-ray Diffraction

X-ray diffraction analyses were performed to obtain crystallographic data of nanocomposites. Rigaku Ultima IV instrument with Cu k_α radiation X-ray source was utilized under powder diffraction mode to conduct the analysis. The samples were cut into small pieces (approximately 2mm in length and 1 mm in diameter) to increase the chance of observing every possible diffraction. The prepared samples were loaded to the sampler, and measurements were taken at 2θ values between 10° – 40° using a 0.5 mm slit.

4.1.6 Uniaxial Tensile Test

Young's modulus, yield strength and percent elongation-at-yield of the nanocomposites were determined using ElectroForce 3200, from TA instruments, with a 450 N capacity load cell.

Extruded samples with approximately 1 mm diameter were cut to 100 mm in length for testing. The two grips of the instrument covered 25 mm of the sample; thus, 75 mm of the sample (distance between the grips) was tested and taken as the initial length for the strain calculations. The displacement rate was 5 mm/min. The Young's modulus of nanocomposites is calculated from the linear region of the stress-strain curve between 0.2 – 1.0% strain. Yield strength and percent elongation-at-yield were calculated using the offset method described in ASTM D-638. A tangent line parallel to the initial straight-line portion of the stress-strain curve was drawn from 0.2 % elongation. The intersection of the drawn line with the stress-strain curve was located. The stress at this intersection was reported as yield strength at 0.2% offset and percent elongation-at-yield. The thickness of the samples was measured from 3 separate regions and then averaged for stress calculations. At least six samples were reported for each nanocomposite concentration.

4.1.7 Transmission Electron Microscope

A transmission electron microscope (TEM) was used to examine CNC morphology before and after formic acid. Further, the TEM was used to analyze the agglomeration and orientation of CNC in nanocomposites. For the analysis, Philips Morgagni 268 TEM, manufactured by FEI Company, Oregon, USA, was operated at 100 kV.

Two different protocols were followed to prepare CNC and nanocomposite samples for the TEM analysis. In the first protocol, CNC was dispersed in deionized water at the concentration of 0.1 mg/mL and a drop of the solvent was left on a carbon-coated copper TEM grid for an hour. After drying, the sample was stained with 4% uranyl acetate for 20 minutes and Reynold's lead citrate for 7 minutes before TEM examination. In the second protocol, nanocomposite samples were embedded into epoxy and waited at 70 °C for curing. Samples within the cured epoxy were microtomed with a glass knife to get a thin section of samples (120~nm) using Reichert-Jung

Ultracut E. The microtomed samples were double-side stained with an extra-long protocol: uranyl acetate for 2.5 hours and lead citrate for 1 hour. The cross-sectional and longitudinal directions were prepared for orientational analysis. All TEM images were analyzed using Fiji ImageJ and MATLAB software.

4.1.8 Image Analysis and Model Implication

In this study, TEM images were utilized to be used as inputs for a previously developed model [28], to predict the elastic modulus of nanocomposites.

4.1.8.1 Image Analysis

Auto local threshold and manual noise removal were performed to obtain clean black and white images for model implication. Raw gray-scale TEM images were converted into 8-bit black and white images using the auto local threshold option provided in Fiji Image J. In the local thresholding method, the threshold is computed for each pixel based on the image properties of a window around these pixels instead of a global threshold. Thus, it can be said that the local thresholding method had advantages over the global thresholding method for low-contrast images. There are nine different methods for local auto threshold in Fiji Image J. Out of these, the Phansalkar method [29] and the Sauvola method [30] provided the best conversion of raw TEM images into 8-bit images. The default values were used for method parameters, and further manual noise removal was performed for each image. Raw TEM images and 8-bit versions of the same images were overlaid, and unmatched pixels were removed manually. After the cleaning process, the pixel size in nanometers was measured using the Fiji Image J software for further image analysis. The flow chart of the image processing for model implication is outlined in Figure 4.2.

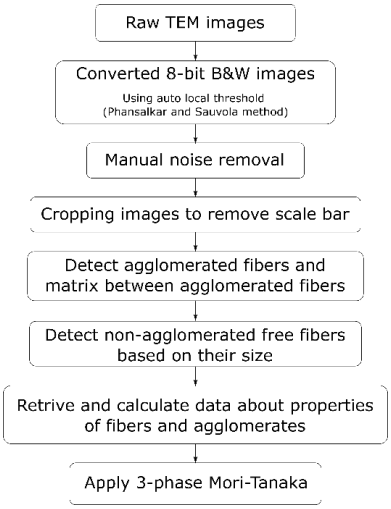

Figure 4.2. Flow chart of the image processing for model implication.

Cleaned 8-bit TEM images were processed in four main steps to complete model application. First, each TEM image was cropped from the bottom by 70-pixel x 1081-pixel to remove the scale bar. Second, fibers were connected based on the closest distance between them. If the closest distance was shorter than the "critical distance" defined in the study [28], the fibers were considered connected/agglomerated fibers. In the second step, the matrix that remained between agglomerated fibers was also considered to belong to the agglomerated region. Third, each agglomerate was analyzed separately to calculate fiber and matrix concentration within agglomerates. In this analysis, each agglomerate's orientation, aspect ratio, and diameter were also recorded. Fourth, free fiber (non-agglomerated) fibers were detected based on the expected maximum area of a single CNC. This image analysis gave us data about the total agglomerate area, fiber area, matrix area, fiber and matrix area within the agglomerates, and orientation and aspect ratio of fibers and agglomerates.

4.1.8.2 Model Application

The model includes six main steps to predict the elastic modulus of nanocomposites, as given in Figure 4.3. First, fibers are dispersed in a computational setting. Second, agglomerated particles are detected using a machine learning method. Third, detected agglomerated regions are averaged based on their volume fraction and fiber concentrations. Fourth, the elastic modulus of the averaged agglomerates is calculated with the Reuss model. Fifth, since the properties of the averaged agglomerate and volume fraction of each constituent are known, a three-phase Mori-Tanaka model is applied to calculate the elastic modulus of nanocomposites. Six, the first five steps are repeated a hundred times to obtain statistically meaningful data. In this study, we applied steps two to five of the previously developed model to predict the elastic modulus of the nanocomposites. In this study steps, 2-5 was used because the first step was not necessary as TEM images already provide us with the location of fibers and the sixth step was not possible as taking a hundred TEM images from various fiber loadings would be challenging and time-consuming. Instead of a hundred images, three images were collected and processed for 1.0, 2.5, 5.0,10, and 15.0 w% CNC/PA12 nanocomposites.

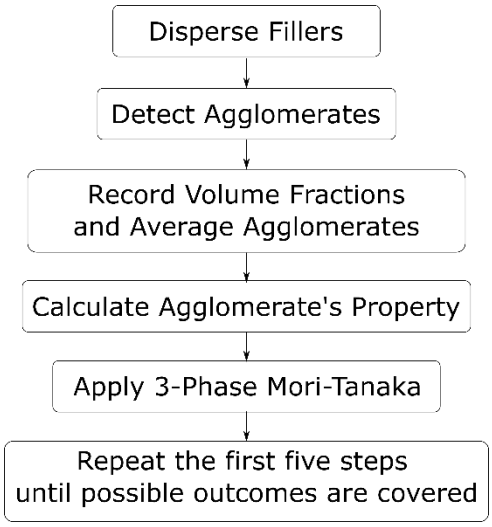

Figure 4.3. Flow chart for the previously developed model.

Based on the data retrieved from image analysis, 3-phase Mori-Tanaka, involving free fiber, agglomerate and matrix phases, was applied to calculate the elastic modulus of nanocomposites. For the 3-phase Mori-Tanaka model, we need the following information about each phase: the volume fractions, the elastic properties, the orientation, and the aspect ratio. The volume fraction of each constituent was found by dividing known areas by the total area of the TEM images. Fiber fractions within agglomerates were averaged and used in the Reuss model to find the elastic properties of agglomerates. The orientation of agglomerates and fibers was found using the MATLAB image toolbox. The MATLAB code treats each agglomerate and fibers as an ellipse, and the orientation is calculated based on their major and minor axes. The aspect ratio of agglomerates was calculated by dividing the major axis length by the minor axis length of these ellipses.

4.3 Results & Discussion

4.1.9 Morphology of Nanocomposites

The nanocomposites that were produced from the print head was tested to understand reinforcing efficiency of CNC in PA12. Since the print head was attached to an aluminium frame and no 3D printing was performed, extrudate nanocomposites were obtained in filament form. The photos of the nanocomposite extrudate production steps, including solvent and melt mixing, are displayed in Figure 4.4.

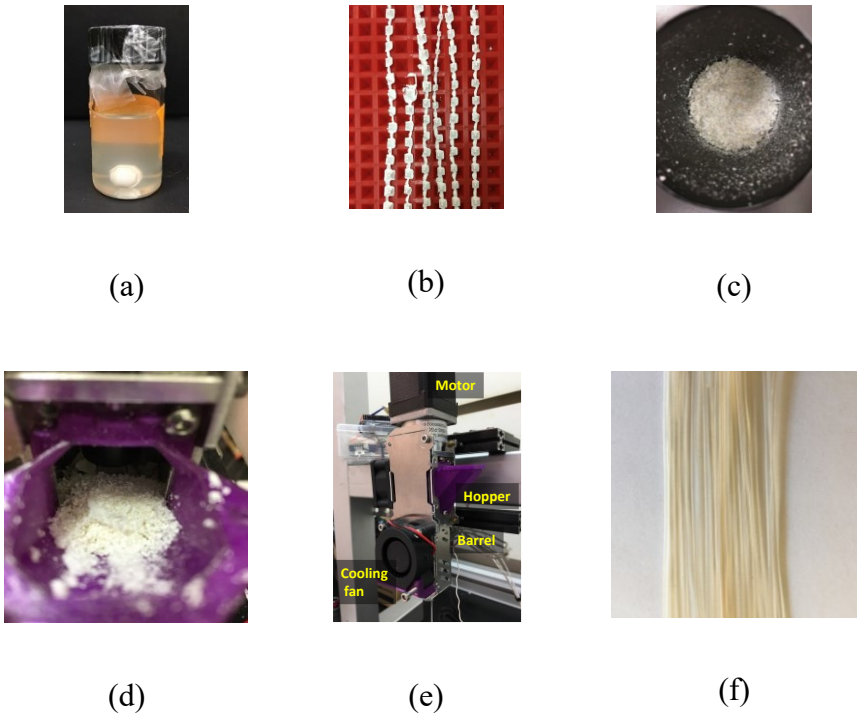

(a) (b) (c)

(d) (e) (f)

Figure 4.4. Preparation of CNC/PA12 Nanocomposites until the extrusion step, CNC and PA12 dissolution (a), solvent casted material (b), obtained powder (c), powder feeding (d), mini extruder (e), and extrudate (f).

The first mixing stage includes mixing CNC and PA12 in formic acid. Figure 4.4-(a) shows a vial containing 1.0 w% CNC–PA12 dissolved in formic acid. It is important to note that CNC was added into formic acid and dissolved before adding PA12 first; reversing the order of CNC and

PA12 addition thickens the solvent and makes CNC dissolution challenging. The solvent was heated to 68 °C to dissolve PA12 because PA12 could not be dissolved at room temperature. The viscous solvent was cast on a silicon mat. The dried material was brittle and bright white. Figure 4.4-(b) shows 24-hour dried solvent mixed and cast 1.0 w% CNC–PA12 material. The dried material was ground and fed into the extruder. Figure 4.4-(c) shows the powder form of 1.0 w% CNC–PA12 material. Figure 4.4-(d) the powder within the hopper. The second mixing stage involves powder feeding and melt mixing/extruding. Figure 4.4-(e) exhibits the single screw small extruder that can be used to produce filament or print 3-dimensional shapes if adopted to a 3D printer. The cooling fan, shown in Figure 4.4-(e), is an essential part of this system as it helps to obtain consistent extrudate. Figure 4.4-(f) shows 1.0 w% CNC–PA12 extrudate produced by the solvent and the melt mixing process.

4.1.10 Fourier-Transform Infrared Spectroscopy

Fourier transform infrared spectroscopy (FTIR) was used to observe whether there is any effect of formic acid on the PA12 extrudates. Two different PA12 extrudates were produced from PA12 pellets and PA12 powder. The PA12 powder was obtained through a solvent process described in section 4.1.9. Thus, the effect of formic acid can be observed in the PA12 extrudate produced from powder. The Fourier transform infrared spectroscopy (FTIR) absorption spectra of PA12 extrudates obtained from the pellets and powder are exhibited in Figure 4.5.

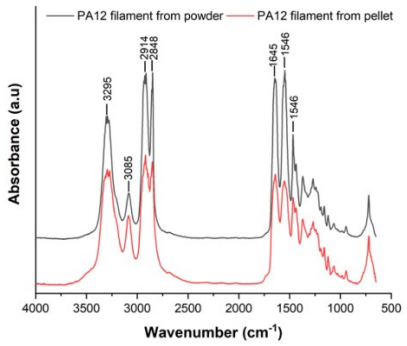

Figure 4.5. FTIR analysis of filaments after the extrusion of powder and pellet PA12.

The PA12 FTIR spectra for both cases are consistent with the data in the literature [22,31][27]. The absorption band at 3290 cm^{-1} is associated with N-H stretching vibration, and the band at 3094 cm^{-1} belongs to Fermi resonance of the *v* (N-H) stretching. The pair of bands at 2910 cm^{-1} and 2850 cm^{-1} are assigned the symmetric and asymmetric $–CH_2–$ stretching vibrations. The characteristic bands for amides, Amide-I and Amide-II, correspond to 1638 and 1561 cm^{-1}. Amide bands as hydrogen-bonded N-H stretching vibrations, Amide-I and Amide-II modes can be treated as the reference. Since the intensity ratios and the position of the bands are almost the same, it can be concluded that formic acid has no effect on the chemistry of PA12.

4.1.11 Crystal Structure of Nanocomposites

X-ray diffraction (XRD) patterns of nanocomposites at different CNC loadings, neat PA12 pellets and solvent cast PA12 are demonstrated in Figure 4.6. Various crystalline polymorphs have been identified for polyamides. However, the two major crystalline structures are the γ and α forms, and others can be considered variants of these structures [32]. PA12 has two main crystal structures similar to the polyamide family: the γ and α phases. The γ phase has a hexagonal structure and shows one strong reflection with d-spacing at about 0.42 nm [33]. The α phase has a monoclinic

structure and demonstrates two peaks corresponding to the d-spacing at 0.37 and 0.44 nm [33]. Whereas in the short-chain polyamides, such as PA4 and PA6, the α phase is more stable and cannot be converted into the γ phase by annealing [33][34], for PA12, the γ phase is more stable [33][35]. Although the γ phase is more stable for PA12, certain conditions, such as solvent casting, can result in the α phase of PA12 [22].

In this study, we observe both α and γ phases based on the processing conditions. The extruded PA12 and neat PA12 pellets show a single peak that belongs to the γ phase. On the other hand, the solvent-cast PA12 powder exhibits two peaks at 19.8 and 23.2, corresponding to the α phase. As shown in Figure 4.6, all extruded nanocomposites are formed from powder composites and show only one peak. The extrusion process includes melting and solidification of powder. This melting and solidification process erased the thermal/process history of PA12 powders and resulted in the stable γ phase for nanocomposites. Therefore, it can be claimed that the mechanical properties of nanocomposites is not affected by the crystal structure of PA12 as the final crystal structure is the same.

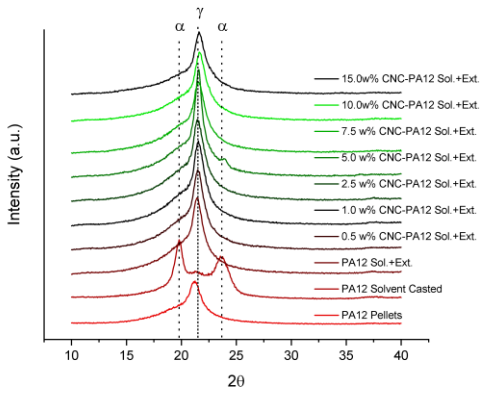

Figure 4.6. XRD analysis of CNC reinforced PA12.

4.1.12 Thermal Analysis of Nanocomposites

The DSC curves of the neat PA12 pellet and the PA12 powder are given in Figure 4.7. It can be observed that the PA12 pellet has only one endothermic melting peak; on the other hand, there are two endothermic peaks for PA12 powder. Two peaks could indicate the existence of two solid phases that go through the melting process or a process that includes phase transformation and melting. Ishikawa et al. [36] observed similar two peaks in the presence of the α phase and the mixture of the α and γ phases. They noted that in the case of only the α phase, the first peak belongs to the melting of the α phase. After the first melting point, the α phase recrystallizes to the γ phase. Thus, the second peak corresponds to the melting of the γ phase. Ma et al. [22] also observed two peaks in the DSC analysis and discussed the existence of the α and γ forms of PA12.

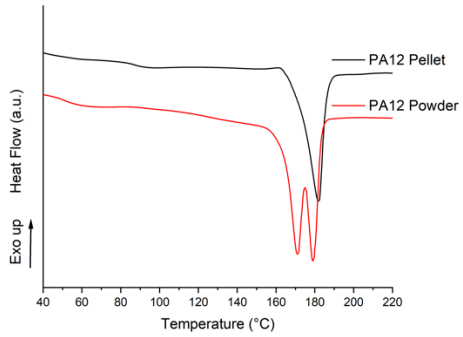

Figure 4.7. DSC curves of neat PA12 pellets and PA12 powder where powders were obtained with the solvent casting process.

XRD results of the PA12 powder and the PA12 pellets also support the differences in the DSC peaks given in Figure 4.7. The XRD pattern of the PA12 pellets has a single peak that belongs to the γ phase. The DSC curve of the PA12 pellets also has a single peak at 182 °C. Thus, it can be concluded that the melting point of the γ phase is measured as 182 °C. The XRD pattern of the PA12 power shows the existence of the α phase and supports two peaks' appearance in the DSC

curve. It is difficult to tell whether the PA12 powder has a mixture of the α and γ phases or not; however, the strong peaks from the α phase in XRD could tell that the α phase has a lower melting point than the γ phase, which can be important different material system or processing conditions.

Figure 4.8 shows the DSC curves of nanocomposite extrudates at CNC loadings between 0 – 15 w% to understand the effect of CNC on the crystallinity of matrix material. All nanocomposites show a single peak similar to the PA12 pellet DSC curve in Figure 4.7. This similarity and XRD results point out that the melting and solidification process results in the γ phase, and CNC has almost no effect on the crystalline type of the polymer.

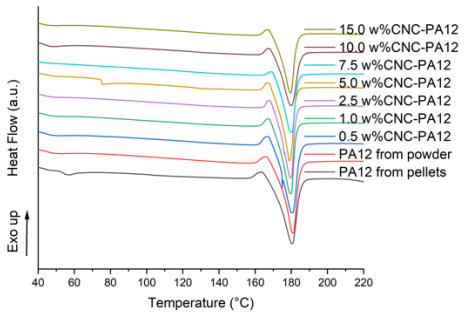

Figure 4.8. DSC curves of nanocomposite filaments.

Table 4.1 shows the crystallinity percent of nanocomposite extrudates at CNC loadings of 0 – 15 w%. The crystallinity percent values were calculated from the DSC curves given in Figure 4.7 and Figure 4.8. The PA12 powder shows the highest crystallinity with 39.5 %. Its high crystallinity lowers to 22.9 % after the extrusion process. This crystallinity change was also notable in the material appearance. Powder PA12 and PA12 ribbon – prior to powder making process – was brittle and bright white. On the other hand, the extrudate from powder PA12 was more ductile and

yellowish. The colour difference between the ribbon and extrudate can be recognized in Figure 4.4-(b) and Figure 4.4-(f). The PA12 pellet shows almost the same crystallinity percent before and after extrusion as opposed to the PA12 powder. The PA12 pellet has 25.4% crystallinity, and the extrudate made of the PA12 pellet has 25.2 % crystallinity.

Table 4.1. Crystallinity percent of various nanocomposites and feeding materials.

Material	Crystallinity percent (%)	
	Before extrusion (pellet/powder)	After extrusion (Filament)
Pellet PA12	25.4	25.2
Powder PA12	39.5	22.9
0.5 w% CNC PA12		23.9
1.0 w% CNC PA12		20.7
2.5 w% CNC PA12		20.1
5.0 w% CNC PA12		20.5
7.5 w% CNC PA12		20.8
10.0 w% CNC PA12		20.4
15.0 w% CNC PA12		20.4

The effect of CNC on crystallinity can be understood when various concentrations are compared with PA12 powder. It is seen that the PA12 powder has 22.9 % crystallinity and 1 – 15 w% CNC/PA12 composites have 20-21 %. The DSC results suggest that CNC addition lowered the crystallinity with a maximum change of 2%. In the literature it was shown that the addition of CNC increased the crystallinity of polylactic acid[40][16], poly(3-hydroxybutyrate-co-3-hydroxy valerate)[41]; however, some studies show that the addition of CNC decreased the crystallinity of low-density polyethylene [39] or did not alter the crystallinity of polyamide 6 [42]. CNC might have been expected to behave as a nucleating agent and increase the crystallinity of the polymer matrix. The increased crystallinity is expected to improve the modulus of elasticity [37,38]; however, it is not the case for this study. CNC addition has lowered the crystallinity percent of the

PA12. The lower crystallinity is expected to show “plasticizing effect” that increase yield strain and lower the elastic modulus [39].

4.1.13 CNC Morphology and Orientation of the Composites

TEM analysis was performed to understand the effect of formic acid on the CNC morphology. CNC was left in formic acid for 4 hours at 68 °C to mimic the solvent mixing process. Figure 4.9-(a) and (b) show the TEM images of CNC prepared from water and waited in and prepared from the formic acid. Based on the images obtained from TEM, it can be concluded that formic acid did not change the morphology of CNC. Many studies used formic acid as a solvent for CNC [43]; however, TEM images ensure that formic acid at high temperature does not deteriorate CNC morphology within 4 hours.

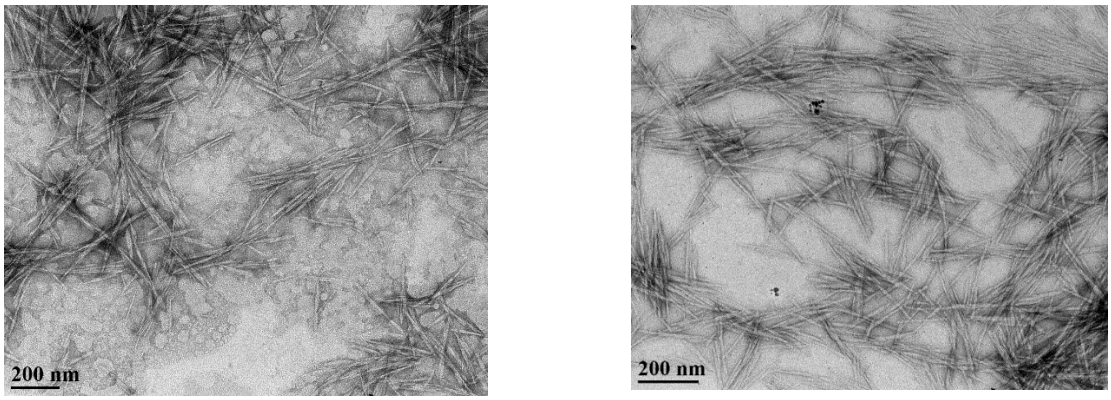

(a) (b)

Figure 4.9. TEM images of CNC (a) no contact with FA and (b) waited in FA for 4 hours at 68 °C.

The TEM analysis was also conducted to understand the orientation of CNC within the matrix material. The extrudate nanocomposites at CNC loadings of 5.0 and 15.0 w% were prepared from cross-sectional and longitudinal directions to explore the CNC orientation. Figure 4.10 shows the

cross-sectional (a) and longitudinal (b) TEM image of 5.0 w% CNC/PA12 and the cross-sectional (c) and longitudinal (d) TEM image of 15.0 w% CNC/PA12.

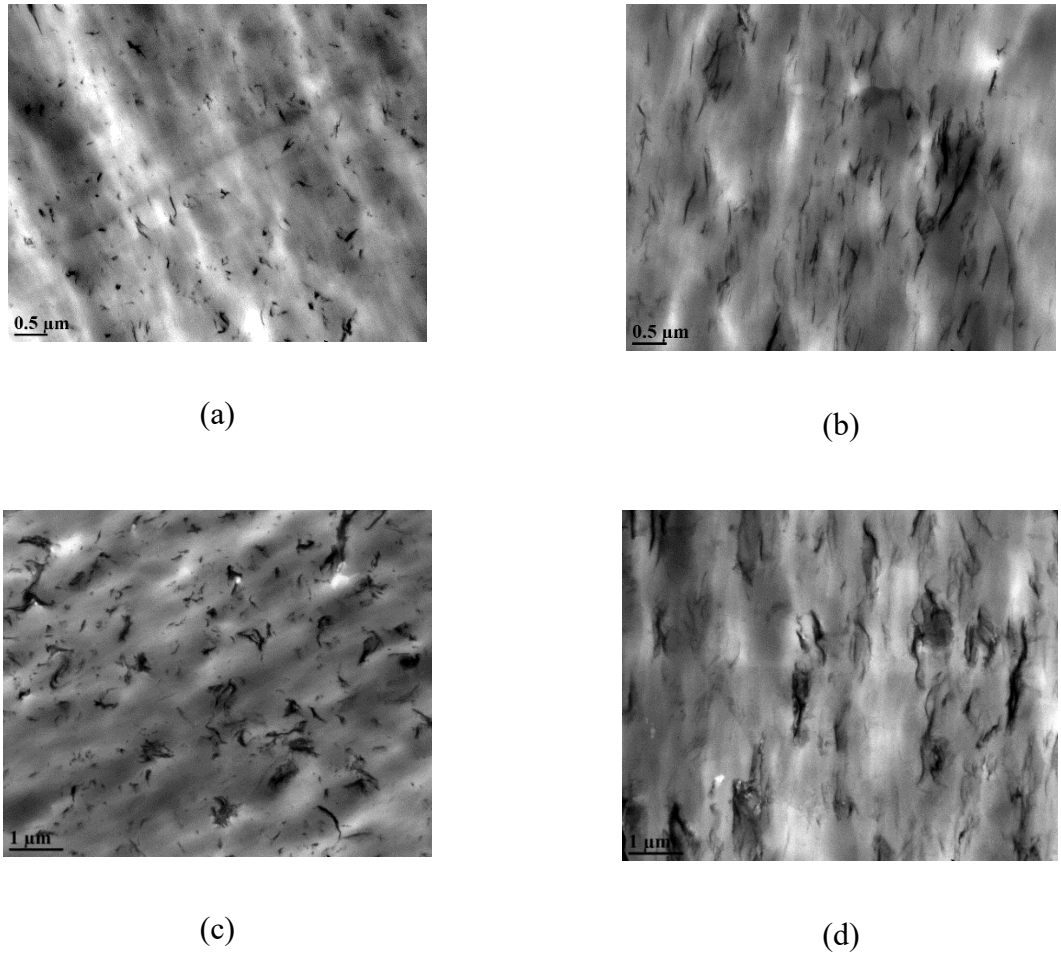

Figure 4.10. Cross-sectional (a) and longitudinal (b) TEM image of 5 w% CNC/PA12 and the cross-sectional (c) and longitudinal (d) TEM image of 15 w% CNC/PA12.

Although the difference in the orientation of CNC between Figure 4.10-(a) and (b), and Figure 4.10-(c) and (d) can be seen qualitatively, the quantitative analysis was also performed using the MATLAB image processing toolbox. The orientation and aspect ratio of CNC particles are given as histograms in

(a)

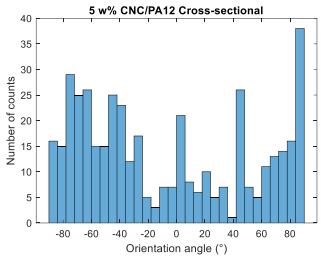

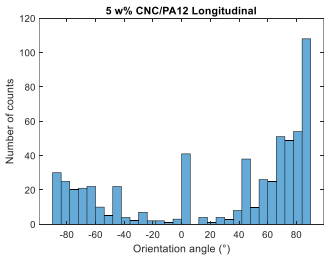

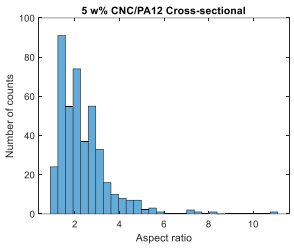

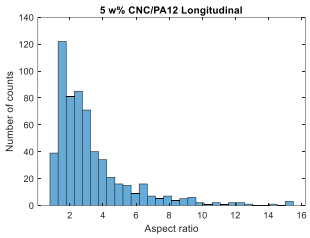

(I) (II)

(b)

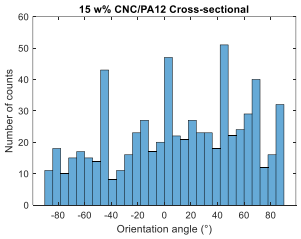

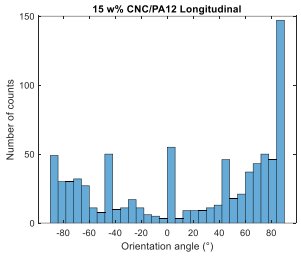

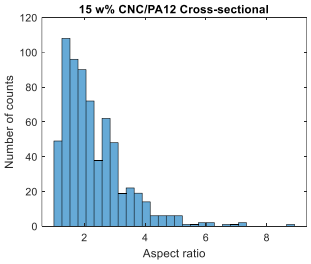

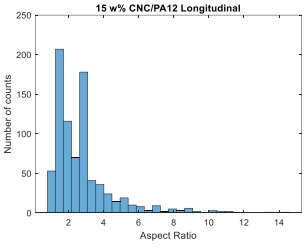

(I) (II)

Figure 4.11. Histograms of cross-sectional (I) and longitudinal (II) aspect ratio and orientation of fibers for TEM image of 5 w% (a) and 15 w% CNC/PA12 (b).

Figure 4.11-columns (I) and (II) should be compared to understand the orientation and aspect ratio of CNC fibers with respect to cross-sectional and longitudinal views. The orientation distribution

of the cross-sectional view, given in Figure 4.11-(a)-column (I), is much more uniform than the orientation distribution of the longitudinal view, presented in Figure 4.11-(a)-column (II). This uniformity is a sign of a randomly orientated case for a cross-sectional view. On the other hand, the non-uniform distribution of the longitudinal view is a sign of alignment. Another indicator of fiber alignment in the extrusion direction is the aspect ratio difference between the cross-sectional and longitudinal TEM images. The aspect ratio distribution of the longitudinal view, given in Figure 4.11-(a)-column (II), has aspect ratio values up to 15, whereas the aspect ratio distribution of the cross-sectional view, given in Figure 4.11-(a)-column (I), has aspect ratio values up to 11. The aspect ratio distribution of the longitudinal view seems as if it is the right-shifted version of the aspect ratio histogram of the cross-sectional view. Thus, it can be concluded that both the aspect ratio and orientation distributions for 5.0 w% illustrate the alignment tendency of CNC.

The aspect ratio and orientation histograms of 15.0 w% CNC/PA12 have similar trends with 5.0 w% CNC/PA12. Uneven distribution of orientation angle for 15.0 w% CNC/PA12 longitudinal view compared to cross-sectional view, given in Figure 4.11-(b) columns (II) and (I), proves the alignment of CNC in the extrusion direction. Another argument that supports the alignment of fibers is the difference between aspect ratios. The maximum aspect ratio is 15 for 15.0 w% CNC/PA12 longitudinal view, whereas 9 for 15.0 w% CNC/PA12 cross-sectional view. Although we cannot tell that there is a perfect alignment in the extrusion direction, qualitatively and quantitively, it can be claimed that CNC fibers are aligned. It should be noted that because extrudates were embedded into epoxy and only ~120 nm thickness of the sample is sectioned, it cannot be proposed that cross-sectional and longitudinal views are perfectly sectioned.

4.1.14 Mechanical Results

The extrudate nanocomposites with average diameter of 1.06 mm (StDev=± 0.09) were tested uniaxially. A photo of a tested sample and a representative stress-strain curve of each CNC loading are given in Figure 4.12-(a) and (b), respectively. Figure 4.12-(b) exhibits the typical behaviour of semicrystalline thermoplastics material. The tested samples either failed close to the middle point, similar to Figure 4.12-(a) or did not break. Maximum elongation was limited to 12 mm due to machine limitation, and because gauge distance was taken as 75 mm, the maximum strain was measured as 0.16 mm/mm.

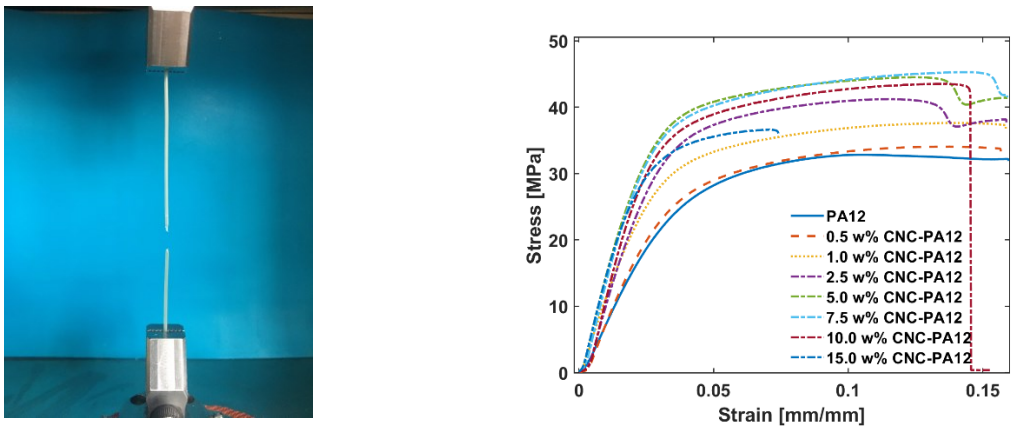

(a) (b)

Figure 4.12. Tensile test photo (a) and representative stress vs strain curves (b).

Figure 4.13 shows the elastic modulus, yield strength and percent elongation-at-yield of nanocomposites. As shown in Figure 4.13-(a) and (b), the trends of the elastic modulus and yield strength are similar. Both the elastic modulus and yield strength values increase up to 10.0 w% CNC with decreasing pace, and they drop at 15.0 w% CNC loading. An increase in the elastic

modulus and yield strength shows that CNC act as a reinforcement in PA12. Percent elongation at yield, on the other hand, shows a constant decrease as CNC loading increases in the composite. Maximum percent elongation-at-yield is observed in pure PA12 extrudate, and the minimum percent elongation-at-yield is observed at 15.0 w% CNC loadings.

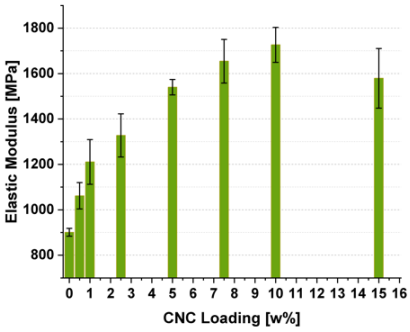

(a)

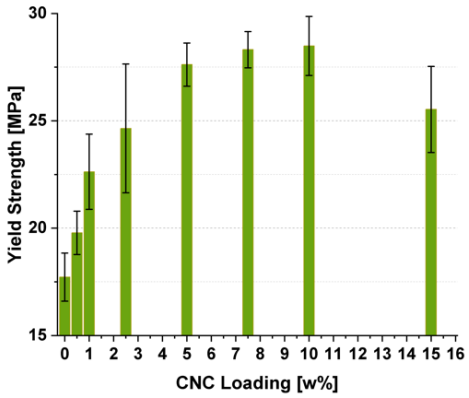

(b)

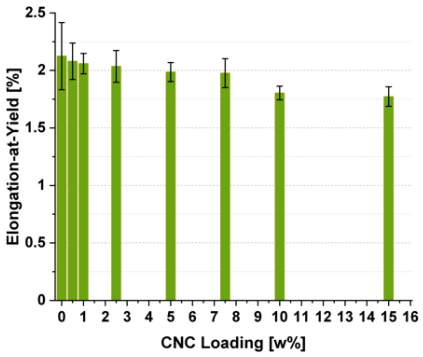

(c)

Figure 4.13. Elastic modulus (a), tensile strength (b) and elongation at yield (c) vs CNC w% in PA12.

The statistical analysis of the elastic modulus of nanocomposites at CNC loading between 0 –15 w% is given in the second column of Table 4.2. The average elastic modulus of the neat PA12

extrudate was calculated as 900.9 MPa (StDev = ± 233.9 MPa). The neat PA12 has the lowest elastic modulus among the nanocomposites at CNC loadings between 0 –15 w%. The addition of 0.5 w% increased the elastic modulus of neat PA12 to 1061.9 MPa (StDev = ± 58.2 MPa), 18 % increase on average. The enhancement in elastic modulus is carried on for 1.0 and 2.5 w% CNC/PA12. The average elastic modulus of 1.0 and 2.5 w% CNC/PA12 was measured as 1210.8 MPa and 1327.7 MPa, respectively. Although the average elastic modulus of 2.5 w% CNC/PA12 is higher than 1.0 w% CNC/PA12, the difference is not significantly important. The elastic modulus of 5.0 w% CNC/PA12 was measured as 1540.0 MPa (StDev = ± 233.9 MPa), significantly higher than the elastic modulus of 2.5 w% CNC/PA12. The addition of 5 w% CNC in elastic modulus increases the elastic modulus of neat PA12 by 71 %. Although the elastic modulus of 7.5 w% CNC/PA12 is higher than the elastic modulus of 5.0, they are statistically equivalent at $p<0.005$, denoted with lower case b in Table 4.2. The highest elastic modulus was obtained with 10.0 w% CNC/PA12; it was measured as 1726.7 MPa (± 77.0 MPa), a 92% increase with respect to neat PA12 extrudate. 15.0 w% CNC/PA12 resulted in a lower elastic modulus than 10.0 w% CNC/PA12. Rahimi and Otaigbe also observed the highest elastic modulus at 10.0 w% CNC loading and reported that 20.0 2% CNC loading was detrimental to the mechanical properties of nanocomposites.

Table 4.2. The statistical analysis of the mechanical properties of nanocomposites

CNC w% in PA12	Elastic Modulus (MPa)	Yield Strength (MPa)	Elongation-at-Yield (%)
0	900.9 ± 17.2^{e}	17.7 ± 1.1^{e}	2.12 ± 0.29^{a}
0.5	1061.9 ± 58.2^{d}	19.8 ± 1.0^{d}	2.08 ± 0.16^{a}

1.0	1210.8 ±98.2^{c}	22.6±1.8^{c}	2.06±0.09^{a}
2.5	1327.7±95.0^{c}	24.6±3.0^{bc}	2.04±0.14^{a}
5.0	1540.0±34.0^{b}	27.6±1.0^{a}	1.99±0.08^{a}
7.5	1620.1±96.0^{b}	28.3±0.8^{a}	1.98±0.13^{a}
10.0	1726.7±77.0^{a}	28.5±1.4^{a}	1.80±0.06^{b}
15.0	1579.2±131.2^{b}	25.5±2.0^{b}	1.77±0.08^{b}

The superscripts (a,b,c,d, and e) demonstrate the statistically significant differences ($p<0.005$), as determined via one-way ANOVA analysis and two tail T-test. The superscripts are ordered alphabetically, and the largest mean comes first in the alphabet. Yield strength and percent elongation-at-yield were determined at 0.2 % offset.

The statistical analysis of the yield strength of nanocomposites at CNC loading between 0 –15 w% is also shown in the third column of Table 4.2. The yield strength was determined at 0.2 % offset elongation. The lowest yield strength is observed in neat PA12 extrudates with 17.7 MPa (StDev = ±1.1 MPa). The addition of 0.5 w% CNC increases the yield strength significantly to 19.8 MPa (StDev = ±1.0 MPa). The average yield strength increases up to 10.0 w% and reaches its maximum value of 28.5 MPa (StDev = ±1.4 MPa). The total increase in the yield strength from 0 to 10.0 w% corresponds to 61.0 %. Although the maximum yield strength is observed at 10.0 w%, there is no significant difference in yield strengths at 5.0, 7.5, and 10.0 w% CNC loadings. The yield strength for the CNC loading of 15.0 w% composites is lower than the yield strength of 10.0 w% CNC loading by 10.5%.

The elastic modulus and yield strength improvement are primarily due to the load transfer from the matrix to the nanoparticle and the low polymer chain mobility. Uniform dispersion and non-

agglomerated particles provide the highest efficiency for load transfer as they increase the surface-to-volume ratio and polymer particle interaction regions. Further, the existence of nanoparticles restrains the polymer chain movement and lowers the plasticity of the polymer matrix. Non-uniform dispersion and agglomerated particles, on the other hand, would decrease the efficiency of load transfer from matrix to particles. Higher particle loadings than an optimal point become detrimental to nanocomposites' elastic modulus and yield strength, which is a clue of agglomeration. This negative effect is observed at 15.0 w% CNC/PA12 in this study. CNC loading of 15.0 w% for observing the adverse impact is high compared to existing literature. Wu et al. [44] observed that the yield strength of nanocomposites starts to decrease at 3.0 w% CNC in poly(butylene succinate). Marmir et al. [41] observed a decrease in the yield strength after 2.0 w% CNC. Gwon et al. [45] reported a reduction in elastic modulus and yield strength after 5.0 w% CNC in polypropylene. Obtaining high mechanical properties at high CNC loadings in this study demonstrates the production method's exceptional benefits.

Percent elongation-at-yield has a different behaviour than the nanocomposites' elastic modulus and yield strength. It decreases with increasing CNC loading as opposed to the increase of the elastic modulus and yield strength. The elongation-at-break values of nanocomposites are given in the fourth column of Table 4.2. The neat PA12 extrudate has the highest value of percent elongation-at-yield with 2.12 % (StDev = ±0.29 %). Although the average elongation-at-yield constantly decreases, elongation-at-yield at 0, 0.5.1.0, 2.5, 5.0, and 7.5 w% CNC loadings are statistically equivalent. CNC loading of 15.0 w% has the minimum elongation-at-break value of 1.77 % (StDev = ±0.08 %). It is seen that 15.0 w% CNC decreased in elongation-at-break by 16.5 % with respect to neat PA12. Increasing CNC loading is expected to lower the chain movement and make the polymer stiffer and more brittle. We see that in the trend of elongation-at-yield. Further,

agglomeration of CNC could behave as stress concentration points. These stress concentration points lead to the early yielding of the polymer matrix. Many studies [46][47][48] suggest similar trends for elongation-at-yield or elongation-at-break.

4.1.15 Model Implication based on TEM Images

A previously developed analytical model was based on synthetically developed fiber dispersion and application of 3-phase Mori-Tanaka (free fiber, agglomerate, and matrix phases). In this study, instead of synthetic fiber dispersion, three TEM images from five different CNC loadings (1.0, 2.5, 5.0, 10.0, and 15.0 w% CNC/PA12) were processed, and fractions of each phase were determined. Figure 4.14 shows TEM images at CNC loadings of 1.0 w% (a), 2.5 w%, (b) 5.0% (c), 10.0 w% (d) and 15.0 w% (e). Light gray colour in TEM images corresponds to the matrix material, and dark gray/black colour corresponds to the CNC fibers as they were stained. The black regions at higher concentrations, e.g., 10 w% CNC/PA12 are more obvious than low ones, e.g., 1.0 w% CNC/PA12. This appearance difference is not only due to the higher CNC loading but also due to the particle agglomeration. The agglomeration can be understood from the size of black particles. The black regions in the TEM images of 15.0 w% CNC/PA12 are bigger than the black regions in 1.0 w% TEM images, which gives clues about the agglomeration of CNC in nanocomposites. The process of retrieving necessary data for model implication was completed via image analysis described in Section 0.

(a) 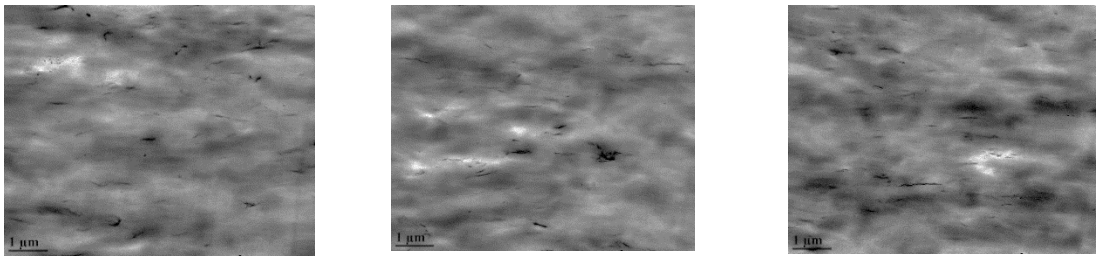

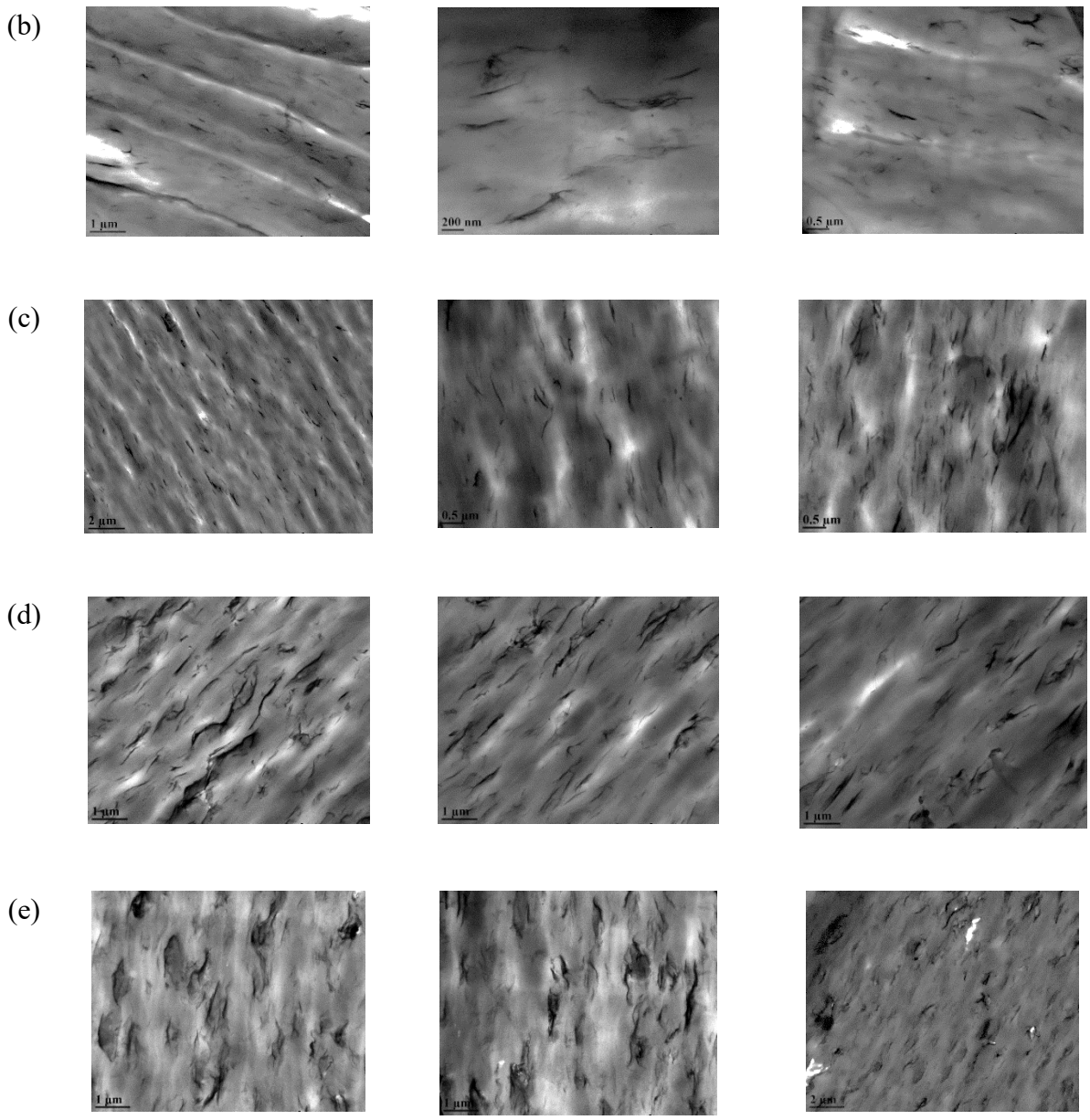

Figure 4.14. The raw TEM images at CNC loadings of 1.0 w% (a), 2.5 w% (b), 5.0% (c), 10.0 w% (d) and 15.0 w% (e). These images were processed for model implication.

Figure 4.15 shows the image processing results for a TEM image of 5.0 % CNC/PA12. Figure 4.15-(a) demonstrates the raw TEM image of 5.0 w% CNC loading in the PA12 matrix. The image is in gray-scale and has bright white regions from thin matrix areas and dark fiber-regions from

CNC. This image needs to be converted into a black and white image for detailed analysis. Figure 4.15-(b) shows the TEM image's cropped, black and white version. The black spots in Figure 4.15-(a) seem white, and the rest of the TEM image in Figure 14-(a) appears black. In the next step, agglomerated fibers are detected based on the critical distance. When the distance between the closest fibers is shorter than a CNC's diameter, they are counted as connected/agglomerated fibers. The matrix between these fibers is also considered to belong to the agglomerated region. Figure 4.15-(c) shows agglomerated regions and free fibers in black and white colours. Fibers with a smaller size than the maximum size of CNC are thought to be free fiber. The free fibers were removed from Figure 4.15-(c) to observe agglomerated regions without free fibers. Figure 4.15-(d) shows agglomerated regions without free fibers. Figure 4.15-(e) shows the coloured version of Figure 4.15-(c) to understand the agglomerate detection system better. Agglomerated regions belonging to the same agglomerate are painted in the same colour. We also need to know the fiber concentration in each agglomerate. Thus, fibers within agglomerates are extracted and shown in Figure 4.15-(f). This image analysis was performed for each image that is given in Figure 4.14.

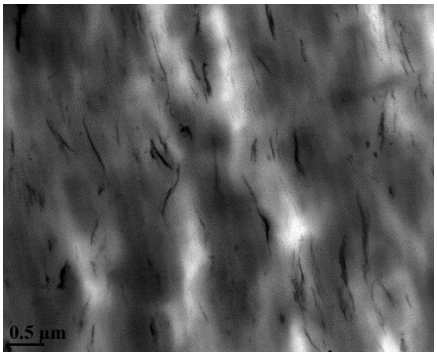

(a)

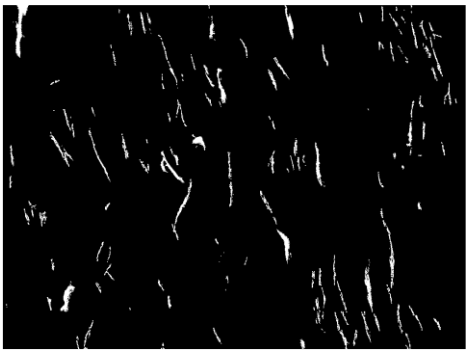

(b)

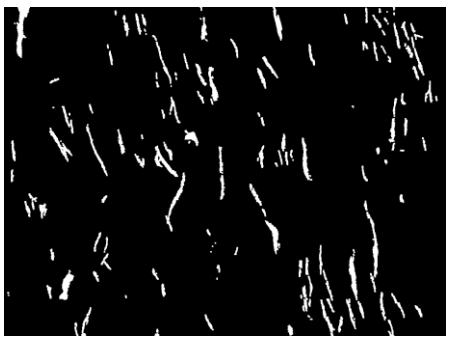

(c)

(d)

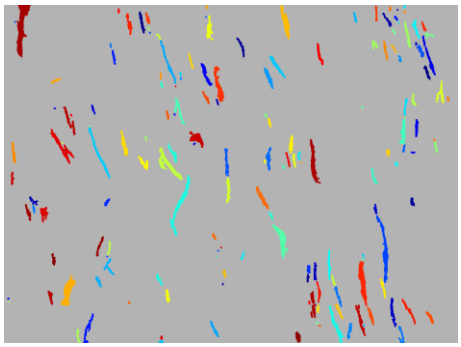

(g)

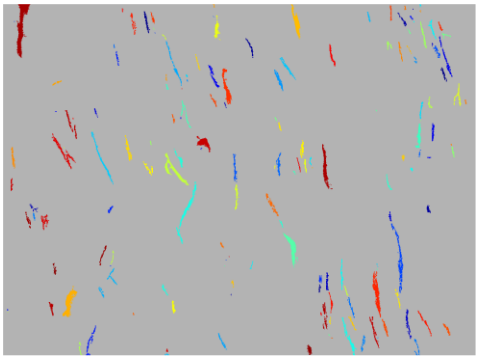

(f)

Figure 4.15. Step by step Image processing results of 5.0 w% CNC/PA12 for model implication.

The data extracted from image analysis was used to predict the elastic modulus of nanocomposites. Because there were three images for each CNC loading, we predicted three elastic moduli for each CNC loading. The predictions and the experimental results of each CNC loading are displayed in Figure 4.16. Figure 4.16 also has one TEM image from each CNC loading for the reader to relate images with the experimental results. The model predictions track the experimental results relatively well. Except for 10.0 w% CNC loading, two out of three predictions match the experimental results and one out of three is close to the experimental results. The average prediction for 10.0 w% CNC loading is off approximately by 20% of the experimental results.

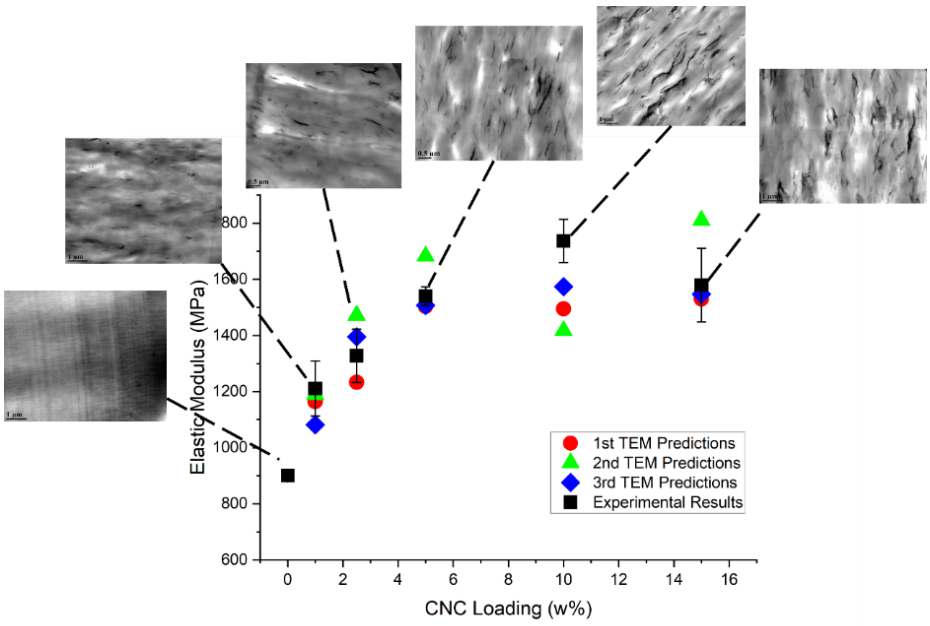

Figure 4.16. Model predictions and experimental results along with TEM images of certain CNC loadings.

The discrepancies between model predictions and the experimental results can be due to the low number of images. We only processed three images for each loading due to difficulties in TEM sample preparation and assumed that TEM images were representative. The higher number of images would provide a better picture of the dispersion state and predictions closer to the experimental outputs. Further, image processing brings inevitable data loss while converting raw images to black and white. This data loss is mostly due to the high local differences in brightness and contracts, auto local threshold algorithm and manual data cleaning. These variances result in discrepancies between model predictions and the experimental results.

Another reason for differences between predictions and experimental results could be related to geometrical assumptions and image processing. We assumed that the size and orientation of fibers were uniform, but in reality, these are found in distribution form. The size and orientation distribution could be incorporated into the model for a better prediction. It is important to note that

these distributions are not easy to obtain for every nanocomposite system, and assumptions might be needed.

The model can be applied to various nanocomposite systems to predict their elastic modulus. TEM/SEM images or the dispersion state of particles in a matrix are required to obtain reliable outcomes. Agglomerates' effects on nanocomposite's elastic modulus can be captured with this model for high particle loadings.

4.4 Conclusion

In this study, we explored an innovative production method that possibly eliminates filament production step for extrusion-based 3D printing and provide well-dispersed nanoparticles in polymer matrices. In this method, first the solvent mixing, and then the melt mixing were performed, and a small pellet extruder designed as a 3D printer head was used to reinforce a polymer with nanoparticles.

The proposed production method was studied by investigating the effects of CNC on the mechanical and crystallographic properties of PA12. PA12 extrudates at CNC loading of 0 – 15 w% were uniaxially pulled for mechanical testing. The elastic modulus and yield strength of nanocomposites increased with increasing the CNC loading up to a certain point and then decreased. The elastic modulus and yield strength were increased with respect to the neat PA12 by 90% and 61% respectively with the addition of 10 w% CNC. Percent elongation-at-yield showed a different behaviour than the trend of the elastic modulus and yield strength, and it is constantly decreased with increasing CNC loading. It is shown that while the addition of CNC strongly changed the mechanical properties of nanocomposites, it did not have a strong impact on the

crystallinity of PA12. Therefore, it can be concluded that CNC is the solely contributor to the mechanical properties of the PA12.

Detailed TEM analysis was performed to apply a previously developed model. The model was developed to predict the elastic modulus of nanocomposites based on synthetically dispersed particles in a computer setting. In this study, instead of synthetic dispersion, TEM images were processed to predict the elastic modulus of the nanocomposites CNC/PA12 nanocomposites. The data retrieved from images were incorporated into the 3-phase Mori-Tanaka model. The predictions showed good agreement with the experimental results.

This work introduces a significant method in the development of novel 3D nanocomposite production method, highlights the reinforcing potential of CNC for PA12, and verifies a previously developed model. The proposed production method can be used with different polymer matrices and modified for extrusion-based additive manufacturing e.g., direct 3D printing, where no filament production is needed.

REFERENCES

[1] A. Dufresne, Nanocellulose: a new ageless bionanomaterial, Mater. Today. 16 (2013) 220–227. https://doi.org/https://doi.org/10.1016/j.mattod.2013.06.004.

[2] A. Dufresne, Cellulose nanomaterials as green nanoreinforcements for polymer nanocomposites, Philos. Trans. A. Math. Phys. Eng. Sci. 376 (2018) 20170040. https://doi.org/10.1098/rsta.2017.0040.

[3] T. Ebeling, M. Paillet, R. Borsali, O. Diat, A. Dufresne, J.-Y. Cavaillé, H. Chanzy, Shear-induced orientation phenomena in suspensions of cellulose microcrystals, revealed by small angle X-ray scattering, Langmuir. 15 (1999) 6123–6126. https://doi.org/10.1021/la990046+.

[4] M.N. Anglès, A. Dufresne, Plasticized starch/tunicin whiskers nanocomposites, Struct Anal Macromol. 33 (2000) 8344–8353, 8344–8353, https://doi.org/10.1021/ma0008701..

[5] K. Tashiro, M. Kobayashi, Theoretical evaluation of three-dimensional elastic constants of native and regenerated celluloses: role of hydrogen bonds, Polymer (Guildf). 32 (1991) 1516–1526. https://doi.org/https://doi.org/10.1016/0032-3861(91)90435-L.

[6] A. Šturcová, G.R. Davies, S.J. Eichhorn, Elastic Modulus and Stress-Transfer Properties of Tunicate Cellulose Whiskers, Biomacromolecules. 6 (2005) 1055–1061. https://doi.org/10.1021/bm049291k.

[7] J. Sapkota, J.C. Natterodt, A. Shirole, E.J. Foster, C. Weder, Fabrication and Properties of Polyethylene/Cellulose Nanocrystal Composites, Macromol. Mater. Eng. 302 (2017) 1600300. https://doi.org/10.1002/mame.201600300.

[8] H. Sojoudiasli, M.-C. Heuzey, P.J. Carreau, Mechanical and morphological properties of

cellulose nanocrystal-polypropylene composites, Polym. Compos. 39 (2018) 3605–3617. https://doi.org/10.1002/pc.24383.

[9] Y. Peng, D.J. Gardner, Y. Han, Characterization of mechanical and morphological properties of cellulose reinforced polyamide 6 composites, Cellulose. 22 (2015) 3199–3215. https://doi.org/10.1007/s10570-015-0723-y.

[10] J.-G. Gwon, H.-J. Cho, S.-J. Chun, S. Lee, Q. Wu, S.-Y. Lee, Physiochemical, optical and mechanical properties of poly(lactic acid) nanocomposites filled with toluene diisocyanate grafted cellulose nanocrystals, RSC Adv. 6 (2016) 9438–9445. https://doi.org/10.1039/c5ra26337a.

[11] J. Shojaeiarani, D. Bajwa, Functionalized cellulose nanocrystals for improving the mechanical properties of poly(lactic acid), in: ASME Int. Mech. Eng. Congr. Expo. Proc., Department of Mechanical Engineering, North Dakota State University, Fargo, ND, United States, 2018. https://doi.org/10.1115/IMECE2018-87691.

[12] S.K. Rahimi, J.U. Otaigbe, The effects of the interface on microstructure and rheo-mechanical properties of polyamide 6/cellulose nanocrystal nanocomposites prepared by in-situ ring-opening polymerization and subsequent melt extrusion, Polym. (United Kingdom). 127 (2017) 269–285. https://doi.org/10.1016/j.polymer.2017.08.064.

[13] J.-G. Gwon, H.-J. Cho, D. Lee, D.-H. Choi, S. Lee, Q. Wu, S.-Y. Lee, Physicochemical and Mechanical Properties of Polypropylene-cellulose Nanocrystal Nanocomposites: Effects of Manufacturing Process and Chemical Grafting, Bioresour. Vol 13, No 1. (2018). http://ojs.cnr.ncsu.edu/index.php/BioRes/article/view/BioRes_13_1_1619_Gwon_Polypropylene_Nanocrystal_Nanocomposites_Chemical_Grafting/5839.

[14] S. Aitha, N. Vasanthan, Effect of cellulose nanocrystals on crystallization, morphology and phase transition of polyamide 6, Compos. Interfaces. (2019). https://doi.org/10.1080/09276440.2019.1637213.

[15] M.R. Kamal, V. Khoshkava, Effect of cellulose nanocrystals (CNC) on rheological and mechanical properties and crystallization behavior of PLA/CNC nanocomposites, Carbohydr. Polym. 123 (2015) 105–114. https://doi.org/10.1016/j.carbpol.2015.01.012.

[16] D.J. Gardner, G.S. Oporto, R. Mills, M.A.S.A. Samir, Adhesion and surface issues in cellulose and nanocellulose, J. Adhes. Sci. Technol. 22 (2008) 545–567. https://doi.org/10.1163/156856108X295509.

[17] A. Iwatake, M. Nogi, H. Yano, Cellulose nanofiber-reinforced polylactic acid, Compos. Sci. Technol. 68 (2008) 2103–2106. https://doi.org/10.1016/j.compscitech.2008.03.006.

[18] D.M. Panaitescu, A.N. Frone, C. Nicolae, Micro- and nano-mechanical characterization of polyamide 11 and its composites containing cellulose nanofibers, Eur. Polym. J. 49 (2013) 3857–3866. https://doi.org/10.1016/j.eurpolymj.2013.09.031.

[19] A.M. Gohn, J. Seo, T. Ferris, P. Venkatraman, E.J. Foster, A.M. Rhoades, Quiescent and flow-induced crystallization in polyamide 12/cellulose nanocrystal composites, Thermochim. Acta. 677 (2019) 99–108. https://doi.org/10.1016/j.tca.2019.03.034.

[20] A. Nicharat, J. Sapkota, C. Weder, E. Johan Foster, Melt processing of polyamide 12 and cellulose nanocrystals nanocomposites, J. Appl. Polym. Sci. 132 (2015) 1–10. https://doi.org/10.1002/app.42752.

[21] M.S. Reid, M. Villalobos, E.D. Cranston, Benchmarking Cellulose Nanocrystals: From the Laboratory to Industrial Production, Langmuir. 33 (2017) 1583–1598.

https://doi.org/10.1021/acs.langmuir.6b03765.

[22] O. van den Berg, J.R. Capadona, C. Weder, Preparation of Homogeneous Dispersions of Tunicate Cellulose Whiskers in Organic Solvents, Biomacromolecules. 8 (2007) 1353–1357. https://doi.org/10.1021/bm061104q.

[23] S. Gogolewski, K. Czerntawska, M. Gastorek, Effect of annealing on thermal properties and crystalline structure of polyamides. Nylon 12 (polylaurolactam), Colloid Polym. Sci. 258 (1980) 1130–1136. https://doi.org/10.1007/BF01382456.

[24] P. Chen, M. Tang, W. Zhu, L. Yang, S. Wen, C. Yan, Z. Ji, H. Nan, Y. Shi, Systematical mechanism of Polyamide-12 aging and its micro-structural evolution during laser sintering, Polym. Test. 67 (2018) 370–379. https://doi.org/10.1016/j.polymertesting.2018.03.035.

[25] E.C. Demir, A. Benkaddour, D. Aldrich, M.T. Mcdermott, C. Il Kim, C. Ayranci, A predictive model towards understanding the effect of reinforcement agglomeration on the stiffness of nanocomposites, J. Compos. Mater. (2022). https://doi.org/10.1177/00219983221076639.

[26] N. Phansalkar, S. More, A. Sabale, M. Joshi, Adaptive local thresholding for detection of nuclei in diversity stained cytology images, in: 2011 Int. Conf. Commun. Signal Process., 2011: pp. 218–220. https://doi.org/10.1109/ICCSP.2011.5739305.

[27] J. Sauvola, M. Pietikäinen, Adaptive document image binarization, Pattern Recognit. 33 (2000) 225–236. https://doi.org/10.1016/S0031-3203(99)00055-2.

[28] N. Ma, W. Liu, L. Ma, S. He, H. Liu, Z. Zhang, A. Sun, M. Huang, C. Zhu, Crystal transition and thermal behavior of Nylon 12, E-Polymers. 20 (2020) 346–352. https://doi.org/10.1515/epoly-2020-0039.

[29] G.S. Martynková, A. Slíva, G. Kratošová, K.Č. Barabaszová, S. Študentová, J. Klusák, S. Brožová, T. Dokoupil, S. Holešová, Polyamide 12 materials study of morpho-structural changes during laser sintering of 3d printing, Polymers (Basel). 13 (2021). https://doi.org/10.3390/polym13050810.

[30] N.S. Murthy, Hydrogen bonding, mobility, and structural transitions in aliphatic polyamides, J. Polym. Sci. Part B Polym. Phys. 44 (2006) 1763–1782. https://doi.org/https://doi.org/10.1002/polb.20833.

[31] L. Li, M.H.J. Koch, W.H. De Jeu, Crystalline structure and morphology in nylon-12: A small- and wide-angle X-ray scattering study, Macromolecules. 36 (2003) 1626–1632. https://doi.org/10.1021/ma025732l.

[32] J. Pepin, V. Gaucher, J.M. Lefebvre, A. Stroeks, Biaxial stretching behavior as a probe of H-bond organization in semi-crystalline polyamides, Polymer (Guildf). 101 (2016) 217–224. https://doi.org/10.1016/j.polymer.2016.08.078.

[33] S. Gogolewski, K. Czerniawska, M. Gasiorek, Effect of annealing on thermal properties and crystalline structure of polyamides. Nylon 12 (polylaurolactam), 1136 (1980) 1130–1136.

[34] T. Ishikawa, S. Nagai, N. Kasai, Thermal behavior of α nylon-12, J. Polym. Sci. Polym. Phys. Ed. 18 (1980) 1413–1419. https://doi.org/https://doi.org/10.1002/pol.1980.180180619.

[35] J. Shojaeiarani, D.S. Bajwa, K. Hartman, Esterified cellulose nanocrystals as reinforcement in poly(lactic acid) nanocomposites, Cellulose. 26 (2019) 2349–2362. https://doi.org/10.1007/s10570-018-02237-4.

[36] J. Shojaeiarani, D.S. Bajwa, N.M. Stark, Spin-coating: A new approach for improving dispersion of cellulose nanocrystals and mechanical properties of poly (lactic acid) composites, Carbohydr. Polym. 190 (2018) 139–147. https://doi.org/https://doi.org/10.1016/j.carbpol.2018.02.069.

[37] S. Malmir, B. Montero, M. Rico, L. Barral, R. Bouza, Y. Farrag, PHBV/CNC bionanocomposites processed by extrusion: Structural characterization and properties, Polym. Compos. 40 (2019) E275–E284. https://doi.org/10.1002/pc.24634.

[38] A. Anžlovar, M. Kunaver, A. Krajnc, E. Žagar, Nanocomposites of LLDPE and surface-modified cellulose nanocrystals prepared by melt processing, Molecules. 23 (2018). https://doi.org/10.3390/molecules23071782.

[39] D.A. Osorio, E. Niinivaara, N.C. Jankovic, E.C. Demir, A. Benkaddour, V. Jarvis, C. Ayranci, M.T. Mcdermott, D. Lannoy, E.D. Cranston, Cellulose Nanocrystals In fl uence the Polyamide 6 Crystal Structure , 2 Spherulite Uniformity , and Mechanical Performance of 3 Nanocomposite Films, (2021). https://doi.org/10.1021/acsapm.1c00765.

[40] J. Peng, P.J. Walsh, R.C. Sabo, L.-S. Turng, C.M. Clemons, Water-assisted compounding of cellulose nanocrystals into polyamide 6 for use as a nucleating agent for microcellular foaming, Polymer (Guildf). 84 (2016) 158–166. https://doi.org/10.1016/j.polymer.2015.12.050.

[41] C. Wu, X. Zhang, X. Wang, Q. Gao, X. Li, Surface modification of cellulose nanocrystal using succinic anhydride and its effects on poly(butylene succinate) based composites, Cellulose. 26 (2019) 3167–3181. https://doi.org/10.1007/s10570-019-02292-5.

[42] Y. He, J. Zhu, W. Wang, H. Ni, Surface modification of cellulose nanocrystals with

different acid anhydrides for improved dispersion in poly(butylene succinate), RSC Adv. 8 (2018) 38305–38314. https://doi.org/10.1039/c8ra07597b.

[43] N.H. Inai, A.E. Lewandowska, O.R. Ghita, S.J. Eichhorn, Interfaces in polyethylene oxide modified cellulose nanocrystal - polyethylene matrix composites, Compos. Sci. Technol. 154 (2018) 128–135. https://doi.org/https://doi.org/10.1016/j.compscitech.2017.11.009.

Chapter 5

A Study on Filamentless Extrusion-Based Additive Manufacturing of Cellulose Nanocrystals Reinforced Polyamide 12

5.1 Introduction

Extrusion-based additive manufacturing (EBAM) is a promising tool to produce prototypes, low-volume end-use products and customized parts such as patient-specifical biomedical devices. It is also one of the most used additive manufacturing methods because of its low cost and simple operation technique. In a common EBAM process, a thermoplastic filament is fed into the heating element and then extruded through a nozzle. The extruded material is deposited onto the heated bed while the nozzle and/or bed move in the x-y plane and/or in the z-direction to fabricate the parts layer-by-layer. 3-dimensional (3D) parts are formed as a result of these movements and the deposition process.

Developing additive manufacturing technologies and the demand for multifunctional materials inspired researchers to work on polymer nanocomposites produced by 3D printing[1,2]. For example, Kim et. al.,[3] produced flexible piezoelectric polymer nanocomposite with $BaTiO_3$ and poly(vinylidene fluoride) using fused deposition modelling (FDM). They utilized solvent mixing and filament production before FDM processes. Francis and Jain,[4], produced silicate reinforced

acrylonitrile butadiene styrene (ABS) using FDM. They first created a master bench and then produced filaments for better dispersion of silicate in ABS. Hunian et. al.,[5], used an aerosol-based 3D printing method to add nano-titania into poly-lactide-co-glycolide. They noted that well-dispersed nanoparticles showed better biological and mechanical responses than nanocomposites with agglomerated nanoparticles. In another study, Chen et. al., [6] used FMD to create porous polylactic acid/nano-hydroxyapatite scaffolds. They produced the filaments by melt extrusion and then used these filaments to perform 3D printing. Well dispersed nanoparticles provided the desired compressive strength and good biocompatibility[6]. Dul et. al., [7] 3D printed multi-wall and single-wall carbon nanotube ABS for electromechanical devices. Before the 3D printing process, they melt compounded carbon nanotubes with ABS using a twin-screw extruder which provides better dispersion compared to a single screw extruder. These studies show that promising nanocomposites can be 3D printed for various applications when good dispersion of nanoparticles in polymer matrices is obtained.

Many researchers mix nanoparticles with polymers during filaments production for extrusion-based 3D printing [4,8–13], at the same time, they also try to maximize nanoparticle dispersion in the polymer matrix [4,8–13]. Melt mixing leads to inevitable nanoparticle agglomeration due to nanoparticles' interactive forces[14–18] and the high viscosity of the polymer [19–22]. Thus, filament production with melt mixing is difficult to obtain well-dispersed nanoparticles unless a special mixing element is used. Further, the requirement of filament production challenges the research where only a small amount of reinforcing agent or polymer is available. Therefore, these studies point out the need for a new production method that can provide well-dispersed nanoparticles and eliminate filament use.

In this study, we demonstrate an innovative direct 3D printing method to produce nanocomposites. The method includes solvent mixing and the melt extrusion of powder/pellets. This method eliminates the need of forming and using a filament and provides flexibility to adjust reinforcement volume fraction easily. The feasibility of the method was studied with bio-based cellulose nanocrystals (CNC) reinforced polyamide 12 (PA12) nanocomposites. To the authors' best knowledge, PA12 is 3D printed with CNC for the first time. The effect of CNC loading on the mechanical properties of PA12 is also reported. While this study cultivates scalable and adjustable 3D printing applications for CNC and PA12 nanocomposites, it promotes the direct printing method for other nanocomposite systems.

5.2 Experimental Method

5.2.1 Materials

Extrusion grade PA12 was purchased in the form of pellets from Arkema Inc under the product name of Rilsamid AESNO MED. PA12's melting range was given as 160 – 175 °C in the technical data sheet. Its density or molecular weight was not reported in the technical data sheet; however, its chemical name is provided as Azacyclotridenecan-2-one. Wood pulp-derived CNC was purchased from Celluforce in the form of a spray-dried powder. Formic acid, CH_2O_2, (98+% pure), was obtained from ACROS Organics in liquid form. A commercial silicone baking mat and a coffee grinder were used to prepare powders. V4 pellets extruder was purchased from Mahor XYZ Industrial Additive Manufacturing. The pellets extruder was adapted to the ADIMLab 3D printer to produce dumbbell specimens.

5.2.2 Preparation of CNC/PA12 mixture

Solvent casting was used to prepare CNC/PA12 mixtures at CNC loadings of 0 – 10 w%. We followed the 20 w/v solid to the liquid ratio for each CNC loading. CNC was dispersed in formic acid because formic acid can dissolve both CNC and PA12. Crest ultrasonic bath sonicator was used for 30 minutes at room temperature to disperse CNC. Once the colour of the solution was transparent and no agglomerated CNC was seen, the PA12 pellets were added to the vial according to the designated CNC loading level. The sealed vials were heated to 68 °C and stirred at 150 rpm for 6 hours on Slicogex hotplates in aluminum quarter reaction blocks. The vials were vibrated using a vortex mixer from Fisher Scientific every hour for approximately 30 seconds. It took 4-6 hours to dissolve PA12. Once PA12 pellets were invisible to the human eye, the solution was cast onto the silicone baking mat to obtain CNC/PA12 mixture ribbons. The cast-mixture remained in the fume hood for 24 hours for drying.

5.2.3 Direct 3D printing

Pure PA12, formic acid-treated pure PA12, and 1, 5, and 10 w% CNC loaded PA12 dog-bone specimens were produced using the direct 3D printing method. The direct 3D printing method uses either pellets or powder. Except for pure PA12, the dog-bone specimens were produced from powder. For this production method, the cast CNC/PA12 mixture was removed from the silicone mat and put into a grinder to obtain the powder form of the mixture. The powder was loaded into a vacuum oven at 100 °C with a pressure of 20 – 25 inHg for 24 hours to remove any remaining moisture in the powder.

The V4 pellets extruder was modified and adapted to ADIMLab 3D to produce specimens. Figure 5.1 shows the modified 3D printer. The print head of the ADIMLAB 3D printer was replaced with

a V4 pellets extruder. Since the size of the 3D printer head and the pellets extruder were different, the location of the printer's control switches was changed for appropriate printing.

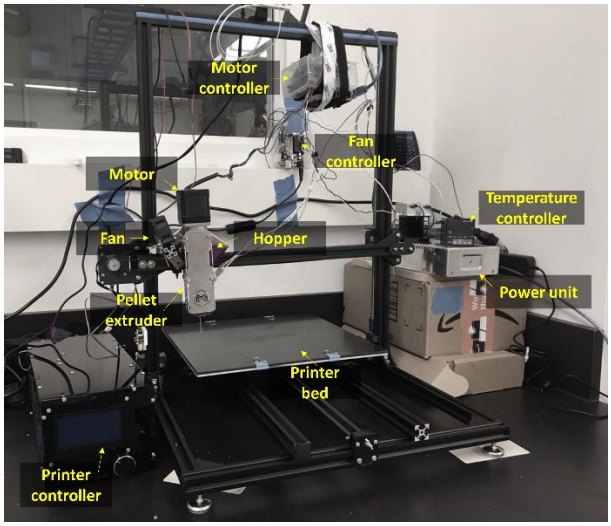

Figure 5.1. In-house direct extrusion-based 3D printer.

We used 3 controllers to print specimens: the controller of the extruder heating, the controller of the extruder motor and the controller of the 3D printer. The pellets extruder could be heated and rotated separately from than 3D printer with the in-house Arduino-based code and controllers. Independently, movements of the 3D printer in x, y and z directions were controlled by the 3D printer controller and the G-code generated from Ultimaker Cura software. In a typical 3D printing process, the 3D geometry is designed using a CAD program and then moved to a 3D printing slicer software. The slicer software, such as Ultimaker Cura and Simplify 3D, enable users to alter the 3D printing settings such as print structure, print speed, and percent fill via its slicing GUI. Once everything is set up, the software slices the geometry and provides a G-code. In this study, G104 and G109 lines were removed manually before printing as the heating of the extruder was controlled separately.

Since the print head was controlled separately, a few parameters were set differently than the default printing settings. Table 5.1 shows the changed print parameters and corresponding default values suggested in Ultimaker Cura software.

Table 5.1. 3D printing parameters

Print Parameters	Default value	Values in this study
Nozzle size	0.8 mm	1.0 mm
Layer height	0.1 mm	0.2 mm
Initial layer height	0.3 mm	0.2 mm
Wall thickness	0.8 mm	1.0 mm
Skin Overlap	5 %	25 %
Infill density	20 %	100 %
Infill patter	Grid	Line
Infill line directions	[ ]	[0]
Infill overlap	10	25%
Build plate temperature	60	60
Print speed	60 mm/s	20.0 mm/s
Initial layer travel speed	60 mm/s	20.0 mm/s

Brim width	8.00 mm	5.0 mm

Specimen geometry was designed according to ASTM-638 Type V specimen with 2 mm thickness. Figure 5.2 demonstrates the isometric view of the sliced 3D printing model.

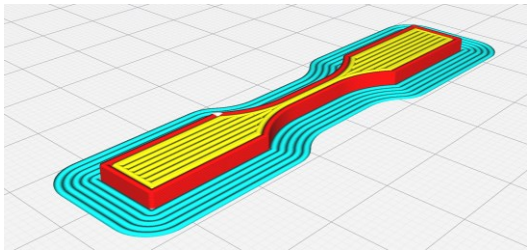

Figure 5.2. Isometric view of the sliced 3D printing model.

5.2.4 Uniaxial Testing

The dog-bone specimens were uniaxially tested according to ASTM-638 using Instron 5565 system. The grip distance was set to 25.4 mm. The speed of the test was 1 mm/min to ensure that the specimens rupture within 0.5 to 5 minutes of testing time. Strain measurement was completed with the Digital Image Correlation method and stress was calculated from the load data collected from the Instron system. The load was recorded every 0.5 seconds. The recorded data was divided by the cross-sectional area to obtain stress.

The stress-strain curves were formed to calculate the elastic modulus, 0.2% offset yield strength and 0.2% offset yield strain of the specimens. The elastic modulus of the specimens was calculated by dividing the stress difference by the corresponding strain difference in the linear portion of the stress-strain curve. The stress at which the strain exceeds by 0.2% extension of the initial portion

of the stress-strain curve was reported as the 0.2% offset yield strength. The strain corresponding to 0.2% offset yield strength was reported as the 0.2% offset yield strain.

5.2.5 Strain Measurement-Digital Image Correlation

The strain in the specimens was measured using a 2D digital image correlation (DIC) technique. Before uniaxial testing, the surfaces of dog-bone specimens were prepared for DIC measurement. Figure 5.3 shows a photo of a dog-bone specimen painted for DIC measurement. The front and back surface of the specimens was first painted black. Then, a white speckle pattern was created on the front surface with a mixture of white paint and reducer. An airbrush at 20 mmHg pressure was used to create this white speckle pattern. The high contrast speckle pattern is necessary for an accurate 2D DIC strain measurement.

Figure 5.3. A dog-bone specimen was painted for DIC measurement.

Images of the dog-bone specimens were recorded at a rate of 2Hz with a high-resolution Basler acA3800-10gm camera and Pylon camera software. The camera was equipped with Tamron AF 70-300mm f/4.0-5.6 Di LD Macro lens. Figure 5.4 shows the testing and strain measurement setup. The light source and camera were positioned such that no shade occurred on the sample. Image acquisition and uniaxial testing were started simultaneously to synchronize the load cell and image acquisition data. The collected data were processed using Digital Image Correlation Engine (DICe) to calculate strain values. We used DICe's default settings. The analysis model was set subset-

based full-field and the subset size was set to 33 pixels. The subset size was adjusted such that it contained 3 speckles. Once image processing was completed with DICe, Paraview software was used for the strain analysis. Paraview software can provide strain values of each pixel on the images over time.

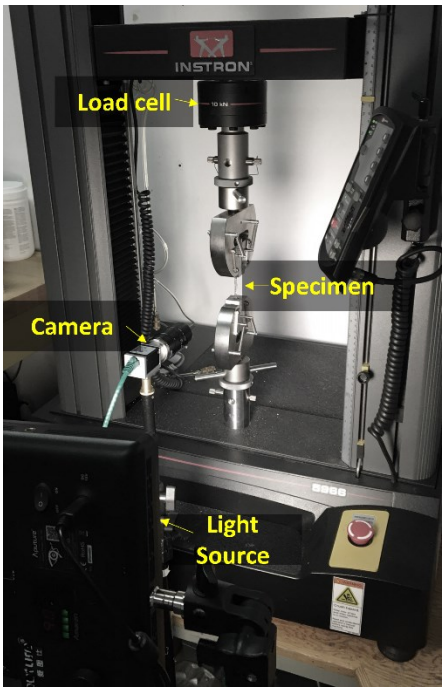

Figure 5.4. Uniaxial testing machine with strain measurement setup.

5.3 Results and Discussion

5.3.1 Specimen Appearance

CNC reinforced PA12 specimens were produced using a novel direct extrusion-based 3D printing method. This method involves three main steps: Solvent mixing of PA12 and CNC in formic acid, powder making by solvent casting, and pellets extrusion with the 3D printer to obtain the dog-bone specimens. The photos of the 3D printed CNC – PA12 specimens at CNC loading of 0 − 10 w% are given in Figure 5.5. Figure 5.5 (a) and (b) have no CNC in PA12 because two different

pure PA12 specimens were produced as a reference point: PA12 specimens from the pellets and PA12 specimens from powder. The process of PA12 specimens from the PA12 pellets did not include PA12 dissolution in formic acid. The PA12 pellets were directly fed into the pellets extruder. The process of PA12 specimens from powder, on the other hand, includes PA12 dissolution in formic acid and obtaining powder. The obtained powder, then, was fed into the pellets extruder.

(a) (b) (c) (d) (e)

Figure 5.5. 3D printed specimens: the neat PA12 from pellets (a), the neat PA12 from powder (b), 1.0 w% CNC-PA12 (c), 5.0 w% CNC-PA12 (d) and 10.0 w% CNC-PA12 (e).

Specimens' colour became gradually darker brown as the CNC loading increased from 0 to 10 w%. in PA12. Similar to our observation, the colour change was observed in CNC-PA6 and CNC-PA12 studies[23][24]. Peng et. al.,[24], related this colour change to the degradation of CNC and noted that this colour change is expected at high-temperature melt mixing processes of CNC. Direct 3D printing was conducted between 260−270°C. This temperature range could seem high for PA12 melt extrusion; however, short barrel length and time, and the presence of CNC coerce us to increase the temperature. Higher CNC loadings needed higher processing temperature, which

could be a reason to observe the darkest colour at 10 w% CNC. Further, degradation was also related to the amount of CNC in the composite. As the concentration of degraded dark colour CNC increases, overall composite colour is expected to be darker, which confirms the darkest colour of 10.0 w% CNC-PA12 specimens. Besides CNC degradation, a slight yellow effect was observed when formic acid was involved in the process. Specimen chemistry was analyzed using the FTIR method in a previous study and no difference was observed between neat PA12 specimens from pellets and powder.

5.3.2 Digital Image Correlation

Digital image correlation was performed to calculate strain in the specimens. While DIC could measure the strain at any point on the specimen surface, an average strain was computed to determine the bulk strain measurement of the specimens and to form stress-strain curves. A similar averaging method was used by Kier et al. [25] and Melenka and Carey [26] to determine the effective strain of the specimens. Since strain within the gauge distance was the region of interest, a rectangular area within the gauge distance was isolated in Paraview for the analysis. Figure 5.6 (a) shows an acquired image of a specimen to be analyzed for DIC and Figure 5.6 (b) shows the rectangular pink region that is isolated for the averaging purpose.

(a) (b)

Figure 5.6. An image acquired by a high-resolution camera for DIC analysis (a) and a screenshot from Paraview software showing the area where the averaging process was applied (b).

While we were expecting to observe total deformation during test time, image acquisition was stopped at the point where the paint was not able to elongate as much as the specimens did. Figure 5.7 shows a photo of a specimen during the test where paint failed to elongate and large cracks were already formed on the paint. Since it was impossible to track speckles after the crack formation on the paint, strain values were extrapolated from the initial deformation zone at high deformations.

Figure 5.7. A specimen during mechanical testing.

5.3.3 Mechanical Results

Figure 5.8 exhibits the elastic modulus, yield strength and percent elongation-at-yield of the nanocomposites at various CNC loadings. Most specimens fractured layer by layer, thus elongation at break and ultimate tensile strength were not reported here. The elastic modulus of the specimens increases with increasing CNC loading. This trend in elastic modulus shows that CNC reinforces the PA12; however, the yield strength of the nanocomposites does not show the same trend. The yield strength increases with the addition of 1.0 w% CNC and then decreases at 5.0 and 10.0 w% CNC. As opposed to the elastic modulus and yield strength, the elongation-at-yield constantly decreases with the addition of CNC to PA12.

We observed a similar trend in elastic modulus, yield strength and elongation-at-yield in a previous study where filaments were produced at different CNC loadings. A drop in the yield strength was observed at 15.0 w% in the previous study; on the other hand, the drop was observed at 5.0 w% CNC in this study, which could be due to the faults in 3D printed specimens. Further, yield strength and elastic modulus values of the 3D printed specimens were observed to be lower than

filaments. This difference is again related to the low bonding quality of layers, and possible voids between the layers.

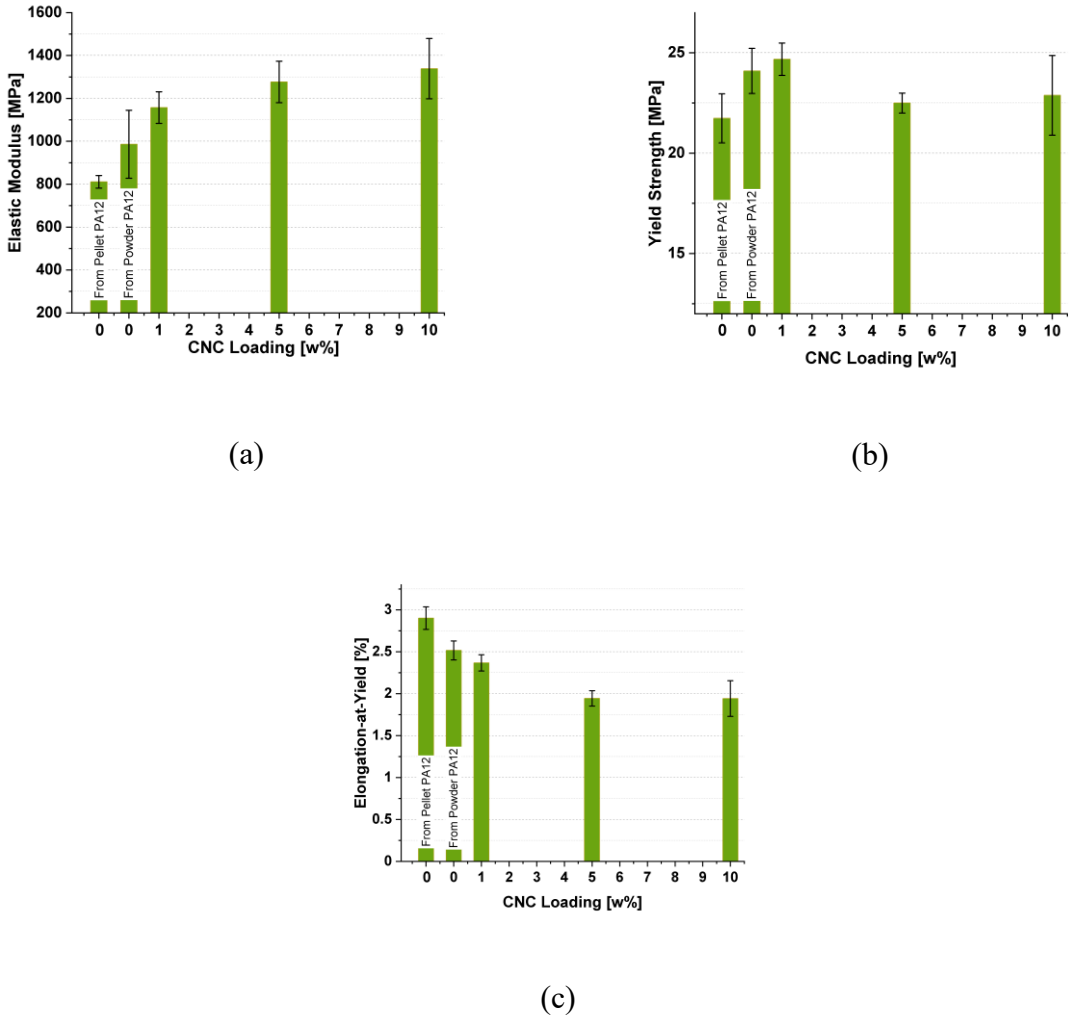

Figure 5.8. Bar charts of elastic modulus (a), yield strength (b) and percent elongation-at-yield. Yield strength and percent elongation-at-yield was determined at 0.2% offset (c).

The second column of Table 5.2 shows the statistical analysis of the elastic modulus at various CNC loading levels. The lowest elastic modulus was calculated as 897.7±236.9 MPa for the neat PA12 produced from pellets. Interestingly, powder making process enhanced the elastic modulus

of the neat PA12 specimens to 986.2±158.3 MPa. The improvement was amplified with the addition of CNC. The addition of 1.0 w% CNC resulted in a 17.3 % improvement in elastic modulus with respect to the neat PA12 produced from powder. The addition of 5 w% CNC increased the average elastic modulus of 1.0 w% CNC-PA12 specimens by 9 %. The highest average elastic modulus was observed at 10.0 w% CNC as 1338.9±140.4 MPa. It is 49.2 % higher than the neat PA12 from pellets and 35.8 % higher than the neat PA12 from the powder. The substantial increase in elastic modulus can be related to the good dispersion of CNC as a solvent mixing process was involved in this study. Nicharat et. al. observed a similar improvement for non-modified CNC. They also noted that improvement is much better when CNC is modified. In their study, modification of CNC results in a higher aspect ratio, which could be the main reason for a higher elastic modulus.

The statistical analysis of yield strength is provided in the third column of Table 5.2. The maximum average yield strength was observed at 1.0 w% CNC; however, it was not significantly different than the neat PA12 produced from powder. It was surprising to observe that the difference in yield strength values was not significant as the elastic modulus of nanocomposites. In our recent study, the trend of yield strength was similar to the trend of the elastic modulus. The main difference in this study is that the tested specimens were 3D printed as opposed to the extrudate in the previous study given in Chapter 4. Because the yield strength of a material can be defined as maximum stress that can be tolerated before a permanent shape change and since 3D printed specimens are produced layer by layer, any weak bonded layer can result in material yielding easier. Thus, the reinforcing effect of CNC in yield strength may not be as strong as the elastic modulus.

Table 5.2. The statistical analysis of the mechanical properties of the nanocomposites.

CNC w% in PA12	Elastic Modulus (MPa)	Yield Strength (MPa)	Elongation-at-Yield (%)
0 from pellets	897.7 ± 236.9^{d}	21.7 ± 1.2^{b}	2.90 ± 0.13^{a}
0 from powder	986.2 ± 158.3^{c}	24.1 ± 1.2^{a}	2.51 ± 0.11^{b}
1.0	1157.2 ± 73.3^{b}	24.7 ± 0.8^{a}	2.37 ± 0.10^{b}
5.0	1276.7 ± 96.7^{a}	22.5 ± 0.5^{b}	1.95 ± 0.09^{c}
10.0	1338.9 ± 140.4^{a}	22.9 ± 2.0^{b}	1.94 ± 0.21^{c}

The superscripts (a, b, c, and d) show the statistically significant differences ($p<0.005$), as determined via one-factor ANOVA analysis and two tail T-test. The superscripts are ordered alphabetically, and the largest mean comes first in the alphabet. Yield strength and percent elongation-at-yield were determined at 0.2 % offset.

The percent elongation-at-yield decreased with increasing CNC loading in this study. The statistical analysis of percent elongation-at-yield is shown in the fourth column of Table 5.2.The highest elongation at break was observed for the neat PA12 and the lowest elongation at break was observed at 10.0 w% CNC addition. The addition of CNC is expected to make the polymer stiffer. Stiffer material would show a lower elongation at yield or elongation at break. Further, CNC addition may worsen the adhesion of 3D printing layers which could create stress concentration points. These points could result in early yielding points.

A previously developed model is used to predict the elastic modulus of 3D printed specimens. Figure 5.9 shows the comparison between model predictions and experimental results. The model

predictions were calculated in the previous study (provided in Chapter 4) based on the TEM images of extrudates for particular CNC loading and reported here to examine the validity of the model in the case of 3D printing. Since three images were used for each CNC loading, three predictions were calculated for each loading.

Experimental results of 3D printed specimens are directly compared to the previous model outputs because the mechanical behaviour of 3D printed specimens is expected to be similar to the mechanical properties of extrudates given in the previous study (provided in Chapter 4). We speculate that the orientation and dispersion of the particles would stay the same in the case of 3D printing because 3D printed specimens were designed in such a way that the lines were oriented in the [0] direction. Although the orientation and the dispersion are expected to be similar, 3D printing specimens have inevitable defects between each layer and between printing lines. These defects are expected to result in lower mechanical properties in the 3D printed specimens compared to extrudates. The discrepancy between the model predictions and experimental results could be mainly related to these defects. While predictions are close at the CNC loadings of 1.0 and 5.0 w%, the highest discrepancy was observed at 10.0 w% CNC PA12 specimens. The average model prediction is 26% higher than the experimental results of 10.0 w% CNC PA12 nanocomposites. This higher difference could also be related to changes in the layer adhesions due to CNC loading. The model can be improved by incorporating the effects of layer adhesion, which might depend on various factors including nanoparticle loadings.

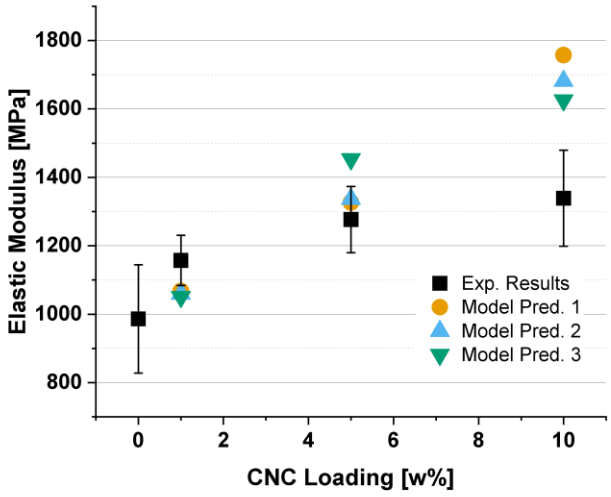

Figure 5.9. Model predictions and experimental results.

Future work is necessary to improve the mechanical properties of 3D printed specimens in this work. This study is a proof-of-concept study showing that CNC and PA12 could be printed efficiently using a novel 3D printing method. The method parameters could easily be optimized to obtain better mechanical properties. For example, lowering the nozzle size and changing the infill line directionality would decrease the defects and provide better adhesion between layers. With studied parameters, the addition of CNC improved elastic modulus significantly; however, resulted in a slight increase in the yield strength. Thus, the parameters and method in this study could be used for stiffness-critical applications. Engineers should give importance to their yield strength in their design not to allow unexpected plastic deformation in their parts.

5.4 Conclusion

Nanocomposite production using EBAM has gained significant attention due to its promising properties of nanocomposites for customized and/or low-number high-end products, particularly in biomedical and sensory applications. A common EBAM production uses a filament as the build

material which can result in nanoparticle agglomeration and require a high amount of material. These two can be challenging for advanced nanocomposite production at the lab scale. In this study, we developed an innovative direct extrusion-based 3D printing technology that uses pellets and/or powder as the build material. This method promotes well dispersion of nanoparticles as it includes solvent mixing and allows researchers to work with a small amount of material for prototyping and customized parts. Further, it gives the ability to control nanoparticle concentration as opposed to the limited commercially available filament options.

A commercial 3D printer was customized and equipped with a pellets extruder that was run separately using Arduino. Heating and extrusion were controlled with an in-house controller unit, and movements in the x,y and z-direction were controlled with the commercial 3D printer and Ultimaker cura software.

The modified 3D printer was used to explore the effects of CNC on the mechanical properties of PA12. The dog-bone PA12 specimens at CNC loading of 0 – 10 w% were produced and pulled uniaxially for mechanical analysis. The elastic modulus of nanocomposites was substantially improved with 10 w% CNC addition, while the yield strength was slightly improved at 1 w% CNC. The elongation at yield, on the other hand, decreased with increasing CNC loading. The average elongation at a yield of 10 w% CNC-PA12 lowered by 33% with respect to the neat PA12. It is shown that the developed technology can be used for stiffness-critical applications, but the 3D printing parameters need to be optimized for high-strength nanocomposites.

This work introduces an innovative direct extrusion-based 3D printing application and shows for the first time that PA12 can be 3D printed with CNC reinforcement. The printing parameters can be optimized for better mechanical properties and the suggested technology can be improved further for different polymer-nanoparticle systems. Lastly, this work provides a promising

alternative for 3D nanocomposite production where the nanoparticle or polymer materials are limited or costly for research-level studies.

REFERENCES

[1] T.D. Ngo, A. Kashani, G. Imbalzano, K.T.Q. Nguyen, D. Hui, Additive manufacturing (3D printing): A review of materials, methods, applications and challenges, Compos. Part B Eng. 143 (2018) 172–196. https://doi.org/10.1016/j.compositesb.2018.02.012.

[2] S.C. Ligon, R. Liska, J. Stampfl, M. Gurr, R. Mülhaupt, Polymers for 3D Printing and Customized Additive Manufacturing, Chem. Rev. 117 (2017) 10212–10290. https://doi.org/10.1021/acs.chemrev.7b00074.

[3] H. Kim, T. Fernando, M. Li, Y. Lin, T.L.B. Tseng, Fabrication and characterization of 3D printed BaTiO3/PVDF nanocomposites, J. Compos. Mater. 52 (2018) 197–206. https://doi.org/10.1177/0021998317704709.

[4] V. Francis, P.K. Jain, Experimental investigations on fused deposition modelling of polymer-layered silicate nanocomposite, Virtual Phys. Prototyp. 11 (2016) 109–121. https://doi.org/10.1080/17452759.2016.1172431.

[5] H. Liu, T.J. Webster, Enhanced biological and mechanical properties of well-dispersed nanophase ceramics in polymer composites: From 2D to 3D printed structures, Mater. Sci. Eng. C. 31 (2011) 77–89. https://doi.org/10.1016/j.msec.2010.07.013.

[6] X. Chen, C. Gao, J. Jiang, Y. Wu, P. Zhu, G. Chen, 3D printed porous PLA/nHA composite scaffolds with enhanced osteogenesis and osteoconductivityin vivo for bone regeneration, Biomed. Mater. 14 (2019). https://doi.org/10.1088/1748-605X/ab388d.

[7] S. Dul, B.J.A. Gutierrez, A. Pegoretti, J. Alvarez-Quintana, L. Fambri, 3D printing of ABS Nanocomposites. Comparison of processing and effects of multi-wall and single-wall carbon nanotubes on thermal, mechanical and electrical properties, J. Mater. Sci. Technol.

121 (2022) 52–66. https://doi.org/10.1016/j.jmst.2021.11.064.

[8] A. Cataldi, D. Rigotti, V.D.H. Nguyen, A. Pegoretti, Polyvinyl alcohol reinforced with crystalline nanocellulose for 3D printing application, Mater. Today Commun. 15 (2018) 236–244. https://doi.org/10.1016/j.mtcomm.2018.02.007.

[9] D. Zhu, Y. Ren, G. Liao, S. Jiang, F. Liu, J. Guo, G. Xu, Thermal and mechanical properties of polyamide 12/graphene nanoplatelets nanocomposites and parts fabricated by fused deposition modeling, J. Appl. Polym. Sci. 134 (2017) 1–13. https://doi.org/10.1002/app.45332.

[10] S. Dinesh Kumar, K. Venkadeshwaran, M.K. Aravindan, Fused deposition modelling of PLA reinforced with cellulose nanocrystals, Mater. Today Proc. 33 (2020) 868–875. https://doi.org/10.1016/j.matpr.2020.06.404.

[11] B. Huang, H. He, S. Meng, Y. Jia, Optimizing 3D printing performance of acrylonitrile-butadiene-styrene composites with cellulose nanocrystals/silica nanohybrids, Polym. Int. 68 (2019) 1351–1360. https://doi.org/10.1002/pi.5824.

[12] R. Hashemi Sanatgar, C. Campagne, V. Nierstrasz, Investigation of the adhesion properties of direct 3D printing of polymers and nanocomposites on textiles: Effect of FDM printing process parameters, Appl. Surf. Sci. 403 (2017) 551–563. https://doi.org/10.1016/j.apsusc.2017.01.112.

[13] A.D. Valino, J.R.C. Dizon, A.H. Espera, Q. Chen, J. Messman, R.C. Advincula, Advances in 3D printing of thermoplastic polymer composites and nanocomposites, Prog. Polym. Sci. 98 (2019) 101162. https://doi.org/10.1016/j.progpolymsci.2019.101162.

[14] M.M. Khattab, N.A. Abdel-Hady, Y. Dahman, 21 - Cellulose nanocomposites:

Opportunities, challenges, and applications, in: M. Jawaid, S. Boufi, A.K.B.T.-C.-R.N.C. H.P.S. (Eds.), Woodhead Publ. Ser. Compos. Sci. Eng., Woodhead Publishing, 2017: pp. 483–516. https://doi.org/https://doi.org/10.1016/B978-0-08-100957-4.00021-8.

[15] J. Li, Z. Song, D. Li, S. Shang, Y. Guo, Cotton cellulose nanofiber-reinforced high density polyethylene composites prepared with two different pretreatment methods, Ind. Crops Prod. 59 (2014) 318–328. https://doi.org/https://doi.org/10.1016/j.indcrop.2014.05.033.

[16] T.C. Mokhena, J.S. Sefadi, E.R. Sadiku, M.J. John, M.J. Mochane, A. Mtibe, Thermoplastic processing of PLA/cellulose nanomaterials composites, Polymers (Basel). 10 (2018). https://doi.org/10.3390/polym10121363.

[17] L. Jiang, E. Morelius, J. Zhang, M. Wolcott, J. Holbery, Study of the Poly(3-hydroxybutyrate-co-3-hydroxyvalerate)/Cellulose Nanowhisker Composites Prepared by Solution Casting and Melt Processing, J. Compos. Mater. 42 (2008) 2629–2645. https://doi.org/10.1177/0021998308096327.

[18] H.-Y. Yu, Z.-Y. Qin, C.-F. Yan, J.-M. Yao, Green Nanocomposites Based on Functionalized Cellulose Nanocrystals: A Study on the Relationship between Interfacial Interaction and Property Enhancement, ACS Sustain. Chem. Eng. 2 (2014) 875–886. https://doi.org/10.1021/sc400499g.

[19] R. Socher, B. Krause, M.T. Müller, R. Boldt, P. Pötschke, The influence of matrix viscosity on MWCNT dispersion and electrical properties in different thermoplastic nanocomposites, Polymer (Guildf). 53 (2012) 495–504. https://doi.org/https://doi.org/10.1016/j.polymer.2011.12.019.

[20] T. Villmow, B. Kretzschmar, P. Putschke, Influence of screw configuration, residence time,

and specific mechanical energy in twin-screw extrusion of polycaprolactone/multi-walled carbon nanotube composites, Compos. Sci. Technol. 70 (2010) 2045–2055. https://doi.org/10.1016/j.compscitech.2010.07.021.

[21] S. Pegel, P. Pötschke, G. Petzold, I. Alig, S.M. Dudkin, D. Lellinger, Dispersion, agglomeration, and network formation of multiwalled carbon nanotubes in polycarbonate melts, Polymer (Guildf). 49 (2008) 974–984. https://doi.org/10.1016/j.polymer.2007.12.024.

[22] G.R. Kasaliwal, S. Pegel, A. Göldel, P. Pötschke Petra, G. Heinrich, Analysis of agglomerate dispersion mechanisms of multiwalled carbon nanotubes during melt mixing in polycarbonate, Polymer (Guildf). 51 (2010) 2708–2720. https://doi.org/10.1016/j.polymer.2010.02.048.

[23] A. Nicharat, J. Sapkota, C. Weder, E. Johan Foster, Melt processing of polyamide 12 and cellulose nanocrystals nanocomposites, J. Appl. Polym. Sci. 132 (2015) 1–10. https://doi.org/10.1002/app.42752.

[24] Y. Peng, D.J. Gardner, Y. Han, Characterization of mechanical and morphological properties of cellulose reinforced polyamide 6 composites, Cellulose. 22 (2015) 3199–3215. https://doi.org/10.1007/s10570-015-0723-y.

[25] Z.T. Kier, A. Salvi, G. Theis, A.M. Waas, K. Shahwan, Estimating mechanical properties of 2D triaxially braided textile composites based on microstructure properties, Compos. Part B Eng. 68 (2015) 288–299. https://doi.org/10.1016/j.compositesb.2014.08.039.

[26] G.W. Melenka, J.P. Carey, Experimental analysis of diamond and regular tubular braided composites using three-dimensional digital image correlation, J. Compos. Mater. 51 (2017)

3887–3907. https://doi.org/10.1177/0021998317695418.

Chapter 6

Conclusions and Future Work

6.1 Conclusions

Polymer nanocomposites offer advantages over traditional composite materials as nanomaterials could confer extraordinary properties to the polymer matrix at low concentrations. Realizing the full potential of polymer nanocomposites requires a comprehensive understanding of nanocomposite behaviour via predictive models. In this study, an accurate analytical model was developed to predict the elastic modulus of polymer nanocomposites, and an innovative extrusion-base direct 3D printing method was investigated for nanocomposite prototyping for customized products. CNC reinforced polyamide nanocomposites were produced to verify the model and study the feasibility of the 3D printing method.

The stiffness of polymers can be improved with the addition of nanoparticles; however, in practical applications, this improvement does not show a linear trend, and the stiffness can decrease at nanoparticle loadings that are higher than the optimum level. In literature, this behaviour is mostly related to the agglomeration of nanoparticles. The existing analytical models do not account for the agglomeration of nanoparticles or lack clear definition of the state of the agglomerated particles. In this study, a novel approach where the three-phase Mori-Tanaka model is coupled

with the Monte-Carlo method is applied to capture the effects of agglomeration on the elastic modulus of nanocomposites. The three phases are agglomerate, free particles and matrix phases. A computational environment is used to have randomly dispersed particles and define each phase of the composite. After particles are dispersed in computational setting, in-house code uses a machine learning method to detects agglomerated particles based on the distance between them. The hierarchical clustering method is used, and the "critical distance" parameter is introduced to classify agglomerated particles. This agglomerate detection system in this study is another novelty that this thesis contributes to the literature. Once each phase is detected, the Mori-Tanaka is used to predict elastic modulus, and the Monte-Carlo is used to obtain statistically meaningful information. TEM analysis was performed to investigate the alignment of CNC in the matrix and the morphology of the CNC. The collected information was implemented into the model. The model predictions showed great agreement with experimental results compared to conventional analytical models.

Later, a parametric study of the developed model was conducted to highlight the effect of agglomeration and the model parameters on the elastic properties of nanocomposites. The parameters studied in this work are the aspect ratio, critical distance, particle orientation, agglomerate property, and dispersion state of particles. The critical distance and agglomerate property parameters are the dominating factors for the elastic modulus of the nanocomposite, particularly at high nanoparticle loadings. The higher critical distance parameter results in more agglomeration and the agglomeration property prevail over nanoparticles' contribution o the elastic modulus of nanocomposites. It is concluded that the value of critical distance would depend on the material system. Further, it is observed that aligned particles provide higher stiffness compared to randomly oriented particles at any nanoparticle loading. The proposed systematic

study exhibited the capabilities of the model to capture the elastic modulus of nanocomposites, particularly CNC reinforced PA6 nanocomposites.

Thirdly, an innovative method toward filamentless extrusion-base additive manufacturing is explored for nanocomposite production. The solvent mixing and casting method are combined to obtain nanoparticles-loaded polymer powder. This powder is directly fed into a small extruder that is designed as a 3D printing head. The feasibility of the method is studied by observing the effects of CNC on the mechanical and crystallographic properties of PA12. While the addition of CNC substantially increased the elastic modulus and yield strength of PA12, the crystallinity of PA12 stayed approximately around 22 %. The elastic modulus of nanocomposite at CNC loading of 10.0 w% is increased by 92% with respect to neat PA12. On the other hand, the elongation-at-yield is constantly decreases and reaches its lowest point at CNC loading of 15 %. This decrease is related to agglomerate formation based on TEM images and tt is concluded that the change in the mechanical properties of the nanocomposites is mostly related to the presence of CNC rather than the crystal structure of PA12 according to XRD results. Detailed TEM analysis is conducted to incorporate the particle dispersion into the model. In-house image processing code is developed in MATLAB to detect agglomerated regions, free particles and the matrix. The data obtained from image analysis is used in the model to predict the elastic modulus of CNC-PA12 nanocomposites. Excellent agreement is obtained between the predictions and the experimental results. This agreement verifies the applicability of the proposed model. In conclusion, this part of the study provides a great method for nanocomposite production, shows the reinforcing potential of CNC in PA12, and verifies the model.

Lastly, an FDM printer is modified, and small pellet extruder is attached to the printer for filamentless 3D printing. Reproducible EBAM printing. A substantial increase, 49 %, in the elastic

modulus with respect to neat PA12 and a slight increase, 5.5 %, in the yield strength of nanocomposites are observed at a CNC loading of 10.0 w%. The low increase in the yield strength of nanocomposites can be related to low adhesion between printing lines or voids as they are possible stress concentration points which leads to material deformations easier. Nevertheless, this work showed the feasibility of the direct extrusion-based 3D printing method and the reinforcing effect of CNC in engineering polymers particularly in PA12. The printing parameters can be optimized, and this method can be applied to other nanocomposite systems for customized parts.

6.2 Future work

This thesis contributes to the modelling of polymer nanocomposites, the development of an innovative 3D printing method and the characterization of CNC-Polyamide composite systems. The recommendations for further investigation are listed below:

- The model development was performed in a 2D computational setting and the 3rd dimension of the nanofibers was included in the Mori-Tanaka model. Although an excellent agreement between predictions and experimental results was obtained, the 3D computational setting could be more robust for any material system.
- Aspect ratio and orientation of particles were averaged and assumed to be constant in this work; however, they are in range and can be represented by a distribution. In the future, the distribution of parameters could be included for more accurate model predictions.
- Critical distance and agglomerate property are the key model parameters for an accurate prediction. The critical distance parameter is considered to be specific to material systems as the interaction between the nanofiller and the matrix is expected to change the critical distance. A detailed literature survey can be conducted to find the correlation between

critical distance parameters and material systems. There is limited knowledge of agglomerate properties in the literature. Theoretical work on agglomeration could be performed to understand agglomeration response under mechanical load for composites.

- Particles were dispersed randomly using uniform and lognormal distribution functions to examine their effect on agglomeration and nanocomposites' elastic modulus. Image analysis on TEM and SEM images that already exist in literature can be conducted and machine learning methods can be implemented to establish a relationship between particle dispersion and production method.
- The solvent mixing and evaporation processes could be improved for better nanoparticle dispersion. A better mixing method or different solid to solvent ratio could be studied.
- The proposed 3D printing can be improved further by developing a system to recycle and reuse the chemical solvent. Varios nanocomposite systems should be worked to validate the feasibility of the study.
- PA12 extrudates with aligned CNC reinforcement showed great improvement in mechanical properties. The extrudates diameter of the nanocomposites was limited to 1 mm due to small extruder. Alignment of CNC in larger diameters could be challenging and further investigation is needed to have an industry-scale application if wanted.
- The yield strength of the 3D printed CNC-PA12 specimens was not increased as expected. The reason could be the low adhesion between layers. A method can be developed to test layer adhesion so that printing can be improved. Another reason could be the high diameter nozzle size and [0] print direction. These settings could have formed voids and defets in the specimens. A further study is needed to determine the causes and fix the problems.

- Parameters of the developed innovative 3D production method can be fine-tuned to obtain the best mechanical results. Once all parameters are optimized, different material systems can be used to show the feasibility of the production method for different systems.

BIBLIOGRAPHY

A. Anžlovar, M. Kunaver, A. Krajnc, E. Žagar, Nanocomposites of LLDPE and surface-modified cellulose nanocrystals prepared by melt processing, Molecules. 23 (2018). https://doi.org/10.3390/molecules23071782.

A. Cataldi, D. Rigotti, V.D.H. Nguyen, A. Pegoretti, Polyvinyl alcohol reinforced with crystalline nanocellulose for 3D printing application, Mater. Today Commun. 15 (2018) 236–244. https://doi.org/10.1016/j.mtcomm.2018.02.007.

A. Dasari, Y. Zhong-Zhen, Y.-W. Mai, Polymer Nanocomposites: Towards Multi-Functionality, 2016. http://dx.doi.org/10.1021/bk-2002-0804.ch011.

A. Dufresne, Cellulose nanomaterials as green nanoreinforcements for polymer nanocomposites, Philos. Trans. A. Math. Phys. Eng. Sci. 376 (2018) 20170040. https://doi.org/10.1098/rsta.2017.0040.

A. Dufresne, Nanocellulose: a new ageless bionanomaterial, Mater. Today. 16 (2013) 220–227. https://doi.org/https://doi.org/10.1016/j.mattod.2013.06.004.

A. Giubilini, G. Siqueira, F.J. Clemens, C. Sciancalepore, M. Messori, G. Nyström, F. Bondioli, 3D-Printing Nanocellulose-Poly(3-hydroxybutyrate- co-3-hydroxyhexanoate) Biodegradable Composites by Fused Deposition Modeling, ACS Sustain. Chem. Eng. 8 (2020) 10292–10302. https://doi.org/10.1021/acssuschemeng.0c03385.

A. Golbang, M.H.N. Famili, M.M.M. Shirvan, A method for quantitative characterization of agglomeration degree in nanocomposites, Compos. Sci. Technol. 145 (2017) 181–186. https://doi.org/10.1016/j.compscitech.2017.04.013.

A. Iwatake, M. Nogi, H. Yano, Cellulose nanofiber-reinforced polylactic acid, Compos. Sci. Technol. 68 (2008) 2103–2106. https://doi.org/10.1016/j.compscitech.2008.03.006.

A. Junior de Menezes, G. Siqueira, A.A.S. Curvelo, A. Dufresne, Extrusion and characterization of functionalized cellulose whiskers reinforced polyethylene nanocomposites, Polymer (Guildf). 50 (2009) 4552–4563. https://doi.org/10.1016/j.polymer.2009.07.038.

A. Mora, P. Verma, S. Kumar, Electrical conductivity of CNT/polymer composites: 3D printing, measurements and modeling, Compos. Part B Eng. 183 (2020) 107600. https://doi.org/10.1016/j.compositesb.2019.107600.

A. Nicharat, J. Sapkota, C. Weder, E. Johan Foster, Melt processing of polyamide 12 and cellulose nanocrystals nanocomposites, J. Appl. Polym. Sci. 132 (2015) 1–10. https://doi.org/10.1002/app.42752.

A. Nouri, A. Rohani Shirvan, Y. Li, C. Wen, Additive manufacturing of metallic and polymeric load-bearing biomaterials using laser powder bed fusion: A review, J. Mater. Sci. Technol. 94 (2021) 196–215. https://doi.org/10.1016/j.jmst.2021.03.058.

A. Okada, Y. Fukushima, M. Kawasumi, S. Inagaki, A. Usuki, S. Sugiyama, J. Wiley, C. Chemical, T. Dictionary, U.S. 4,739,007, (1988).

A. Patil, A. Patel, R. Purohit, An overview of Polymeric Materials for Automotive Applications, Mater. Today Proc. 4 (2017) 3807–3815. https://doi.org/10.1016/j.matpr.2017.02.278.

A. Šturcová, G.R. Davies, S.J. Eichhorn, Elastic Modulus and Stress-Transfer Properties of Tunicate Cellulose Whiskers, Biomacromolecules. 6 (2005) 1055–1061. https://doi.org/10.1021/bm049291k.

A.C. Corrêa, K.B.R. Teodoro, J.A. Simão, P.I.C. Claro, E. de Morais Teixeira, L.H.C. Mattoso, J.M. Marconcini, Cellulose nanocrystals from curaua fibers and poly[ethylene-co-(vinyl acetate)] nanocomposites: Effect of drying process of CNCs on thermal and mechanical properties, Polym. Compos. n/a (2020). https://doi.org/10.1002/pc.25493.

A.D. Valino, J.R.C. Dizon, A.H. Espera, Q. Chen, J. Messman, R.C. Advincula, Advances in 3D printing of thermoplastic polymer composites and nanocomposites, Prog. Polym. Sci. 98 (2019) 101162. https://doi.org/10.1016/j.progpolymsci.2019.101162.

A.M. Gohn, J. Seo, T. Ferris, P. Venkatraman, E.J. Foster, A.M. Rhoades, Quiescent and flow-induced crystallization in polyamide 12/cellulose nanocrystal composites, Thermochim. Acta. 677 (2019) 99–108. https://doi.org/10.1016/j.tca.2019.03.034.

A.M. Hameed, M.T. Hamza, Characteristics of polymer concrete produced from wasted construction materials, Energy Procedia. 157 (2019) 43–50. https://doi.org/10.1016/j.egypro.2018.11.162.

ASTM International, ASTM D882: Standard Test Method for Tensile Properties of Thin Plastic Sheeting, ASTM Stand. (2012) 12. https://doi.org/10.1520/D0882-12.2.

B. Adhikari, S. Majumdar, Polymers in sensor applications, Prog. Polym. Sci. 29 (2004) 699–766. https://doi.org/10.1016/j.progpolymsci.2004.03.002.

B. Arash, Q. Wang, V.K. Varadan, Mechanical properties of carbon nanotube/polymer composites, Sci. Rep. 4 (2014) 1–8. https://doi.org/10.1038/srep06479.

B. Huang, H. He, S. Meng, Y. Jia, Optimizing 3D printing performance of acrylonitrile-butadiene-styrene composites with cellulose nanocrystals/silica nanohybrids, Polym. Int. 68 (2019) 1351–1360. https://doi.org/10.1002/pi.5824.

B. Wetzel, F. Haupert, M. Qiu Zhang, Epoxy nanocomposites with high mechanical and tribological performance, Compos. Sci. Technol. 63 (2003) 2055–2067. https://doi.org/https://doi.org/10.1016/S0266-3538(03)00115-5.

B.K. Kandola, 6 - Nanocomposites, in: A.R. Horrocks, D.B.T.-F.R.M. Price (Eds.), Woodhead Publishing, 2001: pp. 204–219. https://doi.org/https://doi.org/10.1533/9781855737464.204.

B.M. Tyson, R.K. Abu Al-Rub, A. Yazdanbakhsh, Z. Grasley, A quantitative method for analyzing the dispersion and agglomeration of nano-particles in composite materials, Compos. Part B Eng. 42 (2011) 1395–1403. https://doi.org/10.1016/j.compositesb.2011.05.020.

C. Weiler, M. Egen, M. Trunk, P. Langguth, Force control and powder dispersibility of spray dried particles for inhalation, J. Pharm. Sci. 99 (2010) 303–316. https://doi.org/10.1002/jps.21849.

C. Wu, X. Zhang, X. Wang, Q. Gao, X. Li, Surface modification of cellulose nanocrystal using succinic anhydride and its effects on poly(butylene succinate) based composites, Cellulose. 26 (2019) 3167–3181. https://doi.org/10.1007/s10570-019-02292-5.

C.A. Harper, Handbook of Plastics, Elastomers, and Composites, Fourth Edition, 4th ed., McGraw-Hill Education, New York, 2002. https://www.accessengineeringlibrary.com/content/book/9780071384766.

C.C. Roach, Y.C. Lu, Analytical modeling of effect of interlayer on effective moduli of layered graphene-polymer nanocomposites, J. Mater. Sci. Technol. 33 (2017) 827–833. https://doi.org/10.1016/j.jmst.2017.03.007.

C.E.E. Armbrister, O.I. Okoli, S. Shanbhag, Micromechanics predictions for two-phased nanocomposites and three-phased multiscale composites: A review, J. Reinf. Plast. Compos. 34 (2015) 605–613. https://doi.org/10.1177/0731684415574297.

C.L. Morelli, M.N. Belgacem, M.C. Branciforti, M. C. B. Salon, J. Bras, R.E.S. Bretas, Nanocomposites of PBAT and cellulose nanocrystals modified by in situ polymerization and melt extrusion, Polym. Eng. Sci. 56 (2016) 1339–1348. https://doi.org/10.1002/pen.24367.

D. Fengel, G. Wegener, Wood: chemistry, ultrastructure, reactions, Walter de Gruyter, 2011. https://doi.org/10.1002/pol.1985.130231112

D. Jun, Z. Guomin, P. Mingzhu, Z. Leilei, L. Dagang, Z. Rui, Crystallization and mechanical properties of reinforced PHBV composites using melt compounding: Effect of CNCs and CNFs, Carbohydr. Polym. 168 (2017) 255–262. https://doi.org/https://doi.org/10.1016/j.carbpol.2017.03.076.

D. Musino, A.-C. Genix, E. Chauveau, T. Bizien, J. Oberdisse, Structural identification of percolation of nanoparticles, Nanoscale. 12 (2020) 3907–3915. https://doi.org/10.1039/c9nr09395h.

D. Zhu, Y. Ren, G. Liao, S. Jiang, F. Liu, J. Guo, G. Xu, Thermal and mechanical properties of polyamide 12/graphene nanoplatelets nanocomposites and parts fabricated by fused deposition modeling, J. Appl. Polym. Sci. 134 (2017) 1–13. https://doi.org/10.1002/app.45332.

D.-L. Shi, X.-Q. Feng, Y.Y. Huang, K.-C. Hwang, H. Gao, The effect of nanotube waviness and agglomeration on the elastic property of carbon nanotube-reinforced composites, J. Eng. Mater. Technol. Trans. ASME. 126 (2004) 250–257. https://doi.org/10.1115/1.1751182.

D.A. Osorio, E. Niinivaara, N.C. Jankovic, E.C. Demir, A. Benkaddour, V. Jarvis, C. Ayranci, M.T. McDermott, C.-F. De Lannoy, E.D. Cranston, Cellulose Nanocrystals Influence Polyamide 6 Crystal Structure, Spherulite Uniformity, and Mechanical Performance of Nanocomposite Films, ACS Appl. Polym. Mater. 3 (2021) 4673–4684. https://doi.org/10.1021/acsapm.1c00765.

D.J. Gardner, G.S. Oporto, R. Mills, M.A.S.A. Samir, Adhesion and surface issues in cellulose and nanocellulose, J. Adhes. Sci. Technol. 22 (2008) 545–567. https://doi.org/10.1163/156856108X295509.

D.J. Karras, Statistical methodology: II. Reliability and validity assessment in study design, part B, Acad. Emerg. Med. 4 (1997) 144–147. https://doi.org/10.1111/j.1553-2712.1997.tb03723.x.

D.L. Shi, X.Q. Feng, Y.Y. Huang, K.C. Hwang, H. Gao, The effect of nanotube waviness and agglomeration on the elastic property of carbon nanotube-reinforced composites, J. Eng. Mater. Technol. Trans. ASME. 126 (2004) 250–257. https://doi.org/10.1115/1.1751182.

D.M. Panaitescu, A.N. Frone, C. Nicolae, Micro- and nano-mechanical characterization of polyamide 11 and its composites containing cellulose nanofibers, Eur. Polym. J. 49 (2013) 3857–3866. https://doi.org/10.1016/j.eurpolymj.2013.09.031.

E. Esmizadeh, G. Naderi, M.H.R. Ghoreishy, Modification of Theoretical models to predict mechanical behavior of PVC/NBR/organoclay nanocomposites, J. Appl. Polym. Sci. 130 (2013) 3229–3239. https://doi.org/10.1002/app.39556.

E. Fortunati, D. Puglia, F. Luzi, C. Santulli, J.M. Kenny, L. Torre, Binary PVA bio-nanocomposites containing cellulose nanocrystals extracted from different natural sources: Part I, Carbohydr. Polym. 97 (2013) 825–836. https://doi.org/https://doi.org/10.1016/j.carbpol.2013.03.075.

E.C. Demir, A. Benkaddour, D. Aldrich, M.T. Mcdermott, C. Il Kim, C. Ayranci, A predictive model towards understanding the effect of reinforcement agglomeration on the stiffness of nanocomposites, J. Compos. Mater. (2022). https://doi.org/10.1177/00219983221076639.

E.P. Giannelis, Polymer Layered Silicate Nanocomposites, Adv. Mater. 8 (1996) 29–35. https://doi.org/10.1002/adma.19960080104.

E.T. Thostenson, C. Li, T.W. Chou, Nanocomposites in context, Compos. Sci. Technol. 65 (2005) 491–516. https://doi.org/10.1016/j.compscitech.2004.11.003.

F. Lin, Y. Xiang, H.S. Shen, Temperature dependent mechanical properties of graphene reinforced polymer nanocomposites – A molecular dynamics simulation, Compos. Part B Eng. 111 (2017) 261–269. https://doi.org/10.1016/j.compositesb.2016.12.004.

F. Nielsen, Hierarchical Clustering BT - Introduction to HPC with MPI for Data Science, in: F. Nielsen (Ed.), Springer International Publishing, Cham, 2016: pp. 195–211. https://doi.org/10.1007/978-3-319-21903-5_8.

F. Tanaka, T. Iwata, Estimation of the Elastic Modulus of Cellulose Crystal by Molecular Mechanics Simulation, Cellulose. 13 (2006) 509–517. https://doi.org/10.1007/s10570-006-9068-x.

F.G. Ronald, Principles of Composite Material Mechanics, CRC Press, 2016, https://doi.org/10.1201/b19626

F.H. Gojny, M.H.G. Wichmann, U. Köpke, B. Fiedler, K. Schulte, Carbon nanotube-reinforced epoxy-composites: Enhanced stiffness and fracture toughness at low nanotube content, Compos. Sci. Technol. 64 (2004) 2363–2371. https://doi.org/10.1016/j.compscitech.2004.04.002.

G. Postiglione, G. Natale, G. Griffini, M. Levi, S. Turri, Conductive 3D microstructures by direct 3D printing of polymer/carbon nanotube nanocomposites via liquid deposition modeling, Compos. Part A Appl. Sci. Manuf. 76 (2015) 110–114. https://doi.org/10.1016/j.compositesa.2015.05.014.

G. Wypych, PA-12 polyamide-12, Handb. Polym. 171 (2016) 246–250. https://doi.org/10.1016/b978-1-895198-92-8.50077-x.

G. Wypych, PA-6 polyamide-6, Handb. Polym. (2016) 215–220. https://doi.org/10.1016/b978-1-895198-92-8.50070-7.

G.M. Odegard, T.C. Clancy, T.S. Gates, Modeling of the mechanical properties of nanoparticle/polymer composites, Polymer (Guildf). 46 (2005) 553–562. https://doi.org/10.1016/j.polymer.2004.11.022.

G.P. Carman, K.L. Reifsnider, Micromechanics of short-fiber composites, Compos. Sci. Technol. 43 (1992) 137–146. https://doi.org/10.1016/0266-3538(92)90004-M.

G.P. Tandon, G.J. Weng, The effect of aspect ratio of inclusions on the elastic properties of unidirectionally aligned composites, Polym. Compos. 5 (1984) 327–333. https://doi.org/10.1002/pc.750050413.

G.R. Kasaliwal, S. Pegel, A. Göldel, P. Pötschke Petra, G. Heinrich, Analysis of agglomerate dispersion mechanisms of multiwalled carbon nanotubes during melt mixing in polycarbonate, Polymer (Guildf). 51 (2010) 2708–2720. https://doi.org/10.1016/j.polymer.2010.02.048.

G.S. Martynková, A. Slíva, G. Kratošová, K.Č. Barabaszová, S. Študentová, J. Klusák, S. Brožová, T. Dokoupil, S. Holešová, Polyamide 12 materials study of morpho-structural changes during laser sintering of 3d printing, Polymers (Basel). 13 (2021). https://doi.org/10.3390/polym13050810.

G.W. Melenka, J.P. Carey, Experimental analysis of diamond and regular tubular braided composites using three-dimensional digital image correlation, J. Compos. Mater. 51 (2017) 3887–3907. https://doi.org/10.1177/0021998317695418.

H. Kargarzadeh, M. Mariano, J. Huang, N. Lin, I. Ahmad, A. Dufresne, S. Thomas, Recent developments on nanocellulose reinforced polymer nanocomposites: A review, Polymer (Guildf). 132 (2017) 368–393. https://doi.org/https://doi.org/10.1016/j.polymer.2017.09.043.

H. Kim, T. Fernando, M. Li, Y. Lin, T.L.B. Tseng, Fabrication and characterization of 3D printed BaTiO3/PVDF nanocomposites, J. Compos. Mater. 52 (2018) 197–206. https://doi.org/10.1177/0021998317704709.

H. Liu, T.J. Webster, Enhanced biological and mechanical properties of well-dispersed nanophase ceramics in polymer composites: From 2D to 3D printed structures, Mater. Sci. Eng. C. 31 (2011) 77–89. https://doi.org/10.1016/j.msec.2010.07.013.

H. Sojoudiasli, M.-C. Heuzey, P.J. Carreau, Mechanical and morphological properties of cellulose nanocrystal-polypropylene composites, Polym. Compos. 39 (2018) 3605–3617. https://doi.org/10.1002/pc.24383.

H. Yousefian, D. Rodrigue, Effect of nanocrystalline cellulose on morphological, thermal, and mechanical properties of Nylon 6 composites, Polym. Compos. 37 (2016) 1473–1479. https://doi.org/10.1002/pc.23316.

H.-Y. Yu, Z.-Y. Qin, C.-F. Yan, J.-M. Yao, Green Nanocomposites Based on Functionalized Cellulose Nanocrystals: A Study on the Relationship between Interfacial Interaction and Property Enhancement, ACS Sustain. Chem. Eng. 2 (2014) 875–886. https://doi.org/10.1021/sc400499g.

H.S. Khare, D.L. Burris, A quantitative method for measuring nanocomposite dispersion, Polymer (Guildf). 51 (2010) 719–729. https://doi.org/https://doi.org/10.1016/j.polymer.2009.12.031.

H.W. Wang, H.W. Zhou, R.D. Peng, L. Mishnaevsky, Nanoreinforced polymer composites: 3D FEM modeling with effective interface concept, Compos. Sci. Technol. 71 (2011) 980–988. https://doi.org/10.1016/j.compscitech.2011.03.003.

I. Taha, Y.F. Abdin, Modeling of strength and stiffness of short randomly oriented glass fiber—polypropylene composites, J. Compos. Mater. 45 (2011) 1805–1821. https://doi.org/10.1177/0021998310389089.

J. Ha, Y. Song, N. Song, J.S. Yun, D. Lee, Designing an interpenetrating network of silane-functionalized nanocomposites for enhanced particle dispersity and interfacial bonding strength, Ceram. Int. 48 (2022) 1827–1835. https://doi.org/10.1016/j.ceramint.2021.09.264.

J. Hwang, T. Yoon, S.H. Jin, J. Lee, T.-S. Kim, S.H. Hong, S. Jeon, Enhanced mechanical properties of graphene/copper nanocomposites using a molecular-level mixing process, Adv. Mater. 25 (2013) 6724–6729. https://doi.org/10.1002/adma.201302495.

J. Li, Z. Song, D. Li, S. Shang, Y. Guo, Cotton cellulose nanofiber-reinforced high density polyethylene composites prepared with two different pretreatment methods, Ind. Crops Prod. 59 (2014) 318–328. https://doi.org/https://doi.org/10.1016/j.indcrop.2014.05.033.

J. Liu, Y. Gao, D. Cao, L. Zhang, Z. Guo, Nanoparticle Dispersion and Aggregation in Polymer Nanocomposites: Insights from Molecular Dynamics Simulation, Langmuir. 27 (2011) 7926–7933. https://doi.org/10.1021/la201073m.

J. Peng, P.J. Walsh, R.C. Sabo, L.-S. Turng, C.M. Clemons, Water-assisted compounding of cellulose nanocrystals into polyamide 6 for use as a nucleating agent for microcellular foaming, Polymer (Guildf). 84 (2016) 158–166. https://doi.org/10.1016/j.polymer.2015.12.050.

J. Pepin, V. Gaucher, J.M. Lefebvre, A. Stroeks, Biaxial stretching behavior as a probe of H-bond organization in semi-crystalline polyamides, Polymer (Guildf). 101 (2016) 217–224. https://doi.org/10.1016/j.polymer.2016.08.078.

J. Sapkota, A. Gooneie, A. Shirole, J.C. Martinez Garcia, A refined model for the mechanical properties of polymer composites with nanorods having different length distributions, J. Appl. Polym. Sci. 134 (2017). https://doi.org/10.1002/app.45279.

J. Sapkota, J.C. Natterodt, A. Shirole, E.J. Foster, C. Weder, Fabrication and Properties of Polyethylene/Cellulose Nanocrystal Composites, Macromol. Mater. Eng. 302 (2017) 1600300. https://doi.org/10.1002/mame.201600300.

J. Sauvola, M. Pietikäinen, Adaptive document image binarization, Pattern Recognit. 33 (2000) 225–236. https://doi.org/10.1016/S0031-3203(99)00055-2.

J. Segurado, C. González, J. LLorca, A numerical investigation of the effect of particle clustering on the mechanical properties of composites, Acta Mater. 51 (2003) 2355–2369. https://doi.org/10.1016/S1359-6454(03)00043-0.

J. Shojaeiarani, D. Bajwa, Functionalized cellulose nanocrystals for improving the mechanical properties of poly(lactic acid), in: ASME Int. Mech. Eng. Congr. Expo. Proc., Department of Mechanical Engineering, North Dakota State University, Fargo, ND, United States, 2018. https://doi.org/10.1115/IMECE2018-87691.

J. Shojaeiarani, D.S. Bajwa, K. Hartman, Esterified cellulose nanocrystals as reinforcement in poly(lactic acid) nanocomposites, Cellulose. 26 (2019) 2349–2362. https://doi.org/10.1007/s10570-018-02237-4.

J. Shojaeiarani, D.S. Bajwa, N.M. Stark, Spin-coating: A new approach for improving dispersion of cellulose nanocrystals and mechanical properties of poly (lactic acid) composites, Carbohydr. Polym. 190 (2018) 139–147. https://doi.org/https://doi.org/10.1016/j.carbpol.2018.02.069.

J. Vera-Agullo, A. Glória-Pereira, H. Varela-Rizo, J.L. Gonzalez, I. Martin-Gullon, Comparative study of the dispersion and functional properties of multiwall carbon nanotubes and helical-ribbon carbon nanofibers in polyester nanocomposites, Compos. Sci. Technol. 69 (2009) 1521–1532. https://doi.org/https://doi.org/10.1016/j.compscitech.2008.11.032.

J.-G. Gwon, H.-J. Cho, D. Lee, D.-H. Choi, S. Lee, Q. Wu, S.-Y. Lee, Physicochemical and Mechanical Properties of Polypropylene-cellulose Nanocrystal Nanocomposites: Effects of Manufacturing Process and Chemical Grafting, Bioresour. Vol 13, No 1. (2018). http://ojs.cnr.ncsu.edu/index.php/BioRes/article/view/BioRes_13_1_1619_Gwon_Polypropylene_Nanocrystal_Nanocomposites_Chemical_Grafting/5839.

J.-G. Gwon, H.-J. Cho, S.-J. Chun, S. Lee, Q. Wu, S.-Y. Lee, Physiochemical, optical and mechanical properties of poly(lactic acid) nanocomposites filled with toluene diisocyanate grafted cellulose nanocrystals, RSC Adv. 6 (2016) 9438–9445. https://doi.org/10.1039/c5ra26337a.

J.-J. Luo, I.M. Daniel, Characterization and modeling of mechanical behavior of polymer/clay nanocomposites, Compos. Sci. Technol. 63 (2003) 1607–1616. https://doi.org/https://doi.org/10.1016/S0266-3538(03)00060-5.

J.B. Hooper, K.S. Schweizer, Contact Aggregation, Bridging, and Steric Stabilization in Dense Polymer−Particle Mixtures, Macromolecules. 38 (2005) 8858–8869. https://doi.org/10.1021/ma051318k.

J.C.H. Affdl, J.L. Kardos, The Halpin-Tsai equations: A review, Polym. Eng. Sci. 16 (1976) 344–352. https://doi.org/10.1002/pen.760160512.

J.D. Eshelby, R.E. Peierls, The determination of the elastic field of an ellipsoidal inclusion, and related problems, Proc. R. Soc. London. Ser. A. Math. Phys. Sci. 241 (1957) 376–396. https://doi.org/10.1098/rspa.1957.0133.

J.H.D. Foard, D. Rollason, A.N. Thite, C. Bell, Polymer composite Belleville springs for an automotive application, Compos. Struct. 221 (2019) 110891. https://doi.org/10.1016/j.compstruct.2019.04.063.

J.K.W. Sandler, S. Pegel, M. Cadek, F. Gojny, M. Van Es, J. Lohmar, W.J. Blau, K. Schulte, A.H. Windle, M.S.P. Shaffer, A comparative study of melt spun polyamide-12 fibres reinforced with carbon nanotubes and nanofibres, Polymer (Guildf). 45 (2004) 2001–2015. https://doi.org/10.1016/j.polymer.2004.01.023.

J.R. Potts, D.R. Dreyer, C.W. Bielawski, R.S. Ruoff, Graphene-based polymer nanocomposites, Polymer (Guildf). 52 (2011) 5–25. https://doi.org/10.1016/j.polymer.2010.11.042.

J.W. Leenslag, A.J. Pennings, R.R.M. Bos, F.R. Rozema, G. Boering, Resorbable materials of poly(l-lactide). VII. In vivo and in vitro degradation, Biomaterials. 8 (1987) 311–314. https://doi.org/10.1016/0142-9612(87)90121-9.

K. Baek, H. Shin, T. Yoo, M. Cho, Two-step multiscale homogenization for mechanical behaviour of polymeric nanocomposites with nanoparticulate agglomerations, Compos. Sci. Technol. 179 (2019) 97–105. https://doi.org/https://doi.org/10.1016/j.compscitech.2019.05.006.

K. Hbaieb, Q.X. Wang, Y.H.J. Chia, B. Cotterell, Modelling stiffness of polymer/clay nanocomposites, Polymer (Guildf). 48 (2007) 901–909. https://doi.org/10.1016/j.polymer.2006.11.062.

K. Kim, J. Park, J. hoon Suh, M. Kim, Y. Jeong, I. Park, 3D printing of multiaxial force sensors using carbon nanotube (CNT)/thermoplastic polyurethane (TPU) filaments, Sensors Actuators, A Phys. 263 (2017) 493–500. https://doi.org/10.1016/j.sna.2017.07.020.

K. Oksman, Y. Aitomäki, A.P. Mathew, G. Siqueira, Q. Zhou, S. Butylina, S. Tanpichai, X. Zhou, S. Hooshmand, Review of the recent developments in cellulose nanocomposite processing, Compos. Part A Appl. Sci. Manuf. 83 (2016) 2–18. https://doi.org/10.1016/j.compositesa.2015.10.041.

K. Tashiro, M. Kobayashi, Theoretical evaluation of three-dimensional elastic constants of native and regenerated celluloses: role of hydrogen bonds, Polymer (Guildf). 32 (1991) 1516–1526. https://doi.org/https://doi.org/10.1016/0032-3861(91)90435-L.

K.-T. Lau, M. Chipara, H.-Y. Ling, D. Hui, On the effective elastic moduli of carbon nanotubes for nanocomposite structures, Compos. Part B Eng. 35 (2004) 95–101. https://doi.org/https://doi.org/10.1016/j.compositesb.2003.08.008.

K.M. Cantor, P. Watts, Part I : Plastics , Elastomeric and Nanocomposite Materials, Appl. Plast. Eng. Handb. (2011).

K.N.M. Amin, N. Amiralian, P.K. Annamalai, G. Edwards, C. Chaleat, D.J. Martin, Scalable processing of thermoplastic polyurethane nanocomposites toughened with nanocellulose, Chem. Eng. J. 302 (2016) 406–416. https://doi.org/10.1016/j.cej.2016.05.067.

L. Cao, C. Liu, D. Zou, S. Zhang, Y. Chen, Using cellulose nanocrystals as sustainable additive to enhance mechanical and shape memory properties of PLA/ENR thermoplastic vulcanizates, Carbohydr. Polym. 230 (2020) 115618. https://doi.org/https://doi.org/10.1016/j.carbpol.2019.115618.

L. Hui, R.C. Smith, X. Wang, J.K. Nelson, L.S. Schadler, Quantification of Particulate Mixing in Nanocomposites, in: 2008 Annu. Rep. Conf. Electr. Insul. Dielectr. Phenom., 2008: pp. 317–320. https://doi.org/10.1109/CEIDP.2008.4772831.

L. Jiang, E. Morelius, J. Zhang, M. Wolcott, J. Holbery, Study of the Poly(3-hydroxybutyrate-co-3-hydroxyvalerate)/Cellulose Nanowhisker Composites Prepared by Solution Casting and Melt Processing, J. Compos. Mater. 42 (2008) 2629–2645. https://doi.org/10.1177/0021998308096327.

L. Li, M.H.J. Koch, W.H. De Jeu, Crystalline structure and morphology in nylon-12: A small- and wide-angle X-ray scattering study, Macromolecules. 36 (2003) 1626–1632. https://doi.org/10.1021/ma025732l.

L. Rokach, O. Maimon, Clustering Methods BT - Data Mining and Knowledge Discovery Handbook, in: O. Maimon, L. Rokach (Eds.), Springer US, Boston, MA, 2005: pp. 321–352. https://doi.org/10.1007/0-387-25465-X_15.

L.M. Hamming, R. Qiao, P.B. Messersmith, L. Catherine Brinson, Effects of dispersion and interfacial modification on the macroscale properties of TiO2 polymer-matrix nanocomposites, Compos. Sci. Technol. 69 (2009) 1880–1886. https://doi.org/10.1016/j.compscitech.2009.04.005.

M. Amjadi, A. Pichitpajongkit, S. Lee, S. Ryu, I. Park, Highly Stretchable and Sensitive Strain Sensor Based on Silver Nanowire–Elastomer Nanocomposite, ACS Nano. 8 (2014) 5154–5163. https://doi.org/10.1021/nn501204t.

M. Arroyo, T. Belytschko, Continuum mechanics modeling and simulation of carbon nanotubes, Meccanica. 40 (2005) 455–469. https://doi.org/10.1007/s11012-005-2133-y.

M. Moradibistouni, B. Vale, N. Isaacs, Evaluating the use of polymers in residential buildings: Case study of a single storey detached house in New Zealand, J. Build. Eng. 32 (2020) 101517. https://doi.org/10.1016/j.jobe.2020.101517.

M. Ouederni, Polymers in textiles, INC, 2020. https://doi.org/10.1016/b978-0-12-816808-0.00010-x.

M. Pereda, N.E. Kissi, A. Dufresne, Extrusion of polysaccharide nanocrystal reinforced polymer nanocomposites through compatibilization with poly(ethylene oxide), ACS Appl. Mater. Interfaces. 6 (2014) 9365–9375. https://doi.org/10.1021/am501755p.

M. Rouway, M. Nachtane, M. Tarfaoui, N. Chakhchaoui, L.E. Omari, F. Fraija, O. Cherkaoui, Mechanical Properties of a Biocomposite Based on Carbon Nanotube and Graphene Nanoplatelet Reinforced Polymers: Analytical and Numerical Study, J. Compos. Sci. . 5 (2021). https://doi.org/10.3390/jcs5090234.

M. Yourdkhani, P. Hubert, Quantitative Dispersion Analysis of Inclusions in Polymer Composites, ACS Appl. Mater. Interfaces. 5 (2013) 35–41. https://doi.org/10.1021/am301459q.

M.A. Ashraf, W. Peng, Y. Zare, K.Y. Rhee, Effects of Size and Aggregation/Agglomeration of Nanoparticles on the Interfacial/Interphase Properties and Tensile Strength of Polymer Nanocomposites, Nanoscale Res. Lett. 13 (2018) 214. https://doi.org/10.1186/s11671-018-2624-0.

M.A. Bhuiyan, R. V Pucha, K. Kalaitzidou, 3D RVE Models Able to Capture and Quantify the Dispersion, Agglomeration, and Orientation State of CNT in CNT/PP Nanocomposites, Front. Mater. 3 (2016) 2. https://doi.org/10.3389/fmats.2016.00002.

M.M. Khattab, N.A. Abdel-Hady, Y. Dahman, 21 - Cellulose nanocomposites: Opportunities, challenges, and applications, in: M. Jawaid, S. Boufi, A.K.B.T.-C.-R.N.C. H.P.S. (Eds.), Woodhead Publ. Ser. Compos. Sci. Eng., Woodhead Publishing, 2017: pp. 483–516. https://doi.org/https://doi.org/10.1016/B978-0-08-100957-4.00021-8.

M.M.J. Treacy, T.W. Ebbesen, J.M. Gibson, Exceptionally high Young's modulus observed for individual carbon nanotubes, Nature. 381 (1996) 678. https://doi.org/http://dx.doi.org/10.1038/381678a0.

M.N. Anglès, A. Dufresne, Plasticized starch/tunicin whiskers nanocomposites, Struct Anal Macromol. 33 (2000) 8344–8353, https://doi.org/10.1021/ma0008701.

M.R. Kamal, V. Khoshkava, Effect of cellulose nanocrystals (CNC) on rheological and mechanical properties and crystallization behavior of PLA/CNC nanocomposites, Carbohydr. Polym. 123 (2015) 105–114. https://doi.org/10.1016/j.carbpol.2015.01.012.

M.S. Laad, Polymers in sports, INC, 2020. https://doi.org/10.1016/b978-0-12-816808-0.00015-9.

M.S. Reid, M. Villalobos, E.D. Cranston, Benchmarking Cellulose Nanocrystals: From the Laboratory to Industrial Production, Langmuir. 33 (2017) 1583–1598. https://doi.org/10.1021/acs.langmuir.6b03765.

M.T. Postek, A. Vladár, J. Dagata, N. Farkas, B. Ming, R. Wagner, A. Raman, R.J. Moon, R. Sabo, T.H. Wegner, J. Beecher, Development of the metrology and imaging of cellulose nanocrystals, Meas. Sci. Technol. 22 (2011). https://doi.org/10.1088/0957-0233/22/2/024005.

M.Z. Rong, M.Q. Zhang, Y.X. Zheng, H.M. Zeng, R. Walter, K. Friedrich, Structure-property relationships of irradiation grafted nano-inorganic particle filled polypropylene composites, Polymer (Guildf). 42 (2001) 167–183. https://doi.org/10.1016/S0032-3861(00)00325-6.

N. Hu, H. Fukunaga, C. Lu, M. Kameyama, B. Yan, Prediction of Elastic Properties of Carbon Nanotube Reinforced Composites, Proc. Math. Phys. Eng. Sci. 461 (2005) 1685–1710. https://doi.org/10.1098/rspa.2004.1422

N. Lin, A. Dufresne, Physical and/or chemical compatibilization of extruded cellulose nanocrystal reinforced polystyrene nanocomposites, Macromolecules. 46 (2013) 5570–5583. https://doi.org/10.1021/ma4010154.

N. Ma, W. Liu, L. Ma, S. He, H. Liu, Z. Zhang, A. Sun, M. Huang, C. Zhu, Crystal transition and thermal behavior of Nylon 12, E-Polymers. 20 (2020) 346–352. https://doi.org/10.1515/epoly-2020-0039.

N. Mohan, P. Senthil, S. Vinodh, N. Jayanth, A review on composite materials and process parameters optimisation for the fused deposition modelling process, Virtual Phys. Prototyp. 12 (2017) 47–59. https://doi.org/10.1080/17452759.2016.1274490.

N. Phansalkar, S. More, A. Sabale, M. Joshi, Adaptive local thresholding for detection of nuclei in diversity stained cytology images, in: 2011 Int. Conf. Commun. Signal Process., 2011: pp. 218–220. https://doi.org/10.1109/ICCSP.2011.5739305.

N. Sheng, M.C. Boyce, D.M. Parks, G.C. Rutledge, J.I. Abes, R.E. Cohen, Multiscale micromechanical modeling of polymer/clay nanocomposites and the effective clay particle, Polymer (Guildf). 45 (2004) 487–506. https://doi.org/https://doi.org/10.1016/j.polymer.2003.10.100.

N.H. Inai, A.E. Lewandowska, O.R. Ghita, S.J. Eichhorn, Interfaces in polyethylene oxide modified cellulose nanocrystal - polyethylene matrix composites, Compos. Sci. Technol. 154 (2018) 128–135. https://doi.org/https://doi.org/10.1016/j.compscitech.2017.11.009.

N.S. Murthy, Hydrogen bonding, mobility, and structural transitions in aliphatic polyamides, J. Polym. Sci. Part B Polym. Phys. 44 (2006) 1763–1782. https://doi.org/https://doi.org/10.1002/polb.20833.

O. van den Berg, J.R. Capadona, C. Weder, Preparation of Homogeneous Dispersions of Tunicate Cellulose Whiskers in Organic Solvents, Biomacromolecules. 8 (2007) 1353–1357. https://doi.org/10.1021/bm061104q.

P. Chen, M. Tang, W. Zhu, L. Yang, S. Wen, C. Yan, Z. Ji, H. Nan, Y. Shi, Systematical mechanism of Polyamide-12 aging and its micro-structural evolution during laser sintering, Polym. Test. 67 (2018) 370–379. https://doi.org/10.1016/j.polymertesting.2018.03.035.

P.K. Valavala, G.M. Odegard, Modeling techniques for determination of mechanical properties of polymer nanocomposites, Rev. Adv. Mater. Sci. 9 (2005) 34–44, https: doi=10.1.1.543.5381.

P.M. Visakh, S. Thomas, K. Oksman, A.P. Mathew, Cellulose nanofibres and cellulose nanowhiskers based natural rubber composites: Diffusion, sorption, and permeation of aromatic organic solvents, J. Appl. Polym. Sci. 124 (2012) 1614–1623. https://doi.org/10.1002/app.35176.

R. Guzmán de Villoria, A. Miravete, Mechanical model to evaluate the effect of the dispersion in nanocomposites, Acta Mater. 55 (2007) 3025–3031. https://doi.org/https://doi.org/10.1016/j.actamat.2007.01.007.

R. Hashemi Sanatgar, C. Campagne, V. Nierstrasz, Investigation of the adhesion properties of direct 3D printing of polymers and nanocomposites on textiles: Effect of FDM printing process parameters, Appl. Surf. Sci. 403 (2017) 551–563. https://doi.org/10.1016/j.apsusc.2017.01.112.

R. Jones, Mechanics Of Composite Materials, in: 2nd ed., CRC Press, Boca Raton, 1999. https://doi.org/10.1201/9781498711067.

R. Socher, B. Krause, M.T. Müller, R. Boldt, P. Pötschke, The influence of matrix viscosity on MWCNT dispersion and electrical properties in different thermoplastic nanocomposites, Polymer (Guildf). 53 (2012) 495–504. https://doi.org/https://doi.org/10.1016/j.polymer.2011.12.019.

R.C. Bernardi, M.C.R. Melo, K. Schulten, Enhanced sampling techniques in molecular dynamics simulations of biological systems, Biochim. Biophys. Acta - Gen. Subj. 1850 (2015) 872–877. https://doi.org/10.1016/j.bbagen.2014.10.019.

R.P. Singh, M. Zhang, D. Chan, Toughening of a brittle thermosetting polymer : Effects of reinforcement, J. Mater. Sci. 37 (2002) 781–788, https://doi.org/10.1023/A:1013844015493.

S. Aitha, N. Vasanthan, Effect of cellulose nanocrystals on crystallization, morphology and phase transition of polyamide 6, Compos. Interfaces. (2019). https://doi.org/10.1080/09276440.2019.1637213.

S. Azizi, R. Mohamad, Mechanical and barrier properties of kappa-carrageenan/cellulose nanocrystals bio-nanocomposite films, in: IOP Conf. Ser. Mater. Sci. Eng., Department of Bioprocess Technology, Bioprocessing and Biomanufacturing Research Centre, Faculty of Biotechnology and Biomolecular Sciences, Universiti Putra Malaysia, Selangor, 43400, Malaysia, 2018. https://doi.org/10.1088/1757-899X/368/1/012013.

S. Dinesh Kumar, K. Venkadeshwaran, M.K. Aravindan, Fused deposition modelling of PLA reinforced with cellulose nanocrystals, Mater. Today Proc. 33 (2020) 868–875. https://doi.org/10.1016/j.matpr.2020.06.404.

S. Dul, B.J.A. Gutierrez, A. Pegoretti, J. Alvarez-Quintana, L. Fambri, 3D printing of ABS Nanocomposites. Comparison of processing and effects of multi-wall and single-wall carbon nanotubes on thermal, mechanical and electrical properties, J. Mater. Sci. Technol. 121 (2022) 52–66. https://doi.org/10.1016/j.jmst.2021.11.064.

S. Fu, Z. Sun, P. Huang, Y. Li, N. Hu, Some basic aspects of polymer nanocomposites: A critical review, Nano Mater. Sci. 1 (2019) 2–30. https://doi.org/10.1016/j.nanoms.2019.02.006.

S. Geng, M.M.-U. Haque, K. Oksman, Crosslinked poly(vinyl acetate) (PVAc) reinforced with cellulose nanocrystals (CNC): Structure and mechanical properties, Compos. Sci. Technol. 126 (2016) 35–42. https://doi.org/https://doi.org/10.1016/j.compscitech.2016.02.013.

S. Gogolewski, K. Czerntawska, M. Gastorek, Effect of annealing on thermal properties and crystalline structure of polyamides. Nylon 12 (polylaurolactam), Colloid Polym. Sci. 258 (1980) 1130–1136. https://doi.org/10.1007/BF01382456.

S. Malmir, B. Montero, M. Rico, L. Barral, R. Bouza, Y. Farrag, PHBV/CNC bionanocomposites processed by extrusion: Structural characterization and properties, Polym. Compos. 40 (2019) E275–E284. https://doi.org/10.1002/pc.24634.

S. Pegel, P. Pötschke, G. Petzold, I. Alig, S.M. Dudkin, D. Lellinger, Dispersion, agglomeration, and network formation of multiwalled carbon nanotubes in polycarbonate melts, Polymer (Guildf). 49 (2008) 974–984. https://doi.org/10.1016/j.polymer.2007.12.024.

S.-Y. Fu, X.-Q. Feng, B. Lauke, Y.-W. Mai, Effects of particle size, particle/matrix interface adhesion and particle loading on mechanical properties of particulate–polymer composites, Compos. Part B Eng. 39 (2008) 933–961. https://doi.org/https://doi.org/10.1016/j.compositesb.2008.01.002.

S.A. Begum, A.V. Rane, K. Kanny, Applications of compatibilized polymer blends in automobile industry, Elsevier Inc., 2019. https://doi.org/10.1016/B978-0-12-816006-0.00020-7.

S.C. Ligon, R. Liska, J. Stampfl, M. Gurr, R. Mülhaupt, Polymers for 3D Printing and Customized Additive Manufacturing, Chem. Rev. 117 (2017) 10212–10290. https://doi.org/10.1021/acs.chemrev.7b00074.

S.D. Purohit, R. Bhaskar, H. Singh, I. Yadav, M.K. Gupta, N.C. Mishra, Development of a nanocomposite scaffold of gelatin–alginate–graphene oxide for bone tissue engineering, Int. J. Biol. Macromol. 133 (2019) 592–602. https://doi.org/https://doi.org/10.1016/j.ijbiomac.2019.04.113.

S.G. Advani, C.L. Tucker, The Use of Tensors to Describe and Predict Fiber Orientation in Short Fiber Composites, J. Rheol. (N. Y. N. Y). 31 (1987) 751–784. https://doi.org/10.1122/1.549945.

S.H. Sung, Y. Chang, J. Han, Development of polylactic acid nanocomposite films reinforced with cellulose nanocrystals derived from coffee silverskin, Carbohydr. Polym. 169 (2017) 495–503. https://doi.org/https://doi.org/10.1016/j.carbpol.2017.04.037.

S.K. Rahimi, J.U. Otaigbe, The effects of the interface on microstructure and rheo-mechanical properties of polyamide 6/cellulose nanocrystal nanocomposites prepared by in-situ ring-opening polymerization and subsequent melt extrusion, Polym. (United Kingdom). 127 (2017) 269–285. https://doi.org/10.1016/j.polymer.2017.08.064.

S.P. Vinodhini, J.R. Xavier, Effect of graphene oxide wrapped functional silicon carbide on structural, surface protection, water repellent, and mechanical properties of epoxy matrix for automotive structural components, Colloids Surfaces A Physicochem. Eng. Asp. 639 (2022) 128300. https://doi.org/10.1016/j.colsurfa.2022.128300.

S.R. Bakshi, R.G. Batista, A. Agarwal, Quantification of carbon nanotube distribution and property correlation in nanocomposites, Compos. Part A Appl. Sci. Manuf. 40 (2009) 1311–1318. https://doi.org/https://doi.org/10.1016/j.compositesa.2009.06.004.

S.W. Ghori, R. Siakeng, M. Rasheed, N. Saba, M. Jawaid, The role of advanced polymer materials in aerospace, Elsevier Ltd, 2018. https://doi.org/10.1016/B978-0-08-102131-6.00002-5.

T. Ebeling, M. Paillet, R. Borsali, O. Diat, A. Dufresne, J.-Y. Cavaillé, H. Chanzy, Shear-induced orientation phenomena in suspensions of cellulose microcrystals, revealed by small angle X-ray scattering, Langmuir. 15 (1999) 6123–6126. https://doi.org/10.1021/la990046+.

T. Ebeling, M. Paillet, R. Borsali, O. Diat, A. Dufresne, J.-Y. Cavaillé, H. Chanzy, Shear-induced orientation phenomena in suspensions of cellulose microcrystals, revealed by small angle X-ray scattering, Langmuir. 15 (1999) 6123–6126. https://doi.org/10.1021/la990046+.

T. Glaskova, M. Zarrelli, A. Borisova, K. Timchenko, A. Aniskevich, M. Giordano, Method of quantitative analysis of filler dispersion in composite systems with spherical inclusions, Compos. Sci. Technol. 71 (2011) 1543–1549. https://doi.org/https://doi.org/10.1016/j.compscitech.2011.06.009.

T. Ishikawa, S. Nagai, N. Kasai, Thermal behavior of α nylon-12, J. Polym. Sci. Polym. Phys. Ed. 18 (1980) 1413–1419. https://doi.org/https://doi.org/10.1002/pol.1980.180180619.

T. Mori, K. Tanaka, Average stress in matrix and average elastic energy of materials with misfitting inclusions, Acta Metall. 21 (1973) 571–574. https://doi.org/https://doi.org/10.1016/0001-6160(73)90064-3.

T. Mura, Micromechanics of defects in solids, 2nd ed., Springer, Dordrecht, 1987. https://doi.org/https://doi.org/10.1007/978-94-009-3489-4.

T. Thorvaldsen, Modelling the elastic stiffness of nanocomposites using the Mori-Tanaka method, 2015. https://doi.org/9788246425559.

T. Villmow, B. Kretzschmar, P. Putschke, Influence of screw configuration, residence time, and specific mechanical energy in twin-screw extrusion of polycaprolactone/multi-walled carbon nanotube composites, Compos. Sci. Technol. 70 (2010) 2045–2055. https://doi.org/10.1016/j.compscitech.2010.07.021.

T.C. Mokhena, J.S. Sefadi, E.R. Sadiku, M.J. John, M.J. Mochane, A. Mtibe, Thermoplastic processing of PLA/cellulose nanomaterials composites, Polymers (Basel). 10 (2018). https://doi.org/10.3390/polym10121363.

T.D. Fornes, D.R. Paul, Modeling properties of nylon 6/clay nanocomposites using composite theories, Polymer (Guildf). 44 (2003) 4993–5013. https://doi.org/10.1016/S0032-3861(03)00471-3.

T.D. Ngo, A. Kashani, G. Imbalzano, K.T.Q. Nguyen, D. Hui, Additive manufacturing (3D printing): A review of materials, methods, applications and challenges, Compos. Part B Eng. 143 (2018) 172–196. https://doi.org/10.1016/j.compositesb.2018.02.012.

V. Anumandla, R.F. Gibson, A comprehensive closed form micromechanics model for estimating the elastic modulus of nanotube-reinforced composites, Compos. Part A Appl. Sci. Manuf. 37 (2006) 2178–2185. https://doi.org/https://doi.org/10.1016/j.compositesa.2005.09.016.

V. Francis, P.K. Jain, Experimental investigations on fused deposition modelling of polymer-layered silicate nanocomposite, Virtual Phys. Prototyp. 11 (2016) 109–121. https://doi.org/10.1080/17452759.2016.1172431.

V. Mirjalili, M. Yourdkhani, P. Hubert, Dispersion stability in carbon nanotube modified polymers and its effect on the fracture toughness, Nanotechnology. 23 (2012) 315701. https://doi.org/10.1088/0957-4484/23/31/315701.

W. Xu, X. Wang, N. Sandler, S. Willför, C. Xu, Three-Dimensional Printing of Wood-Derived Biopolymers: A Review Focused on Biomedical Applications, ACS Sustain. Chem. Eng. 6 (2018) 5663–5680. https://doi.org/10.1021/acssuschemeng.7b03924.

X. Chen, C. Gao, J. Jiang, Y. Wu, P. Zhu, G. Chen, 3D printed porous PLA/nHA composite scaffolds with enhanced osteogenesis and osteoconductivityin vivo for bone regeneration, Biomed. Mater. 14 (2019). https://doi.org/10.1088/1748-605X/ab388d.

X. Guan, B. Xu, J. Gong, Hierarchically architected polydopamine modified BaTiO3@P(VDF-TrFE) nanocomposite fiber mats for flexible piezoelectric nanogenerators and self-powered sensors, Nano Energy. 70 (2020) 104516. https://doi.org/10.1016/j.nanoen.2020.104516.

Y. Benveniste, A new approach to the application of Mori-Tanaka's theory in composite materials, Mech. Mater. 6 (1987) 147–157. https://doi.org/10.1016/0167-6636(87)90005-6.

Y. Chen, I.T. Garces, T. Tang, C. Ayranci, Cellulose nanocrystals reinforced shape memory polymer cardiovascular stent, Rapid Prototyp. J. 27 (2021) 37–44. https://doi.org/10.1108/RPJ-01-2020-0019.

Y. He, J. Zhu, W. Wang, H. Ni, Surface modification of cellulose nanocrystals with different acid anhydrides for improved dispersion in poly(butylene succinate), RSC Adv. 8 (2018) 38305–38314. https://doi.org/10.1039/c8ra07597b.

Y. Li, A.M. Waas, E.M. Arruda, A closed-form, hierarchical, multi-interphase model for compositesDerivation, verification and application to nanocomposites, J. Mech. Phys. Solids. 59 (2011) 43–63. https://doi.org/10.1016/j.jmps.2010.09.015.

Y. Lu, M.C. Biswas, Z. Guo, J.-W. Jeon, E.K. Wujcik, Recent developments in bio-monitoring via advanced polymer nanocomposite-based wearable strain sensors, Biosens. Bioelectron. 123 (2019) 167–177. https://doi.org/https://doi.org/10.1016/j.bios.2018.08.037.

Y. Peng, D.J. Gardner, Y. Han, Characterization of mechanical and morphological properties of cellulose reinforced polyamide 6 composites, Cellulose. 22 (2015) 3199–3215. https://doi.org/10.1007/s10570-015-0723-y.

Y. Wang, K.S. Chen, J. Mishler, S.C. Cho, X.C. Adroher, A review of polymer electrolyte membrane fuel cells: Technology, applications, and needs on fundamental research, Appl. Energy. 88 (2011) 981–1007. https://doi.org/10.1016/j.apenergy.2010.09.030.

Y. Wang, Z.M. Huang, Analytical micromechanics models for elastoplastic behavior of long fibrous composites: A critical review and comparative study, Materials (Basel). 11 (2018). https://doi.org/10.3390/ma11101919.

Y. Xia, M. Rubino, R. Auras, Interaction of nanoclay-reinforced packaging nanocomposites with food simulants and compost environments, 1st ed., Elsevier Inc., 2019. https://doi.org/10.1016/bs.afnr.2019.02.001.

Y. Zare, Study of nanoparticles aggregation/agglomeration in polymer particulate nanocomposites by mechanical properties, Compos. Part A Appl. Sci. Manuf. 84 (2016) 158–164. https://doi.org/10.1016/j.compositesa.2016.01.020.

Y. Zhu, S. Murali, W. Cai, X. Li, J.W. Suk, J.R. Potts, R.S. Ruoff, Graphene and Graphene Oxide: Synthesis, Properties, and Applications, Adv. Mater. 22 (2010) 3906–3924. https://doi.org/https://doi.org/10.1002/adma.201001068.

Y.J. Liu, X.L. Chen, Evaluations of the effective material properties of carbon nanotube-based composites using a nanoscale representative volume element, Mech. Mater. 35 (2003) 69–81. https://doi.org/https://doi.org/10.1016/S0167-6636(02)00200-4.

Z. Ouyang, H.-Y. Yu, M. Song, J. Zhu, D. Wang, Ultrasensitive and robust self-healing composite films with reinforcement of multi-branched cellulose nanocrystals, Compos. Sci. Technol. 198 (2020) 108300. https://doi.org/10.1016/j.compscitech.2020.108300.

Z.-M. Huang, Y.-Z. Zhang, M. Kotaki, S. Ramakrishna, A review on polymer nanofibers by electrospinning and their applications in nanocomposites, Compos. Sci. Technol. 63 (2003) 2223–2253. https://doi.org/https://doi.org/10.1016/S0266-3538(03)00178-7.

Z.P. Luo, J.H. Koo, Quantifying the dispersion of mixture microstructures, J. Microsc. 225 (2007) 118–125. https://doi.org/10.1111/j.1365-2818.2007.01722.x.

Z.P. Luo, J.H. Koo, Quantitative study of the dispersion degree in carbon nanofiber/polymer and carbon nanotube/polymer nanocomposites, Mater. Lett. 62 (2008) 3493–3496. https://doi.org/https://doi.org/10.1016/j.matlet.2008.03.010.

Z.P. Luo, J.H. Koo, Quantitative study of the dispersion degree in carbon nanofiber/polymer and carbon nanotube/polymer nanocomposites, Mater. Lett. 62 (2008) 3493–3496. https://doi.org/https://doi.org/10.1016/j.matlet.2008.03.010.

Z.T. Kier, A. Salvi, G. Theis, A.M. Waas, K. Shahwan, Estimating mechanical properties of 2D triaxially braided textile composites based on microstructure properties, Compos. Part B Eng. 68 (2015) 288–299. https://doi.org/10.1016/j.compositesb.2014.08.039.

Z.X. Khoo, J.E.M. Teoh, Y. Liu, C.K. Chua, S. Yang, J. An, K.F. Leong, W.Y. Yeong, 3D printing of smart materials: A review on recent progresses in 4D printing, Virtual Phys. Prototyp. 10 (2015) 103–122. https://doi.org/10.1080/17452759.2015.1097054.

Appendices

Appendices

A. The Copyright Permission related to Chapter 1

The copyright permission for Figure 1.2 is provided in this section.

CCC Marketplace™

This is a License Agreement between Eyup Can Demir ("User") and Copyright Clearance Center, Inc. ("CCC") on behalf of the Rightsholder identified in the order details below. The license consists of the order details, the Marketplace Order General Terms and Conditions below, and any Rightsholder Terms and Conditions which are included below.

All payments must be made in full to CCC in accordance with the Marketplace Order General Terms and Conditions below.

Order Date	09-Aug-2022	Type of Use	Republish in a thesis/dissertation
Order License ID	1256214-1		
ISSN	0957-0233	Publisher	IOP Publishing
		Portion	Image/photo/illustration

LICENSED CONTENT

Publication Title	Measurement Science and Technology	Rightsholder	IOP Publishing, Ltd
		Publication Type	Journal
Article Title	Development of the metrology and imaging of cellulose nanocrystals	Start Page	024005
		Issue	2
Author/Editor	Institute of Physics (Great Britain)	Volume	22
Date	01/01/1990		
Language	English		
Country	United Kingdom of Great Britain and Northern Ireland		

REQUEST DETAILS

Portion Type	Image/photo/illustration	Distribution	Worldwide
Number of images / photos / illustrations	1	Translation	Original language of publication
Format (select all that apply)	Print, Electronic	Copies for the disabled?	No
		Minor editing privileges?	No
Who will republish the content?	Academic institution	Incidental promotional use?	No
Duration of Use	Life of current edition	Currency	CAD
Lifetime Unit Quantity	Up to 499		
Rights Requested	Main product		

NEW WORK DETAILS

Title	Elastic Modulus Prediction of Polymer Nanocomposites: Production and Characterization of Cellulose Nanocrystals Polyamide Nanocomposites	Institution name	University of Alberta
		Expected presentation date	2022-09-15
Instructor name	Eyup Can Demir		

ADDITIONAL DETAILS

Order reference number	N/A	The requesting person / organization to appear on the license	Eyup Can Demir

REUSE CONTENT DETAILS

Title, description or numeric reference of the portion(s)	Figure 1. Structure of wood from the tree to the CNCs (after [2]). ML = middle lamellae between tracheids, P = primary cell wall, S1, S2, S3 = cell wall layers	Title of the article/chapter the portion is from	Development of the metrology and imaging of cellulose nanocrystals
		Author of portion(s)	Postek, Michael T; Vladár, András; Dagata, John; Farkas, Natalia; Ming, Bin; Wagner, Ryan; Raman, Arvind; Moon, Robert J; Sabo, Ronald; Wegner, Theodore H; Beecher, James
Editor of portion(s)	Postek, Michael T; Vladár, András; Dagata, John; Farkas, Natalia; Ming, Bin; Wagner, Ryan; Raman, Arvind; Moon, Robert J; Sabo, Ronald; Wegner, Theodore H; Beecher, James	Issue, if republishing an article from a serial	2
		Publication date of portion	2010-12-20
Volume of serial or monograph	22		
Page or page range of portion	024005		

RIGHTSHOLDER TERMS AND CONDITIONS

These special terms and conditions are in addition to the standard terms and conditions for CCC's Republication Service and, together with those standard terms and conditions, govern the use of the Works. As the User you will make all reasonable efforts to contact the author(s) of the article which the Work is to be reused from, to seek consent for your intended use. Contacting one author who is acting expressly as authorised agent for their co-author(s) is acceptable. User will reproduce the following wording prominently alongside the Work: the source of the Work, including author, article title, title of journal, volume number, issue number (if relevant), page range (or first page if this is the only information available) and date of first publication; and a link back to the article (via DOI); and if practicable, and IN ALL CASES for new works published under any of the Creative Commons licences, the words "© IOP Publishing. Reproduced with permission. All rights reserved" Without the express permission of the author(s) and the Rightsholder of the article from which the Work is to be reused, User shall not use it in any way which, in the opinion of the Rightsholder, could: (i) distort or alter the author(s)' original intention(s) and meaning; (ii) be prejudicial to the honour or reputation of the author(s); and/or (iii) imply endorsement by the author(s) and/or the Rightsholder. This licence does not apply to any article which is credited to another source and which does not have the copyright line '© IOP Publishing Ltd'. User must check the copyright line of the article from which the Work is to be reused to check that IOP Publishing Ltd has all the necessary rights to be able to grant permission. User is solely responsible for identifying and obtaining separate licences and permissions from the copyright owner for reuse of any such third party material/figures which the Rightsholder is not the copyright owner of. The Rightsholder shall not reimburse any fees which User pays for a republication license for

such third party content. This licence does not apply to any material/figure which is credited to another source in the Rightsholder's publication or has been obtained from a third party. User must check the Version of Record of the article from which the Work is to be reused, to check whether any of the material in the Work is third party material. Third party citations and/or copyright notices and/or permissions statements may not be included in any other version of the article from which the Work is to be reused and so cannot be relied upon by the User. User is solely responsible for identifying and obtaining separate licences and permissions from the copyright owner for reuse of any such third party material/figures where the Rightsholder is not the copyright owner. The Rightsholder shall not reimburse any fees which User pays for a republication license for such third party content. User and CCC acknowledge that the Rightsholder may, from time to time, make changes or additions to these special terms and conditions without express notification, provided that these shall not apply to permissions already secured and paid for by User prior to such change or addition. User acknowledges that the Rightsholder (which includes companies within its group and third parties for whom it publishes its titles) may make use of personal data collected through the service in the course of their business. If User is the author of the Work, User may automatically have the right to reuse it under the rights granted back when User transferred the copyright in the article to the Rightsholder. User should check the copyright form and the relevant author rights policy to check whether permission is required. If User is the author of the Work and does require permission for proposed reuse of the Work, User should select 'Author of requested content' as the Requestor Type. The Rightsholder shall not reimburse any fees which User pays for a republication license. If User is the author of the article which User wishes to reuse in User's thesis or dissertation, the republication licence covers the right to include the Version of Record of the article, provided it is not then shared or deposited online. User must include citation details. Where User wishes to share their thesis or dissertation online, they should remove the Version of Record before uploading it. User may include a Preprint or the Accepted Manuscript (after the embargo period) in the online version of the thesis or dissertation, provided they do so in accordance with the Rightsholder's policies on sharing Preprints or Accepted Manuscripts. User may need to obtain separate permission for any third party content included within the article. User must check this with the copyright owner of such third party content. Any online or commercial use of User's thesis or dissertation containing the article, including publication via ProQuest, would need to be expressly notified in writing to the Rightsholder at the time of request and would require separate written permission from the Rightsholder. As well as CCC, the Rightsholder shall have the right to bring any legal action that it deems necessary to enforce its rights should it consider that the Work infringes those rights in any way. For content reuse requests that qualify for permission under the STM Permissions Guidelines, which may be updated from time to time, the STM Permissions Guidelines supplement the terms and conditions contained in this license.

Marketplace Order General Terms and Conditions

The following terms and conditions ("General Terms"), together with any applicable Publisher Terms and Conditions, govern User's use of Works pursuant to the Licenses granted by Copyright Clearance Center, Inc. ("CCC") on behalf of the applicable Rightsholders of such Works through CCC's applicable Marketplace transactional licensing services (each, a "Service").

1) Definitions. For purposes of these General Terms, the following definitions apply:

"License" is the licensed use the User obtains via the Marketplace platform in a particular licensing transaction, as set forth in the Order Confirmation.

"Order Confirmation" is the confirmation CCC provides to the User at the conclusion of each Marketplace transaction. "Order Confirmation Terms" are additional terms set forth on specific Order Confirmations not set forth in the General Terms that can include terms applicable to a particular CCC transactional licensing service and/or any Rightsholder-specific terms.

"Rightsholder(s)" are the holders of copyright rights in the Works for which a User obtains licenses via the Marketplace platform, which are displayed on specific Order Confirmations.

"Terms" means the terms and conditions set forth in these General Terms and any additional Order Confirmation Terms collectively.

"User" or "you" is the person or entity making the use granted under the relevant License. Where the person accepting the Terms on behalf of a User is a freelancer or other third party who the User authorized to accept the General Terms on the User's behalf, such person shall be deemed jointly a User for purposes of such Terms.

"Work(s)" are the copyright protected works described in relevant Order Confirmations.

2) Description of Service. CCC's Marketplace enables Users to obtain Licenses to use one or more Works in accordance

with all relevant Terms. CCC grants Licenses as an agent on behalf of the copyright rightsholder identified in the relevant Order Confirmation.

3) Applicability of Terms. The Terms govern User's use of Works in connection with the relevant License. In the event of any conflict between General Terms and Order Confirmation Terms, the latter shall govern. User acknowledges that Rightsholders have complete discretion whether to grant any permission, and whether to place any limitations on any grant, and that CCC has no right to supersede or to modify any such discretionary act by a Rightsholder.

4) Representations; Acceptance. By using the Service, User represents and warrants that User has been duly authorized by the User to accept, and hereby does accept, all Terms.

5) Scope of License; Limitations and Obligations. All Works and all rights therein, including copyright rights, remain the sole and exclusive property of the Rightsholder. The License provides only those rights expressly set forth in the terms and conveys no other rights in any Works

6) General Payment Terms. User may pay at time of checkout by credit card or choose to be invoiced. If the User chooses to be invoiced, the User shall: (i) remit payments in the manner identified on specific invoices, (ii) unless otherwise specifically stated in an Order Confirmation or separate written agreement, Users shall remit payments upon receipt of the relevant invoice from CCC, either by delivery or notification of availability of the invoice via the Marketplace platform, and (iii) if the User does not pay the invoice within 30 days of receipt, the User may incur a service charge of 1.5% per month or the maximum rate allowed by applicable law, whichever is less. While User may exercise the rights in the License immediately upon receiving the Order Confirmation, the License is automatically revoked and is null and void, as if it had never been issued, if CCC does not receive complete payment on a timely basis.

7) General Limits on Use. Unless otherwise provided in the Order Confirmation, any grant of rights to User (i) involves only the rights set forth in the Terms and does not include subsequent or additional uses, (ii) is non-exclusive and non-transferable, and (iii) is subject to any and all limitations and restrictions (such as, but not limited to, limitations on duration of use or circulation) included in the Terms. Upon completion of the licensed use as set forth in the Order Confirmation, User shall either secure a new permission for further use of the Work(s) or immediately cease any new use of the Work(s) and shall render inaccessible (such as by deleting or by removing or severing links or other locators) any further copies of the Work. User may only make alterations to the Work if and as expressly set forth in the Order Confirmation. No Work may be used in any way that is defamatory, violates the rights of third parties (including such third parties' rights of copyright, privacy, publicity, or other tangible or intangible property), or is otherwise illegal, sexually explicit, or obscene. In addition, User may not conjoin a Work with any other material that may result in damage to the reputation of the Rightsholder. User agrees to inform CCC if it becomes aware of any infringement of any rights in a Work and to cooperate with any reasonable request of CCC or the Rightsholder in connection therewith.

8) Third Party Materials. In the event that the material for which a License is sought includes third party materials (such as photographs, illustrations, graphs, inserts and similar materials) that are identified in such material as having been used by permission (or a similar indicator), User is responsible for identifying, and seeking separate licenses (under this Service, if available, or otherwise) for any of such third party materials; without a separate license, User may not use such third party materials via the License.

9) Copyright Notice. Use of proper copyright notice for a Work is required as a condition of any License granted under the Service. Unless otherwise provided in the Order Confirmation, a proper copyright notice will read substantially as follows: "Used with permission of [Rightsholder's name], from [Work's title, author, volume, edition number and year of copyright]; permission conveyed through Copyright Clearance Center, Inc." Such notice must be provided in a reasonably legible font size and must be placed either on a cover page or in another location that any person, upon gaining access to the material which is the subject of a permission, shall see, or in the case of republication Licenses, immediately adjacent to the Work as used (for example, as part of a by-line or footnote) or in the place where substantially all other credits or notices for the new work containing the republished Work are located. Failure to include the required notice results in loss to the Rightsholder and CCC, and the User shall be liable to pay liquidated damages for each such failure equal to twice the use fee specified in the Order Confirmation, in addition to the use fee itself and any other fees and charges specified.

10) Indemnity. User hereby indemnifies and agrees to defend the Rightsholder and CCC, and their respective employees and directors, against all claims, liability, damages, costs, and expenses, including legal fees and expenses, arising out of any use of a Work beyond the scope of the rights granted herein and in the Order Confirmation, or any use of a Work which has been altered in any unauthorized way by User, including claims of defamation or infringement of rights of copyright, publicity, privacy, or other tangible or intangible property.

11) Limitation of Liability. UNDER NO CIRCUMSTANCES WILL CCC OR THE RIGHTSHOLDER BE LIABLE FOR ANY DIRECT, INDIRECT, CONSEQUENTIAL, OR INCIDENTAL DAMAGES (INCLUDING WITHOUT LIMITATION DAMAGES FOR LOSS OF BUSINESS PROFITS OR INFORMATION, OR FOR BUSINESS INTERRUPTION) ARISING OUT OF THE USE OR INABILITY TO USE A WORK, EVEN IF ONE OR BOTH OF THEM HAS BEEN ADVISED OF THE POSSIBILITY OF SUCH DAMAGES. In any event, the total liability of the Rightsholder and CCC (including their respective employees and directors) shall not exceed the total amount actually paid by User for the relevant License. User assumes full liability for the actions and omissions of its principals, employees, agents, affiliates, successors, and assigns.

12) Limited Warranties. THE WORK(S) AND RIGHT(S) ARE PROVIDED "AS IS." CCC HAS THE RIGHT TO GRANT TO USER THE RIGHTS GRANTED IN THE ORDER CONFIRMATION DOCUMENT. CCC AND THE RIGHTSHOLDER DISCLAIM ALL OTHER WARRANTIES RELATING TO THE WORK(S) AND RIGHT(S), EITHER EXPRESS OR IMPLIED, INCLUDING WITHOUT LIMITATION IMPLIED WARRANTIES OF MERCHANTABILITY OR FITNESS FOR A PARTICULAR PURPOSE. ADDITIONAL RIGHTS MAY BE REQUIRED TO USE ILLUSTRATIONS, GRAPHS, PHOTOGRAPHS, ABSTRACTS, INSERTS, OR OTHER PORTIONS OF THE WORK (AS OPPOSED TO THE ENTIRE WORK) IN A MANNER CONTEMPLATED BY USER; USER UNDERSTANDS AND AGREES THAT NEITHER CCC NOR THE RIGHTSHOLDER MAY HAVE SUCH ADDITIONAL RIGHTS TO GRANT.

13) Effect of Breach. Any failure by User to pay any amount when due, or any use by User of a Work beyond the scope of the License set forth in the Order Confirmation and/or the Terms, shall be a material breach of such License. Any breach not cured within 10 days of written notice thereof shall result in immediate termination of such License without further notice. Any unauthorized (but licensable) use of a Work that is terminated immediately upon notice thereof may be liquidated by payment of the Rightsholder's ordinary license price therefor; any unauthorized (and unlicensable) use that is not terminated immediately for any reason (including, for example, because materials containing the Work cannot reasonably be recalled) will be subject to all remedies available at law or in equity, but in no event to a payment of less than three times the Rightsholder's ordinary license price for the most closely analogous licensable use plus Rightsholder's and/or CCC's costs and expenses incurred in collecting such payment.

14) Additional Terms for Specific Products and Services. If a User is making one of the uses described in this Section 14, the additional terms and conditions apply:

a) *Print Uses of Academic Course Content and Materials (photocopies for academic coursepacks or classroom handouts).* For photocopies for academic coursepacks or classroom handouts the following additional terms apply:

i) The copies and anthologies created under this License may be made and assembled by faculty members individually or at their request by on-campus bookstores or copy centers, or by off-campus copy shops and other similar entities.

ii) No License granted shall in any way: (i) include any right by User to create a substantively non-identical copy of the Work or to edit or in any other way modify the Work (except by means of deleting material immediately preceding or following the entire portion of the Work copied) (ii) permit "publishing ventures" where any particular anthology would be systematically marketed at multiple institutions.

iii) Subject to any Publisher Terms (and notwithstanding any apparent contradiction in the Order Confirmation arising from data provided by User), any use authorized under the academic pay-per-use service is limited as follows:

A) any License granted shall apply to only one class (bearing a unique identifier as assigned by the institution, and thereby including all sections or other subparts of the class) at one institution;

B) use is limited to not more than 25% of the text of a book or of the items in a published collection of essays, poems or articles;

C) use is limited to no more than the greater of (a) 25% of the text of an issue of a journal or other periodical or (b) two articles from such an issue;

D) no User may sell or distribute any particular anthology, whether photocopied or electronic, at more than one institution of learning;

E) in the case of a photocopy permission, no materials may be entered into electronic memory by User except in order to produce an identical copy of a Work before or during the academic term (or analogous period) as to which any particular permission is granted. In the event that User shall choose to retain materials that are the subject of a photocopy permission in electronic memory for purposes of producing

identical copies more than one day after such retention (but still within the scope of any permission granted), User must notify CCC of such fact in the applicable permission request and such retention shall constitute one copy actually sold for purposes of calculating permission fees due; and

F) any permission granted shall expire at the end of the class. No permission granted shall in any way include any right by User to create a substantively non-identical copy of the Work or to edit or in any other way modify the Work (except by means of deleting material immediately preceding or following the entire portion of the Work copied).

iv) Books and Records; Right to Audit. As to each permission granted under the academic pay-per-use Service, User shall maintain for at least four full calendar years books and records sufficient for CCC to determine the numbers of copies made by User under such permission. CCC and any representatives it may designate shall have the right to audit such books and records at any time during User's ordinary business hours, upon two days' prior notice. If any such audit shall determine that User shall have underpaid for, or underreported, any photocopies sold or by three percent (3%) or more, then User shall bear all the costs of any such audit; otherwise, CCC shall bear the costs of any such audit. Any amount determined by such audit to have been underpaid by User shall immediately be paid to CCC by User, together with interest thereon at the rate of 10% per annum from the date such amount was originally due. The provisions of this paragraph shall survive the termination of this License for any reason.

b) *Digital Pay-Per-Uses of Academic Course Content and Materials (e-coursepacks, electronic reserves, learning management systems, academic institution intranets).* For uses in e-coursepacks, posts in electronic reserves, posts in learning management systems, or posts on academic institution intranets, the following additional terms apply:

i) The pay-per-uses subject to this Section 14(b) include:

A) Posting e-reserves, course management systems, e-coursepacks for text-based content, which grants authorizations to import requested material in electronic format, and allows electronic access to this material to members of a designated college or university class, under the direction of an instructor designated by the college or university, accessible only under appropriate electronic controls (e.g., password);

B) Posting e-reserves, course management systems, e-coursepacks for material consisting of photographs or other still images not embedded in text, which grants not only the authorizations described in Section 14(b)(i)(A) above, but also the following authorization: to include the requested material in course materials for use consistent with Section 14(b)(i)(A) above, including any necessary resizing, reformatting or modification of the resolution of such requested material (provided that such modification does not alter the underlying editorial content or meaning of the requested material, and provided that the resulting modified content is used solely within the scope of, and in a manner consistent with, the particular authorization described in the Order Confirmation and the Terms), but not including any other form of manipulation, alteration or editing of the requested material;

C) Posting e-reserves, course management systems, e-coursepacks or other academic distribution for audiovisual content, which grants not only the authorizations described in Section 14(b)(i)(A) above, but also the following authorizations: (i) to include the requested material in course materials for use consistent with Section 14(b)(i)(A) above; (ii) to display and perform the requested material to such members of such class in the physical classroom or remotely by means of streaming media or other video formats; and (iii) to "clip" or reformat the requested material for purposes of time or content management or ease of delivery, provided that such “clipping” or reformatting does not alter the underlying editorial content or meaning of the requested material and that the resulting material is used solely within the scope of, and in a manner consistent with, the particular authorization described in the Order Confirmation and the Terms. Unless expressly set forth in the relevant Order Conformation, the License does not authorize any other form of manipulation, alteration or editing of the requested material.

ii) Unless expressly set forth in the relevant Order Confirmation, no License granted shall in any way: (i) include any right by User to create a substantively non-identical copy of the Work or to edit or in any other way modify the Work (except by means of deleting material immediately preceding or following the entire portion of the Work copied or, in the case of Works subject to Sections 14(b)(1)(B) or (C) above, as described in such Sections) (ii) permit "publishing ventures" where any particular course materials would be systematically marketed at multiple institutions.

iii) Subject to any further limitations determined in the Rightsholder Terms (and notwithstanding any apparent contradiction in the Order Confirmation arising from data provided by User), any use authorized under the electronic course content pay-per-use service is limited as follows:

A) any License granted shall apply to only one class (bearing a unique identifier as assigned by the institution, and thereby including all sections or other subparts of the class) at one institution;

B) use is limited to not more than 25% of the text of a book or of the items in a published collection of essays, poems or articles;

C) use is limited to not more than the greater of (a) 25% of the text of an issue of a journal or other periodical or (b) two articles from such an issue;

D) no User may sell or distribute any particular materials, whether photocopied or electronic, at more than one institution of learning;

E) electronic access to material which is the subject of an electronic-use permission must be limited by means of electronic password, student identification or other control permitting access solely to students and instructors in the class;

F) User must ensure (through use of an electronic cover page or other appropriate means) that any person, upon gaining electronic access to the material, which is the subject of a permission, shall see:

- a proper copyright notice, identifying the Rightsholder in whose name CCC has granted permission,
- a statement to the effect that such copy was made pursuant to permission,
- a statement identifying the class to which the material applies and notifying the reader that the material has been made available electronically solely for use in the class, and
- a statement to the effect that the material may not be further distributed to any person outside the class, whether by copying or by transmission and whether electronically or in paper form, and User must also ensure that such cover page or other means will print out in the event that the person accessing the material chooses to print out the material or any part thereof.

G) any permission granted shall expire at the end of the class and, absent some other form of authorization, User is thereupon required to delete the applicable material from any electronic storage or to block electronic access to the applicable material.

iv) Uses of separate portions of a Work, even if they are to be included in the same course material or the same university or college class, require separate permissions under the electronic course content pay-per-use Service. Unless otherwise provided in the Order Confirmation, any grant of rights to User is limited to use completed no later than the end of the academic term (or analogous period) as to which any particular permission is granted.

v) Books and Records; Right to Audit. As to each permission granted under the electronic course content Service, User shall maintain for at least four full calendar years books and records sufficient for CCC to determine the numbers of copies made by User under such permission. CCC and any representatives it may designate shall have the right to audit such books and records at any time during User's ordinary business hours, upon two days' prior notice. If any such audit shall determine that User shall have underpaid for, or underreported, any electronic copies used by three percent (3%) or more, then User shall bear all the costs of any such audit; otherwise, CCC shall bear the costs of any such audit. Any amount determined by such audit to have been underpaid by User shall immediately be paid to CCC by User, together with interest thereon at the rate of 10% per annum from the date such amount was originally due. The provisions of this paragraph shall survive the termination of this license for any reason.

c) *Pay-Per-Use Permissions for Certain Reproductions (Academic photocopies for library reserves and interlibrary loan reporting) (Non-academic internal/external business uses and commercial document delivery).* The License expressly excludes the uses listed in Section (c)(i)-(v) below (which must be subject to separate license from the applicable Rightsholder) for: academic photocopies for library reserves and interlibrary loan reporting; and non-academic internal/external business uses and commercial document delivery.

i) electronic storage of any reproduction (whether in plain-text, PDF, or any other format) other than on a transitory basis;

ii) the input of Works or reproductions thereof into any computerized database;

iii) reproduction of an entire Work (cover-to-cover copying) except where the Work is a single article;

iv) reproduction for resale to anyone other than a specific customer of User;

v) republication in any different form. Please obtain authorizations for these uses through other CCC services or directly from the rightsholder.

Any license granted is further limited as set forth in any restrictions included in the Order Confirmation and/or in these Terms.

d) *Electronic Reproductions in Online Environments (Non-Academic-email, intranet, internet and extranet).* For "electronic reproductions", which generally includes e-mail use (including instant messaging or other electronic transmission to a defined group of recipients) or posting on an intranet, extranet or Intranet site (including any display or performance incidental thereto), the following additional terms apply:

i) Unless otherwise set forth in the Order Confirmation, the License is limited to use completed within 30 days for any use on the Internet, 60 days for any use on an intranet or extranet and one year for any other use, all as measured from the "republication date" as identified in the Order Confirmation, if any, and otherwise from the date of the Order Confirmation.

ii) User may not make or permit any alterations to the Work, unless expressly set forth in the Order Confirmation (after request by User and approval by Rightsholder); provided, however, that a Work consisting of photographs or other still images not embedded in text may, if necessary, be resized, reformatted or have its resolution modified without additional express permission, and a Work consisting of audiovisual content may, if necessary, be "clipped" or reformatted for purposes of time or content management or ease of delivery (provided that any such resizing, reformatting, resolution modification or “clipping” does not alter the underlying editorial content or meaning of the Work used, and that the resulting material is used solely within the scope of, and in a manner consistent with, the particular License described in the Order Confirmation and the Terms.

15) Miscellaneous.

a) User acknowledges that CCC may, from time to time, make changes or additions to the Service or to the Terms, and that Rightsholder may make changes or additions to the Rightsholder Terms. Such updated Terms will replace the prior terms and conditions in the order workflow and shall be effective as to any subsequent Licenses but shall not apply to Licenses already granted and paid for under a prior set of terms.

b) Use of User-related information collected through the Service is governed by CCC's privacy policy, available online at www.copyright.com/about/privacy-policy/.

c) The License is personal to User. Therefore, User may not assign or transfer to any other person (whether a natural person or an organization of any kind) the License or any rights granted thereunder; provided, however, that, where applicable, User may assign such License in its entirety on written notice to CCC in the event of a transfer of all or substantially all of User's rights in any new material which includes the Work(s) licensed under this Service.

d) No amendment or waiver of any Terms is binding unless set forth in writing and signed by the appropriate parties, including, where applicable, the Rightsholder. The Rightsholder and CCC hereby object to any terms contained in any writing prepared by or on behalf of the User or its principals, employees, agents or affiliates and purporting to govern or otherwise relate to the License described in the Order Confirmation, which terms are in any way inconsistent with any Terms set forth in the Order Confirmation, and/or in CCC's standard operating procedures, whether such writing is prepared prior to, simultaneously with or subsequent to the Order Confirmation, and whether such writing appears on a copy of the Order Confirmation or in a separate instrument.

e) The License described in the Order Confirmation shall be governed by and construed under the law of the State of New York, USA, without regard to the principles thereof of conflicts of law. Any case, controversy, suit, action, or proceeding arising out of, in connection with, or related to such License shall be brought, at CCC's sole discretion, in any federal or state court located in the County of New York, State of New York, USA, or in any federal or state court

whose geographical jurisdiction covers the location of the Rightsholder set forth in the Order Confirmation. The parties expressly submit to the personal jurisdiction and venue of each such federal or state court.

B. MATLAB Code related to Chapter 2 and 3


```
%+------------------------------------------------------------------------+
%|                                                                        |
%| FILENAME : startSimulation_m                          VERSION : 1.1.0  |
%|                                                                        |
%| TITLE : startSimulation                          AUTHORS :Eyup Can Demir |
%|                                                            Daniel Aldrich |
%+------------------------------------------------------------------------+
%|                                                                        |
%| DEPENDENT FILES :                                                      |
%|       <none>                                                           |
%|                                                                        |
%| DESCRIPTION :                                                          |
%|       Monte Carlo Simulation for Composite Fibres, original work done  |
%|        by Eyup Can Demir. This work has been adapted from the original |
%|        program, written in Python, to MatLab allowing the progam to    |
%|        benefit from vectorization and parallel programming.            |
%|                                                                        |
%| PUBLIC FUNCTIONS :                                                     |
%|       <none>                                                           |
%|                                                                        |
%| NOTES :                                                                |
%|       This program uses System commands, therefore is only able to run |
%|        on Windows machines.                                            |
%|       This program deletes and creates files in a folder (Data) in the |
%|        same folder as this program, because of this the user is solely |
%|        responsible for any lost data due to this.                      |
%|                                                                        |
%| COPYRIGHT :                                                            |
%|       Copyright (c) 2020 Eyup Can Demir, Daniel Aldrich                |
%{
%|       Permission is hereby granted, free of charge, to any person      |
%|       obtaining a copy of this software and associated documentation   |
%|       files (the "Software"), to deal in the Software without          |
%|       restriction, including without limitation the rights to use,     |
%|       copy, modify, merge, publish, distribute, sublicense, and/or     |
%|       sell copies of the Software, and to permit persons to whom the   |
%|       Software is furnished to do so, subject to the following         |
%|       conditions:                                                      |
%|                                                                        |
%|       The above copyright notice and this permission notice shall be   |
%|       included in all copies or substantial portions of the Software.  |
%|                                                                        |
%|       THE SOFTWARE IS PROVIDED "AS IS", WITHOUT WARRANTY OF ANY KIND,  |
%|       EXPRESS OR IMPLIED, INCLUDING BUT NOT LIMITED TO THE WARRANTIES  |
%|       OF MERCHANTABILITY, FITNESS FOR A PARTICULAR PURPOSE AND         |
%|       NONINFRINGEMENT. IN NO EVENT SHALL THE AUTHORS OR COPYRIGHT      |
%|       HOLDERS BE LIABLE FOR ANY CLAIM, DAMAGES OR OTHER LIABILITY,     |
%|       WHETHER IN AN ACTION OF CONTRACT, TORT OR OTHERWISE, ARISING     |
%|       FROM, OUT OF OR IN CONNECTION WITH THE SOFTWARE OR THE USE OR    |
%|       OTHER DEALINGS IN THE SOFTWARE.                                  |
%}
%|                                                                        |
%| CHANGES :                                                              |
```

```
%|       1.1.0 - Added An Output for the Dendrogram Data                  |
%|                                                                        |
%|       1.0.0 - Added Matlab App to Interface with This Function        |
%|                                                                        |
%+------------------------------------------------------------------------+

function [] = startSimulation(varargin)
import Simulation.*
% <Purpose of this function>


%%%%%%%%%%%%%%%%%%%%%%%%%%%%%%%%%%%%%%%%%%%%%%%%%%%%%%%%%%%%%%%%%%%%%%%%%%%
%%                            DATA STRUCTURE
%%%%%%%%%%%%%%%%%%%%%%%%%%%%%%%%%%%%%%%%%%%%%%%%%%%%%%%%%%%%%%%%%%%%%%%%%%%
%
% agglomerateData - contains all the data that is specific to an individual
%                   agglomerate.
%
% generalData     - contains all the run generic information including
%                   information on the average/general properties for the
%                   agglomerates found within the run.
%
% fibreData       - contains the (x,y) points for each fibre as well as
%                   the number associated with its agglomerate. This
%                   number can range from 0 (Free Fibre) to 'n' (The
%                   number of Agglomerates in the run).
%
% agglomerateData is an n x 6 matrix where n denotes the number of
%     agglomerates in the specific run. The 6 columns are broken down as
%     follows:
%
%     agglomerateData(n,1) - Number of Fibres in the Agglomerate
%     agglomerateData(n,2) - Area of the Agglomerate
%     agglomerateData(n,3) - Fiber Fraction within the Agglomerate
%     agglomerateData(n,4) - x Location of the Centroid
%     agglomerateData(n,5) - y Location of the Centroid
%     agglomerateData(n,6) - Radius of the Agglomerated Area
%
%
% generalData is a 1 x 12 vector of data, which is broken down as follows:
%
%     generalData(1)  - Number of fibres in the Rectangular Volume Element
%     generalData(2)  - Elastic Modulus as found by the Mori-Tanaka Method
%     generalData(3)  - Matrix Volume Fraction of the RVE
%     generalData(4)  - Number of Free Fibres (Non-Agglomerated Fibres)
%     generalData(5)  - Fibre Volume Fraction of the Free Fibres of the RVE
%     generalData(6)  - Fraction of Fibres that are Non-Agglomerated
%     generalData(7)  - Number of Agglomerated Fibres in the RVE
%     generalData(8)  - Average Fibre Volume Fraction of an Agglomerate
%     generalData(9)  - Volume Fraction of Agglomerates in the RVE
%     generalData(10) - Total Area of Agglomerates in the RVE
%     generalData(11) - Agglomerate Elastic Modulus
%     generalData(12) - Number of Agglomerates in the RVE
```

```
%     generalData(13) - Seating Positions
%     generalData(14) - Fibre Radius
%     generalData(15) - Length of Fibres
%     generalData(16) - Minimum Fibre Fraction
%     generalData(17) - Increment for the Fibre Fraction
%     generalData(18) - Maximum Fibre Fraction
%     generalData(19) - Fibre Elastic Modulus
%     generalData(20) - Fibre Poisson's Ratio
%     generalData(21) - Matrix Elastic Modulus
%     generalData(22) - Matrix Poisson's Ratio
%     generalData(23) - Is Uniform Distribution Enabled
%     generalData(24) - Lognormal 'Mean'
%     generalData(23) - Lognormal 'Standard Deviation'
%     generalData(26) - Fiber Alignment on/off
%
%
% fibreData is an m x 3 matrix of data where m is the number of fibres in
%     the run. The columns contain the (x,y) data points and the
%     agglomerate grouping, which are broken down as follows:
%
%     fibreData(m,1)  - x position of fibre
%     fibreData(m,2)  - y position of fibre
%     fibreData(m,3)  - Agglomerate Group number (0 represents Free Fibre)

%%%%%%%%%%%%%%%%%%%%%%%%%%%%%%%%%%%%%%%%%%%%%%%%%%%%%%%%%%%%%%%%%%%%%%%%%%%%%%%
%%                                INPUT PARSING
%%%%%%%%%%%%%%%%%%%%%%%%%%%%%%%%%%%%%%%%%%%%%%%%%%%%%%%%%%%%%%%%%%%%%%%%%%%%%%%
s      = varargin{1};
totRun = varargin{2}; % number of run for monte-carlo

fibRad = varargin{3}; % radius of fiber
fibLen = varargin{4}; % length of fiber

minFibFrac = varargin{5}; % min fiber percentage (loading%)
intFibFrac = varargin{6}; % steps for fiber percentage
maxFibFrac = varargin{7}; % max fiber percentage (loading%)

Ef  = varargin{8}; % Young's Modulus of Fibres
nuF = varargin{9}; % Poisson's Ratio of Fibres

Em  = varargin{10};% Young's Modulus of Matrix
nuM = varargin{11};% Poisson's Ratio of Matrix

progressBar = varargin{12}; % Level of Progress Bars to Display
runParallel = varargin{13}; % Enable Parallel Mode

uniDistr = varargin{14};
agMethod = varargin{15};
fibAlign = varargin{16};
mu       = varargin{17}; % Determines shape of the lognormal distribution
sigma    = varargin{18}; % Determines shape of the lognormal distribution

disForAgglo = varargin{19}; % Critical distance to form agglomerate
```

```
saveDir = varargin{20}; % Location of the folder to save the Data

initialData(1)  = s;
initialData(2)  = fibRad;
initialData(3)  = fibLen;
initialData(4)  = minFibFrac;
initialData(5)  = intFibFrac;
initialData(6)  = maxFibFrac;
initialData(7)  = Ef;
initialData(8)  = nuF;
initialData(9)  = Em;
initialData(10) = nuM;
initialData(11) = uniDistr;
initialData(12) = mu;
initialData(13) = sigma;
if strcmpi(fibAlign,'Random')
    initialData(14) = 0;
else
    initialData(14) = 1;
end

if exist(saveDir,'dir')
    system(sprintf('rmdir /s /q "%s"',saveDir));
end

system(sprintf('mkdir "%s"',saveDir));
tic

%% Initial Parameters

fibArea = pi*fibRad^2; % area of fiber 2D
%fibVol = fibArea*fibLen; % volume of fiber for 3D

rveWidth = s+2*fibRad;
rveArea  = (rveWidth)^2; % area of RVE in 2D
%rveVol   = (rveWidth)^3; % volume of RVE in 3D

s = rveWidth - 2*fibRad; % seating positions

M = genStiffnessMat(Em, nuM);
F = genStiffnessMat(Ef, nuF);

fibFrac = minFibFrac:intFibFrac:maxFibFrac;
fibNum  = floor(rveArea*fibFrac/fibArea);

if runParallel
    runParallel = inf;
else
    runParallel = 0;
end

if ~isa(progressBar,'matlab.ui.dialog.ProgressDialog')
```

```
    progressBar = [];
end

%%%%%%%%%%%%%%%%%%%%%%%%%%%%%%%%%%%%%%%%%%%%%%%%%%%%%%%%%%%%%%%%%%%%%%%%%%%%%%%
%%                                  MAIN LOOP
%%%%%%%%%%%%%%%%%%%%%%%%%%%%%%%%%%%%%%%%%%%%%%%%%%%%%%%%%%%%%%%%%%%%%%%%%%%%%%%

for i = 1:length(fibFrac)
    ii = fibFrac(i);
    numberOfFibres = fibNum(i);

    curfibFrac = sprintf('fibFrac%03i',round(ii*1000));
    system(sprintf('mkdir "%s\\%s"',saveDir,curfibFrac));
    progressBar.Value =  (i-1)/length(fibFrac);
    parfor (j = 1:totRun,runParallel)
    %%%%%%%%%%%%%%%%%%%%%%%%%%%%%%%%%%%%%%%%%%%%%%%%%%%%%%%%%%%%%%%%%%%%%%%%%%%%%%%
    %%                          MONTE-CARLO SIMULATION
    %%%%%%%%%%%%%%%%%%%%%%%%%%%%%%%%%%%%%%%%%%%%%%%%%%%%%%%%%%%%%%%%%%%%%%%%%%%%%%%

        generalData = zeros(1,26);

        generalData(13:26) = initialData;

        generalData(1) = numberOfFibres;
        fibreData = zeros(generalData(1),3);

        currun = sprintf('run%03i',j);

        fibreData(:,1:2) = generateRandomFibres(s,generalData(1),fibRad, ...
                uniDistr,mu,sigma);
    %%%%%%%%%%%%%%%%%%%%%%%%%%%%%%%%%%%%%%%%%%%%%%%%%%%%%%%%%%%%%%%%%%%%%%%%%%%%%%%
    %%                       AGGLOMERATION CALCULATION
    %%%%%%%%%%%%%%%%%%%%%%%%%%%%%%%%%%%%%%%%%%%%%%%%%%%%%%%%%%%%%%%%%%%%%%%%%%%%%%%
        [clusterLables,uniqueLables,fibresInCluster,linkageData] =  ...
                genCluster(fibreData(:,1:2),disForAgglo);

        generalData(4) = sum(fibresInCluster==1);

        generalData(12) = length(uniqueLables) - generalData(4);
        orderedAgglo = uniqueLables(fibresInCluster>1);

        agglomerateData = zeros(generalData(12),6);

        [~,~,ic] = unique(~prod(clusterLables~=orderedAgglo',2) ...
                          .*clusterLables);

        if generalData(4)
            fibreData(:,3) = ic-1;
        else
            fibreData(:,3) = ic;
        end

        %Free fiber Calculations
```

```
        generalData(5) = fibArea*generalData(4)/rveArea;
        generalData(6) = generalData(4)/generalData(1);

        % Creating Space for Each Aggomerate Data
        if generalData(12)

            % I have list named as "pos" shows the position of each fiber in atating ↙
area as [x,y]
            % They are assigned uniformly and each element of it shows the position ↙
of fibers.
            % Now I labelled them in clusters but I do not know their position.
            % I need to find position of "same" labeled fibers to find area of ↙
agglomerates or fiber
            % fraction in agglomerate.
            for k = 1:generalData(12) %length(orderedAgglo)
                [rows,~] = find(fibreData(:,3)==k);  % I find the which position is↙
labelled same.

                agglomerateData(k,4:5) = mean(fibreData(rows,1:2));

                % I find centroid of agglomerate
                agglomerateData(k,6) = max(calculateDistance( ...
                        fibreData(rows,1:2), ...
                        agglomerateData(k,4:5)));

                agglomerateData(k,2) = pi*(agglomerateData(k,6)+fibRad)^2;
                agglomerateData(k,1) = length(rows);

            end
            agglomerateData(:,3) = agglomerateData(:,1).*fibArea./agglomerateData(:, ↙
2);
            generalData(8)  = sum(agglomerateData(:,3)) / generalData(12);
            generalData(7)  = sum(agglomerateData(:,1));
            % TODO: Check if this can be replaced with sum(aD(:,2))
            generalData(10) = generalData(7)*fibArea/generalData(8);
            generalData(9)  = generalData(10) / rveArea;

            % TODO: Check if this IF-Statement is possible to enter.
            if generalData(10) >= rveArea
                generalData(8)  = ii;
                generalData(10) = rveArea;
                generalData(9)  = 1;
            end
            VfInA = generalData(8);
            AspectRatio = fibLen/(2*fibRad);
            switch agMethod
                case 'Halpin Tsai'
                    generalData(11) = HalpinTsai(Ef,Em,VfInA,AspectRatio);
                case 'IROM'
                    generalData(11) = IROM(Ef,Em,VfInA);
            end
        end
```

```
        Ea = generalData(11);
        Va = generalData(9);

        Vff = generalData(5);
        Vm = 1 - (Vff + Va);
        generalData(3) = Vm;
        generalData(2) = MoriTanaka(Ef,Ea,Em,Vff,Va,Vm, ...
                                    nuM,M,F,fibLen,fibRad,fibAlign);

        saveData(saveDir,curfibFrac,currun, ...
            generalData,agglomerateData,fibreData,linkageData)
    end
end
toc
end
```

```
% %
% s      = varargin{1};
% totRun = varargin{2}; % number of run for monte-carlo
% fibRad = varargin{3}; % radius of fiber
% fibLen = varargin{4}; % length of fiber
%
s = 1000;
totRun = 2;
fibRad = 2.5;
fibLen = 200;
% minFibFrac = varargin{5}; % min fiber percentage (loading%)
% intFibFrac = varargin{6}; % steps for fiber percentage
% maxFibFrac = varargin{7}; % max fiber percentage (loading%)
%
minFibFrac = 11.31051753/100;
intFibFrac = 0.1;
maxFibFrac = 0.12;
% Ef  = varargin{8}; % Young's Modulus of Fibres
% nuF = varargin{9}; % Poisson's Ratio of Fibres
%
Ef = 150000;
nuF = 0.35;
% Em  = varargin{10};% Young's Modulus of Matrix
% nuM = varargin{11};% Poisson's Ratio of Matrix
%
Em = 911;
nuM = 0.35;
% progressBar = varargin{12}; % Level of Progress Bars to Display
% runParallel = varargin{13}; % Enable Parallel Mode
progressBar = 1;
runParallel = inf;

%
% uniDistr = varargin{14};
% agMethod = varargin{15};
% fibAlign = varargin{16};
% mu       = varargin{17}; % Determines shape of the lognormal distribution
% sigma    = varargin{18}; % Determines shape of the lognormal distribution
uniDistr = 0;
agMethod = "ROM";
fibAlig = "Aligned";
mu = 2;
sigma = 0.5;

%
% disForAgglo = varargin{19}; % Critical distance to form agglomerate
disForAgglo = 5;
intDisForAgglo = 1;
maxDisForAgglo = 20;
% saveDir = varargin{20}; % Location of the folder to save the Data
saveDir = fullfile(getenv('tmp'),'Data');

for disForAgglo = disForAgglo:intDisForAgglo:maxDisForAgglo
```

```
    for mu = 2:0.2:5
        for sigma = 1
           sub = sprintf('cr%04i mu%04i sig%04i',round(disForAgglo*100),...
               round(mu*100), round(sigma*100));
           saveDir = fullfile(getenv('tmp'),'Data',sub);
           startSimulation(s, totRun, fibRad, fibLen, minFibFrac, intFibFrac, ↙
maxFibFrac, Ef, ...
    nuF, Em, nuM, progressBar, runParallel, uniDistr, agMethod, fibAlig, mu, sigma, ↙
disForAgglo, saveDir)
        end
    end
end
```

```
function [dist] = calculateDistance(xy1,xyn)
    dist = sqrt(sum((xy1-xyn).^2,2));
end
```

```
function [dist] = calculateSquareDistance(xy1,xyn)
    dist = sum((xy1-xyn).^2,2);
end
```

```
function [clusterLables,uniqueLables,fibresInCluster,linkageData] = genCluster(pos, ↙
disForAgglo)
linkageData = linkage(pos,'single','euclidean');
clusterLables = cluster(linkageData,'cutoff',disForAgglo,'Criterion','distance');
[uniqueLables,~,ic] = unique(clusterLables);
%nClusters = length(uniqueLables);
fibresInCluster = accumarray(ic,1);
```

```
function [fibPositions] = generateRandomFibres(rveWidth,nFibres,rFibre,mode,mu, ↙
sigma)
import Simulation.calculateSquareDistance
if nargin <6
    sigma = 1;
    if nargin < 5
        mu = 0;
        if nargin < 4
            mode = true;
        end
    end
end

flag = 0;

% Data Validation
nFibres = floor(nFibres);

% Space Preallocation
fibPositions = zeros(nFibres,2);
distanceThresh = (2*rFibre).^2;

for fibre = 1:nFibres
    while true
        if mode || fibre==1
            xy = rveWidth*rand(1,2);
        else
            while true
                d = lognrnd(mu, sigma, 1);
                theta = 2*pi*rand;
                xy = [d*cos(theta),d*sin(theta)]+xy;
                if ~any([xy>rveWidth,xy<=0])
                    break;
                 else
                    xy = rveWidth*rand(1,2);
                    break;
                end
            end
        end

        distance = calculateSquareDistance(...
            fibPositions(1:fibre,:),xy);

        if (fibre == 1) || ~any(distance < distanceThresh)
            fibPositions(fibre,:) = xy;
            break;
%           else
%               xy = rveWidth*rand(1,2);
%               break;
        end

    end
end
```

```
function [Mat] = genStiffnessMat(E, nu)
% Calculate the material stiffness constants
const0 = (E*(1-nu))/((1+nu)*(1-2*nu));

const1 = const0*nu/(1-nu);
const2 = const0*(1-2*nu)/(2*(1-nu));

% Generate the Stiffness Matrix
Mat = [ const0 const1 const1      0      0      0
        const1 const0 const1      0      0      0
        const1 const1 const0      0      0      0
             0      0      0 const2      0      0
             0      0      0      0 const2      0
             0      0      0      0      0 const2 ];
```

```
function [Ea] = HalpinTsai(Ef,Em,VfInA,AspectRatio)
    fi = 2.*AspectRatio;
    nul = (Ef./Em - 1)./(Ef./Em + fi);
    nut = (Ef./Em - 1)./(Ef./Em + 2);
    Ea = Em.*(3./8.*((1+fi.*nul.*VfInA)./(1-nul.*VfInA))+ ...
        5./8.*((1+2.*nut.*VfInA)./(1-nut.*VfInA)));
end
```

```
function [Ea] = IROM(Ef,Em,VfInA)
    Ea = 1./(VfInA./Ef+(1-VfInA)./Em);
end
```

```
function [vec] = mat2vec(mat)
    vec = zeros(1,12);
    vec(1)  = mat(1,1);
    vec(2)  = mat(2,2);
    vec(3)  = mat(3,3);
    vec(4)  = mat(1,2);
    vec(5)  = mat(2,1);
    vec(6)  = mat(1,3);
    vec(7)  = mat(3,1);
    vec(8)  = mat(2,3);
    vec(9)  = mat(3,2);
    vec(10) = mat(4,4);
    vec(11) = mat(5,5);
    vec(12) = mat(6,6);
```

```
function [Ec11] = MoriTanaka(~, Ea, ~, Vff, Va, Vm, nuM, M , F, fibLen, fibRad, ↙
fibAlign) % Ef and Em not used
    import Simulation.genStiffnessMat
    import Simulation.mat2vec
    import Simulation.vec2mat

    if strcmp(fibAlign,'Random')
        alignment = 0;
    else
        alignment = 1;
    end

    nuA = 0.35;
    A = genStiffnessMat(Ea,nuA);

    l = fibLen;
    d = 2*fibRad;
    a = l/d;
    a2 = a^2;
    g = ((a/(a2-1)^1.5))*(a*(a2-1)^(1/2)-acosh(a));
    b = 1/(1-nuM);
    c = 1-2*nuM;
    e = 1/(a2-1);

    Sf_1111 = 0.5*b*(c + e*(3*a2-1)-(c+3*e*a2)*g);
    Sf_2222 = (3/8)*b*e*a2+0.25*b*(c-(9/4)*e)*g;
    Sf_3333 = Sf_2222;
    Sf_2233 = 0.25*b*(0.5*e*a2-(c+0.75*e)*g);
    Sf_3322 = Sf_2233;
    Sf_2211 = -0.5*b*e*a2 + 0.25*b*(3*e*a2-c)*g;
    Sf_3311 = Sf_2211;
    Sf_1122 = -0.5*b*(c+e)+0.5*b*(c+1.5*e)*g;
    Sf_1133 = Sf_1122;
    Sf_2323 = 0.25*b*(0.5*e*a2 + (c-0.75*e)*g);
    %Sf_3232 = Sf_2323;
    Sf_1212 = 0.25*b*(c-(a2+1)*e-0.5*(c-3*e*(a2+1))*g);
    Sf_1313 = Sf_1212;
    Sf_3131 = Sf_1313;
    Sf = zeros(6,6);
    % Matrix form:
    Sf(1,1) = Sf_1111;
    Sf(1,2) = Sf_1122;
    Sf(1,3) = Sf_1133;
    Sf(2,1) = Sf_2211;
    Sf(2,2) = Sf_2222;
    Sf(2,3) = Sf_2233;
    Sf(3,1) = Sf_3311;
    Sf(3,2) = Sf_3322;
    Sf(3,3) = Sf_3333;
    Sf(4,4) = 2*Sf_1212;
    Sf(5,5) = 2*Sf_2323;
    Sf(6,6) = 2*Sf_3131;
```

```
Sa_1111 = (7-5*nuM)/(15*(1-nuM));
Sa_2222 = Sa_1111;
Sa_3333 = Sa_1111;
Sa_1122 = (5*nuM-1)/(15*(1-nuM));
Sa_1133 = Sa_1122;
Sa_2211 = Sa_1122;
Sa_2233 = Sa_1122;
Sa_3311 = Sa_1122;
Sa_3322 = Sa_1122;
Sa_1212 = (4-5*nuM)/(15*(1-nuM));
%Sa_1221 = Sa_1212;
Sa_2323 = Sa_1212;
%Sa_2332 = Sa_1212;
Sa_3131 = Sa_1212;
%Sa_3113 = Sa_1212;
% Eshelby tensor (using engineering strains)
Sa = zeros(6,6);
%Matrix form:
Sa(1,1) = Sa_1111;
Sa(1,2) = Sa_1122;
Sa(1,3) = Sa_1133;
Sa(2,1) = Sa_2211;
Sa(2,2) = Sa_2222;
Sa(2,3) = Sa_2233;
Sa(3,1) = Sa_3311;
Sa(3,2) = Sa_3322;
Sa(3,3) = Sa_3333;
Sa(4,4) = 2*Sa_1212;
Sa(5,5) = 2*Sa_2323;
Sa(6,6) = 2*Sa_3131;


I = eye(6);

Ta_dil = inv(I+(Sa*(M\(A-M))));
Tf_dil = inv(I+(Sf*(M\(F-M))));

%Random Average Tensor
if alignment ==1
    R = eye(12);
else
    R = (1/120)*([ 24  64   0  16  16   0   0   0   0   0   0  64
                   24   9  45   6   6  10  10   5   5  20  40  24
                   24   9  45   6   6  10  10   5   5  20  40  24
                    8   8   0  12  32  20   0  40   0   0   0 -32
                    8   8   0  32  12   0  20   0  40   0   0 -32
                    8   8   0  12  32  20   0  40   0   0   0 -32
                    8   8   0  32  12   0  20   0  40   0   0 -32
                    8   3  15   2   2  30  30  15  15 -20 -40   8
                    8   3  15   2   2  30  30  15  15 -20 -40   8
```

```
                    8   3  15   2   2 -10 -10  -5  -5  20  40   8
                    8   8   0  -8  -8   0   0   0   0  40  20  28
                    8   8   0  -8  -8   0   0   0   0  40  20  28]);
    end

    % Averaging of the agglomerates

    A_Ta_dil = (A*Ta_dil); %#ok<MINV>
    % Averaging of FTa_dil
    A_Ta_dil_vec = mat2vec(A_Ta_dil);

    A_Ta_dil_aver_vec = (R* A_Ta_dil_vec');
    A_Ta_dil_aver = vec2mat(A_Ta_dil_aver_vec);

    %Avearging Ta_dil
    Ta_dil_vec = mat2vec(Ta_dil);

    Ta_dil_aver_vec = (R* Ta_dil_vec');
    Ta_dil_aver = vec2mat(Ta_dil_aver_vec);

    % Avearing Fiber

    F_Tf_dil = (F*Tf_dil); %#ok<MINV>
    % Averaging of FTa_dil
    F_Tf_dil_vec = mat2vec(F_Tf_dil);

    F_Tf_dil_aver_vec = (R* F_Tf_dil_vec');
    F_Tf_dil_aver = vec2mat(F_Tf_dil_aver_vec);

    %Avearging Tf_dil
    Tf_dil_vec = mat2vec(Tf_dil);

    Tf_dil_aver_vec = (R* Tf_dil_vec');
    Tf_dil_aver = vec2mat(Tf_dil_aver_vec);


    %T0 = inv(Vm*I +Vff*Tf_dil_aver + Va*Ta_dil_aver);
    Ec = (Vm*M + Vff*F_Tf_dil_aver + Va*A_Ta_dil_aver)/(Vm*I +Vff*Tf_dil_aver + ↙
Va*Ta_dil_aver);

    Scom = inv(Ec);
    Ec11 = 1/(Scom(1,1));

    %nuC= Ec(1,2)/(2*Ec(4,4)+Ec(1,2))
    %Ec11=(Ec(1,1)-2*nuC*Ec(1,2));
end
```

```
function [cancel,figh] = multiWaitbar( label, varargin )
%multiWaitbar: add, remove or update an entry on the multi waitbar
%
%   multiWaitbar(LABEL,VALUE) adds a waitbar for the specified label, or
%   if it already exists updates the value. LABEL must be a string and
%   VALUE a number between zero and one or the string 'Close' to remove the
%   entry Setting value equal to 0 or 'Reset' will cause the progress bar
%   to reset and the time estimate to be re-initialized.
%
%   multiWaitbar(LABEL,COMMAND,VALUE,...)  or
%   multiWaitbar(LABEL,VALUE,COMMAND,VALUE,...)
%   passes one or more command/value pairs for changing the named waitbar
%   entry. Possible commands include:
%   'Value'       Set the value of the named waitbar entry. The
%                 corresponding value must be a number between 0 and 1.
%   'Increment'   Increment the value of the named waitbar entry. The
%                 corresponding value must be a number between 0 and 1.
%   'Color'       Change the color of the named waitbar entry. The
%                 value must be an RGB triple, e.g. [0.1 0.2 0.3], or a
%                 single-character color name, e.g. 'r', 'b', 'm'.
%   'Relabel'     Change the label of the named waitbar entry. The
%                 value must be the new name.
%   'Reset'       Set the named waitbar entry back to zero and reset its
%                 timer. No value need be specified.
%   'CanCancel'   [on|off] should a "cancel" button be shown for this bar
%                 (default 'off').
%   'CancelFcn'   Function to call in the event that the user cancels.
%   'ResetCancel' Reset the "cancelled" flag for an entry (ie. if you
%                 decide not to cancel).
%   'Close'       Remove the named waitbar entry.
%   'Busy'        Puts this waitbar in "busy mode" where a small bar
%                 bounces back and forth. Return to normal progress display
%                 using the 'Reset' command.
%
%   cancel = multiWaitbar(LABEL,VALUE) also returns whether the user has
%   clicked the "cancel" button for this entry (true or false). Two
%   mechanisms are provided for cancelling an entry if the 'CanCancel'
%   setting is 'on'. The first is just to check the return argument and if
%   it is true abort the task. The second is to set a 'CancelFcn' that is
%   called when the user clicks the cancel button, much as is done for
%   MATLAB's built-in WAITBAR. In either case, you can use the
%   'ResetCancel' command if you don't want to cancel after all.
%
%   multiWaitbar('CLOSEALL') closes the waitbar window.
%
%   Example:
%   multiWaitbar( 'CloseAll' );
%   multiWaitbar( 'Task 1', 0 );
%   multiWaitbar( 'Task 2', 0.5, 'Color', 'b' );
%   multiWaitbar( 'Task 3', 'Busy');
%   multiWaitbar( 'Task 1', 'Value', 0.1 );
%   multiWaitbar( 'Task 2', 'Increment', 0.2 );
%   multiWaitbar( 'Task 3', 'Reset' ); % Disables "busy" mode
```

```
%   multiWaitbar( 'Task 3', 'Value', 0.3 );
%   multiWaitbar( 'Task 2', 'Close' );
%   multiWaitbar( 'Task 3', 'Close' );
%   multiWaitbar( 'Task 1', 'Close' );
%
%   Example:
%   multiWaitbar( 'Task 1', 0, 'CancelFcn', @(a,b) disp( ['Cancel ',a] ) );
%   for ii=1:100
%      abort = multiWaitbar( 'Task 1', ii/100 );
%      if abort
%         % Here we would normally ask the user if they're sure
%         break
%      else
%         pause( 1 )
%      end
%   end
%   multiWaitbar( 'Task 1', 'Close' )
%
%   Example:
%   multiWaitbar( 'CloseAll' );
%   multiWaitbar( 'Red...',    7/7, 'Color', [0.8 0.0 0.1] );
%   multiWaitbar( 'Orange...', 6/7, 'Color', [1.0 0.4 0.0] );
%   multiWaitbar( 'Yellow...', 5/7, 'Color', [0.9 0.8 0.2] );
%   multiWaitbar( 'Green...',  4/7, 'Color', [0.2 0.9 0.3] );
%   multiWaitbar( 'Blue...',   3/7, 'Color', [0.1 0.5 0.8] );
%   multiWaitbar( 'Indigo...', 2/7, 'Color', [0.4 0.1 0.5] );
%   multiWaitbar( 'Violet...', 1/7, 'Color', [0.8 0.4 0.9] );
%
%    Thanks to Jesse Hopkins for suggesting the "busy" mode.
%   Author: Ben Tordoff
%   Copyright 2007-2020 The MathWorks, Inc.
persistent FIGH;
cancel = false;
% Check basic inputs
error( nargchk( 1, inf, nargin ) ); %#ok<NCHKN> - kept for backwards compatibility
if ~ischar( label )
    error( 'multiWaitbar:BadArg', 'LABEL must be the name of the progress entry (i. ↙
e. a string)' );
end
% Try to get hold of the figure
if isempty( FIGH ) || ~ishandle( FIGH )
    FIGH = findall( 0, 'Type', 'figure', 'Tag', 'multiWaitbar:Figure' );
    if isempty(FIGH)
        FIGH = iCreateFig();
    else
        FIGH = handle( FIGH(1) );
    end
end
% Check for close all and stop early
if any( strcmpi( label, {'CLOSEALL','CLOSE ALL'} ) )
    iDeleteFigure(FIGH);
    figh = [];
    return;
```

```
end
if nargout>1
    figh = FIGH;
end
% Make sure we're on-screen
if ~strcmpi( FIGH.Visible, 'on' )
    FIGH.Visible = 'on';
end
% Make sure the timer is still valid - it can be found and deleted
% externally.
if ~isvalid( getappdata( FIGH, 'BusyTimer' ) )
    setappdata( FIGH, 'BusyTimer', iCreateTimer(FIGH) );
end
% Get the list of entries and see if this one already exists
entries = getappdata( FIGH, 'ProgressEntries' );
if isempty(entries)
    idx = [];
else
    idx = find( strcmp( label, {entries.Label} ), 1, 'first' );
end
bgcol = getappdata( FIGH, 'DefaultProgressBarBackgroundColor' );
% If it doesn't exist, create it
needs_redraw = false;
entry_added = isempty(idx);
if entry_added
    % Create a new entry
    defbarcolor = getappdata( FIGH, 'DefaultProgressBarColor' );
    entries = iAddEntry( FIGH, entries, label, 0, defbarcolor, bgcol );
    idx = numel( entries );
end
% Check if the user requested a cancel
if nargout
    cancel = entries(idx).Cancel;
end
% Parse the inputs. We shortcut the most common case as an efficiency
force_update = false;
if nargin==2 && isnumeric( varargin{1} )
    entries(idx).LastValue = entries(idx).Value;
    entries(idx).Value = max( 0, min( 1, varargin{1} ) );
    entries(idx).Busy = false;
    needs_update = true;
else
    [params,values] = iParseInputs( varargin{:} );

    needs_update = false;
    for ii=1:numel( params )
        switch upper( params{ii} )
            case 'BUSY'
                entries(idx).Busy = true;
                needs_update = true;

            case 'VALUE'
                entries(idx).LastValue = entries(idx).Value;
```

```
                entries(idx).Value = max( 0, min( 1, values{ii} ) );
                entries(idx).Busy = false;
                needs_update = true;

            case {'INC','INCREMENT'}
                entries(idx).LastValue = entries(idx).Value;
                entries(idx).Value = max( 0, min( 1, entries(idx).Value + values{ii} ↙
) );
                entries(idx).Busy = false;
                needs_update = true;

            case {'COLOR','COLOUR'}
                entries(idx).CData = iMakeColors( values{ii}, 16 );
                needs_update = true;
                force_update = true;

            case {'RELABEL', 'UPDATELABEL'}
                % Make sure we have a string as the value and that it
                % doesn't already appear
                if ~ischar( values{ii} )
                    error( 'multiWaitbar:BadString', 'Value for ''Relabel'' must be↙
a string.' );
                end
                if ismember( values{ii}, {entries.Label} )
                    error( 'multiWaitbar:NameAlreadyExists', 'Cannot relabel an↙
entry to a label that already exists.' );
                end
                entries(idx).Label = values{ii};
                if ~isempty(entries(idx).CancelButton)
                    set( entries(idx).CancelButton, 'Callback', @(src,evt)↙
iCancelEntry(src, values{ii}) );
                end
                needs_update = true;
                force_update = true;

            case {'CANCANCEL'}
                if ~ischar( values{ii} ) || ~any( strcmpi( values{ii}, { 'on','off'}↙
) )
                    error( 'multiWaitbar:BadString', 'Parameter ''CanCancel'' must↙
be a ''on'' or ''off''.' );
                end
                entries(idx).CanCancel = strcmpi( values{ii}, 'on' );
                entries(idx).Cancel = false;
                needs_redraw = true;

            case {'RESETCANCEL'}
                entries(idx).Cancel = false;
                needs_redraw = true;

            case {'CANCELFCN'}
                if ~isa( values{ii}, 'function_handle' )
                    error( 'multiWaitbar:BadFunction', 'Parameter ''CancelFcn'' must↙
be a valid function handle.' );
```

```
                end
                entries(idx).CancelFcn = values{ii};
                if ~entries(idx).CanCancel
                    entries(idx).CanCancel = true;
                end
                needs_redraw = true;

            case {'CLOSE','DONE'}
                if ~isempty(idx)
                    % Remove the selected entry
                    entries = iDeleteEntry( entries, idx );
                end
                if isempty( entries )
                    iDeleteFigure( FIGH );
                    % With the window closed, there's nothing else to do
                    return;
                else
                    needs_redraw = true;
                end
                % We can't continue after clearing the entry, so jump out
                break;

            otherwise
                error( 'multiWaitbar:BadArg', 'Unrecognized command: ''%s'''', params↙
{ii} );

        end
    end
end
% Now work out what to update/redraw
if needs_redraw
    setappdata( FIGH, 'ProgressEntries', entries );
    iRedraw( FIGH );
    % NB: Redraw includes updating all bars, so never need to do both
elseif needs_update
    [entries(idx),needs_redraw] = iUpdateEntry( entries(idx), force_update );
    setappdata( FIGH, 'ProgressEntries', entries );
    % NB: if anything was updated onscreen, "needs_redraw" is now true.
end
if entry_added || needs_redraw
    % If the shape or size has changed, do a full redraw, including events
    drawnow();
end
% If we have any "busy" entries, start the timer, otherwise stop it.
myTimer = getappdata( FIGH, 'BusyTimer' );
if any([entries.Busy])
    if strcmpi(myTimer.Running,'off')
        start(myTimer);
    end
else
    if strcmpi(myTimer.Running,'on')
        stop(myTimer);
    end
```

```
end
end % multiWaitbar
%-------------------------------------------------------------------------%
function [params, values] = iParseInputs( varargin )
% Parse the input arguments, extracting a list of commands and values
idx = 1;
params = {};
values = {};
if nargin==0
    return;
end
if isnumeric( varargin{1} )
    params{idx} = 'Value';
    values{idx} = varargin{1};
    idx = idx + 1;
end
while idx <= nargin
    param = varargin{idx};
    if ~ischar( param )
        error( 'multiWaitbar:BadSyntax', 'Additional properties must be supplied as property-value pairs' );
    end
    params{end+1,1} = param; %#ok<AGROW>
    values{end+1,1} = []; %#ok<AGROW>
    switch upper( param )
        case {'DONE','CLOSE','RESETCANCEL'}
            % No value needed, and stop
            break;
        case {'BUSY'}
            % No value needed but parsing should continue
            idx = idx + 1;
        case {'RESET','ZERO','SHOW'}
            % All equivalent to saying ('Value', 0)
            params{end} = 'Value';
            values{end} = 0;
            idx = idx + 1;
        otherwise
            if idx==nargin
                error( 'multiWaitbar:BadSyntax', 'Additional properties must be supplied as property-value pairs' );
            end
            values{end,1} = varargin{idx+1};
            idx = idx + 2;
    end
end
if isempty( params )
    error( 'multiWaitbar:BadSyntax', 'Must specify a value or a command' );
end
end % iParseInputs
%-------------------------------------------------------------------------%
function fobj = iCreateFig()
% Create the progress bar group window
bgcol = get(0,'DefaultUIControlBackgroundColor');
```

```
f = figure( ...
    'Name', 'Progress', ...
    'Tag', 'multiWaitbar:Figure', ...
    'Color', bgcol, ...
    'MenuBar', 'none', ...
    'ToolBar', 'none', ...
    'WindowStyle', 'normal', ... % We don't want to be docked!
    'HandleVisibility', 'off', ...
    'IntegerHandle', 'off', ...
    'Visible', 'off', ...
    'NumberTitle', 'off' );
% Resize and centre on the first screen
screenSize = get(0,'ScreenSize');
figSz = [360 42];
figPos = ceil((screenSize(1,3:4)-figSz)/2);
fobj = handle( f );
fobj.Position = [figPos, figSz];
setappdata( fobj, 'ProgressEntries', [] );
% Make sure we have the image
defbarcolor = [0.8 0.0 0.1];
barbgcol = uint8( 255*0.75*bgcol );
setappdata( fobj, 'DefaultProgressBarBackgroundColor', barbgcol );
setappdata( fobj, 'DefaultProgressBarColor', defbarcolor );
setappdata( fobj, 'DefaultProgressBarSize', [350 16] );
setappdata( fobj, 'MaxEntryRows', 10 );
% Create the timer to use for "Busy" mode, being sure to delete any
% existing ones
delete( timerfind('Tag', 'MultiWaitbarTimer') );
myTimer = iCreateTimer(f);
setappdata( fobj, 'BusyTimer', myTimer );
% Setup the resize function after we've finished setting up the figure to
% avoid excessive redraws
fobj.ResizeFcn = @iRedraw;
fobj.CloseRequestFcn = @iCloseFigure;
end % iCreateFig
%--------------------------------------------------------------------------%
function t = iCreateTimer(fig)
t = timer( ...
    'TimerFcn', @(src,evt) iTimerFcn(fig), ...
    'Period', 0.02, ...
    'ExecutionMode', 'FixedRate', ...
    'Tag', 'MultiWaitbarTimer' );
end
%--------------------------------------------------------------------------%
function cdata = iMakeColors( baseColor, height )
% Creates a shiny bar from a single base color
lightColor = [1 1 1];
badColorErrorID = 'multiWaitbar:BadColor';
badColorErrorMsg = 'Colors must be a three element vector [R G B] or a single ↙
character (''r'', ''g'' etc.)';
if ischar(baseColor)
    switch upper(baseColor)
        case 'K'
```

```
            baseColor = [0.1 0.1 0.1];
        case 'R'
            baseColor = [0.8 0 0];
        case 'G'
            baseColor = [0 0.6 0];
        case 'B'
            baseColor = [0 0 0.8];
        case 'C'
            baseColor = [0.2 0.8 0.9];
        case 'M'
            baseColor = [0.6 0 0.6];
        case 'Y'
            baseColor = [0.9 0.8 0.2];
        case 'W'
            baseColor = [0.9 0.9 0.9];
        otherwise
            error( badColorErrorID, badColorErrorMsg );
    end
else
    if numel(baseColor) ~= 3
        error( badColorErrorID, badColorErrorMsg );
    end
    if isa( baseColor, 'uint8' )
        baseColor = double( baseColor ) / 255;
    elseif isa( baseColor, 'double' )
        if any(baseColor>1) || any(baseColor<0)
            error( 'multiWaitbar:BadColorValue', 'Color values must be in the range↙
0 to 1 inclusive.' );
        end
    else
        error( badColorErrorID, badColorErrorMsg );
    end
end
% By this point we should have a double precision 3-element vector.
cols = repmat( baseColor, [height, 1] );
breaks = max( 1, round( height * [1 25 50 75 88 100] / 100 ) );
cols(breaks(1),:) = 0.6*baseColor;
cols(breaks(2),:) = lightColor - 0.4*(lightColor-baseColor);
cols(breaks(3),:) = baseColor;
cols(breaks(4),:) = min( baseColor*1.2, 1.0 );
cols(breaks(5),:) = min( baseColor*1.4, 0.95 ) + 0.05;
cols(breaks(6),:) = min( baseColor*1.6, 0.9 ) + 0.1;
y = 1:height;
cols(:,1) = max( 0, min( 1, interp1( breaks, cols(breaks,1), y,  'pchip' ) ) );
cols(:,2) = max( 0, min( 1, interp1( breaks, cols(breaks,2), y,  'pchip' ) ) );
cols(:,3) = max( 0, min( 1, interp1( breaks, cols(breaks,3), y,  'pchip' ) ) );
cdata = uint8( 255 * cat( 3, cols(:,1), cols(:,2), cols(:,3) ) );
end % iMakeColors
%--------------------------------------------------------------------------%
function cdata = iMakeBackground( baseColor, height )
% Creates a shaded background
if isa( baseColor, 'uint8' )
    baseColor = double( baseColor ) / 255;
```

```
end
ratio = 1 - exp( -0.5-2*(1:height)/height )';
cdata = uint8( 255 * cat( 3, baseColor(1)*ratio, baseColor(2)*ratio, baseColor(3) ↙
*ratio ) );
end % iMakeBackground
%-------------------------------------------------------------------------%
function entries = iAddEntry( parent, entries, label, value, color, bgcolor )
% Add a new entry to the progress bar
% Create bar coloring
psize = getappdata( parent, 'DefaultProgressBarSize' );
cdata = iMakeColors( color, 16 );
% Create background image
barcdata = iMakeBackground( bgcolor, psize(2) );
% Work out the size in advance
mypanel = uipanel( 'Parent', parent, 'Units', 'Pixels', 'BorderType', 'beveledout'↙
);
labeltext = uicontrol( 'Style', 'Text', ...
    'String', label, ...
    'Parent', parent, ...
    'HorizontalAlignment', 'Left' );
etatext = uicontrol( 'Style', 'Text', ...
    'String', '', ...
    'Parent', parent, ...
    'HorizontalAlignment', 'Right' );
progresswidget = uicontrol( 'Style', 'Checkbox', ...
    'String', '', ...
    'Parent', parent, ...
    'Position', [5 5 psize], ...
    'CData', barcdata );
cancelwidget = uicontrol( 'Style', 'PushButton', ...
    'String', '', ...
    'FontWeight', 'Bold', ...
    'Parent', parent, ...
    'Position', [5 5 16 16], ...
    'CData', iMakeCross( 8 ), ...
    'Callback', @(src,evt) iCancelEntry( src, label ), ...
    'Visible', 'off' );
newentry = struct( ...
    'Label', label, ...
    'Value', value, ...
    'LastValue', inf, ...
    'Created', tic(), ...
    'LabelText', labeltext, ...
    'ETAText', etatext, ...
    'ETAString', '', ...
    'Progress', progresswidget, ...
    'ProgressSize', psize, ...
    'Panel', mypanel, ...
    'BarCData', barcdata, ...
    'CData', cdata, ...
    'BackgroundCData', barcdata, ...
    'CanCancel', false, ...
    'CancelFcn', [], ...
```

```
    'CancelButton', cancelwidget, ...
    'Cancel', false, ...
    'Busy', false );
if isempty( entries )
    entries = newentry;
else
    entries = [entries;newentry];
end
% Store in figure before the redraw
setappdata( parent, 'ProgressEntries', entries );
if strcmpi( get( parent, 'Visible' ), 'on' )
    iRedraw( parent, [] );
else
    set( parent, 'Visible', 'on' );
end
end % iAddEntry
%-------------------------------------------------------------------------%
function entries = iDeleteEntry( entries, idx )
delete( entries(idx).LabelText );
delete( entries(idx).ETAText );
delete( entries(idx).CancelButton );
delete( entries(idx).Progress );
delete( entries(idx).Panel );
entries(idx,:) = [];
end % iDeleteEntry
%-------------------------------------------------------------------------%
function entries = iCancelEntry( src, name )
figh = ancestor( src, 'figure' );
entries = getappdata( figh, 'ProgressEntries' );
if isempty(entries)
    % The entries have been lost - nothing can be done.
    return
end
idx = find( strcmp( name, {entries.Label} ), 1, 'first' );
% Set the cancel flag so that the user is told on next update
entries(idx).Cancel = true;
setappdata( figh, 'ProgressEntries', entries );
% If a user function is supplied, call it
if ~isempty( entries(idx).CancelFcn )
    feval( entries(idx).CancelFcn, name, 'Cancelled' );
end
end % iCancelEntry
%-------------------------------------------------------------------------%
function [entry,updated] = iUpdateEntry( entry, force )
% Update one progress bar
% Deal with busy entries separately
if entry.Busy
    entry = iUpdateBusyEntry(entry);
    updated = true;
    return;
end
% Some constants
marker_weight = 0.8;
```

```
% Check if the label needs updating
updated = force;
val = entry.Value;
lastval = entry.LastValue;
% Now update the bar
psize = entry.ProgressSize;
filled = max( 1, round( val*psize(1) ) );
lastfilled = max( 1, round( lastval*psize(1) ) );
% We do some careful checking so that we only redraw what we have to. This
% makes a small speed difference, but every little helps!
if force || (filled<lastfilled)
    % Create the bar background
    startIdx = 1;
    bgim = entry.BackgroundCData(:,ones( 1, ceil(psize(1)-filled) ),:);
    barim = iMakeBarImage(entry.CData, startIdx, filled);
    progresscdata = [barim,bgim];

    % Add light/shadow around the markers
    markers = round( (0.1:0.1:val)*psize(1) );
    markers(markers<=startIdx | markers>(filled-2)) = [];
    highlight = [marker_weight*entry.CData, 255 - marker_weight*(255-entry.CData)];
    for ii=1:numel( markers )
        progresscdata(:,markers(ii)+[-1,0],:) = highlight;
    end

    % Set the image into the checkbox
    entry.BarCData = progresscdata;
    set( entry.Progress, 'cdata', progresscdata );
    updated = true;

elseif filled > lastfilled
    % Just need to update the existing data
    progresscdata = entry.BarCData;
    startIdx = max(1,lastfilled-1);
    % Repmat is the obvious way to fill the bar, but BSXFUN is often
    % faster. Indexing is obscure but faster still.
    progresscdata(:,startIdx:filled,:) = iMakeBarImage(entry.CData, startIdx, ↙
filled);

    % Add light/shadow around the markers
    markers = round( (0.1:0.1:val)*psize(1) );
    markers(markers<startIdx | markers>(filled-2)) = [];
    highlight = [marker_weight*entry.CData, 255 - marker_weight*(255-entry.CData)];
    for ii=1:numel( markers )
        progresscdata(:,markers(ii)+[-1,0],:) = highlight;
    end

    entry.BarCData = progresscdata;
    set( entry.Progress, 'CData', progresscdata );
    updated = true;
end
% As an optimization, don't update any text if the bar didn't move and the
% percentage hasn't changed
```

```
decval = round( val*100 );
lastdecval = round( lastval*100 );
if ~updated && (decval == lastdecval)
    return
end
% Now work out the remaining time
minTime = 3; % secs
if val <= 0
    % Zero value, so clear the eta
    entry.Created = tic();
    elapsedtime = 0;
    etaString = '';
else
    elapsedtime = round(toc( entry.Created )); % in seconds

    % Only show the remaining time if we've had time to estimate
    if elapsedtime < minTime
        % Not enough time has passed since starting, so leave blank
        etaString = '';
    else
        % Calculate a rough ETA
        eta = elapsedtime * (1-val) / val;
        etaString = iGetTimeString( eta );
    end
end
if ~isequal( etaString, entry.ETAString )
    set( entry.ETAText, 'String', etaString );
    entry.ETAString = etaString;
    updated = true;
end
% Update the label too
if force || elapsedtime > minTime
    if force || (decval ~= lastdecval)
        labelstr = [entry.Label, sprintf( ' (%d%%)', decval )];
        set( entry.LabelText, 'String', labelstr );
        updated = true;
    end
end
end % iUpdateEntry
function eta = iGetTimeString( remainingtime )
if remainingtime > 172800 % 2 days
    eta = sprintf( '%d days', round(remainingtime/86400) );
else
    if remainingtime > 7200 % 2 hours
        eta = sprintf( '%d hours', round(remainingtime/3600) );
    else
        if remainingtime > 120 % 2 mins
            eta = sprintf( '%d mins', round(remainingtime/60) );
        else
            % Seconds
            remainingtime = round( remainingtime );
            if remainingtime > 1
                eta = sprintf( '%d secs', remainingtime );
```

```
            elseif remainingtime == 1
                eta = '1 sec';
            else
                eta = ''; % Nearly done (<1sec)
            end
        end
    end
end
end % iGetTimeString
%-------------------------------------------------------------------------%
function entry = iUpdateBusyEntry( entry )
% Update a "busy" progress bar
% Make sure the widget is still OK
if ~ishandle(entry.Progress)
    return
end
% Work out the new position. Since the bar is 0.1 long and needs to bounce,
% the position varies from 0 up to 0.9 then back down again. We achieve
% this with judicious use of "mod" with 1.8.
entry.Value = mod(entry.Value+0.01,1.8);
val = entry.Value;
if val>0.9
    % Moving backwards
    val = 1.8-val;
end
psize = entry.ProgressSize;
startIdx = max( 1, round( val*psize(1) ) );
endIdx = max( 1, round( (val+0.1)*psize(1) ) );
barLength = endIdx - startIdx + 1;
% Create the image
bgim = entry.BackgroundCData(:,ones( 1, psize(1) ),:);
barim = iMakeBarImage(entry.CData, 1, barLength);
bgim(:,startIdx:endIdx,:) = barim;
% Put it into the widget
entry.BarCData = bgim;
set( entry.Progress, 'CData', bgim );
end % iUpdateBusyEntry
%-------------------------------------------------------------------------%
function barim = iMakeBarImage(strip, startIdx, endIdx)
shadow1_weight = 0.4;
shadow2_weight = 0.7;
barLength = endIdx - startIdx + 1;
% Repmat is the obvious way to fill the bar, but BSXFUN is often
% faster. Indexing is obscure but faster still.
barim = strip(:,ones(1, barLength),:);
% Add highlight to the start of the bar
if startIdx <= 2 && barLength>=2
    barim(:,1,:) = 255 - shadow1_weight*(255-strip);
    barim(:,2,:) = 255 - shadow2_weight*(255-strip);
end
% Add shadow to the end of the bar
if endIdx>=4 && barLength>=2
    barim(:,end,:) = shadow1_weight*strip;
```

```
    barim(:,end-1,:) = shadow2_weight*strip;
end
end % iMakeBarImage
%-------------------------------------------------------------------------%
function iCloseFigure( fig, evt ) %#ok<INUSD>
% Closing the figure just makes it invisible
set( fig, 'Visible', 'off' );
end % iCloseFigure
%-------------------------------------------------------------------------%
function iDeleteFigure( fig )
% Actually destroy the figure
busyTimer = getappdata( fig, 'BusyTimer' );
if isvalid( busyTimer )
    stop( busyTimer );
end
delete( busyTimer );
delete( fig );
end % iDeleteFigure
%-------------------------------------------------------------------------%
function iRedraw( fig, evt ) %#ok<INUSD>
entries = getappdata( fig, 'ProgressEntries' );
fobj = handle( fig );
p = fobj.Position;
% p = get( fig, 'Position' );
border = 5;
textheight = 16;
barheight = 16;
panelheight = 10;
maxRows = getappdata( fig, 'MaxEntryRows' );
N = max( 1, numel( entries ) );
Nrows = min(maxRows, N);
Ncols = ceil(N ./ Nrows);
% Check the height is correct
heightperentry = textheight+barheight+panelheight;
requiredheight = 2*border + Nrows*heightperentry - panelheight;
if ~isequal( p(4), requiredheight )
    p(2) = p(2) + p(4) - requiredheight;
    p(4) = requiredheight;
    % In theory setting the position should re-trigger this callback, but
    % in practice it doesn't, probably because we aren't calling "drawnow".
    set( fig, 'Position', p )
end
width = floor((p(3) - Ncols*2*border) ./ Ncols);
setappdata( fig, 'DefaultProgressBarSize', [width barheight] );
for ii=1:numel( entries )
    col = ceil(ii./Nrows)-1;
    row = ii - col.*Nrows - 1;
    xpos = border + (width+2*border).*col;
    ypos = p(4) - border - heightperentry.*row;

    set( entries(ii).Panel, 'Position', [xpos-border ypos+panelheight/2- ↙
heightperentry width+2*border heightperentry] );
    set( entries(ii).LabelText, 'Position', [xpos ypos-textheight width*0.75 ↙
```

```
textheight] );
    set( entries(ii).ETAText, 'Position', [xpos+width*0.75 ypos-textheight width*0.↙
25 textheight] );
    ypos = ypos - textheight;

    if entries(ii).CanCancel
        set( entries(ii).Progress, 'Position', [xpos ypos-barheight max(1,width-↙
barheight+1) barheight] );
        entries(ii).ProgressSize = max(1,[width-barheight barheight]);
        set( entries(ii).CancelButton, 'Visible', 'on', 'Position', [p(3)-border-↙
barheight ypos-barheight barheight barheight] );
    else
        set( entries(ii).Progress, 'Position', [xpos ypos-barheight width+1↙
barheight] );
        entries(ii).ProgressSize = [width barheight];
        set( entries(ii).CancelButton, 'Visible', 'off' );
    end
    entries(ii) = iUpdateEntry( entries(ii), true );
end
setappdata( fig, 'ProgressEntries', entries );
end % iRedraw
function cdata = iMakeCross( sz )
% Create a cross-shape icon of size sz*sz*3
cdata = diag(ones(sz,1),0) + diag(ones(sz-1,1),1) + diag(ones(sz-1,1),-1);
cdata = cdata + flip(cdata,2);
% Convert zeros to nans (transparent) and non-zeros to zero (black)
cdata(cdata == 0) = nan;
cdata(~isnan(cdata)) = 0;
% Convert to RGB
cdata = cat( 3, cdata, cdata, cdata );
end % iMakeCross
function iTimerFcn(fig)
% Timer callback for updating stuff every so often
entries = getappdata( fig, 'ProgressEntries' );
for ii=1:numel(entries)
    if entries(ii).Busy
        entries(ii) = iUpdateBusyEntry(entries(ii));
    end
end
setappdata( fig, 'ProgressEntries', entries );
end % iTimerFcn
```

```
function [Ea] = ROM(Ef,Em,VfInA)
    Ea = VfInA.*Ef + (1-VfInA).*Em;
end
```

```
function saveData(saveDir,curfibFrac,currun, ...
    generalData,agglomerateData,fibreData,linkageData)
    save([saveDir,sprintf('\\%s\\%s',curfibFrac,currun)], ...
        'generalData','agglomerateData','fibreData','linkageData','-v6')
end
```

```
function [mat] = vec2mat(vec)
    mat = zeros(6,6);
    mat(1,1) = vec(1);
    mat(2,2) = vec(2);
    mat(3,3) = vec(3);
    mat(1,2) = vec(4);
    mat(2,1) = vec(5);
    mat(1,3) = vec(6);
    mat(3,1) = vec(7);
    mat(2,3) = vec(8);
    mat(3,2) = vec(9);
    mat(4,4) = vec(10);
    mat(5,5) = vec(11);
    mat(6,6) = vec(12);
```